A NOVEL APPROACH TO MINERAL CARBONATION: ENHANCING CARBONATION WHILE AVOIDING MINERAL PRETREATMENT PROCESS COST

Type of Report:	Final
Reporting Period Start Date:	June 22, 2004
Reporting Period End Date:	June 21, 2007
Principal Authors:	Andrew V.G. Chizmeshya,* Michael J. McKelvy, Kyle Squires, Ray W. Carpenter, and Hamdallah Béarat.
Date Report Issued:	December 2007
DOE Award Number:	DE-FG26-04NT42124
Submitting Organization:	Arizona State University Department of Chemistry and Biochemistry, Center for Solid State Science, Science and Engineering of Materials Graduate Program, and Department of Mechanical and Aerospace Engineering Tempe, AZ 85287-1604

*Department of Chemistry and Biochemistry,
Phone: (480) 965-6072; FAX: (480) 965-2747;
E-mail: chizmesh@asu.edu

DISCLAIMER

ABSTRACT

Known fossil fuel reserves, especially coal, can support global energy demands for centuries to come, ***if*** the environmental problems associated with CO_2 emissions can be overcome. Unlike other CO_2 sequestration candidate technologies that propose long-term storage, mineral sequestration provides permanent disposal by forming geologically stable mineral carbonates. Carbonation of the widely occurring mineral olivine (e.g., forsterite, Mg_2SiO_4) is a large-scale sequestration process candidate for regional implementation, which converts CO_2 into the environmentally benign mineral magnesite ($MgCO_3$). The primary goal is cost-competitive process development. As the process is exothermic, it inherently offers low-cost potential. Enhancing carbonation reactivity is key to economic viability. Recent studies at the U.S. DOE Albany Research Center have established that aqueous-solution carbonation using supercritical CO_2 is a promising process; even without olivine activation, 30-50% carbonation has been achieved in an hour. Mechanical activation (e.g., attrition) has accelerated the carbonation process to an industrial timescale (i.e., near completion in less than an hour), at reduced pressure and temperature. However, the activation cost is too high to be economical and lower cost pretreatment options are needed.

We have discovered that robust silica-rich passivating layers form on the olivine surface during carbonation. As carbonation proceeds, these passivating layers thicken, fracture and eventually exfoliate, exposing fresh olivine surfaces during rapidly-stirred/circulating carbonation. We are exploring the mechanisms that govern carbonation reactivity and the impact that (i) modeling/controlling the slurry fluid-flow conditions, (ii) varying the aqueous ion species/size and concentration (e.g., Li^+, Na^+, K^+, Rb^+, Cl^-, HCO_3^-), and (iii) incorporating select sonication offer to enhance exfoliation and carbonation. *Thus far, we have succeeded in nearly doubling the extent of carbonation observed compared with the optimum procedure previously developed by the Albany Research Center.* Aqueous carbonation reactivity was found to be a strong function of the ionic species present and their aqueous activities, as well as the slurry fluid flow conditions incorporated. High concentration sodium, potassium, and sodium/potassium bicarbonate aqueous solutions have been found to be the most effective solutions for enhancing aqueous olivine carbonation to date. Slurry-flow modeling using Fluent indicates that the slurry-flow dynamics are a strong function of particle size and mass, suggesting that controlling these parameters may offer substantial potential to enhance carbonation.

During the first project year we developed a new sonication exfoliation apparatus with a novel sealing system to carry out the sonication studies. We also initiated investigations to explore the potential that sonication may offer to enhance carbonation reactivity. During the second project year, we extended our investigations of the effects of sonication on the extent of carbonation as a function of the following parameters: particle size distribution, the mass of solid reactant, volume fraction of aqueous solution present, sonication power, time, temperature, and CO_2 pressure. *To date, none of the conditions investigated have significantly enhanced carbonation.* Mechanistic investigations of the stirred (~1,500 rpm) aqueous olivine carbonation process indicate the carbonation process involves both incongruent magnesium dissolution and silica precipitation, which results in robust silica-rich passivating layer formation. Secondary ion mass spectrometry observation of H within the passivating layer that forms during static carbonation suggests $2H^+/Mg^{2+}$ ion exchange is associated with incongruent dissolution. Apparently, H_2O

forms at or near the olivine/passivating-layer interface during the process and diffuses out through the passivating layers during the carbonation reaction. This is also consistent with the observation that magnesite nanocrystals form within the passivating layers, further indicating the layers offer significant permeability to the key solution reaction species present during carbonation (e.g., Mg^{2+}, H^{+}, H_2O, CO_2, and HCO_3^{-}). Cracking of the passivating layer surface during carbonation is routinely observed and can be related to the tensile stress associated with the dramatic volume decrease as olivine forms silica at the reaction surface. In our YEAR 2 studies *we also demonstrated that the addition of quartz particles as an abrasive slurry component significantly enhanced carbonation*, further substantiating the importance of particle-particle abrasion in enhancing passivating layer exfoliation and carbonation.

Work during the no-cost extension period focused on the completion of various subtasks initiated in YEAR 2 aimed at elucidating the carbonations mechanisms including: (a) Extension of the CFD slurry-flow simulation studies to the case of 75 μm olivine particles, (b) studies of the effect of intrinsic nickel impurities in olivine, and the role of external parasitic nickel impurities on the olivine carbonation process and (c) investigation of the nano-morphology of olivine reacted in 2.5M $KHCO_3$ under and 5.5M $KHCO_3$ solutions.

TABLE OF CONTENTS

EXECUTIVE SUMMARY

CO_2 mineral sequestration provides permanent disposal by forming geologically stable and environmentally benign mineral carbonates. Carbonation of olivine (e.g., forsterite, Mg_2SiO_4) is a large-scale sequestration process candidate for regional implementation. Cost-effectively enhancing carbonation reactivity is central to economically viable process development. Aqueous-solution carbonation shows particular promise. However, the associated mineral activation cost currently needed to suitably enhance carbonation is too high. Lower cost pretreatment options are needed.

Collectively our work to date indicates that carbonation reactivity is a very complicated function of the aqueous solution species and their activities. Studies varying the aqueous alkali cation species present in the optimum solution developed by the ARC (0.64M $NaHCO_3$ + 1.00M NaCl) were undertaken to selectively compare cation effectiveness in enhancing carbonation/exfoliation. The alkali cation species present and their ratio were found to dramatically impact carbonation reactivity, with extent of carbonation varying by a factor of 20 from the least to the most effective alkali cation combination. The most promising solutions for enhancing carbonation to date have provided substantial increases in extent of carbonation, nearly doubling it. High concentrations of $NaHCO_3$ (2.5M) and $KHCO_3$ (5.5M) were found to be particularly effective at enhancing carbonation, with the extent of carbonation again exhibiting a strong dependence on the alkali cation species present. In contrast, the alkali chloride solutions studied to date have exhibited poor carbonation reactivity by themselves, but can substantially enhance carbonation reactivity in combination with alkali bicarbonate under select conditions. CO_2(aq) and HCO_3^- play key synergistic roles in enhancing carbonation, as carbonation drops off dramatically in the presence of HCO_3^-(aq) or CO_2 (aq) alone.

During the 2 year performance period of this project multi-phase fluid modeling and experimental investigations were also carried out to elucidate important slurry-flow parameters that enhance exfoliation and carbonation (e.g., via particle-particle and particle-wall collisions). A new microscopic wall roughness model was developed and extensively validated. Subsequent computational investigations were found to indicate wall roughness can strongly enhance cross-stream transport, particle-particle collisions and carbonation. The Fluent code was validated for application to multiphase flows to assess the complex effects governing flow. Calculation of whole systems, such as the flow loop reactor at the ARC, remains a substantial challenge. However, initial results for system components have revealed the radial distribution of flow in a component pipe can be a strong function of particle mass/size distribution and mixing history. As particle mass was found to be an important factor in cross-stream particle transport, we initiated a series of studies to explore the effect of particle mass/size distribution on exfoliation and carbonation in collaboration with the ARC using the ARC flow loop reactor and the ASU batch reactor. Initial results demonstrate that the flow dynamics and particle mass/size distribution present can substantially impact exfoliation/carbonation.

Finally, a controlled pressure and temperature 20 kHz sonication system was successfully developed for these studies during the first year. During the second year the system was refined to utilize an improved sonic probe design that substantially extends the lifetime of the probe. During the second year, the system has been utilized to explore the effects of sonication on the

extent of carbonation as a function of the weight % olivine present, particle size distribution, volume fraction of aqueous solution present, and sonication power, time, temperature, and CO_2 pressure. None of the conditions investigated significantly enhanced carbonation. As sonication is energy intensive, we have refocused our efforts to deepen our studies of the effects that aqueous solution chemistry and multiphase fluid flow can have on carbonation reactivity, as they offer the greatest promise for cost-effectively enhancing aqueous olivine carbonation.

Mechanistic investigations have extended the fundamental understanding of the passivating layer formation process during the second project year, with many of these results discussed in our recently published article "Carbon Sequestration via Aqueous Olivine Mineral Carbonation: Role of Passivating Layer Formation," in *Environmental Science and Technology (2006).*[1] These investigations indicate both incongruent magnesium dissolution and silica precipitation contribute to silica-rich passivating layer formation. Secondary ion mass spectrometry observations of the hydrogen concentration within the passivating layer suggests $2H^+/Mg^{2+}$ ion exchange occurs in association with incongruent dissolution. In the process, H_2O forms in the olivine/passivating-layer interface region and diffuses out through the layers. Internal passivating-layer diffusion of key reaction species is also consistent with our observation of magnesite nanocrystals having formed within the passivating layers. Thus, during carbonation the layers have significant permeability to key reaction species such as Mg^{2+}, H^+, H_2O, CO_2, and HCO_3^-. Cracking of the passivating layer surface during carbonation is routinely observed during both static and stirred investigations. This is related to the tensile stress at the interface between the silica-rich passivating layer and the underlying olivine host, due to the large volume reduction as the silica forms from its olivine host. The impact of abrasion on passivating layer exfoliation and carbonation was investigated via the addition of significant weight fractions of similarly sized quartz particles as an abrasive slurry. This process significantly enhanced carbonation under otherwise identical conditions, further substantiating the importance of particle-particle abrasion as a pathway for enhancing both passivating layer exfoliation and carbonation.

Studies during the no-cost extension period emphasized the impact that controlled aqueous speciation and activity and slurry-flow dynamics have on the mechanisms that control carbonation reactivity, as they offer the greatest potential to substantially reduce olivine mineral sequestration process cost. Specifically, work during the no-cost extension period focused on the completion of various subtasks initiated in year 2 aimed at elucidating the carbonations mechanisms including: (a) Extension of the CFD slurry-flow simulation studies to the intermediate 75 μm case, (b) studies of the effect of intrinsic nickel impurities in olivine, and the role of parasitic impurities on the olivine carbonation process in high concentration salt H_2O-CO_2 solutions and (c) investigation of the nano-morphology of olivine reacted in 2.5M $KHCO_3$ under and 5.5M $KHCO_3$ solutions.

INTRODUCTION

Coal, in particular, and fossil fuels, in general, are well positioned to supply the world's energy needs for centuries to come if carbon sequestration technology can be developed that is (i) permanent, (ii) environmentally benign, and (iii) economically viable.[1] CO_2 mineral sequestration provides permanent disposal, by forming geologically stable mineral carbonates.[2-5]

The materials produced are also environmentally benign and found in vast quantities in nature. The primary challenge is economically viable process development. As permanent disposal inherently avoids the ongoing monitoring, remediation and liability costs associated with long-term storage, the key is reducing mineral sequestration process cost. Cost effectively enhancing carbonation reactivity is critical. Enhancing mineral carbonation during geological (below-ground) sequestration is highly desirable as well, as it can similarly ensure long-term sequestration stability via the formation of thermodynamically stable mineral carbonates.[6]
Carbonation of Mg-rich olivine minerals (e.g., forsterite, Mg_2SiO_4) is a leading mineral sequestration process candidate.[7,8] These minerals are available worldwide in quantities sufficient to support the regional implementation of above-ground mineral sequestration.[8] Their low-cost (~$4-5/ton for mined and milled feedstock)[7,8] and exothermic carbonation (reaction 1) (8), provide the potential for economically viable process development.

(1) $\frac{1}{2}Mg_2SiO_4 + CO_2 \rightarrow MgCO_3 + \frac{1}{2}SiO_2 + 88$ kJ/mol

Recent studies at the Albany Research Center indicate aqueous solution carbonation is a promising approach.[7,8] Even without special activation, 30-50% carbonation has been achieved in an hour for <37 micron olivine reacted at 185 ^oC and 150 bar CO_2. Mechanical pretreatment via intense attrition accelerates carbonation to near completion in less than an hour and at reduced pressures and temperatures. However, the activation cost is too high for cost-effective sequestration.[8]

OBJECTIVES

Long-term, economically viable CO_2 sequestration process development will require novel approaches that enhance mineral carbonation reactivity, while bypassing costly mineral pretreatment. The potential to develop low-cost chemical pretreatment processes has been explored for years, but success remains elusive.[6] Enhancing carbonation, while avoiding the expense of olivine pretreatment, would substantially reduce process cost and provide a significant advance. We recently discovered that aqueous olivine mineral carbonation is associated with robust passivating layer formation, which substantially inhibits mineral carbonation. In this project we explored novel low-cost approaches with the potential to facilitate passivating layer exfoliation to enhance carbonation and develop an atomic level understanding of the associated mechanisms. *The goal is to develop the understanding needed to engineer new low-cost carbonation processes that avoid the cost of pretreatment activation. The primary focus is on enhancing passivating layer exfoliation, which has the potential to substantially enhance carbonation without the need for pretreatment activation.*

ACCOMPLISHMENTS

YEAR 1 Highlights:

- A controlled pressure (1 to 200 atm) and temperature (20 to 250 ^oC) 20 kHz 1500 watt sonication system was successfully developed for these studies. Elaborate tests were carried out to verify the system integrity over the high-temperature and high-pressure range of carbonation reaction conditions of interest. Initial studies of the effects of

sonication temperature, pressure and time at full power indicated no enhancement in carbonation.

- Studies varying the aqueous alkali cation species present in the optimum solution developed by the ARC (0.64M $NaHCO_3$ + 1.00M NaCl) were undertaken to selectively compare cation effectiveness in enhancing carbonation/exfoliation. *Both the alkali cation species and their ratio were found to dramatically impact carbonation reactivity, with extent of carbonation varying by a factor of 20 from the least to the most effective alkali cation combination.* The most promising solutions for enhancing carbonation to date have provided substantial increases in extent of carbonation, nearly doubling it. High concentrations of *$NaHCO_3$ (2.5M) and $KHCO_3$ (5.5M) were found to be particularly effective at enhancing carbonation*, with the extent of carbonation again exhibiting a strong dependence on the alkali cation species present. In contrast, the alkali chloride solutions studied to date have exhibited poor carbonation reactivity by themselves, but can substantially enhance carbonation reactivity in combination with alkali bicarbonate under select conditions. CO_2(aq) and HCO_3^- play key synergistic roles in enhancing carbonation, as carbonation drops off dramatically in the presence of HCO_3^-(aq) or CO_2 (aq) alone.

- Multi-phase fluid modeling and experimental investigations were also carried out to elucidate important slurry-flow parameters that enhance exfoliation and carbonation (e.g., via particle-particle and particle-wall collisions). A new microscopic wall roughness model was developed and extensively validated. Subsequent computational investigations showed that wall roughness can strongly enhance cross-stream transport, particle-particle collisions and carbonation. The Fluent code was validated for application to multiphase flows to assess the complex effects governing flow. Calculation of whole systems, such as the flow loop reactor at the ARC, remained a substantial challenge. However, initial results for system components revealed that the radial distribution of flow in a component pipe can be a strong function of particle mass/size distribution and mixing history. As particle mass was found to be an important factor in cross-stream particle transport, we initiated a series of studies to explore the effect of particle mass/size distribution on exfoliation and carbonation in collaboration with the ARC using the ARC flow loop reactor and the ASU batch reactor. Our CFD results demonstrate that the flow dynamics and particle mass/size distribution present can substantially impact exfoliation/carbonation.

YEAR 2 Highlights:

- During the second year the sonication system was refined to utilize an improved sonic probe design that substantially extends the lifetime of the probe. During the second year, the system has been utilized to explore the effects of sonication on the extent of carbonation as a function of the weight % olivine present, particle size distribution, volume fraction of aqueous solution present, and sonication power, time, temperature, and CO_2 pressure.

- Mechanistic investigations have extended the fundamental understanding of the passivating layer formation process during the second project year, with many of these results discussed in our recently published article "Carbon Sequestration via Aqueous Olivine Mineral Carbonation: Role of Passivating Layer Formation" *Environmental Science & Technology* **40**(15), 4802-4808 (2006). These investigations indicate both incongruent magnesium dissolution and silica precipitation contribute to silica-rich passivating layer formation.

- The impact of abrasion on passivating layer exfoliation and carbonation was investigated via the addition of significant weight fractions of similarly sized quartz particles as an abrasive slurry. This process significantly enhanced carbonation under otherwise identical conditions, further substantiating the importance of particle-particle abrasion as a pathway for enhancing both passivating layer exfoliation and carbonation.

- Hostile operating conditions prevent direct experimental measurements of velocity fields and volume fraction distribution of solids and the aqueous phase within stirred reactors used in sequestration applications. Numerical models therefore have an important role to play, allowing access to details of the flow that cannot be measured. We developed highly detailed CFD models of the flow within our stirred CO_2 mineral sequestration reactor. In this setting slurry-flow dynamics have been found to be a strong function of particle size and mass via macroscopic simulations using Fluent, suggesting that controlling these parameters may offer substantial potential to enhance passivating-layer abrasion/exfoliation and carbonation.

SIGNIFICANCE TO FOSSIL ENERGY PROGRAMS

Fossil fuels, especially coal, can support the energy demands of the world for centuries to come, if the environmental problems associated with CO_2 emissions can be overcome. Mineralization of stationary-source CO_2 emissions as carbonates can provide safe capture and long-term sequestration. Carbonation of Mg-rich olivine-based silicate minerals is a leading "above-ground" sequestration process candidate, which generates the stable, naturally-occurring mineral magnesite ($MgCO_3$). Optimizing the carbonation reaction rate and its degree of completion are key to process cost and viability. Collectively the studies reported from this project have significantly advanced our understanding of one of the key limiting factors in the above-ground mineral sequestration process based on the use of Mg-rich olivine silicate minerals. As such they supplement and augment the knowledge-base of mineral carbonation and treatment processes based on the olivine class of feedstock minerals and contribute to one of the research pathways being pursued by the Breakthrough Concepts focus area of DOE's Carbon Sequestration Program. Although below-ground injection has recently been adopted as a promising near-term, low-cost solution the long-term legacy issues and associate monitoring costs are not well understood. In this regard many of the outcomes of the present project are also relevant to the below-ground process in which some degree of mineralization of CO_2 is expected to occur, albeit at slightly lower temperatures than those considered here.

EXPERIMENTAL

The starting material for most of the work undertaken in our project is single crystal olivine from San Carlos, Arizona. This particular source of olivine was used to explore the effects of aqueous solution chemistry, particle size and sonication on olivine carbonation reactivity, as well as the mechanisms that govern passivating layer formation and exfoliation processes. The elemental composition was determined to be $(Mg_{0.915}Fe_{0.085})_2SiO_4$ by electron microprobe and particle induced X-ray emission analysis. X-ray diffraction (XRD) of powdered samples showed the lattice constants are in good agreement with those observed for olivine containing ~8% Fe (a = 4.763Å, b = 10.223Å, c = 5.993Å).[9,10] Trace impurities observed were well below 1%, with Ca being the principle trace impurity. Single crystals and single crystal fragments were used to facilitate microscopic observation of passivating layer formation/exfoliation and the reaction surfaces and interfaces that form during carbonation. Synthetic forsterite (Mg_2SiO_4) (99% Mg_2SiO_4; Alfa Aesar) was also used for select carbonation investigations. Twin Sisters olivine was used for the flow-loop reactor studies carried out in collaboration with the Albany Research Center.[7] The flow-loop reactor has been previously described.[8] All of the olivine size fractions investigated herein (<37 micron, 37-75 micron, < 75 micron, 75-150 micron and <150 micron) were wet screened. The extent of carbonation observed is compared with the optimum process to date for enhancing carbonation developed by the Albany Research Center (ARC),[7,8] which is summarized below for forsterite carbonation.

$$Mg_2SiO_4 + 2\,CO_2 \xrightarrow[0.64\ M\ NaHCO_3,\ 1\ M\ NaCl]{\sim 185\ ^\circ C,\ \sim 150\ atm\ CO_2} 2\,MgCO_3 + SiO_2$$

Reactions were carried out using a variety of aqueous species (e.g., Li^+, Na^+, K^+, Rb^+, Cl^-, HCO_3^-) and species activities, particle size ranges and reaction times to probe their effect on carbonation and passivating layer formation/exfoliation. 1,500 rpm stirring was used to replicate the ARC process in the studies at Arizona State University. These mineral carbonation reactions were performed using a 100ml Autoclave Engineers EZE-Seal Hastelloy C-276 reactor, which is a smaller scale version of the 2,000 ml EZE-Seal Hastelloy C-276 reactor used at the Albany Research Center. Unstirred (static) experiments were undertaken to explore passivating layer formation in the absence of particle abrasion. San Carlos olivine single crystals (~1x1x0.1cm) with well-defined initial surface morphologies were incorporated to follow the reaction interface that forms down to the atomic level.

The extent of carbonation and hydrogen content of the product materials were assessed using a Perkin Elmer Series II CHNS Elemental Analyzer. Comparative standards gave total carbon and hydrogen accuracies of ± 0.3 wt%. Extent of carbonation observations were compared with XRD intensity analysis of the product materials and found to be in good agreement. Select reaction products were analyzed structurally, morphologically, and analytically versus their extent of reaction to probe the mechanisms that govern carbonation.

XRD patterns were obtained using a Rigaku D/MAX-IIB X-ray diffractometer with Cu$K\alpha$ radiation. Scans were taken over different 2θ ranges between 10º to 70º, with 0.01°/s steps. Reaction products were imaged using a Hitachi S-4700 field-emission scanning electron microscope (FESEM) or a FEI XL-30 Environmental FESEM. Elemental analysis of individual product particles was accomplished via energy dispersive X-ray spectroscopy (EDS). Cross-sectioned samples of reaction interfaces were analyzed via FESEM and EDS mapping and high-

resolution transmission electron microscopy (HRTEM) using a JEOL 2010 with EDS and electron energy loss spectroscopy (EELS) capabilities.

Controlled pressure and temperature studies of the impact of sonication on olivine exfoliation/carbonation were carried out using our batch mineral carbonation reaction system described above and our specially developed controlled pressure and temperature sonication system described below. Sonication/carbonation studies have been carried out in stages. Hourlong carbonation studies are separated into three stages: (1) a half hour long run in the batch reactor, followed by (2) controlled sonication in the sonication system (e.g., one minute) and (3) a second half hour in the batch reactor. The above sonication runs are compared to both the standard one-hour carbonation runs using the batch reactor and runs that incorporate the sonication reaction stages (1/2 hour plus 1/2 hour batch reaction format), but without sonication.

RESULTS AND DISCUSSION

1. Investigation of the Potential that Sonication for Enhancing Exfoliation and Carbonation

1.1 Development of a Sonic Exfoliation System In this project a controlled pressure and temperature 20 kHz sonication system was successfully developed for particle exfoliation studies. The system is based on a Sonics 1500 watt power supply and a special probe to adapt to our custom controlled pressure (1 to 200 atm) and temperature (20 to 250 ^{o}C) sonication vessel. The pressure and temperature control system used is the same system used to conduct our aqueous carbonation reactions. The impeller driven stirring system is replaced by the sonic probe. Other than the interchangeable sonication and impeller components, the remainder of the system remains essentially the same. Substantial development time was required to provide an effective sealing system between the sonic probe and the controlled pressure and temperature system. The sealing system was initially arranged to be designed and developed industrially. However, the required time table was not met by the vendor, necessitating in-house design and development, significantly delaying initial system deployment (months). By end of YEAR 1 the system was fully operational over the complete range of carbonation reaction conditions of interest.

Sonication/carbonation studies were carried out in stages. Hourlong carbonation studies are separated into three stages: (1) a half hour long run in the batch reactor, followed by (2) controlled sonication in the sonication system (e.g., one minute) and (3) a second half hour in the batch reactor. The above sonication runs are compared to both the standard one-hour carbonation runs using the batch reactor and runs that incorporate the sonication reaction stages (1/2 hour plus 1/2 hour batch reaction format), but without sonication.

Initial sonication experiments were conducted by stopping the standard mineral carbonation reaction after a half hour, introducing a brief sonication period of 1-10 minutes, followed by a second half hour exposure to the standard mineral carbonation process. The overall carbonation reaction conditions remained the same as the standard carbonation conditions throughout the two halfhour mineral carbonation steps. Extent of carbonation runs that mimic the sonication runs, but without the intermediate sonication exposure, were used for baseline comparison. In each case 15 wt% <38μ San Carlos olivine was mixed with 50ml of the standard aqueous solution

(1M NaCl + 0.64 M $NaHCO_3$) and added to the batch reaction system. After 30 min of stirred reaction under the standard conditions, the reaction was stopped and rapidly cooled by using the internal cooling coil and placing the reaction vessel in ice water. This results in the temperature dropping to ~40°C within 10min. After cooling is complete, the system is depressurized and the batch reaction stirring system is replaced with the sonication system (Figure 1). The system is purged with CO_2 and subsequently brought to the starting sonication temperature and pressure. Once at temperature and pressure, sonication is then run for 1 or 10 min at full power. Once the sonication is done, the vessel rapidly cooled in ice water and depressurized. The vessel containing the reaction solution is then reattached to the batch reaction system and the second half hour carbonation step is performed.

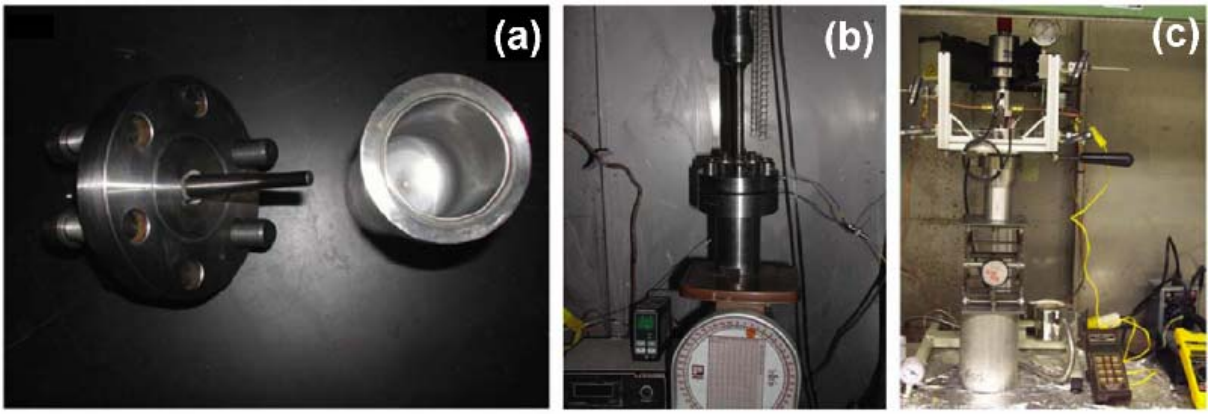

Figure 1: *The sonication and batch reaction systems at Arizona State University: (a) The sonication probe and reaction vessel; (b) the reaction vessel sealed to its sonication assembly; (c) the same reaction vessel shown in a and b sealed to the batch reactor stirring assembly.*

The extent of carbonation observed for combined ½ hour carbonation/sonication/½ hour carbonation runs is described in the YEAR 1 report (Appendix B). Under the pressures and temperatures investigated to date, sonication has not enhanced carbonation. Given that the extent of carbonation varies by as much as ±5% for the same reaction conditions, the results suggest that sonication using the initial conditions explored may even inhibit carbonation. This suggests that high power (1500 watt) sonication exposure may significantly reduce the olivine particle interactions that enhance exfoliation during the second half hour of carbonation. FESEM analysis of the particle size distribution as a function of sonication conditions was initiated at the end of the first project year to explore this effect. Samples taken before and after the sonication step were also investigated.

1.2 Enhancing the Sonic Exfoliation System During the second year, the sonic probe failed prematurely, and it became apparent that the design of the probe needed to be modified. The design was refined and improved in collaboration with Sonics Inc. based on the failure mode for the first generation of probes. The new design has substantially extended the life of the probe and has been utilized for the second year sonication studies.

Exp #	Particle Size	Mass (g) Olivine	Sonication Conditions	*Extent of carbonation**
303	<38μ	10	1min, 185 °C, 2200psi CO_2, 40% power	**8.16**
304	<38μ	10	no sonication	**31.14**
305	<38μ	10	1min, 100 °C, 2200psi CO_2, 40% power	**9.20**
306	<38μ	10	1min, 100 °C, 900psi CO_2, 40% power	**10.39**
307	<38μ	10	1min, 100 °C, 900psi CO_2, 30% power	**13.55**
308	<75μ	10	1min, 100 °C, 900psi CO_2, 40% power	**4.40**
309	<38μ	20	1min, 100 °C, 900psi CO_2, 40% power	**29.08**
310	<38μ	10	5min, 100 °C, 900psi CO_2, 40% power	**22.19**
311	<38μ	10	1min, 100 °C, 900psi CO_2, 40% power	**18.48**
312	<38μ	10	1min, 20 °C, 900psi CO_2, 40% power	**32.91**

* The carbonation reaction conditions are: standard solution of 0.64M $NaHCO_3$ + 1.00M NaCl for ½ hour at 185 °C, 2200psi CO_2 and stirring at ~1500rpm using 50ml of aqueous solution. The only difference is for #311, which used 75ml, instead of 50ml of aqueous solution for both the carbonation and sonication steps. In each case, carbonation is carried out for 30 minutes before and after the above sonication exposures. The run that did not incorporate sonication (#304) replicated the two 30-minute carbonation runs for each of the sonication runs, including the cooling and depressurization cycles between the two 30-minute carbonation runs.

Table 1: *Effect of Sonication on the Extent of San Carlos Olivine Carbonation*

During the second project year, the effects of sonication on the extent of carbonation were explored at reduced power, as the full-power investigations carried out during the first year did not show any indication that full-power sonication could enhance carbonation, let alone enhance it cost effectively. Studies were carried out as a function of the weight % olivine present, the olivine particle-size distribution, the volume fraction of the aqueous solution present, and sonication power, time, temperature, and CO_2 pressure. Representative results are shown in Table 1 above. None of the conditions investigated to date have significantly enhanced carbonation. Indeed, many of the conditions employed appear to inhibit carbonation.

2. Effects of Aqueous Chemical Speciation and Activity on Olivine Carbonation Reactivity

2.1 Variation of the Alkali Cation Species in the Standard ARC Aqueous Solution The effect of the alkali cation species and their activities on the extent of carbonation observed using the standard aqueous bicarbonate and chloride concentrations for the optimum solution developed by the ARC are shown in Table 2. The average extent of carbonation using the standard ARC solution (34%) is shown in red. As both the bicarbonates and chlorides are completely soluble at the indicated concentrations, the reactions primarily differ in the alkali cation species present and their concentrations (i.e., 0.64M vs. 1.00M, vs. 1.64M). Clearly, the extent of carbonation is a strong function of both the alkali cation species and their activities. Perhaps the most intriguing observation is the strong effect of the Na^+/K^+ ratio on extent of carbonation, with a 0.64 ratio resulting in 3% carbonation, while a 1.56 ratio (1.00/0.64) yields 41% carbonation. The strong impact of the Na^+/K^+ ratio on carbonation reactivity is further explored below, as it suggests significant potential to further enhance carbonation reactivity.

2.2 Effect of the Na^+/K^+ molar ratio, at constant $[HCO_3^-]$ and $[Cl^-]$ A significant finding of our study is that at 0.64M HCO_3^- and 1.0M Cl^-, the carbonation reactivity of San Carlos olivine is a strong function of the Na^+/K^+ molar ratio. This further underscores the impact that alkali cation speciation and activity can have on passivating layer effectiveness and carbonation reactivity. The extent of carbonation substantially increases with increasing $[Na^+]/[K^+]$ ratio up to 1.56 and then falls off slightly to within experimental error of the average extent of carbonation observed for the standard 0.64M $NaHCO_3$ + 1.0M NaCl aqueous solution (33.6%). At $[Na^+]/[K^+]$ = 1.56, the improvement in extent of carbonation appears to be significant, suggesting the associated alkali cation combination may better mitigate passivating layer formation and enhance carbonation. Combined with the above results, it is apparent that both the type and relative concentration of alkali cation species present in the aqueous solution can dramatically impact carbonation. The results also underscore the potential that combinations of alkali cation species can act synergistically to enhance carbonation. Based on these results, we undertook studies in YEAR 2 to further explore the potential that different combinations and concentrations of cation species offer to enhance carbonation.

0.64M $AHCO_3$ (A = Li,Na,K)

1.00M ACl (A = Li,Na,K)	Li	Na	K
Li	23%	18%	24%
Na	4%	34%*	41%
K	2%	3%	15%

* Extent of carbonation observed for the optimum aqueous carbonation solution developed by the Albany Research Center

Table 2: *Effect of Exchanging Alkali Cation Species in the Optimum ARC Aqueous Solution (0.64M $NaHCO_3$ + 1.00M NaCl) on the Extent of Carbonation*

2.3. Effect of varying alkali bicarbonate concentration ($NaHCO_3$ and $KHCO_3$) Two series of experiments were conducted for increasing sodium and potassium bicarbonate concentrations, due to their higher solubility limits relative to lithium bicarbonate under mineral carbonation reaction conditions. The extent of carbonation observed as a function of $[MHCO_3]$ M = Na or K is described in detail in our YEAR 2 report (Appendix B). In both cases, increasing the $[MHCO_3]$ substantially increases the extent of carbonation, with 5.5M $KHCO_3$ nearly doubling the extent of carbonation in comparison with the standard 0.64M $NaHCO_3$ + 1.0M NaCl aqueous solution (63% vs. 34%). Both the $[HCO_3^-]$ and alkali cation species present substantially impact the extent of carbonation. This follows, for example, from the extent of carbonation observed for 2.5M $NaHCO_3$ (57%) being much higher than that observed for 2.5M $KHCO_3$ (15%), indicating Na^+ is substantially more effective than K^+ in mitigating passivating layer effectiveness and enhancing carbonation. It also follows from observations described below that alkali chloride solutions exhibit very poor carbonation reactivity, underscoring the importance of HCO_3^-. The importance of the alkali cation species is further underscored by our observation that 7.5M $RbHCO_3$ was found to be substantially less effective in enhancing carbonation (40%) than 5.5M $KHCO_3$ (63%) or 2.5M $NaHCO_3$ (57%).

Another significant observation from our experiments is that the above $NaHCO_3$ and $KHCO_3$ concentrations significantly exceed the aqueous solubility of $NaHCO_3$ and $KHCO_3$ under ambient temperature and pressure, ~ 1.3M and ~3.6 M, respectively, whereas the concentration of $RbHCO_3$ is slightly lower than its ambient solubility of 7.9M. However, these solubilities may

be expected to increase substantially with increasing temperature, with possibly small contributions from increasing pressure as well, allowing higher aqueous concentrations of $NaHCO_3$ and $KHCO_3$ to be utilized under mineral carbonation reaction conditions, as seen in Figure 2. However, the solubility under mineral carbonation reaction conditions will also be impacted by the activity of CO_2 present, which may serve to inhibit alkali bicarbonate solubility. The potential for increased alkali bicarbonate solubility under reaction conditions motivated the above studies, even though the bicarbonate concentrations used exceed the solubility limits for aqueous sodium and potassium bicarbonate solutions under ambient conditions. We have not yet established whether we have reached the solubility limit for these solutions under reaction conditions. To explore this effect we plan to pursue tests at lower temperatures and pressures (which can lower process cost, but can also impact Na/K bicarbonate solubility).

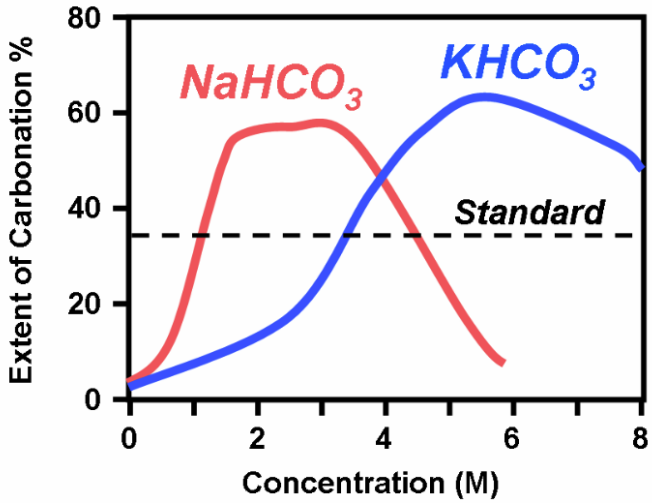

Figure 2: *Extent of carbonation of San Carlos Olivine as a function of $NaHCO_3$ and $KHCO_3$ concentration after 1h at 185°C, 2200psi of CO_2, and stirring at ~1500rpm. Dashed horizontal line represents the extent of carbonation (~34%) of a run using the standard solution 1.0M NaCl + 0.64M $NaHCO_3$.*

2.4. Comparison of the Extent of Carbonation Observed for 2,200 PSI CO_2 and 5.5M $KHCO_3$ Separately and Combined To elucide the origin of the increase in the carbonation reactivity in the above results we carried out a series of experiments in (i) distilled water under 2,200 psi CO_2, (ii) 5.5M $KHCO_3$ under 2,200 psi CO_2, and (iii) 5.5M $KHCO_3$ under 2,200 psi He. Clearly, the aqueous $KHCO_3$ solution has a dramatic effect on carbonation reactivity, with very little carbonation observed using distilled water alone. In the absence of CO_2, i.e., under He, the carbonation reactivity drops substantially compared with that observed for 5.5M $KHCO_3$ under 2,200 psi CO_2. Analysis of the K^+ concentration in the aqueous solution after the reaction is complete (diluted so that all the $KHCO_3$ dissolves under ambient conditions) appears to provide interesting insight into the carbonation mechanism. Initial results indicate that no decrease is observed in the aqueous K^+ concentration after carbonation under 2,200 psi CO_2, whereas a significant decrease is observed for 5.5M $KHCO_3$ under 2,200 psi He. This suggests that $KHCO_3$ may not be consumed during carbonation under CO_2.

2.5. Exploring the Potential that Potassium/Sodium Bicarbonate Solutions Offer to Enhance Aqueous Olivine Carbonation Reactivity In order to more fully explore the potential high aqueous bicarbonate concentrations offer to enhance carbonation reactivity, we investigated the carbonation reactivity associated with the most promising bicarbonate solutions ($NaHCO_3$ and $KHCO_3$) as a function of their aqueous concentration and Na/K ratio. Plots of extent of

carbonation versus [$NaHCO_3$] and [$KHCO_3$] revealed a strong increase in carbonation extent is observed with increasing bicarbonate concentrations for both sodium and potassium bicarbonate, which peaks at relatively high bicarbonate concentrations and begins to decrease at still higher bicarbonate concentrations. The peak extent of carbonation is ~2.5M for $NaHCO_3$ and ~5.5M for $KHCO_3$ (as shown in Figure 2, above). Aqueous solutions containing CO_2(aq) and Na^+ or K^+, and HCO_3^- have provided the best synergistic combination of solution ions for enhancing mineral carbonation to date, nearly doubling the extent of carbonation observed using the standard ARC solution. It is interesting to note the strong positive effect that Na^+ has on carbonation in comparison with similar concentrations of K^+, highlighting the important role that cation species can play in carbonation. It is also important to note that further increasing the bicarbonate concentration eventually leads to lower carbonation extents.

If the above effect were simply associated with reaching the solubility limit of $NaHCO_3$ and $KHCO_3$ at 185 ^oC and 150 atm CO_2, the extent of carbonation might be expected to reach a plateau at the highest bicarbonate concentrations, with any further bicarbonate that is added simply remaining in solid form. Instead, the extent of carbonation decreases significantly for increasingly high Na/K bicarbonate concentrations, which may be associated with decreasing CO_2 solubility with increasing ionic Na/K bicarbonate concentrations. This hypothesis is consistent with previous simulations that indicate that increasing ionic NaCl concentrations may significantly reduce aqueous CO_2 solubility (see below). Future NMR probe and simulation investigations are planned to explore the effect of increasing Na/K bicarbonate concentrations on CO_2 solubility to assess the extent to which the above decrease in carbonation extent may be related to decreasing aqueous CO_2 solubility at very high bicarbonate concentrations.[11,12] We have previously observed that using mixtures of $NaHCO_3$ and $KHCO_3$ and varying the Na^+/K^+ ratio can significantly improve the extent of olivine carbonation when starting with the standard solution of 0.64M $NaHCO_3$ + 1.00 M NaCl (see Figure 3 in the YEAR 2 report, Appendix B). This led us to explore the potential for further enhancing carbonation reactivity by varying the Na^+/K^+ ratio for high bicarbonate concentrations [i.e., 2.5 M (Na/K)HCO_3]. Our reaction studies indicate that the Na^+/K^+ ratio has a dramatic impact on carbonation reactivity. The extent of carbonation dramatically increases with increasing Na^+/K^+ ratio, but does not exceed the value observed for 2.5 M $NaHCO_3$. Although a few more data points are needed at lower Na/K ratios, varying the ratio does not appear to hold much promise for enhancing carbonation.

Finally, we explored the effect of reaction pressure on the extent of carbonation observed using 2.5M $NaHCO_3$. 185°C was selected as the optimal carbonation temperature for 2.5M $NaHCO_3$. The same feedstock material (<38μ San Carlos olivine) was tested with the other reaction conditions identical to those used for the reaction temperature studies. The extent of carbonation is a strong function of CO_2 reaction pressure, exhibiting a strong increase in carbonation with increasing pressure (e.g., from 32% at 1,000 psi to 70% at 3,000 psi), consistent with increasing CO_2(aq) activity increasing the extent of carbonation. It is informative to compare these results with our observations for increasing bicarbonate concentrations. Increasing extents of carbonation with increasing CO_2(aq) activities is further consistent with the hypothesis that increasing bicarbonate concentrations may suppress CO_2(aq) solubility and carbonation for high bicarbonate concentrations. Again, NMR probe and simulation investigations are planned to further explore this possibility by investigating the effect of increasing Na/K bicarbonate concentrations on CO_2(aq) solubility.

3. Multi-phase Fluid Modeling and Experimental Investigations to Elucidate Key Slurry-Flow Parameters that Enhance Exfoliation and Carbonation

Two hierarchies of fluid-flow modeling were pursued to enhance contact with experiments focusing on particle-size effects. The primary aim of is identify and elucidate those effects that may be crucial to optimizing the fluid dynamics of sequestration processes to enhance passivating layer exfoliation and carbonation. One of the two hierarchies of fluid flow modeling focused on "microscopic" modeling of particle-laden flows in which the aim was to investigate stochastic approaches to representing wall roughness. "Macroscopic" modeling approaches were applied to predict the behavior in reactor sections in which the aim is to assess/incorporate current engineering models to predict the average properties of liquid-solid turbulent flows. As described in greater detail below, these calculations were performed using Fluent and applied to conditions representative of those in the flow-loop reactor at the Albany Research Center. The third phase of the effort that was initiated during YEAR 1 was analysis and design of experiments performed at ARC and ASU in which the main goal is to quantify and understand particle size effects on carbonation levels. The primary aim of efforts in this area of the project during YEAR 2 were devoted to further analysis and publication of the experimental measurements focusing on particle size effects and macroscopic fluid flow modeling that will be used for parametric studies of the effect of flow rate, solids loading, and particle size on the average properties of liquid-solid mixtures representative of those encountered in mineral sequestration applications.

3.1 "Microscopic" Fluid Flow Modeling The specific aim of the work on "microscopic" modeling focused on wall roughness and representing the effects of rough surfaces on particle transport. Here the motion of individual particles is considered, in contrast to the "macroscopic" modeling described in the next section, which treats the averaged properties of the particulate phase by solving field equations rather than using Lagrangian tracking of individual particles. A thorough description of our microscopic model is contained in our YEAR 1 report (Appendix B). In brief, the simulations used to assess "microscopic" fluid flow modeling revealed that particle transport and mixing can be enhanced by interactions with roughened surfaces. While our simulations are idealized in order to enable the application of simulation techniques that resolve turbulent fluctuations, the computations highlight the importance of the basic effect of roughness, which is to transfer the mean streamwise momentum of the particles to the fluctuating velocities that are normal to the surface. This is an important mechanism for enhancing transport across the entire channel and facilitating particle-particle and particle-wall collisions, exfoliation and carbonation.

3.2 Macroscopic Fluid Flow Modeling The simulations performed in this phase of the work designed to closely mimic the experiments conducted in the ARC flow loop reactor at the Albany Research Center (see YEAR 1 report, Appendix B). In these simulations we adopted an Eulerian approach, which does not attempt to track individual particles, provides a more computationally efficient method. The simulations provide accurate predictions of flow properties such as the mean velocity, pressure drop, and volume fraction distributions at different zones in the flow loop reactor. Computations were performed with and without the solids phase in order to assess the influence on quantities such as pressure drop. Our initial efforts focused on changing the particle volume fraction distribution by modeling ribs along the inner wall of the

pipe geometry. Flow simulations using ribs have revealed dramatic changes in the particle concentration distribution by the inclusion of ribs along the inner lining of the pipe wall. While preliminary, these results might highlight a possible re-design of the reactor which may enhance carbonation, while avoiding flow mixers, which require cleaning after each run. This may eliminate or reduce the cleaning cycles required using the current design, lowering the cost of system operation. All the computations consider fluid flow through a pipe and are used to assess the effect of physical parameters (e.g., the volume fraction) and numerical procedures used to assist the convergence of the system of equations.

3.3 Effects of Particle Size and Particle Size Distribution The above modeling investigations indicate that the reactant particle size distribution may be a key factor impacting particle collision frequency, momentum transfer, exfoliation and carbonation. During the first year of this project we explored the effect of particle size distribution using the ASU batch reactor and began partner studies in collaboration with the Albany Research Center to explore the effect of size distribution using their Flow-Loop reactor. Initial observations vs. particle size using the Flow-Loop reactor indicate that the extent of carbonation can remain quite high for larger feedstock particles. As the large majority of the grinding cost associated with preparing the <400 mesh feedstock comes in reducing the material from <200 mesh to <400 mesh, the ability to effectively carbonate larger <200 mesh olivine feedstock can substantially reduce process cost. Further details of the studies in this area are contained in our YEAR 2 report (Appendix B).

3.4 Exploring the Effect of Feedstock Particle-Size Distribution on Aqueous Olivine Carbonation Reactivity During the second year of this project we have focused our simulation efforts on the simpler ASU batch reactor, which provides the critical advantage of being able to simulate the multiphase fluid flow for the whole system. This allows direct connection with experimental observations as we seek to utilize our simulations to control the multiphase fluid flow dynamics to enhance particle-particle and particle-reactor passivating-layer abrasion and carbonation. The latter slurry-flow modeling investigations indicate that the spatial olivine particle distribution and the associated velocity vectors during aqueous mineral carbonation (using the 100ml ASU batch reactor) are highly dependent on the feedstock particle size distribution, as discussed below. These studies suggest that controlling the particle size distribution during mineral carbonation may provide a cost-effective avenue to enhance particle abrasion and olivine carbonation.

To begin to explore the associated potential to enhance carbonation, the extent of carbonation was explored as a function of the particle-size distribution associated with 10 gram San Carlos olivine mineral carbonation feedstock samples. The extent of carbonation for particle size fractions of freshly ground and wet-sieved San Carlos olivine were investigated in both the standard 0.64M $NaHCO_3$ + 1M NaCl and 2.5M $NaHCO_3$ aqueous solutions. Duplicate runs using the standard solution gave reproducible extent of carbonation results for these feedstock batches as follows: <38μ feedstock: 37%; 38-75μ feedstock: 5%; 75-150μ feedstock: 4%. The <38μ and 38-75μ batches were mixed to generate <75μ fractions with different weights of the <38μ and 38-75μ particle size fractions. The extent of carbonation observed using the standard aqueous solution (0.64M $NaHCO_3$ + 1M NaCl) for the various particle size distributions showed that varying the particle size distribution by blending different amounts of the 38-75μ fraction with the <38μ fraction did not significantly impact the extent of carbonation observed, indicating in

this case varying the particle size distribution did not significantly impact particle abrasion and exfoliation. In other words, the <38µ and 38 to 75µ feedstock materials appear to experience the same extent of carbonation independent of the wt% ratio used.

The extent of carbonation was also explored for select <38µ, <75µ, and <150µ feedstock materials using an aqueous 2.5M $NaHCO_3$ solution to probe whether the highly reactive aqueous solution chemistry associated with high bicarbonate concentrations impacts the relative reactivity of different particle size distributions. In this case, we explored the relative carbonation reactivity of the above particle size ranges for the standard 0.64M $NaHCO_3$ + 1M NaCl and 2.5M $NaHCO_3$ aqueous solutions. We then compared the average extent of carbonation observed for the above particle-size fractions for both solutions. A 35% improvement in carbonation is observed for the <38µ fraction using 2.5M $NaHCO_3$. By comparison, a 146% and 158% improvement is observed for the <75µ, and <150µ fractions, respectively, suggesting high concentration bicarbonate solutions can substantially further enhance the relative carbonation reactivity of larger olivine particle-size fractions. Being able to effectively carbonate olivine feedstocks with such larger particle-size fractions offers the potential to substantially reduce feedstock grinding cost and substantially lower mineral sequestration process cost.

3.5 Exploring the Effect of Abrasive Slurry Additives on Passivating-Layer Exfoliation and Olivine Carbonation In order to explore the potential of particle abrasion to improve the extent of carbonation, quartz particles were incorporated during olivine mineral carbonation as an abrasive agent for promoting passivating-layer exfoliation and carbonation. In this case, synthetic olivine (forsterite: Mg_2SiO_4) was used as the feedstock. The weight % quartz was varied from 0 to 80% of the 10g feedstock charge used. The carbonation studies were performed using the standard aqueous solution (0.64M $NaHCO_3$ + 1M NaCl), with the reactions carried out for 1h at 185°C under 2200 psi CO_2, with ~1500rpm stirring. Under these conditions our studies showed that the addition of the quartz abrasive yields a ~70% extent of carbonation, increasing to 84% for 60 weight % quartz, consistent with enhanced passivating-layer abrasion, as shown in Figure 3. However, carbonation decreased at higher quartz concentrations (i.e., 80 wt. %). We hypothesize that this may be associated with increasing quartz-quartz particle abrasion reducing its effectiveness at passivating-layer abrasion. To explore this hypothesis, 10g

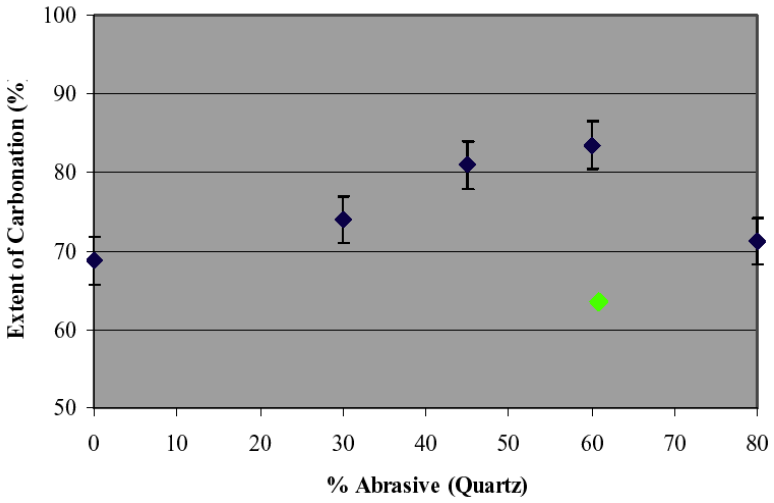

Figure 3: *Extent of carbonation observed for synthetic olivine as a function of the wt. % quartz abrasive added (blue diamonds). Reaction conditions are 0.64M NaHCO3 + 1M NaCl, 1h, 185°C, 2200 psi CO_2, and 1500rpm stirring. The green diamond shows the extent of carbonation observed using self-abraded quartz particles.*

of quartz was run for an hour under the same mineral carbonation conditions, including 1,500 rpm stirring to simulate the enhanced quartz-quartz abrasion that may occur when high quartz concentrations are used as an abrasive to enhance olivine carbonation. The product was filtered, rinsed, and dried. 6g of the "abraded quartz" was run with 4g of forsterite to explore its abrasive potential. Our results confirm that the extent of carbonation is substantially lower than that observed with fresh quartz, consistent with self-abrasion reducing the effectiveness of quartz as a passivating-layer abrasive agent at higher quartz concentrations. Collectively the reduced effectiveness may be associated with both particle-size reduction and smoothing of the quartz particle edges at higher quartz concentrations.

Experiments were also performed to explore the role of temperature and pressure. Here the extent of carbonation was studied over the range of temperatures where carbonation is reasonably effective, indicating that abrasive quartz additives are effective at enhancing passivating-layer exfoliation and carbonation at least from 155 to 215 ^{o}C. It is particularly interesting to note the extent of carbonation observed with and without the quartz abrasive at 185 ^{o}C. In this case, the enhanced extent of carbonation observed is greater per 10g of feedstock (61% vs. 56% per 10g feedstock), even though 20% of the feedstock, quartz, cannot carbonate. This key observation indicates that controlled use of low cost abrasives may offer the potential to reduce mineral sequestration process cost. Any effort to optimize carbonation with such controlled abrasive additions should, of course, be integrated together with control of the slurry fluid-flow conditions to maximize particle abrasion and passivating-layer exfoliation. In the next set of experiments the optimal reaction temperature (185 ^{o}C) was selected, with 20 wt% quartz again used as the passivating-layer abrasive. The quartz abrasive was observed to effectively enhance olivine carbonation over the range of pressures studied to date (1,500 to 3,000 psi) indicating that quartz is effective as a passivating layer abrasive over a range of pressures as well as a range of temperatures. The above studies as a function of pressure and temperature indicate the silica-rich passivating layers that form retain their brittleness and ability to exfoliate over a range of reaction temperatures and pressures relevant to aqueous olivine mineral carbonation. The above observations underscore the importance of passivating-layer exfoliation/abrasion in enhancing olivine carbonation reactivity. In these studies, quartz was selected as a model lowcost abrasive that should not significantly impact the aqueous solution chemistry, hence providing insight into the potential abrasives offer to enhance carbonation.

Collectively, our results suggest that a reaction process that offers the potential to better enhance feedstock abrasion, such as a fluidized-bed approach, may lead to significant further improvements in carbonation reactivity. In either case the associated slurry/fluidized bed flow dynamics can greatly impact the effectiveness of passivating layer abrasion/exfoliation and olivine mineral carbonation reactivity. Further details and discussion are provided in the YEAR 2 report (Appendix B).

3.8 Exploring the Slurry-Flow Dynamics during Olivine Carbonation via Multiphase Fluid Modeling

Simulations of the multiphase flow in the ASU mini-reactor were systematically carried out for two size fractions: a solids phase consisting of 37μm diameter particles and a second simulation using 150μm diameter particles. Simulations for a third, intermediate, size fraction (75μm

diameter particles) were undertaken during the no-cost extension period. The main motivation for the simulations of the slurry in the mini-reactor is to investigate the possible causes contributing to the difference in reaction rates measured in experiments for comparable size fractions used in the ASU 100ml batch reactor (the mini-reactor) and the Albany flow loop reactor.

The ASU mini-reactor geometry is modeled using Gambit in which a computational mesh is created within a computer-aided drawing of the reactor vessel. To reduce the computational expense, symmetry conditions are utilized to advantage with a grid generated for $1/6^{th}$ of the reactor. The top view of the reactor geometry is shown in Figure 4, while a cross-section of the modeled section of the grid is shown in Figure 5. The cross section wireframe view of the geometry (Figure 5) shows the reactor contents at the initial state of the calculation (t=0 seconds), when the paddle wheel is at rest. In the experiments, 10 grams of finely ground olivine ore of a pre-determined size fraction, is added to the reactor (c.f., Figure 5 for a schematic representation). The reactor is then filled with an aqueous solution (50 *ml*) containing 1*M* NaCl + 0.64*M* $NaHCO_3$. This is followed by elevating the temperature and the system pressure to 185°C and 150 atmospheres by injecting CO_2 in the reactor.

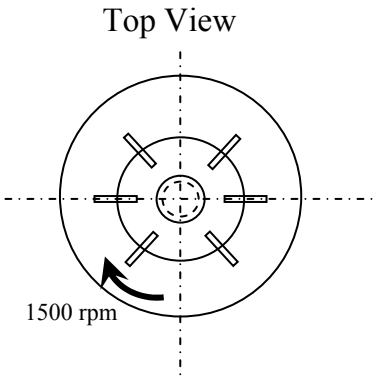

Figure 4: *Computer Aided Design (CAD) wireframe of the ASU mini-reactor*

In the simulations the solids phase is initially prescribed in the bottom of the reactor vessel at the maximum packing limit of 63%. The NIST Chemistry web-book (http://webbook.nist.gov/chemistry/fluid/) is used as a reference to obtain values of density and viscosity of water and CO_2 for use in the simulations. Density values for the water-CO_2 mixture are obtained by taking an average of the densities of water and CO_2. Since the viscosity

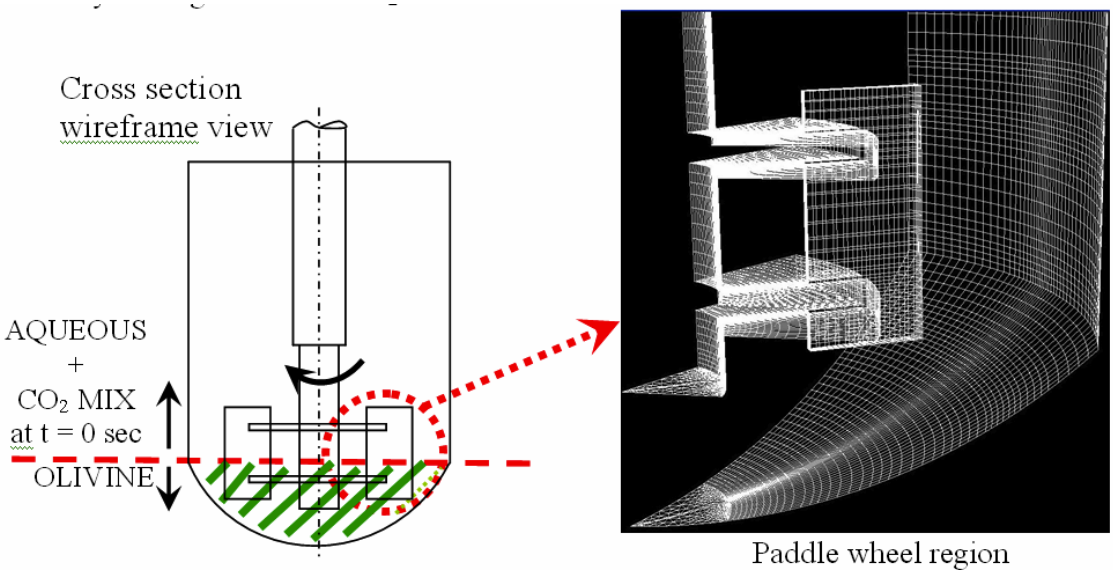

Figure 5: *Cross-sectional wireframe of ASU mini-reactor with zoomed view of the paddle-wheel.*

calculations do not follow the average rule, and since there are no known experimental values of viscosity of the aqueous mixture under the specified temperature and pressure, the current simulations are performed using the viscosity of water at the elevated conditions (150 atm and 185^{o}C) as the viscosity of the aqueous phase. The current simulations do not account for the solution of the energy equation, as the system is being simulated under isothermal conditions. The elevated temperature is reflected in the density and viscosity values of the mixture. Coupling between the phases is achieved using inter-phase momentum transfer terms that account for the momentum transfer between the granular olivine phase and the aqueous phase formed by mixing water and CO_2.

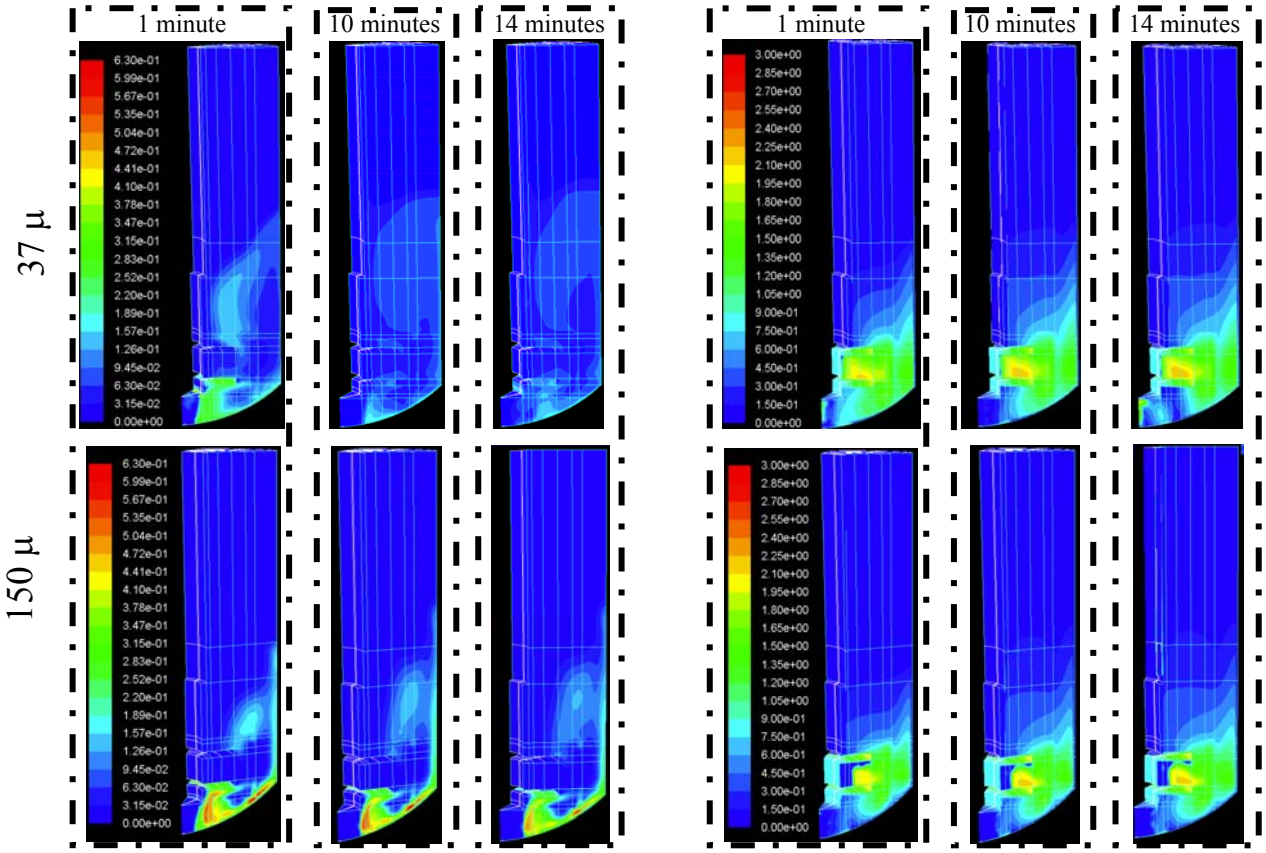

Figure 6: *Contours of (a) volume fraction of olivine, values in fraction, (b) velocity distribution of olivine, values in m/s*

Simulation results which are detailed below were performed using a time step of 1 second. Considering the rotational speed of the impeller in the reactor at 1500 rpm, a time step of 1 second corresponds to 25 revolutions. Initial studies have been performed using this relatively large time step in order to provide a preliminary assessment of the influence of particle size on the subsequent flow field solutions. The results below show that there indeed are differences in the phase distribution and velocity distribution patterns for different size fractions.

Figure 6(a) shows contours of the olivine volume fraction distribution for the 37µm case and the 150µm case for time intervals corresponding to t=1, 10 and 14 minutes from the start of the

paddle-wheel rotation. A clear demarcation can be observed in the contours, red indicating higher values and blue color indicating lowering values of volume fraction. The figure shows that the olivine volume fraction for the 150μm case exhibits a relatively higher concentration at the bottom of the cylinder and that the contours for the 37μm correspond to smaller gradients indicative of a relatively greater mixing of the particles. Figure 6(b) shows contours of the particle velocity distribution for the corresponding cases for the same time intervals. Higher velocity is observed near the vicinity of the paddle wheel due to the rotation of the paddle.

Recent simulations (end of YEAR 2 and no-cost extension period) have been performed using much smaller time steps than in the initial runs, corresponding to a paddle wheel rotation of approximately 5 degrees per step. Numerical tests show that convergence of the system of equations occurs after approximately 25 iterations within each time step. Preliminary simulations performed with smaller time steps (2^o per time step) did not yield significant changes in the results, justifying the timestep corresponding to 5 degrees of revolution. The current simulations using the shorter timesteps are underway, though they have not yet progressed sufficiently far in time to allow accumulation of statistics for analysis.

The volume fraction distribution of the 37μm particles for one second of paddle wheel rotation (corresponding to 25 revolutions) has been animated as a movie (available upon request), which highlights the motion of the olivine phase when subjected to the agitation imposed by the impeller. An analysis of the visualization indicates that, generally throughout the simulation, the rotation of the paddle causes gradual accumulation of the olivine granules along the direction of the paddle rotation. These olivine granules are then ejected upwards due to the high speed of the paddle blades, which causes a swirling motion within the reactor. This build up is another contributing cause to the change in the contour colors as the simulations progress. Analysis of the structural features of the flow in the mini-reactor as well as the statistics of the volume fraction distribution and velocity distribution for the different size fractions are of key interest for enhancing particle abrasion, passivating layer exfoliation and mineral carbonation.

4. Understanding the Mechanisms that Control Passivating Layer Formation and the Impact the Above Approaches Have on Exfoliation and Carbonation Mechanisms

During the second project year, we evaluated the effectiveness of a variety of reaction flow dynamics, alkali cation solution chemistry, and sonication approaches to enhance carbonation. These studies have involved carbon elemental analysis and X-ray powder diffraction of many scores of product samples. The primary objective is to identify those approaches that are most effective in enhancing carbonation. Our mechanistic investigations have substantially focused on enhancing our understanding of passivation layer structure, composition and behavior. The objective is to enhance our fundamental understanding of the passivating-layer formation, growth and exfoliation process, while we are exploring in parallel the impact that reaction flow dynamics, alkali cation solution chemistry, and sonication have on exfoliation/carbonation. Substantial progress has been made in enhancing our understanding of passivating layer formation processes during the second project year. A substantial amount of our progress during the first and second project years is summarized in our recent publication of a comprehensive study describing the silica-rich passivating-layer formation, growth, and exfoliation processes that accompany olivine mineral carbonation (see Appendix A, *Environmental Science &*

Technology **40**(15), 4802-4808 (2006)). Additional studies carried out during the second project year and the no-cost extension period are described below.

The possible role of hydrogen/water within the passivating layers during carbonation is of substantial interest, as proton/Mg^{2+} exchange may occur with water formation near the olivine/passivating-layer interface during olivine dissolution/carbonation. Several investigators have shown that small amounts of water molecules can dissolve and diffuse in SiO_2, forming SiOH groups in the process. The possible sites for such silanol formation are associated with dangling silicon or oxygen bonds in the network or on glass surfaces, as shown schematically in Figure 7. For example, SiOH has been shown to form easily at dangling bonds on amorphous silica fracture surfaces.[9] There are several possible locations for high concentrations of dangling bonds in the passivating layer/ interface regions during carbonation, including free surfaces, vertical cracks that penetrate the passivating layer, and within the passivating layer itself, through which the aqueous carbonation species can diffuse.

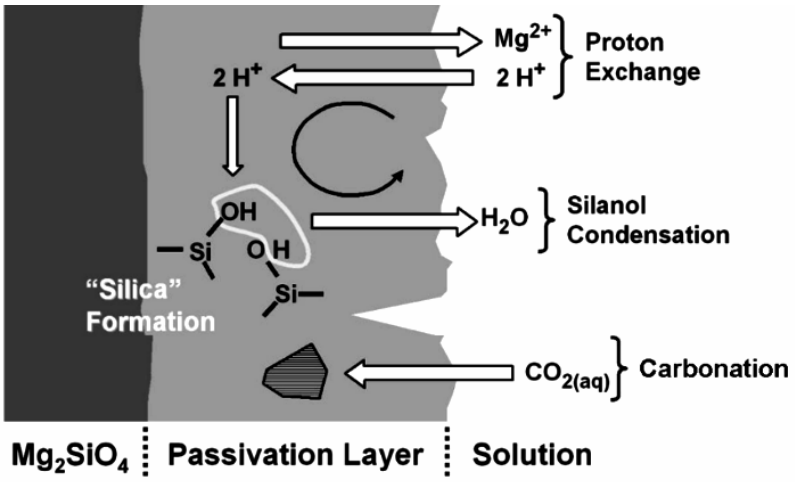

Figure 7. *Schematic illustration of the various reaction mechanisms and diffusion species proposed to be involved in the formation and growth of the silica-rich passivation layers. Dark gray region: forsterite, light gray region: "SiO_2" passivation layer. The reaction front is shown as the discrete boundary between the light and dark gray regions. The proton exchange and silanol condensation processes, shown at the top of the figure, account for the stoichiometric removal of Mg and O from the forsterite lattice. Carbonate formation reactions within the layer may also occur by diffusion of aqueous CO_2 into the passivation layer.*

As discovered in the first project year, the olivine surface reacted under static conditions exhibits a silica-rich sponge-like morphology, as shown in the left of Figure 8. Sonication of the as reacted surface in aqueous media exposes the underlying cracked silica-rich surface morphology shown in the right of Figure 8. Energy dispersive x-ray spectroscopy showed that the passivating-layer regions for both unsonicated and sonicated specimens were silica rich, while the areas at the bottom of the fractures in the sonicated passivating layers corresponded to olivine. Although the former result is not quantitative, as the incident electron beam penetrated through the passivating layer and the x-ray emission volume included regions of passivating layer and the underlying olivine, qualitative observations from multiple samples have clearly established that the passivating layers seen in Figure 8 are silica-rich, in agreement with the above analytical HRTEM observations. The complex morphology of the curled-up silica-rich surface structure of the passivating layer shown in the left of Figure 8 is not entirely due to the stress system developed in the nearsurface region of the specimen, which is discussed below, and in greater detail in the YEAR 2 report (see Appendix B). Part of this morphology is also due to the solubility of SiO_2 in neutral to slightly acidic water with a pH very similar to the aqueous

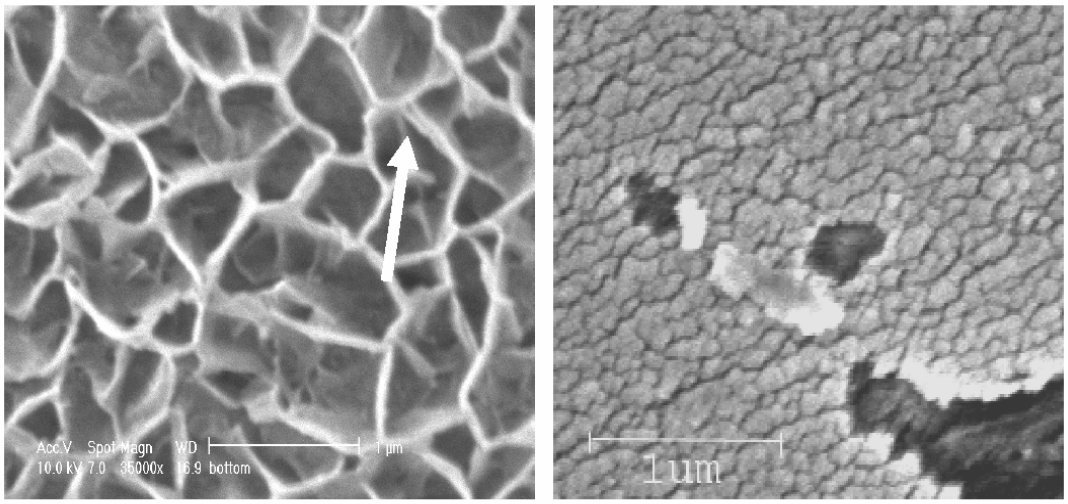

Figure 8: *FESEM images (secondary electron) of the olivine surface after reaction for 4 hours at 185 ₀C under 2,200 psi CO_2. The left image, recorded before sonication, shows the sponge-like character of the silica-rich passivating layer that has curled up/grown away from the olivine reaction interface. One region where two curled up pieces are separated by a narrow crack is highlighted by the arrow. The right image, after sonication, shows that the curled passivating-layer structure is removed by sonication to reveal the underlying fractured, silica-rich island-like structure shown. Some of the silica-rich islands have broken away from the surface to reveal the underlying olivine- rich crystal core.*

solution incorporated herein (pH ~ 6.85).[13,14] Several investigators have shown that small amounts of amorphous SiO_2 will dissolve in neutral to slightly acidic water,[15,16] and the presence of aqueous NaCl can enhance the dissolution kinetics.[17]

In order to better understand the potential roles that $2H^+/Mg^{2+}$ exchange and water diffusion play during passivating-layer formation and carbonation, we explored the passivating-layer/olivine surface reaction region using O^+ SIMS profiling. A layer of Si was deposited by e-beam evaporation under UHV prior to SIMS analysis of the surface, to establish a steady state SIMS profiling rate before beginning to analyze the passivating-layer region. The initial rise of the Si curve is due to the Si cap layer. Analysis of the surface of the passivating layer begins at the left side of the slat Si maximum. Note that the H curve exhibits a maximum at the beginning of the passivating layer, and then a secondary maximum near the passivating-layer/olivine interface. The position of the interface is defined by the steep rise of the Mg curve and the drop in the Si curve from its value in the passivating layer to its lower value in the olivine matrix. The moderate slopes of these curves result from oxygen ion beam induced mixing during the experiment, which is a common feature of any sputter depth profiling procedure. The two most important conclusions to be drawn from our SIMS results are that hydrogen did diffuse through the passivating layer during carbonation, and the resulting hydrogen distribution, likely associated with SiOH formation, is enhanced near the passivating-layer surface and the passivating-layer/olivine interface. Hydrogen diffusion through the passivating layer during carbonation is consistent with proton/Mg^{2+} exchange occurring near the olivine/passivating-layer interface during olivine dissolution/carbonation. It is also probable that SiOH groups form on the

vertical crack surfaces associated with the passivating-layer, as shown in the right side of Figure 8. Future studies are planned using a sputter-deposited gold capping layer to more quantitatively resolve the composition of the near-surface region of the passivating layer.

Close examination of the surface structures in the left of Figure 8 are consistent with (1) silica dissolution being able to occur at the base of and along passivating-layer cracks that extend to the olivine interface and (2) silica precipitating along the vertical silica-rich passivating layer structure as it diffuses away from the passivating layer/olivine interface. Such a process allows for the growth of silica-rich structures away from the interface, as observed in the left panel of Figure 8.

CONCLUSIONS

Robust silica-rich passivating layers have been discovered to form on the olivine surface during mineral carbonation. The detailed studies undertaken as a part of this project indicate that the aqueous olivine carbonation process involves both incongruent magnesium dissolution and silica precipitation, which result in robust silica-rich passivating layer formation. Secondary ion mass spectrometry investigations of the H content and profile within the passivating layers suggests $2H^{+}/Mg^{2+}$ ion exchange is associated with incongruent dissolution. These observations are consistent with H_2O forming at or near the olivine/passivating-layer interface within the passivating layer during the carbonation process. After forming, the water diffuses out through the passivating layers during the carbonation reaction. Together with the observation that magnesite nanocrystals form within the passivating layers during carbonation, this indicates that the passivating layers offer substantial permeability to the key solution reaction species present during carbonation (e.g., Mg^{2+}, H^{+}, H_2O, CO_2, and HCO^{3-}). Our reaction studies have established that these passivating layers thicken, fracture and exfoliate during rapidly stirred carbonation, exposing fresh olivine surfaces that enhance carbonation reactivity. Ultimately the aqueous carbonation reactivity is a strong function of (1) the ionic species present, (2) their aqueous activities, and (3) the slurry flow conditions present during carbonation.

As a potential method for continuously removing the inhibiting passivation layer, we explored sonication. Our project developed a specialized sonication apparatus capable of operating under the above high-temperature/high-pressure aqueous reaction settings. Using our custom designed sonication/exfoliation system we systematically studied the effects sonication on the extent of carbonation as a function of particle size distribution, the mass of solid reactant, volume fraction of aqueous solution present, sonication power, time, temperature, and CO_2 pressure. None of the conditions investigated have significantly enhanced carbonation. As sonication is relatively costly (energy intensive) compared with the other two approaches being investigated (aqueous chemistry and slurry-flow control) and has not shown promise for low-cost enhancement of carbonation, the other two approaches will be primarily explored during the no-cost extension period.

Studies varying the aqueous alkali cation species present in the optimum solution developed by the ARC (0.64M $NaHCO_3$ + 1.00M NaCl) were undertaken to selectively compare cation effectiveness in enhancing carbonation/exfoliation. Both the alkali cation species and their ratio were found to dramatically impact carbonation reactivity, with extent of carbonation varying by

a factor of 20 from the least to the most effective alkali cation combination. The most effective carbonation solutions to date are high concentration sodium, potassium, and sodium/potassium bicarbonate aqueous solutions. The most effective of these solutions (5.5M $KHCO_3$) has been found to nearly double the extent of carbonation observed using the standard aqueous solution developed by the Albany Research Center. High concentration aqueous bicarbonate solutions have also been found to preferentially enhance the relative carbonation reactivity of olivine containing larger particle-size fractions (e.g., <75μ and <150μ vs. <37μ). Being able to effectively carbonate olivine feedstocks containing such larger particle-size fractions offers the potential to substantially reduce feedstock grinding cost and lower mineral sequestration process cost.

Finally, slurry-flow dynamics have been found to be a strong function of particle size and mass via macroscopic simulations using Fluent, suggesting that controlling these parameters may offer substantial potential to enhance passivating-layer abrasion/exfoliation and carbonation. Our simulations show considerable variations in the solids distributions in the reactor for each size fraction. Flow visualizations indicate that a swirling flow develops within the reactor chamber, with the solids pushed to the bottom of the cylinder and gradually crawling along the sidewalls, and finally recirculating downwards along the central axis. Velocity profiles of the granular phase and the aqueous phase indicate differences in velocity profiles and volume fraction distribution for each size fraction computed, which also varies with the size fraction under consideration. The volume fraction distribution of the largest size fraction was concentrated around the reactor walls, unlike the smaller solid size fraction case, where the volume fraction distribution was more uniform. In addition, partial suspension, wherein solids remain at the bottom of the vessel, was observed for the 150μm diameter particles.

The simulation findings suggested that abrasive mechanisms are operative under stirred reaction conditions, and that the tensile strains at the passivating-layer/olivine interface may facilitate the layer cracking and exfoliation. The importance of particle abrasion in enhancing carbonation reactivity was confirmed via the addition of quartz particles as an abrasive slurry, which significantly enhanced carbonation.

Synergistic control of the slurry-flow and aqueous chemistry parameters incorporated during carbonation appears to offer the best potential to further improve carbonation reactivity for unactivated olivine feedstock materials. Future studies should take full advantage of progress to date, further exploring the potential that the aqueous chemistry and slurry-flow dynamics associated with carbonation offer to enhance carbonation reactivity and reduce olivine mineral sequestration process cost.

REFERENCES

1) *Carbon Sequestration Research and Development*, Offices of Science and Fossil Energy, U.S. Department of Energy (December 1999), and references therein.

2) Seifritz, W. *Nature* **345**, 486 (1990).

3) Lackner, K.; Wendt, C.; Butt, D.; Joyce Jr., E.; Sharp, D.; *Energy* **20**, 1153-70 (1995).

4) O'Connor, W., et al. *Proc. 25th Int. Tech. Conf. Coal Util. & Fuel Syst.* pp. 153-64 (2000).

5) O'Connor, W.K., et al. *Proc. 27th Int. Tech. Conf. Coal Util. & Fuel Syst.* pp. 819-30 (2002).

6) *Novel Approaches to Carbon Management* (National Academies Press, Wash. D.C., 2003)

7) O'Connor, W.K.; Walters, R.P.; Dahlin, D.C.; Rush, G.E.; Nilsen, D.N.; Turner, P.C.; *Proc. 26th International Technical Conference on Coal Utilization & Fuel Systems* **2001**, 765.

8) O'Connor, W.K.; Dahlin, D.C.; Rush, G.E.; Gerdemann, S.J.; Penner, L.R. *Proc. 29th International Technical Conference on Coal Utilization & Fuel Systems* **2004**, 71.

9) Yu, S.C.; Proc. Nat. Sci. Counc. A. ROC, **1997,** 21, 173.

10) Ottonello, G.; Princivalle, F.; Della Giusta, A.; *Phys. Chem. Miner.* **1990**, 17, 301.

11) McKelvy, M.J.; Chizmeshya, A.V.G.; Soignard, E.; Marzke, R.; Wolf, G.; Béarat, H.; Doss, B. *Proc. 31st International Technical Conference on Coal Utilization & Fuel Systems* **2006** 1-17.

12) McKelvy, M.J.; Diefenbacher, J.; Chizmeshya, A.V.G.; Wolf, G.; G.; Marzke, R.; Béarat, H.. *Proc. 30th International Technical Conference on Coal Utilization & Fuel Systems* **2005,** 26, 265-79.

13) Wolf, G.H.; Chizmeshya, A.V.G.; Diefenbacher, J.; McKelvy, M. J.; *Environ. Sci. Technol.* **2004**, *38*, 936.

14) Potapov, V.V.; *Glass Physics and Chemistry* **2004**, *30 (1)*, 82.

15) Wogelius, R.A.; Walther, J.V.; *Geochim. Cosmichim. Acta* **1991**, *55*, 943.

16) Jonckbloedt, R.C.L.; *J, Geochem. Explor.* **1998**, *62*, 337.

17) Chen, Y.; Brantley, S.L.; *Chem. Geol.* **2000**, *165*, 267.

APPENDIX A: ARTICLES, PRESENTATIONS, AND STUDENT SUPPORT

Journal Articles

"Carbon Sequestration via Aqueous Olivine Mineral Carbonation: Role of Passivating Layer Formation" Bearat, Hamdallah; McKelvy, Michael J.; Chizmeshya, Andrew V. G.; Gormley, Deirdre; Nunez, Ryan; Carpenter, R. W.; Squires, Kyle; Wolf, George H. *Environmental Science & Technology* **40**(15), 4802-4808 (2006).

"Externally controlled pressure and temperature microreactor for in situ x-ray diffraction, visual and spectroscopic reaction investigations under supercritical and subcritical conditions". Diefenbacher,J.; McKelvy, M.; Chizmeshya, A.V. G.; Wolf, G.H. *Review of Scientific Instruments*, **76**(1), 15103-15110 (2005).

"The Nanoscale Mechanism for San Carlos Olivine Carbonation", Youngchul Kim, Ryan Nunez, R. W. Carpenter, Andrew V. G. Chizmeshya and Michael J. McKelvy, *Microscopy and Microanalysis*, **11**, 1530, (2005).

Conference Papers

"Investigating Geological Sequestration Reaction Processes under *In Situ* Process Conditions" Andrew V.G. Chizmeshya, George Wolf, Michael J. McKelvy, Naoki Ito, Hamdallah Béarat, Brandon Doss and Robert Marzke, *Proceedings of the 32st International Technical Conference on Coal Utilization & Fuel Systems,* **32**, 431 (2007**).**

"Simulation and modeling of a slurry mixture for applications to carbon-dioxide sequestration" Kringan K. Saha, Kyle D. Squires and Michael J. McKelvy, Proceedings of the 6th International Conference on Multiphase Flow, 9 pp. ICMF 2007, Leipzig, Germany in July (2007).

"Laboratory Investigation of Fluid/Solid Sequestration Reaction Processes Under *In itu* Sequestration rocess Conditions" Michael J. McKelvy, Andrew V.G. Chizmeshya, Robert Marzke, Emmanuel Soignard, George Wolf, Hamdallah Béarat, and Brandon Doss, *Proceedings of the 31st International Technical Conference on Coal Utilization & Fuel Systems,* **31**, 383-399 (2006).

"Enhancing the observation of above and below ground carbon sequestration processes under in situ pressure and temperature conditions". McKelvy, Michael J.; Diefenbacher, Jason; Chizmeshya, Andrew V. G.; Wolf, George; Marzke, Robert; Bearat, Hamdallah *Proceedings of the International Technical Conference on Coal Utilization & Fuel Systems,* 30th(Vol.1), 255-269 (2005).

"Developing an atomic-level understanding of the mechanisms that govern CO_2 sequestration mineral carbonation reaction processes". McKelvy, Michael J.; Chizmeshya, Andrew V. G.; Diefenbacher, Jason; Bearat, Hamdallah; Carpenter, R. W.; Wolf, George; Gormley, Deirdre. EPD Congress 2005, *Proceedings of Sessions and Symposia held during the TMS Annual Meeting*, pp. 1133, San Francisco, CA, United States, Feb. 13-17 (2005).

Conference and Professional Presentations

"Investigating Geological Sequestration Reaction Processes under *In Situ* Process Conditions" Andrew V.G. Chizmeshya (presenter), George Wolf, Michael J. McKelvy, Naoki Ito, Hamdallah Béarat, Brandon Doss and Robert Marzke, *Proceedings of the 32st International Technical Conference on Coal Utilization & Fuel Systems,* Clearwater, Florida, (06/2007)**.**

"Energy Strategies in a Carbon Constrained World: Carbon Sequestration and New Alternative Energy Strategies" A.V.G. Chizmeshya (presenter), *Department of Chemistry and Biochemistry, Arizona State University*, Tempe, AZ, September (10/2007).

"Nanomaterials Simulation using High Performance Computing: From Greenhouse Gases to High-Tech Materials" A.V.G. Chizmeshya (presenter) and D. Stanzione, 2nd IEEE/ACM International Workshop on High Performance Computing for Nano-science and Technology, *19th International Conference for High Performance Computing*, Tampa, (11/2006).

"Laboratory Investigation of Fluid/Solid Sequestration Reaction Processes Under *In itu* Sequestration rocess Conditions" Michael J. McKelvy (presenter), Andrew V.G. Chizmeshya, Robert Marzke, Emmanuel Soignard, George Wolf, Hamdallah Béarat, and Brandon Doss, *Proceedings of the 31st International Technical Conference on Coal Utilization & Fuel Systems,* Clearwater, Florida, (05/2006).

"Lamellar Reaction Phenomena: from Intercalation to Nanomaterials Formation", M.J. McKelvy (presenter), A.V.G. Chizmeshya and R. Sharma, 13th International Symposium on Intercalation Compounds (06/2005).

"Furthering the Mechanistic Understanding of Above-Ground CO_2 Mineral Sequestration Reaction Processes" McKelvy, M.J. (presenter), Chizmeshya, A.V.G., Diefenbacher, J., Bearat, H., Carpenter, R.W., and Wolf G.H., 30th International Technical Conference on Coal Utilization & Fuel Systems (04/2005).

"Developing an atomic-level understandingof the mechanisms that govern CO_2 sequestration mineral carbonation reaction processes", McKelvy,M.J. (presenter); Chizmeshya,A.V.G.; Diefenbacher,J.R.; Bearat,H.; Carpenter,R.W.; Wolf,G.H.; Gormley, D., TMS Annual Meeting: EPD Congress (Invited Presentation) (02/2005).

Press Coverage

National: "SEARCH IS ON THE WAY TO TRAP PLANET-HEATING CARBON DIOXIDE", by Jeff Nesmith, *Cox News Service* (30 Newspapers), Friday, August 19, 2005.

"NOW YOU CO_2 NOW YOU DON'T" By: Behar, Michael, *Popular Science*, 01617370, August, Vol. 267, Issue 2, 2005.

"SCIENTISTS LOOKING AT WAYS TO TRAP GREENHOUSE GASES: Arizona Study Aims to Ease Global Warming" By Juliet Eilperin, *Washington Post*, Tuesday, February 22, 2005; Page A02

Local(ASU): "SET IN STONE", *ASU Research Magazine*, Fall 2004 Issue.
"ASU STUDY AIMS TO EASE GLOBAL WARMING: WORK IN TEMPE LAB COULD REDUCE GREENHOUSE GASES", East Valley Tribune, February 23 (2005).

Students Supported under this Grant

Karalee Jarvis: Doctoral candidate in the Science and Engineering Materials Ph.D. Program at Arizona State University.

Kringan Saha: Doctoral candidate in the Science and Engineering Materials Ph.D. Program at Arizona State University.

Firas Alawneh: Science and Engineering Materials Ph.D. (graduated December 2006), Arizona State University.

Youngchul Kim: Science and Engineering Materials Ph.D. (graduated May 2006), Arizona State University.

Laura Gremlich: Barrett Honors College Undergraduate Research Assistant, at Arizona State University

Meredith Reitz: Barrett Honors College Undergraduate Research Assistant, at Arizona State University

APPENDIX B : YEAR 1, 2 AND 3 TECHNICAL PROGRESS REPORTS

A NOVEL APPROACH TO MINERAL CARBONATION: ENHANCING CARBONATION WHILE AVOIDING MINERAL PRETREATMENT PROCESS COST

Type of Report:	Annual
Reporting Period Start Date:	June 22, 2004
Reporting Period End Date:	June 21, 2005
Principal Authors:	Michael J. McKelvy,* Andrew V.G. Chizmeshya, Kyle Squires, Ray W. Carpenter, and Hamdallah Béarat.
Date Report Issued:	October 2005
DOE Award Number:	DE-FG26-04NT42124
Submitting Organization:	Arizona State University Center for Solid State Science, Science and Engineering of Materials Graduate Program, and Department of Mechanical and Aerospace Engineering Tempe, AZ 85287-1704 * Phone: (480) 965-4535; FAX: (480) 965-9004; E-mail: mckelvy@asu.edu

DISCLAIMER

ABSTRACT

Known fossil fuel reserves, especially coal, can support global energy demands for centuries to come, ***if*** the environmental problems associated with CO_2 emissions can be overcome. Unlike other CO_2 sequestration candidate technologies that propose long-term storage, mineral sequestration provides permanent disposal by forming geologically stable mineral carbonates. Carbonation of the widely occurring mineral olivine (e.g., forsterite, Mg_2SiO_4) is a large-scale sequestration process candidate for regional implementation, which converts CO_2 into the environmentally benign mineral magnesite ($MgCO_3$). The primary goal is cost-competitive process development. As the process is exothermic, it inherently offers low-cost potential. Enhancing carbonation reactivity is key to economic viability. Recent studies at the U.S. DOE Albany Research Center have established that aqueous-solution carbonation using supercritical CO_2 is a promising process; even without olivine activation, 30-50% carbonation has been achieved in an hour. Mechanical activation (e.g., attrition) has accelerated the carbonation process to an industrial timescale (i.e., near completion in less than an hour), at reduced pressure and temperature. However, the activation cost is too high to be economical and lower cost pretreatment options are needed. Herein, we report our first year progress in exploring a novel approach that offers the potential to substantially enhance carbonation reactivity while bypassing pretreatment activation.

We have discovered that robust silica-rich passivating layers form on the olivine surface during carbonation. As carbonation proceeds, these passivating layers thicken, fracture and eventually exfoliate, exposing fresh olivine surfaces during rapidly-stirred/circulating carbonation. We are exploring the mechanisms that govern carbonation reactivity and the impact that (i) modeling/controlling the slurry fluid-flow conditions, (ii) varying the aqueous ion species/size and concentration (e.g., Li^+, Na^+, K^+, Rb^+, Cl^-, HCO_3^-), and (iii) incorporating select sonication offer to enhance exfoliation and carbonation. *Thus far, we have succeeded in nearly doubling the extent of carbonation observed compared with the optimum procedure previously developed by the Albany Research Center.* Aqueous carbonation reactivity was found to be a strong function of the ionic species present and their aqueous activities, as well as the slurry fluid flow conditions incorporated. Synergistic control of these parameters offers the potential for further improvements in carbonation reactivity. A new sonication exfoliation system incorporating a novel sealing system was developed to carry out the sonication studies. Our initial studies that incorporate controlled sonication have not yet lead to a significant improvement in the extent of carbonation observed. Year 2 studies will emphasize those approaches that offer the greatest potential to cost effectively enhance carbonation, as well as combined approaches that may further enhance carbonation.

Mechanistic investigations indicate incongruent dissolution results in the observed silica-rich passivating layer formation. Observations of magnesite nanocrystals within the passivating layers that form indicate the layers can exhibit significant permeability to the key reactants present (e.g., Mg^{2+}, H^+, H_2O, CO_2, and HCO_3^-). Atomistic modeling supports the observation of robust passivating layers that retain significant permeability to the key reaction species involved. Studies in Year 2 will emphasize the impact that controlled aqueous speciation and activity and slurry-flow dynamics have on the mechanisms that control carbonation reactivity and the potential they offer to substantially reduce olivine mineral sequestration process cost.

TABLE OF CONTENTS

EXECUTIVE SUMMARY

CO_2 mineral sequestration provides permanent disposal by forming geologically stable and environmentally benign mineral carbonates. Carbonation of olivine (e.g., forsterite, Mg_2SiO_4) is a large-scale sequestration process candidate for regional implementation. Cost-effectively enhancing carbonation reactivity is central to economically viable process development. Aqueous-solution carbonation shows particular promise. However, the associated mineral activation cost currently needed to suitably enhance carbonation is too high. Lower cost pretreatment options are needed. In the first year of this two-year project, we have begun to explore the potential to substantially enhance carbonation reactivity via a novel approach that bypasses pretreatment activation altogether.

Silica-rich passivating layers were discovered to form on the olivine surface during carbonation. As carbonation proceeds, the layers thicken, fracture and exfoliate during rapidly-stirred/circulating carbonation, exposing fresh olivine and enhancing carbonation. Three approaches to cost-effectively enhance carbonation, while avoiding the cost of olivine pretreatment activation, are being explored: (i) controlling the aqueous chemistry (e.g., Li^+, Na^+, K^+, Rb^+, Cl^-, and HCO_3^- activities), (ii) integration of slurry flow modeling with experiment, and (iii) incorporating select sonication. The goal is explore the potential to mitigate the effectiveness of passivating layer formation, enhancing exfoliation and carbonation. *During the first project year we succeeded in nearly doubling the extent of carbonation compared with that observed for the optimum procedure previously developed by the Albany Research Center (ARC).*

Carbonation reactivity was discovered to be a very complicated function of the aqueous solution species and their activities. Studies varying the aqueous alkali cation species present in the optimum solution developed by the ARC (0.64M $NaHCO_3$ + 1.00M NaCl) were undertaken to selectively compare cation effectiveness in enhancing carbonation/exfoliation. The alkali cation species present and their ratio were found to dramatically impact carbonation reactivity, with extent of carbonation varying by a factor of 20 from the least to the most effective alkali cation combination. The most promising solutions for enhancing carbonation to date have provided substantial increases in extent of carbonation, nearly doubling it. High concentrations of $NaHCO_3$ (2.5M) and $KHCO_3$ (5.5M) were found to be particularly effective at enhancing carbonation, with the extent of carbonation again exhibiting a strong dependence on the alkali cation species present. In contrast, the alkali chloride solutions studied to date have exhibited poor carbonation reactivity by themselves, but can substantially enhance carbonation reactivity in combination with alkali bicarbonate under select conditions. CO_2(aq) and HCO_3^- play key synergistic roles in enhancing carbonation, as carbonation drops off dramatically in the presence of HCO_3^-(aq) or CO_2 (aq) alone.

Multi-phase fluid modeling and experimental investigations were initiated to elucidate important slurry-flow parameters that enhance exfoliation and carbonation (e.g., via particle-particle and particle-wall collisions). A new microscopic wall roughness model was developed and extensively validated. Subsequent computational investigations were found to indicate wall roughness can strongly enhance cross-stream transport, particle-particle collisions and carbonation. The Fluent code was validated for application to multiphase flows to assess the

complex effects governing flow. Calculation of whole systems, such as the flow loop reactor at the ARC, remains a substantial challenge. However, initial results for system components have revealed the radial distribution of flow in a component pipe can be a strong function of particle mass/size distribution and mixing history. As particle mass was found to be an important factor in cross-stream particle transport, we initiated a series of studies to explore the effect of particle mass/size distribution on exfoliation and carbonation in collaboration with the ARC using the ARC flow loop reactor and the ASU batch reactor. Initial results demonstrate that the flow dynamics and particle mass/size distribution present can substantially impact exfoliation/carbonation.

A controlled pressure and temperature 20 kHz sonication system was successfully developed for these studies. The system is based on a Sonics 1500 watt power supply and a special probe to adapt to our custom controlled pressure (1 to 200 atm) and temperature (20 to 250 ^{o}C) sonication vessel. System development required substantial R & D to provide an effective sealing system between the sonic probe and the controlled pressure and temperature system. The sealing system was initially arranged to be designed and developed industrially. However, the required time table was not met by the vendor, necessitating in-house design and development, significantly delaying initial system deployment (months). The system is fully operational over the complete range of carbonation reaction conditions of interest. The effects of temperature and pressure on the effectiveness of sonication in enhancing carbonation have been explored. These studies will be expanded in Year 2, together with investigations of the effect of sonication power and time, fluid composition, and reactant particle concentration and size, as well as the effect of combining the most effective parameters observed. Parameters that have been found to be individually effective at cost-effectively enhancing carbonation reactivity (e.g., controlled fluid flow conditions and aqueous chemistry) will be combined to probe the potential to synergistically stimulate exfoliation and enhance carbonation.

Mechanistic investigations have extended fundamental understanding of the passivating layer formation process during the first project year. Incongruent dissolution generally results in silica-rich passivating layer (PL) formation, with silica dissolution-precipitation likely further contributing to PL growth. Observations of magnesite nanocrystals within the passivating layers that form indicate the layers exhibit significant permeability to the key reactants present (e.g., Mg^{2+}, H^{+}, H_2O, CO_2, and HCO_3^{-}). Carbonation increases dramatically with increasing weight % solids in stirred experiments, indicating particle-particle collisions are critical in enhancing exfoliation and carbonation. Addition of abrasive materials, such as quartz, can significantly enhance olivine carbonation, in further support of the importance of particle-particle collisions in exfoliation and carbonation processes. Multi-phase hydrodynamic calculations indicate secondary collisions can account for a large fraction of the abrasion/exfoliation observed. Large-scale atomic-level simulations of the reaction zone are consistent with a PL that possesses a "glassy" but highly defective SiO_2 structure that can permit the diffusion of key reactants during carbonation. Studies in Year 2 will emphasize the impact that controlled aqueous speciation, activity and slurry-flow dynamics have on the mechanisms that control carbonation reactivity, as they appear to offer the greatest potential to substantially reduce olivine mineral sequestration process cost.

INTRODUCTION

Coal, in particular, and fossil fuels, in general, are well positioned to supply the world's energy needs for centuries to come if carbon sequestration technology can be developed that is (i) permanent, (ii) environmentally benign, and (iii) economically viable.[1] CO_2 mineral sequestration provides permanent disposal, by forming geologically stable mineral carbonates.[2-5] The materials produced are also environmentally benign and found in vast quantities in nature. The primary challenge is economically viable process development. As permanent disposal inherently avoids the ongoing monitoring, remediation and liability costs associated with long-term storage, the key is reducing mineral sequestration process cost. Cost effectively enhancing carbonation reactivity is critical. Enhancing mineral carbonation during geological (below-ground) sequestration is highly desirable as well, as it can similarly ensure long-term sequestration stability via the formation of thermodynamically stable mineral carbonates.[6] Investigating and evaluating candidate technologies that incorporate mineral sequestration (above and below ground) is the primary focus of the CO_2 Mineral Sequestration Working Group, which is managed by DOE (Fossil Energy), and consists of members from the Albany Research Center, Argonne National Laboratory, Arizona State University, Los Alamos National Laboratory, and the National Energy Technology Laboratory.

Carbonation of Mg-rich olivine minerals (e.g., forsterite, Mg_2SiO_4) is a leading mineral sequestration process candidate.[7,8] These minerals are available worldwide in quantities sufficient to support the regional implementation of above-ground mineral sequestration.[8] Their low-cost (~$4-5/ton for mined and milled feedstock)[7,8] and exothermic carbonation (reaction 1) (8), provide the potential for economically viable process development.

(1) $\frac{1}{2}Mg_2SiO_4 + CO_2 \rightarrow MgCO_3 + \frac{1}{2}SiO_2 + 88$ kJ/mol

Recent studies at the Albany Research Center indicate aqueous solution carbonation is a promising approach.[7,8] Even without special activation, 30-50% carbonation has been achieved in an hour for <37 micron olivine reacted at 185 ^oC and 150 bar CO_2. Mechanical pretreatment via intense attrition accelerates carbonation to near completion in less than an hour and at reduced pressures and temperatures. However, the activation cost is too high for cost-effective sequestration.[8]

Economically viable process development will require novel approaches that enhance mineral carbonation reactivity, while bypassing costly mineral pretreatment. The potential to develop low-cost chemical pretreatment processes has been explored for years, but success remains elusive.[6] Enhancing carbonation, while avoiding the expense of olivine pretreatment, would substantially reduce process cost and provide a significant advance. We recently discovered that aqueous olivine mineral carbonation is associated with robust passivating layer formation, which substantially inhibits mineral carbonation. Herein, we are exploring novel low-cost approaches with the potential to facilitate passivating layer exfoliation to enhance carbonation and develop an atomic level understanding of the associated mechanisms. The goal is to develop the understanding needed to engineer new low-cost carbonation processes that avoid the cost of pretreatment activation. The primary focus is on enhancing passivating layer exfoliation, which

has the potential to substantially enhance carbonation without the need for pretreatment activation.

EXPERIMENTAL

Single crystal olivine fragments from San Carlos, Arizona, were used to explore the effects of aqueous solution chemistry, particle size and sonication on olivine carbonation reactivity, as well as the mechanisms that govern passivating layer formation and exfoliation processes. The elemental composition was determined to be $(Mg_{0.915}Fe_{0.085})_2SiO_4$ by electron microprobe and particle induced X-ray emission analysis. X-ray diffraction (XRD) of powdered samples showed the lattice constants are in good agreement with those observed for olivine containing ~8% Fe (a = 4.763Å, b = 10.223Å, c = 5.993Å).[9,10] Trace impurities observed were well below 1%, with Ca being the principle trace impurity. Single crystals and single crystal fragments were used to facilitate microscopic observation of passivating layer formation/exfoliation and the reaction surfaces and interfaces that form during carbonation. Synthetic forsterite (Mg_2SiO_4) (99% Mg_2SiO_4; Alfa Aesar) was used for select carbonation investigations. Twin Sisters olivine was used for the flow-loop reactor studies carried out in collaboration with the Albany Research Center.[7] The flow-loop reactor has been previously described.[8] All of the olivine size fractions investigated herein (<37 micron, 37-75 micron, < 75 micron, 75-150 micron and <150 micron) were wet screened. The extent of carbonation observed is compared with the optimum process to date for enhancing carbonation developed by the Albany Research Center (ARC),[7,8] which is summarized below for forsterite carbonation.

$$Mg_2SiO_4 + 2CO_2 \xrightarrow[0.64\ M\ NaHCO_3,\ 1M\ NaCl]{\sim 185\ ^oC,\ \sim 150\ atm\ CO_2} 2MgCO_3 + SiO_2$$

Reactions were carried out using a variety of aqueous species (e.g., Li^+, Na^+, K^+, Rb^+, Cl^-, HCO_3^-) and species activities, particle size ranges and reaction times to probe their effect on carbonation and passivating layer formation/exfoliation. 1,500 rpm stirring was used to replicate the ARC process in the studies at Arizona State University. These mineral carbonation reactions were performed using a 100ml Autoclave Engineers EZE-Seal Hastelloy C-276 reactor, which is a smaller scale version of the 2,000 ml EZE-Seal Hastelloy C-276 reactor used at the Albany Research Center. Unstirred (static) experiments were undertaken to explore passivating layer formation in the absence of particle abrasion. San Carlos olivine single crystals (~1x1x0.1cm) with well-defined initial surface morphologies were incorporated to follow the reaction interface that forms down to the atomic level.

The extent of carbonation and hydrogen content of the product materials were assessed using a Perkin Elmer Series II CHNS Elemental Analyzer. Comparative standards gave total carbon and hydrogen accuracies of ± 0.3 wt%. Extent of carbonation observations were compared with XRD intensity analysis of the product materials and found to be in good agreement. Select reaction products were analyzed structurally, morphologically, and analytically versus their extent of reaction to probe the mechanisms that govern carbonation.

XRD patterns were obtained using a Rigaku D/MAX-IIB X-ray diffractometer with Cu$K\alpha$ radiation. Scans were taken over different 2θ ranges between 10º to 70º, with 0.01°/s steps.

Reaction products were imaged using a Hitachi S-4700 field-emission scanning electron microscope (FESEM) or a FEI XL-30 Environmental FESEM. Elemental analysis of individual product particles was accomplished via energy dispersive X-ray spectroscopy (EDS). Cross-sectioned samples of reaction interfaces were analyzed via FESEM and EDS mapping and high-resolution transmission electron microscopy (HRTEM) using a JEOL 2010 with EDS and electron energy loss spectroscopy (EELS) capabilities.

Controlled pressure and temperature studies of the impact of sonication on olivine exfoliation/carbonation were carried out using our batch mineral carbonation reaction system described above and our specially developed controlled pressure and temperature sonication system described below. Sonication/carbonation studies have been carried out in stages. Hour-long carbonation studies are separated into three stages: (1) a half hour long run in the batch reactor, followed by (2) controlled sonication in the sonication system (e.g., one minute) and (3) a second half hour in the batch reactor. The above sonication runs are compared to both the standard one-hour carbonation runs using the batch reactor and runs that incorporate the sonication reaction stages (1/2 hour plus 1/2 hour batch reaction format), but without sonication.

RESULTS AND DISCUSSION

Technical Accomplishments: Development of a Sonic Exfoliation System

A controlled pressure and temperature 20 kHz sonication system was successfully developed for these studies. The system is based on a Sonics 1500 watt power supply and a special probe to adapt to our custom controlled pressure (1 to 200 atm) and temperature (20 to 250 ^{o}C) sonication vessel. The pressure and temperature control system used is the same system used to conduct our aqueous carbonation reactions. The impeller driven stirring system is replaced by the sonic probe. Other than the interchangeable sonication and impeller components, the remainder of the system remains essentially the same.

System development required substantial R & D to provide an effective sealing system between the sonic probe and the controlled pressure and temperature system. The sealing system was initially arranged to be designed and developed industrially. However, the required time table was not met, necessitating in-house design and development, delaying initial system deployment for months. The system is fully operational. Use of the system is discussed further below.

Scientific Progress: Effects of Aqueous Chemical Speciation and Activity on Olivine Carbonation Reactivity.

We report here the first year results of the effect of aqueous solution species/activity on extent of carbonation using our 100 ml batch carbonation reaction system at the standard conditions of 1 hour, 185 ^{o}C, 2200 psi of CO_2 and stirring at ~ 1500rpm. In all these experiments, 15 wt% <38μ San Carlos olivine (essentially single crystal fragments) was used. The objective of these investigations is to further evaluate (i) the effect of aqueous chemical speciation and concentration on olivine passivating layer formation and carbonation reactivity and (ii) the potential controlling them offers to enhance carbonation. The primary focus is on the effect of alkali cation species and size (e.g., Li^+, Na^+, K^+) and cation and anion activities. The results are

compared to the extent of carbonation observed using the standard 0.64M $NaHCO_3$ + 1.0 M NaCl aqueous solution developed at the Albany Research Center (ARC).[7] Initial investigations explored the effect of alkali cation species and concentrations by varying the alkali cations present with the standard aqueous bicarbonate and chloride concentrations in the sodium bicarbonate/sodium chloride solution developed by the ARC (0.64M $AHCO_3$ + 1.0 M ACl, where A = Li, Na, K). Otherwise, the optimum conditions developed by the ARC were used.

Subsequent investigations discovered strong carbonation enhancement with increasing $NaHCO_3$ and $KHCO_3$ concentrations in the absence of the chloride solution, nearly doubling the extent of carbonation observed for the standard ARC solution. Cation speciation and concentration are also found to substantially impact carbonation, with mixed Na^+/K^+ aqueous solutions showing promise for further enhancing carbonation. The carbonation extents reported are calculated based on elemental carbon analysis of the product materials and semi-quantitatively verified with X-ray powder diffraction analysis. All of the product carbonate formed is identified as magnesite.

1. Effect of Varying the Alkali Cation Species in the Standard ARC Aqueous Solution

The effect of the alkali cation species and their activities on the extent of carbonation observed using the standard aqueous bicarbonate and chloride concentrations for the optimum solution developed by the ARC are shown in Table 1. The average extent of carbonation using the standard ARC solution (34%) is shown in red. As both the bicarbonates and chlorides are completely soluble at the indicated concentrations, the reactions primarily differ in the alkali cation species present and their concentrations (i.e., 0.64M vs. 1.00M, vs. 1.64M). Clearly, the extent of carbonation is a strong function of both the alkali cation species and their activities. Perhaps the most intriguing observation is the strong effect of the Na^+/K^+ ratio on extent of carbonation, with a 0.64 ratio resulting in 3% carbonation, while a 1.56 ratio (1.00/0.64) yields 41% carbonation. The strong impact of the Na^+/K^+ ratio on carbonation reactivity is further explored below, as it suggests significant potential to further enhance carbonation reactivity.

Table 1: Effect of Exchanging Alkali Cation Species in the Optimum ARC Aqueous Solution (0.64M $NaHCO_3$ + 1.00M NaCl) on the Extent of Carbonation

0.64M $AHCO_3$ (A = Li,Na,K)

1.00M ACl (A = Li,Na,K)	Li	Na	K
Li	23%	18%	24%
Na	4%	34%*	41%
K	2%	3%	15%

* Extent of carbonation observed for the optimum aqueous carbonation solution developed by the Albany Research Center

2. Effect of the Na^+/K^+ molar ratio, at constant $[HCO_3^-]$ and $[Cl^-]$

Figure 1 shows that at 0.64M HCO_3^- and 1.0M Cl^-, the carbonation reactivity of San Carlos olivine is a strong function of the Na^+/K^+ molar ratio. This further underscores the impact that alkali cation speciation and activity can have on passivating layer effectiveness and carbonation reactivity. The extent of carbonation substantially increases with increasing $[Na^+]/[K^+]$ ratio up to 1.56 and then falls off slightly to within experimental error of the average extent of carbonation observed for the standard 0.64M $NaHCO_3$ + 1.0M NaCl aqueous solution (33.6%). At $[Na^+]/[K^+]$ = 1.56, the improvement in extent of carbonation appears to be significant, suggesting the associated alkali cation combination may better mitigate passivating layer formation and enhance carbonation. Combined with the above results, it is apparent that both the type and relative concentration of alkali cation species present in the aqueous solution can dramatically impact carbonation. The results also underscore the potential that combinations of alkali cation species can act synergistically to enhance carbonation. Based on the above results, we plan to further explore the potential that different combinations and concentrations of cation species offer to enhance carbonation during Year 2.

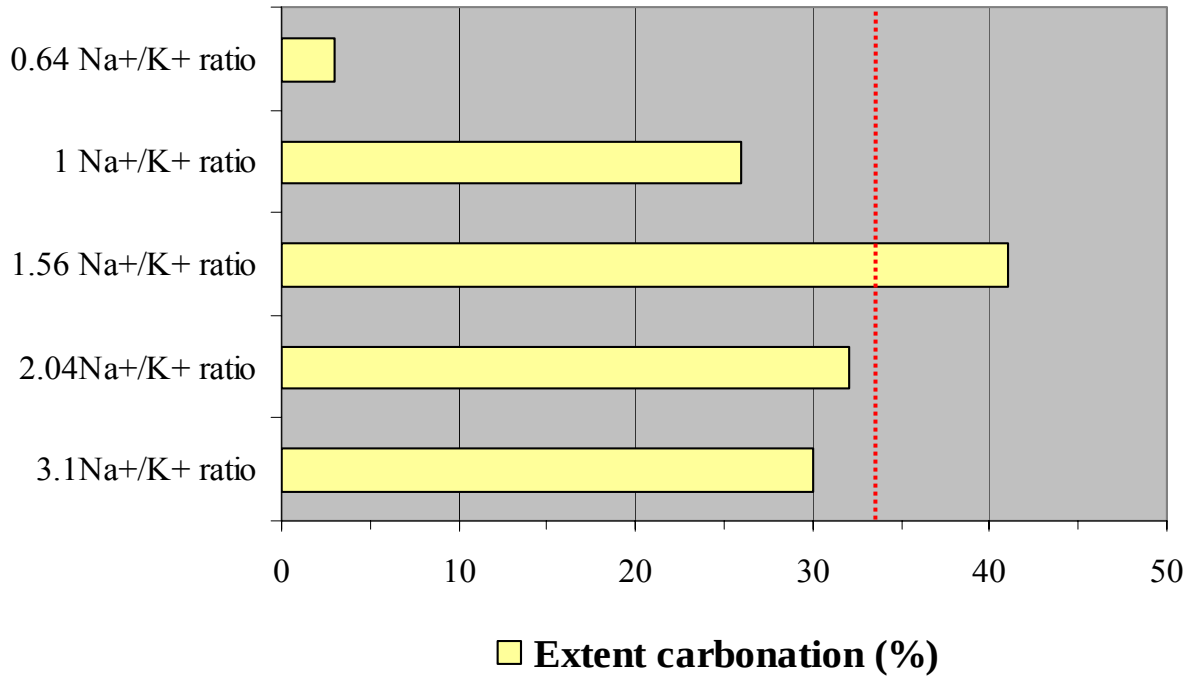

***Figure 1**: Extent of carbonation of San Carlos olivine as a function of Na^+/K^+ molar ratio, at 0.64M HCO_3^-, 1.0M Cl^-, and 1.64M M^+ (M = Na + K). The dotted red line indicates the average extent of carbonation observed using the standard 0.64M $NaHCO_3$ + 1.0M NaCl aqueous solution.*

3. Effect of varying alkali bicarbonate concentration ($NaHCO_3$ and $KHCO_3$)

Two series of experiments were conducted for increasing sodium and potassium bicarbonate concentrations, due to their higher solubility limits relative to lithium bicarbonate under mineral carbonation reaction conditions. Figures 2 & 3 show the extent of carbonation observed as a

function of [$MHCO_3$] M = Na or K. In both cases, increasing the [$MHCO_3$] substantially increases the extent of carbonation, with 5.5M $KHCO_3$ nearly doubling the extent of carbonation in comparison with the standard 0.64M $NaHCO_3$ + 1.0M NaCl aqueous solution (63% vs. 34%).

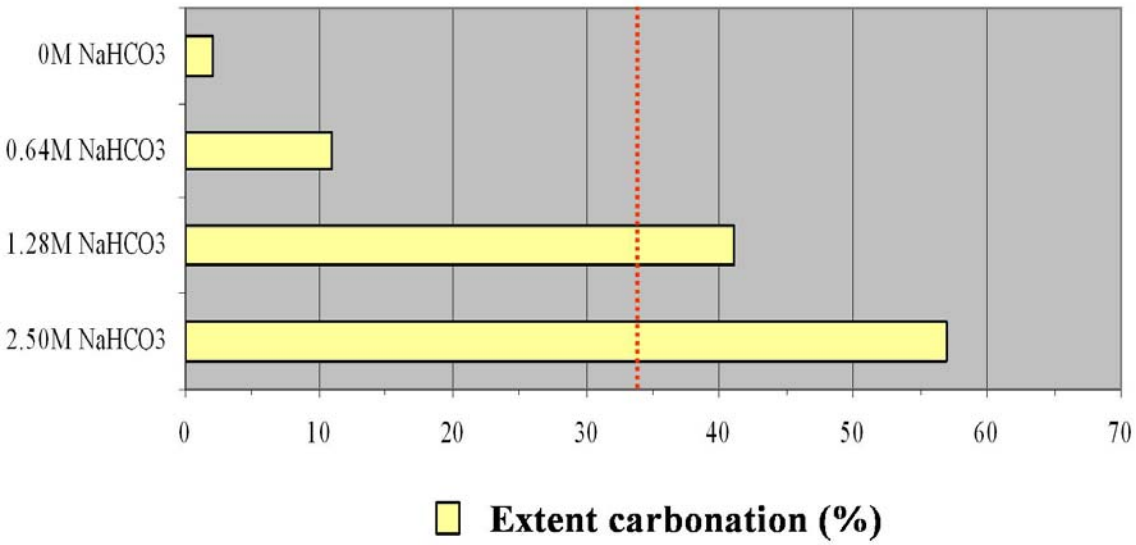

***Figure 2**: Extent of carbonation as a function of $NaHCO_3$ concentration, with no Cl^- present. The dotted red line indicates the average extent of carbonation observed using the standard 0.64M $NaHCO_3$ + 1.0M NaCl aqueous solution.*

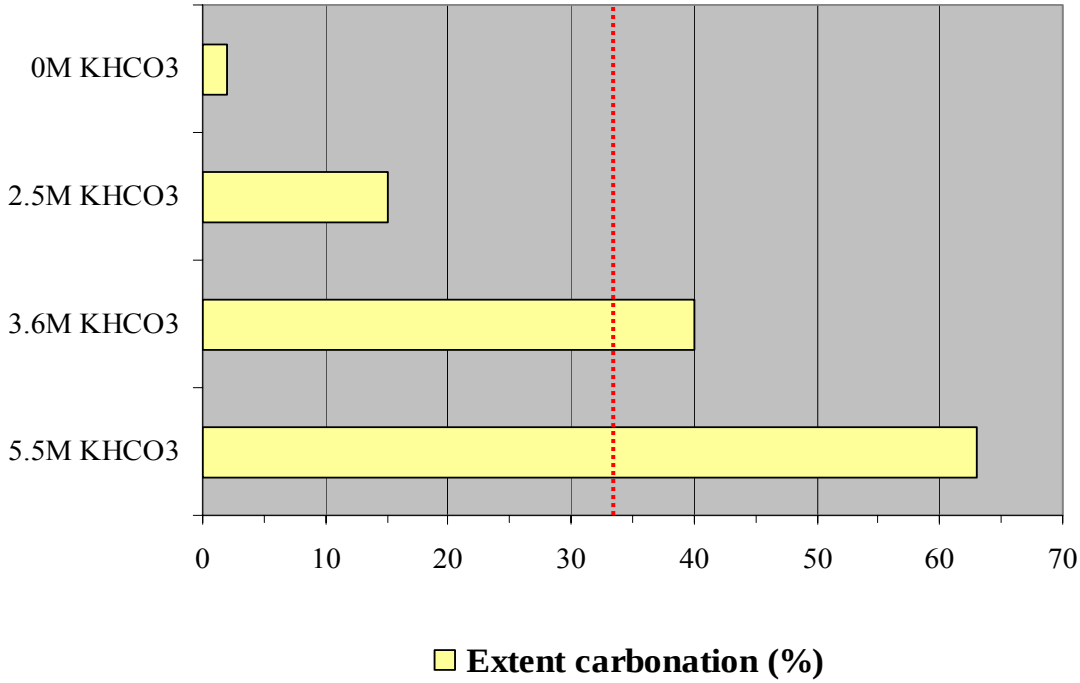

***Figure 3**: Extent of carbonation as a function of $KHCO_3$ concentration, with no Cl^- present. The dotted red line indicates the average extent of carbonation observed using the standard 0.64M $NaHCO_3$ + 1.0M NaCl aqueous solution.*

Both the [HCO_3^-] and alkali cation species present substantially impact the extent of carbonation. This follows, for example, from the extent of carbonation observed for 2.5M $NaHCO_3$ (57%) being much higher than that observed for 2.5M $KHCO_3$ (15%), indicating Na^+ is substantially more effective than K^+ in mitigating passivating layer effectiveness and enhancing carbonation. It also follows from observations described below that alkali chloride solutions exhibit very poor carbonation reactivity, underscoring the importance of HCO_3^-. The importance of the alkali cation species is further underscored in Figure 4, where 7.5M $RbHCO_3$ was found to be substantially less effective in enhancing carbonation (40%) than 5.5M $KHCO_3$ (63%) or 2.5M $NaHCO_3$ (57%).

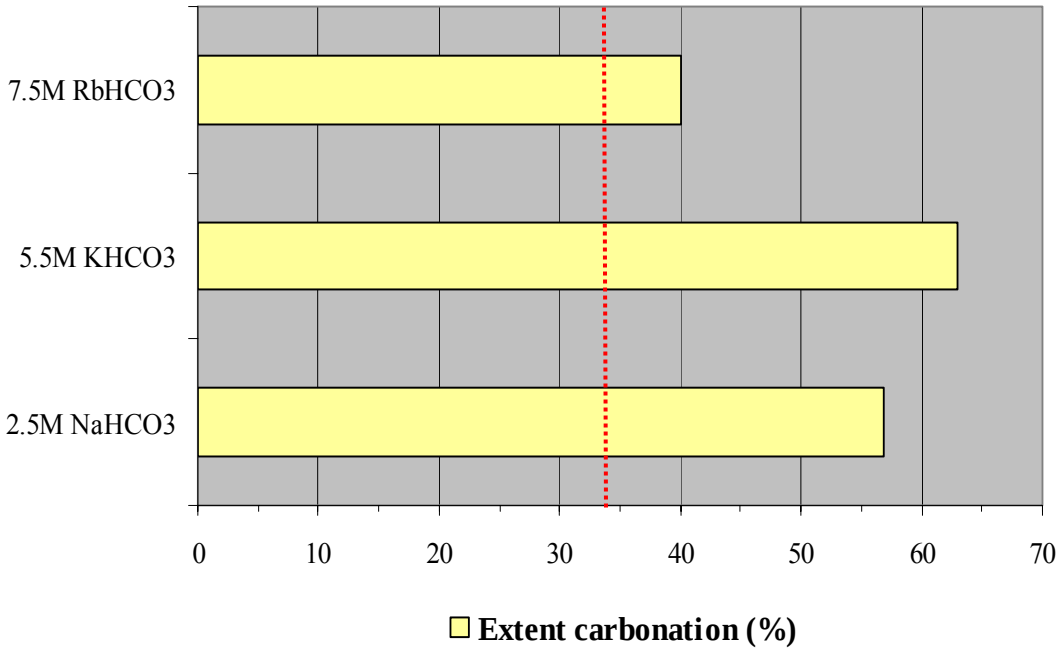

***Figure 4**: Effect of the different type/concentration of alkali bicarbonate on the extent of carbonation, with no Cl^- present. The dotted red line indicates the average extent of carbonation observed using the standard 0.64M $NaHCO_3$ + 1.0M NaCl aqueous solution.*

It is important to note that the above $NaHCO_3$ and $KHCO_3$ concentrations substantially exceed the aqueous solubility of $NaHCO_3$ and $KHCO_3$ under ambient temperature and pressure, ~ 1.3M and ~3.6 M, respectively, whereas the concentration of $RbHCO_3$ is slightly lower than its ambient solubility of 7.9M. However, these solubilities may be expected to increase substantially with increasing temperature, with possibly small contributions from increasing pressure as well, allowing higher aqueous concentrations of $NaHCO_3$ and $KHCO_3$ to be utilized under mineral carbonation reaction conditions, as seen in Figures 2 and 3. However, the solubility under mineral carbonation reaction conditions will also be impacted by the activity of CO_2 present, which may serve to inhibit alkali bicarbonate solubility. The potential for increased alkali bicarbonate solubility under reaction conditions motivated the above studies, even though the bicarbonate concentrations used exceed the solubility limits for aqueous sodium and potassium bicarbonate solutions under ambient conditions. We have not yet established whether we have reached the solubility limit for these solutions under reaction conditions. This will be

explored in Project Year 2, as will be tests at lower temperatures and pressures (which can lower process cost, but can also impact Na/K bicarbonate solubility). Year 2 studies will also include exploring the potential that the combined alkali cation effect offers to further enhance carbonation (e.g., will combined $NaHCO_3$ + $KHCO_3$ aqueous solutions further enhance the carbonation reactivity observed for the individual $NaHCO_3$ + $KHCO_3$ solutions).

4. Comparison of the Extent of Carbonation Observed for 2,200 PSI CO_2 and 5.5M $KHCO_3$ Separately and Combined.

Figure 5 shows the extent of carbonation observed for (i) distilled water under 2,200 psi CO_2 , (ii) 5.5M $KHCO_3$ under 2,200 psi CO_2, and (iii) 5.5M $KHCO_3$ under 2,200 psi He. Clearly, the aqueous $KHCO_3$ solution has a dramatic effect on carbonation reactivity, with very little carbonation observed using distilled water alone. In the absence of CO_2, i.e., under He, the carbonation reactivity drops substantially compared with that observed for 5.5M $KHCO_3$ under 2,200 psi CO_2. Analysis of the K^+ concentration in the aqueous solution after the reaction is complete (diluted so that all the $KHCO_3$ dissolves under ambient conditions) appears to provide interesting insight into the carbonation mechanism. Initial results indicate that no decrease is observed in the aqueous K^+ concentration after carbonation under 2,200 psi CO_2, whereas a significant decrease is observed for 5.5M $KHCO_3$ under 2,200 psi He. This suggests that $KHCO_3$ may not be consumed during carbonation under CO_2. These results are preliminary at this point and need to be verified. Further solution analyses are also planned to determine the product aqueous solution bicarbonate concentrations.

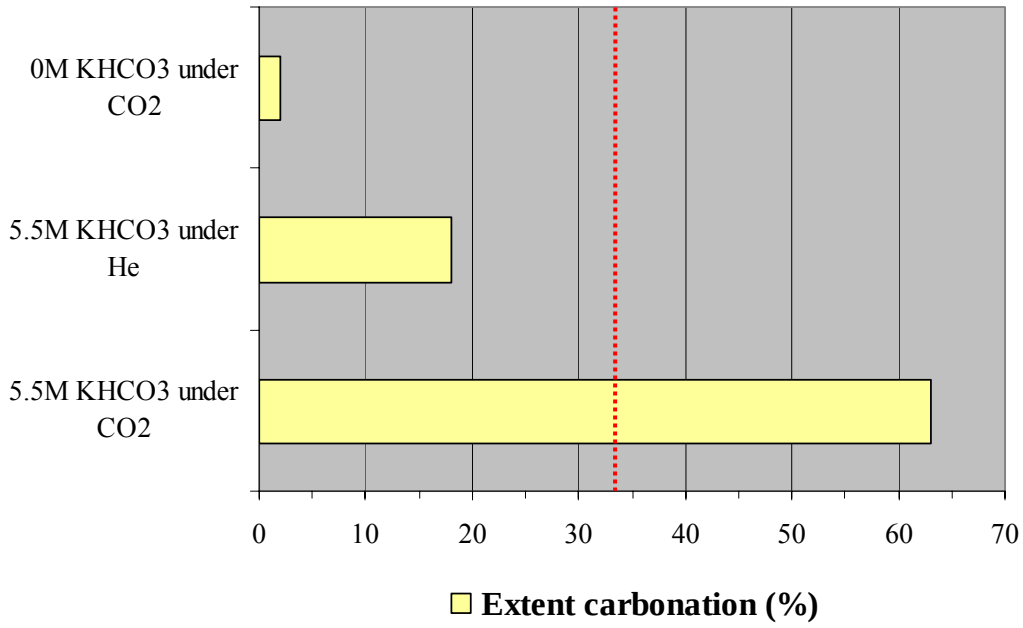

***Figure 5**: Extent of carbonation of San Carlos olivine reacted under 2,200 psi CO_2 or He in the indicated aqueous solution. Distilled water is represented as 0M $KHCO_3$ solution. The dotted red line indicates the average extent of carbonation observed using the standard 0.64M $NaHCO_3$ + 1.0M NaCl solution.*

In the second project year, work exploring the impact that aqueous solution chemistry can have on enhancing carbonation reactivity will emphasize further exploration of the potential that combined alkali cation species offer to enhance carbonation using both pure bicarbonate solutions and solutions that incorporate alkali chloride and bicarbonate.

Scientific Progress: Multi-phase Fluid Modeling and Experimental Investigations to Elucidate Key Slurry-Flow Parameters that Enhance Exfoliation and Carbonation

Work in this area of the project has focused on two hierarchies of fluid-flow modeling in addition to experiments focusing on particle-size effects. The over-arching aim of the investigations in this portion of the project is to attempt to isolate and to understand effects that may be crucial to optimizing the fluid dynamics of sequestration processes to enhance passivating layer exfoliation and carbonation. One of the two hierarchies of fluid flow modeling focused on "microscopic" modeling of particle-laden flows in which the aim was to investigate stochastic approaches to representing wall roughness. "Macroscopic" modeling approaches were applied to predict the behavior in reactor sections in which the aim is to assess/incorporate current engineering models to predict the average properties of liquid-solid turbulent flows. As described in greater detail below, these calculations were performed using Fluent and applied to conditions representative of those in the flow-loop reactor at the Albany Research Center. The third phase of the effort that was initiated during Year 1 was analysis and design of experiments performed at ARC and ASU in which the main goal is to quantify and understand particle size effects on carbonation levels. The primary aim of efforts in this area of the project during Year 2 will be further analysis and publication of the experimental measurements focusing on particle size effects and macroscopic fluid flow modeling that will be used for parametric studies of the effect of flow rate, solids loading, and particle size on the average properties of liquid-solid mixtures representative of those encountered in mineral sequestration applications.

1. "Microscopic" Fluid Flow Modeling

Fluid flow dynamics in industrial flow loop reactors (such as simulated by the lab scale reactor at the Albany Research Center) result in complex interactions between the suspended solids phase, fluid carrier flow, and reactor surfaces. Particle-particle interactions (e.g., surface abrasion by particle friction from rubbing and/or collisions) and particle-wall interactions contribute to passivating layer exfoliation and carbonation. Wall roughness, flow rates (i.e., Reynolds numbers), solids loading, and particle size distributions provide examples of those parameters whose influence on transport and exfoliation are not well understood. Computational models are essential to advancing the understanding of their effects and eventually for use in carbonation process design and optimization.

The specific aim of the work on "microscopic" modeling focused on wall roughness and representing the effects of rough surfaces on particle transport. The modeling in this phase of the work is referred to as "microscopic" since it considered the motion of individual particles, in contrast to the "macroscopic" modeling described in the section that represents the averaged properties of the particulate phase by solving field equations rather than using Lagrangian tracking of individual particles.

Particle tracking approaches were employed in simulations of a geometrically simple flow but still possessing the complicating effects of mean shear in each phase and the presence of solid surfaces. The primary contribution of this part of the work was development of a stochastic model of wall roughness that accounts for the transfer of mean-to-fluctuating particle momentum arising from the impact of a particle with a roughened surface. In particular, in the model that was developed a particle collides with a ``virtual wall" which has a randomly distributed inclination with respect to the plane, smooth wall (c.f., Figure 6). The ``wall roughness angle" is denoted γ in Figure 6 and is sampled from a Gaussian distribution. The stochastic treatment is similar to that employed in Sommerfeld and other related references.[11] Simulations were performed to test the model using three values of the standard deviation, γ', of the distribution of wall roughness angles: 0° (smooth wall), 2.5°, and 5°. These values are within the range of the measurements from Sommerfeld and Huber used to develop and validate roughness models for Lagrangian particle tracking approaches.[12]

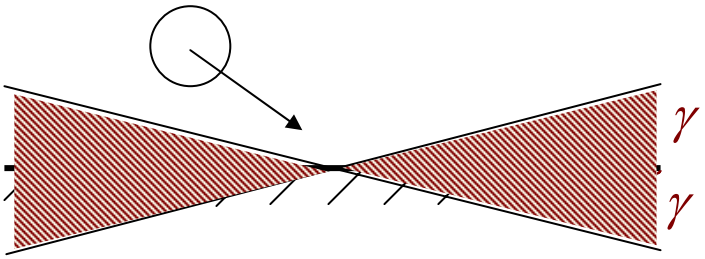

Figure 6. *"Virtual wall" with random orientation, γ*

The flow used to test the roughness model was a vertical, fully-developed turbulent channel flow. The numerical approach is based on Large Eddy Simulation (LES) of the carrier-phase flow and Discrete Particle Simulation (DPS) for prediction of dispersed phase transport. Particle motion is controlled by interactions with the surrounding fluid flow, interactions with other particles (collisions), and interactions with the (roughened) channel walls. The particle diameters are small (specified as one viscous unit), corresponding to diameters of approximately 90μm in applications. The numerical model was idealized and represents a limit case which highlights the effect of surface roughness on particle transport and is well suited for the purpose of assessing the model. Effects such as lubrication forces between particles and the wall were not accounted for in the simulations.

A representative sample of results highlighting the effect of wall roughness is shown in Figure 7. Shown in the figure is the wall-normal profile of the mean particle number density for a heavy particle, i.e., a particle that does not respond to the majority of the turbulent fluctuations of the carrier-phase flow. For the results shown in the figure the influence of particle-particle collisions was not included and therefore the difference in the profiles is due solely to the effect of wall roughness. The curves in the figure are for a smooth-wall case ($\gamma = 0°$) and rough-wall case with $\gamma = 2.5°$. The figure shows that for particle-wall collisions with a smooth wall, the number density distribution peaks at the wall as typically observed in channel flow in which particle-particle collisions are not considered and for which there is a specular reflection of the particle on the wall. Under the influence of wall roughness the number density distribution

becomes more uniform across the channel, indicative of a greater mixing of the particles across the channel, again arising solely due to the effect of wall roughness. Though not shown here, for lighter particles (e.g., lower particle material density) the influence of wall roughness on the concentration profile (number density) is less significant than shown in Figure 7. Lighter particles follow more closely the velocity fluctuations of the carrier-phase flow and impact the wall at shallower angles (grazing-type wall collisions) and also possess, on average, lower streamwise velocities compared to the heavy particles. These factors in turn lessen the effect of wall roughness on their transport since there are fewer wall collisions and a less significant transfer of streamwise particle momentum to the wall-normal fluctuations of the particle velocity that facilitate particle-particle collisions. The difference in response to wall interactions as a function of particle size suggests that relatively broad reactant particle size distributions should favor particle-particle interactions, exfoliation and carbonation by promoting momentum vectors with a greater probability of intersection. As a result, we have begun to explore the effects of particle size distribution, with our initial experimental investigations indicating that broader size distributions can favor carbonation, as described below.

The effect of wall roughness on the streamwise component of the mean particle velocity is shown in Figure 8, again for the heaviest particles used in the tests of the roughness model. Shown in the figure is the profile of the mean fluid velocity on the Eulerian grid used to resolve the fluid flow, the mean fluid velocity around the particles, and the mean particle velocity for the smooth and rough-wall cases. For the smooth-wall case the mean slip between the particles and fluid is small and, consequently, the mean velocity of the particles is close to that of the fluid. Analogous to the more uniform profiles achieved in the number density in Figure 7, for cases in which particles collide with rough walls, Figure 8 shows that the particle mean velocity profile develops a sharper gradient in the near-wall region. The figure also shows that the particle velocity slips relative to the surface (i.e., is not zero), which is compatible with the elastic bouncing of the particles on the wall as considered in the current simulations. Also, not shown, the radial fluctuating particle velocity is increased by wall roughness. Consequently, wall roughness induces a greater cross-stream transport that will promote particle-particle and particle-wall collisions, in addition to greater mixing with the aqueous phase. In particular, the resulting increase in the number of and momentum transfer associated with particle collisions is expected to lead to enhanced exfoliation and carbonation.

In summary, the simulations used to assess "microscopic" fluid flow modeling illustrate that particle transport and mixing can be enhanced by interactions with roughened surfaces. While the current simulations used to assess the roughness model are idealized, in order to enable the application of simulation techniques that resolve turbulent fluctuations, the computations illustrate the importance of the basic effect of roughness, which is to transfer the mean streamwise momentum of the particles to the fluctuating velocities that are normal to the surface. This is an important mechanism for enhancing transport across the entire channel and facilitating particle-particle and particle-wall collisions, exfoliation and carbonation.

2. Macroscopic Fluid Flow Modeling

Advances in computational fluid mechanics have provided the basis for advanced prediction of the dynamics of multiphase flows. Various approaches exist to solving multiphase flows, some of which focus on tracking individual particles, as highlighted in the previous section on

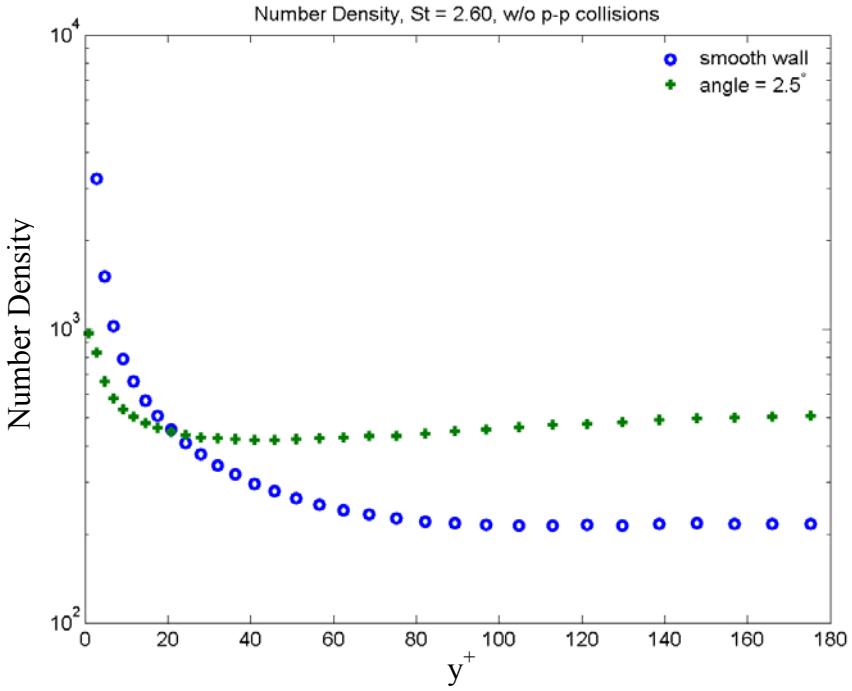

Figure 7. *Roughness influence on mean number density. y^+ represents the distance from the wall during cylindrical pipe flow. 180 represents the pipe center.*

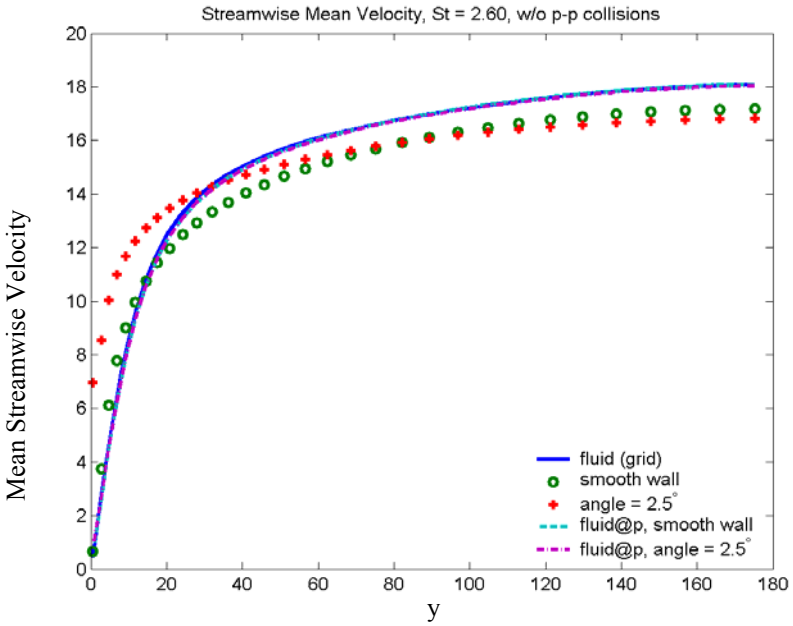

Figure 8. *Roughness influence on streamwise velocity. Fluid (grid) represents the fluid flow mean velocity on the grid. Fluid@p denotes the mean fluid velocity in the vicinity of the particle. Smooth wall represents the particle velocity in the smooth wall model. Angle=2.5 ^{o} similarly represents the particle velocity in the 2.5^o model.*

"microscopic" modeling. Other approaches treat each phase (aqueous carrier flow and dispersed particulates) as continua, referred to as an "Eulerian approach" or "two-fluid" method. The Eulerian approach is adopted in this portion of the work focusing on "macroscopic" modeling in which the aim is to predict the bulk properties of the flow such as the mean velocity, mean pressure drop, and averaged volume fractions.

The simulations performed in this phase of the work are primarily guided by the experiments conducted in the ARC flow loop reactor in collaboration with Larry Penner at the Albany Research Center. In these experiments, approximately 420 grams of finely ground olivine ore is used as a feedstock sample. As a rough estimate, if we consider a mean particle diameter of 30μm, the number of particles in the feedstock sample is approximately 9e+9. Attempting to solve the Navier-Stokes equations for the carrier fluid (the heterogeneous mixture of the aqueous solution and CO_2(sc) phases) and then using Lagrangian tracking of individual particles is unwieldy. The Eulerian approach, which does not attempt to track individual particles, provides a more computationally efficient method.

In the Eulerian approach, the different phases are treated mathematically as interpenetrating continua. The volume fraction of each phase is assumed to be continuous functions of space and time and their sum is equal to one. Fluid and energy conservation equations for each phase are derived to obtain a set of equations, which have similar structure for all phases. A set of momentum and continuity equations are solved for each phase. These equations are closed by providing constitutive relations that are obtained from empirical information. Coupling between the phases is achieved through pressure and interphase exchange coefficients.

Accurate prediction of flow properties such as the mean velocity, pressure drop, and volume fraction distributions at different zones in the flow loop reactor can provide insight into the behavior of the system and hence might prove useful to understanding the dynamics influencing the extent of carbonation observed in the sequestration process.

The flow solution is obtained using a Phase Coupled Semi-Implicit Method for Pressure Linked Equations (PC-SIMPLE) algorithm.[13] As an example, the computation requires approximately 20000 iterations to arrive at a steady state solution for a particle laden multiphase flow in a 32" long, Schedule 80 pipe with an inner diameter of 0.546". This calculation corresponds to a grid generated with 400 points along the streamwise direction (parallel to the flow) and 30 points in the radial direction (perpendicular to the flow). This, when converted to time, translates to approximately 8 hours on a Pentium 4 processor running at 2.8 GHz and with 1 GB RAM.

The flow loop reactor at Albany is equipped with four gauges to measure the pressure drop across various sections of the reactor. The most consistent set of measurements are acquired from gauges mounted across two points 32" apart. Hence, the multiphase flow simulations were carried out using pipe dimensions having the same specifications as this leg of the flow loop reactor at ARC.

Initial computations modeling the flow loop reactor were of the flow in a straight pipe, 32" long and with an inner diameter of 0.546". The computations then progressed to a higher level of geometric complexity by adding a block in the flow, which mimics the presence of a flow mixer

that is installed in the flow loop to enhance mixing of the fluid and dispersed phases and, consequently, enhance reaction. The next level of complexity of the numerical model incorporated a pipe section with two different diameters in the same length of pipe, in turn accounting for the change of the pipe diameter from Schedule 80 (0.546" inner diameter) to Schedule 40 (0.63" inner diameter) (Figure 9) as present in the actual flow loop reactor.

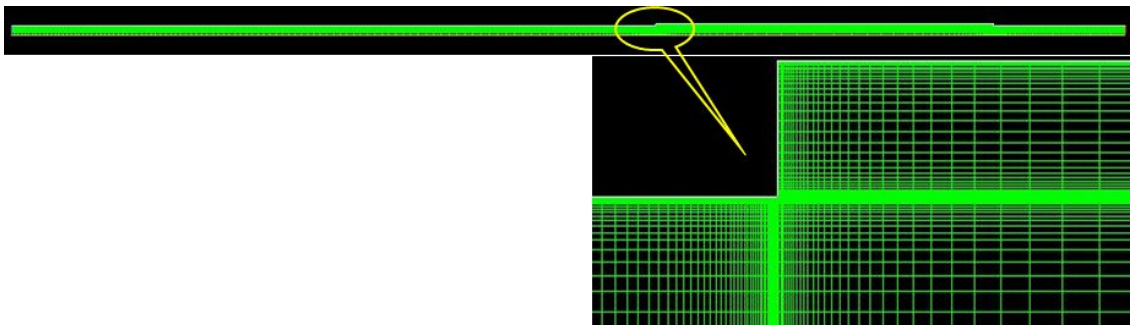

Figure 9. *Cross-section of pipe with zoomed in view of changing diameter. The upper part of the figure shows a low resolution image of the pipe, with a close up of the transition from the schedule 80-40 transition shown below. Both images represent axial cross sections of the upper half of the pipe.*

Given the intricate design of the mixer, which is formed by bolting together small interweaving twisted plates, it is not feasible to model the intricate features of the geometry directly. Instead, the effect of the mixer is modeled as a porous media. Mathematically, the momentum of the flow is reduced by adding a sink to the momentum equations in the porous region of the pipe.

As summarized below, computations were performed with and without the solids phase in order to assess the influence on quantities such as pressure drop. Recent efforts, also summarized below, have focused on changing the particle volume fraction distribution by modeling ribs along the inner wall of the pipe geometry. Flow simulations using ribs have revealed dramatic changes in the particle concentration distribution by the inclusion of ribs along the inner lining of the pipe wall. While preliminary, these results might highlight a possible re-design of the reactor which may enhance carbonation, while avoiding flow mixers, which require cleaning after each run. This may eliminate or reduce the cleaning cycles required using the current design, lowering the cost of system operation. All the computations consider fluid flow through a pipe and are used to assess the effect of physical parameters (e.g., the volume fraction) and numerical procedures used to assist the convergence of the system of equations.

Modeling Strategy: The two-phase (fluid-solid) modeling so far has consisted of analyzing the flow comprised of a mixture of a fluid having properties (density and viscosity) similar to those of a combined mixture of the aqueous solution and supercritical CO_2 under reaction conditions and finely ground olivine ore. The density calculations for the fluid mixture assume a solution formed by the aqueous and supercritical CO_2 components in the ratio of 90% - 10% by volume. The solid phase was represented by particles of diameters 37µm, 75µm and 150µm and having a density of 3300 kg/m^3. Given the symmetry conditions, an axi-symmetric geometry was modeled, and a cross-section of a plane cut along a direction parallel to the flow was meshed. Figure 10 highlights the porous region in the pipe indicating the zone where the mixer is present.

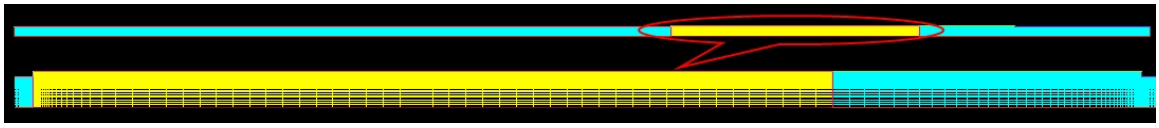

Figure 10. *Reactor with a 7" long porous zone indicating the presence of mixer. The upper part of the figure shows a low resolution image of the pipe containing the yellow porous region, with a close up of the associated region shown below. Both images represent axial cross sections of the upper half of the pipe.*

Turbulence modeling is accomplished using the standard two equation k-ε model with standard values of model constants. Tests to assess the computational procedures (e.g., to calibrate numerical parameters used to ensure convergence of the equations to steady state) have been performed. Certain assumptions have been used for the modeling exercise, most important of which are absence of reactions (due to limitations imposed by the software to solve for reaction and fluid flow simultaneously), no mass transfer, uniform mass flow rate and no roughness along the inner surface of the pipe. The equations are initially converged using a first-order accurate numerical method, which is numerically efficient although not sufficiently accurate. At convergence, the numerical method is switched to an accurate second-order scheme and the simulation continued until convergence is achieved. Initial validation of the computations were based on comparison of predicted pressure drop against the standard Lockhart and Martinelli correlation for predicting pressure drop in mixtures that characterize flow loop reactors.[14] The numerical simulations considered a single particle diameter.

Table 2 shows the pressure drop (δP) results obtained using the porous model without particles in the flow. The comparison shown is made against a similar experimental run with the mixer in the pipe using pressure drop measurements from the flow loop reactor. The porous model employs constants that can be used to initially calibrate the simulation in order to account for effects such as porosity, with refinement done via comparison with empirical data. The CFD predictions in Table 2 were obtained by adjusting the initial constants in order to closely match the experimental measurements at 3.5 gpm. Once calibrated, the model was run for other flow rates; Table 2 shows that the variation of the pressure drop with flow rate is essentially linear.

Table 2. Pressure drop measurements for cases with mixer and without compared with average pressure drop measurements from reactor runs at 185°C and 2200 psi.

Porous media model results (without particles)		
Mass flow (gpm)	δP (psi) 32" long pipe with porous zone (parentheses values without mixer in pipe) – CFD predictions	δP (psi) using reactor data run at 185 C and 2200 psi
2.0	0.79 (0.08)	
3.0	1.40 (0.15)	
3.5	1.72 (0.21)	1.69
4.0	2.00 (0.27)	

Flow rate measurement and pressure drop data that are planned to be obtained in the second year of this project will be used to further refine the model.

Figure 11(a) shows a plot of volume fraction distribution of the olivine particles as a function of their diameter and the radial distance from the pipe center. Shown in Figure 11a is the volume fraction distribution plot down stream from the porous mixer, which is still 18" removed from entering the next mixer (in the flow-loop reactor). The plots are generated for size fractions of 37μm, 75μm, and 150μm. Figure 11(a) indicates that the particle distribution has largely recovered from the effects of passing through the mixer well before encountering the next mixer. This in turn can dramatically reduce the probability of particle collisions and passivating layer exfoliation over more than half of the length of the reactive transport. This suggests an alternative approach of incorporating more, smaller mixers spaced at closer intervals to more effectively enhance particle collisions and exfoliation throughout the reaction transport region.

The near wall particle volume fraction concentration in Figure 11a is higher than the other regions of the pipe. This pattern was observed for each size fraction modeled. While this effect is displayed by all size fractions, the larger size fraction exhibits this behavior more prominently than the smaller size fractions, consistent with the slower recovery of the larger particles to the more uniform profile achieved by the smaller particles. This is further consistent with the ability of the larger particles to better retain their cross-stream velocity component, which can further enhance particle collisions and exfoliation.

A possible configuration to promote more uniform and sustained mixing, optimizing particle collisions and exfoliation in the process, could be based on the substitution of ribs (Figure 12) or studs at frequent equidistant intervals along the inner walls of the reactor pipes. This structural modification is currently being modeled to explore if it can induce higher inter-particle interaction, which can translate to higher carbonation rates. Including such ribbed pipes in the flow loop reactor may also reduce the need for periodic cleaning of the reactor further reducing process cost.

As a first step towards using the simulations for such studies, the domain was modeled with two ribs 0.15" high and 0.5" thick along the inner pipe wall. The particle volume fraction distribution at the exit with and without the ribs are shown in Figure 11(b) for different size fractions. Comparison of Figures 11(a) and 11(b) indicate that the presence of the ribs has drastically altered the solid volume fraction distribution, substantially enhancing particle concentrations downstream from mixing. It is also important to note the enhanced cross-stream velocity component suggested downstream from the ribs, which can lead to enhanced particle interactions and exfoliation. Since the flow solver does not hold the potential to solve for both the reactivity and the flow simultaneously, effect of ribs on the reactivity enhancement is subject to experimental verification. Increasing particle concentrations have been separately associated with enhanced carbonation reactivity using the flow loop reactor and the ASU batch reactor, as discussed below. This observation will be further explored during the second year of

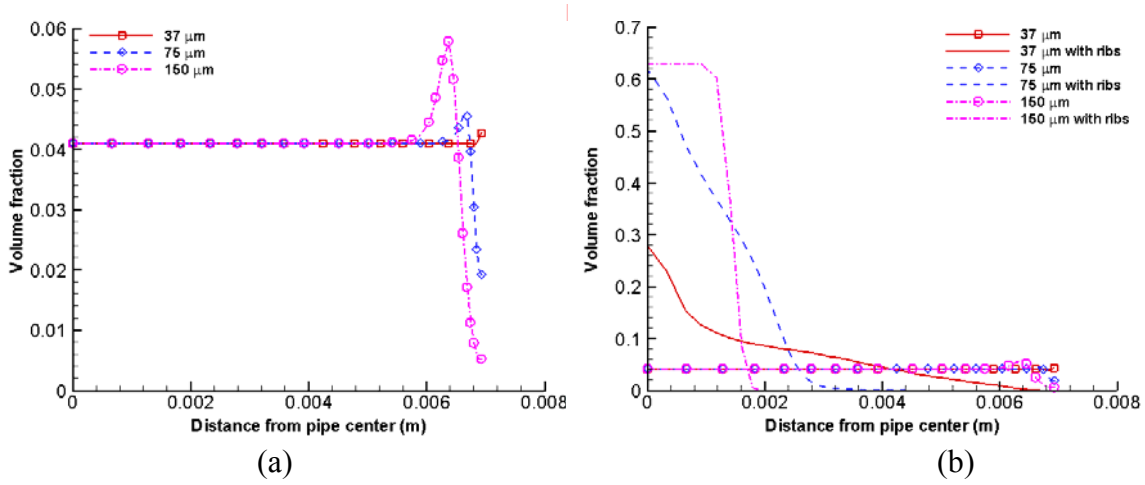

Figure 11. *Volume fraction distribution of olivine at exit of pipe (a) Simulation without ribs for 3 size fractions (b) Comparison for simulation with ribs for the same size fractions.*

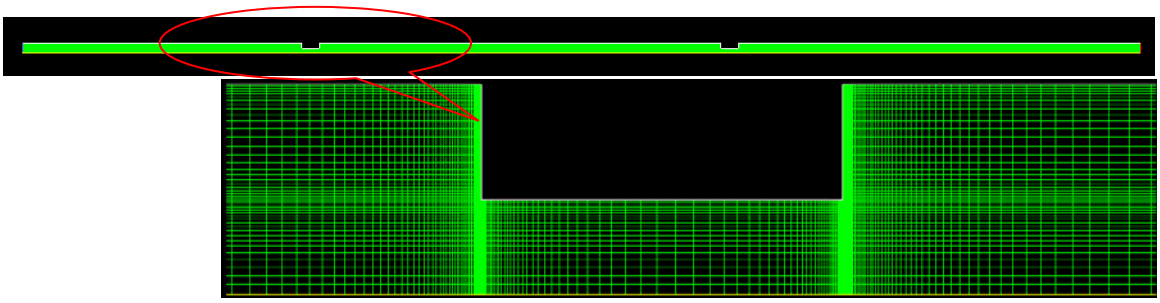

Figure 12. *Cross-sectional profile of the axi-symmetric pipe with ribs included in the geometry. The upper part of the figure shows a low resolution image of the pipe, with a close up of the section highlighted shown below. Both images represent axial cross sections of the upper half of the pipe.*

the project, to further evaluate the potential that ribs offer to enhance particle interactions, exfoliation and carbonation. Efforts are underway to simulate the flow in the 100ml ASU batch reactor with a primary objective to study the distribution of olivine particles. The distribution of the particles in the ASU reactor may shed some light on collision processes and in turn be useful for comparing the extent of carbonation observed using the Flow-Loop reactor at ARC and the batch reactor at ASU.

3. The Effects of Particle Size and Particle Size Distribution

The above modeling investigations indicate that the reactant particle size distribution may be a key factor impacting particle collision frequency, momentum transfer, exfoliation and carbonation. During the first year of this project we explored the effect of particle size distribution using the ASU batch reactor and began partner studies in collaboration with Larry Penner to explore the effect of size distribution using the ARC Flow-Loop reactor. Initial observations vs. particle size using the Flow-Loop reactor are given in Figure 13.

Initial Studies of the Effect of Pump Speed and Particle Size On Olivine Carbonation in the ARC Flow Loop Reactor

Pump Speed (rpm)	Particle Size Fraction	Extent of Carbonation
1198	< 400 mesh (baseline)	72.0%
1002	< 200 mesh	66.9%
1198	< 200 mesh	63.2%
1450	< 200 mesh	73.8%
1750	< 200 mesh	77.9%

ARC Flow Loop Reactor

Figure 13. *The ARC Flow-Loop reactor (right) together with the initial extent of carbonation observed for < 400 mesh and <200 mesh Twin Sisters olivine feedstock.*

Preliminary observations of carbonation vs. particle size fraction using the ARC flow-loop reactor (Figure 13) indicate that the extent of carbonation can remain quite high for larger feedstock particles. As the large majority of the grinding cost associated with preparing the <400 mesh feedstock comes in reducing the material from <200 mesh to <400 mesh, the ability to effectively carbonate larger <200 mesh olivine feedstock can substantially reduce process cost. Further collaborative studies as a function of particle size distribution using the ARC flow-loop reactor have been initiated and will continue in Year 2, to further explore the potential controlling particle size distribution offers to reduce process cost.

We also initiated investigations as a function of particle size fraction using the ASU batch reactor as described below. Single crystal San Carlos olivine fragments are incorporated as the feedstock material. The associated carbonation runs were carried out using the standard ARC solution (1M NaCl & 0.64M $NaHCO_3$) and reaction conditions (1 hour at 185 °C under 2200psi of CO_2, with 1500 rpm stirring). The list of these experiments, their conditions and the extent of carbonation in each are given in Table 3. The average extent of carbonation for 4 runs with the standard feedstock material (<38μ) and two runs each for each particle size fraction are shown, with 34% carbonation observed for the baseline <38μ material. The relatively low overall extent of carbonation observed can be related to the single crystal nature of the feedstock particles used herein to facilitate mechanistic observations of passivating layer formation/exfoliation.

Table 3. Extent of Carbonation Observed as a Function of Particle Size Distribution using San Carlos Olivine and the ASU Batch Reactor

Series	Feedstock Particle Size Fraction	Extent of Carbonation	Extent of Carbonation Predicted*
1	<38 micron	34.0%	--
2	38-75 micron	1.3%	--
3	75-150 micron	0.7%	--
4	<75 micron	27.2%	15.4%
5	<150 micron	21.7%	11.5%

* The extent of carbonation predicted is based on a weighting of the extent of carbonation observed for reaction series 1, 2 and 3 and the wt% of these size fractions used in series 4 and 5.

The coarser fractions, 38-75μ & 75-150μ, show almost no carbonation, exhibiting 1.3% and 0.7% carbonation, respectively. Importantly, the extent of carbonation observed for the <75μ and <150μ series are almost double that predicted based on the weighted average of the extents of carbonation observed for the <38μ, 38-75μ and 75-150μ size fractions incorporated. Hence, there is significant synergism in terms of particle interactions that can substantially enhance carbonation. For example, if we assume the 38-75μ and 75-150μ size fractions remain similarly unreactive, this would translate to 63% and 68% carbonation for the <38μ fraction in the <75μ and <150μ runs, respectively. Incorporating quartz as an abrasive agent can also significantly enhance carbonation, underscoring the importance of particle-particle interactions in enhancing carbonation. Controlling the particle size distribution appears to offer intriguing potential to enhance carbonation. We will further explore this potential in Year 2, comparing and contrasting observations for the different flow conditions present in the ARC and ASU reactors.

Scientific Progress: Investigation of the Potential that Sonication Offers to Enhance Exfoliation and Carbonation

Sonication experiments were conducted by stopping the standard mineral carbonation reaction after a half hour, introducing a brief sonication period of 1-10 minutes, followed by a second half hour exposure to the standard mineral carbonation process. The overall carbonation reaction conditions remained the same as the standard carbonation conditions throughout the two half-hour mineral carbonation steps. Extent of carbonation runs that mimic the sonication runs, but without the intermediate sonication exposure, were used for baseline comparison. In each case 15 wt% <38μ San Carlos olivine was mixed with 50ml of the standard aqueous solution (1M NaCl + 0.64 M $NaHCO_3$) and added to the batch reaction system. After 30 min of stirred reaction under the standard conditions, the reaction was stopped and rapidly cooled by using the internal cooling coil and placing the reaction vessel in ice water. This results in the temperature dropping to ~40°C within 10min. After cooling is complete, the system is depressurized and the batch reaction stirring system is replaced with the sonication system (Figure 14). The system is purged with CO_2 and subsequently brought to the starting sonication temperature and pressure. Once at temperature and pressure, sonication is then run for 1or 10 min at full power. Once the sonication is done, the vessel rapidly cooled in ice water and depressurized. The vessel containing the reaction solution is then reattached to the batch reaction system and the second half hour carbonation step is performed.

The extent of carbonation observed for combined ½ hour carbonation/sonication/½ hour carbonation runs is given in Table 4. Under the pressures and temperatures investigated to date, sonication has not enhanced carbonation. Given that the extent of carbonation varies by as much as ±5% for the same reaction conditions, the results suggest that sonication using the initial conditions explored may even inhibit carbonation. This suggests that high power (1500 watt) sonication exposure may significantly reduce the olivine particle interactions that enhance exfoliation during the second half hour of carbonation. FESEM analysis of the particle size distribution as a function of sonication conditions was initiated at the end of the first project year to explore this effect. Samples taken before and after the sonication step are also being investigated. These studies will be completed in Year 2. As sonication is relatively costly (energy intensive) compared with the other two approaches being investigated (chemical and slurry flow modeling control) and did not show initial promise for low-cost enhancement of

Figure 14. *The sonication and batch reaction systems at Arizona State University: (a) The sonication probe and reaction vessel; (b) the reaction vessel sealed to its sonication assembly; (c) the same reaction vessel shown in a and b sealed to the batch reactor stirring assembly.*

carbonation, the other two approaches were emphasized during Year 1. We will complete our studies of the effect of temperature, pressure, and sonication power and time on the effectiveness of sonication in enhancing carbonation in Year 2, together with investigations of the effect of fluid composition, and reactant particle concentration and size. If any of the above studies offer hope for low-cost enhanced carbonation, we will investigate combinations of the most effective parameters observed as well.

Scientific Progress: Understanding the Mechanisms that Control Passivating Layer Formation and the Impact the Above Approaches Have on Exfoliation and Carbonation Mechanisms

During the first project year, we have evaluated the effectiveness of a variety of reaction flow dynamics, alkali cation solution chemistry, and sonication approaches to enhance carbonation. These studies have involved carbon elemental analysis and X-ray powder diffraction of scores of product samples. The primary objective in the first project year is to identify those approaches that are most effective in enhancing carbonation. During the first project year, our mechanistic investigations substantially focused on enhancing our understanding of passivation layer structure, composition and behavior associated with the baseline process developed by the ARC.

Table 4: Effect of sonication on carbonation of San Carlos olivine (<38μ). The total carbonation time is 1h.^

Exp. #	Sonication Conditions	Extent of Carbonation (%)
132^{B}	10 min; 20°C; 900 psi CO_2	**25.9**
202^{D}	1 min; 20°C; 15psi CO_2	**25.4**
203^{D}	1 min; 20°C; 900psi CO_2	**40.0**
207^{D}	1 min; 20°C; 2200psi CO_2	**36.5**
205^{D}	1 min; 185°C; 15psi CO_2	**36.5**
206^{D}	1 min; 185°C; 900psi CO_2	**21.3**
208^{D}	1 min; 185°C; 2200psi CO_2	**35.5**
$147^{B,*}$	none	**39.5**
201^{D*}	none	**41.5**
$137^{B,**}$	none	**34.1**
$204^{D,**}$	none	**47.8**

* One hour standard runs; **two half hour runs, B = olivine batch B; D = olivine batch D

^ Note: the temperatures and pressures given are the starting pressures and temperatures associated with sonication. Both T & P increase significantly during sonication.

The objective is to enhance baseline understanding, while we are exploring in parallel the impact that reaction flow dynamics, alkali cation solution chemistry, and sonication have on exfoliation/carbonation.[15] In Year 2, we will explore the impact that the approaches that are identified as being most effective in enhancing carbonation have on the mechanisms that govern passivation layer formation, properties, exfoliation, and carbonation reactivity. Substantial progress has been made in enhancing our understanding of passivating layer formation processes during the first year. A summary of the overall understanding developed is given below.

1. Olivine: A Naturally Occurring Solid Solution Series $(Mg_xFe_{1-x})_2SiO_4$.

Olivine forms a solid solution series between its end members forsterite (Mg_2SiO_4) and fayalite (Fe_2SiO_4), with naturally occurring olivine generally richer in magnesium.[16] It adopts an orthorhombic structure, with Mg and Fe interchangeably occupying the same lattice sites. The cell parameters generally increase with increasing Fe content, exhibiting Vegard-like behavior between the forsterite and fayalite end members (e.g., Mg_2SiO_4: a = 4.76Å, b = 10.20Å, and c = 5.98Å; Fe_2SiO_4: a = 4.82Å, b = 10.48Å, c = 6.11Å).[16] The single crystal San Carlos olivine fragments used in the following investigation of the mechanisms that control carbonation at the aqueous solution/olivine reaction interface contain ~8.5% Fe - $(Mg_{0.915}Fe_{0.085})_2SiO_4$.

2. Investigation of the Carbonation Reaction Products:

X-ray diffraction (XRD) indicates the products that form during aqueous olivine mineral carbonation are magnesite and amorphous silica, as seen in Figure 15. The only crystalline phases observed are the product magnesite ($MgCO_3$) and the unreacted forsterite. The expected

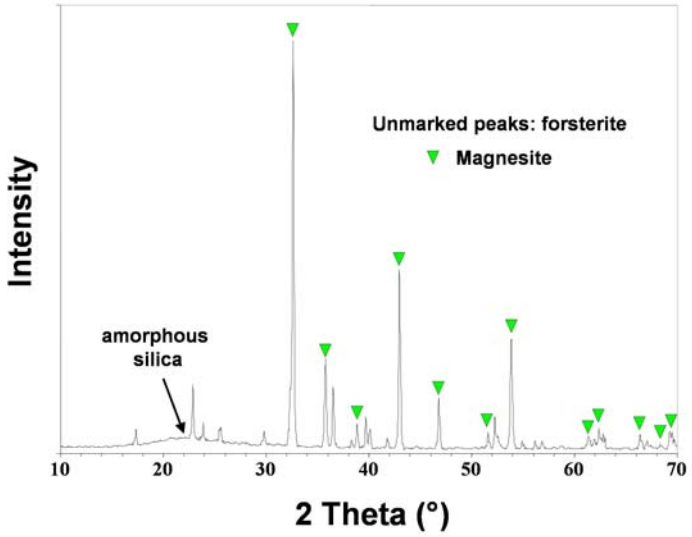

Figure 15. *XRD pattern of the aqueous mineral carbonation reaction products showing magnesite, residual forsterite, and the broad increase in scattering intensity centered at ~22°, which is indicative of amorphous silica formation.*[17]

silicon-containing product is identified as an amorphous silica-containing material by its characteristic broad scattering intensity around 22° 2-theta.[17] FESEM imaging of the product materials that form during carbonation reveal two characteristic particle shapes, (i) crystals and (ii) irregularly shaped product particles, as shown in Figure 16. The crystals and particles are most frequently observed separately, but a small fraction are intergrown in clusters as well. The morphology of the irregularly shaped particles, as well as the broad XRD intensity around 22°, are consistent with those observed for hydrothermally-formed amorphous silica.[17] EDS confirms the irregularly shaped particles exhibit the strong Si and O signals expected for silica and the polyhedral crystals exhibit the expected strong Mg and O signals for magnesite. Elemental analysis of the reaction products shows they do not contain H within experimental error (± 0.3 wt%), indicating the silica-rich material is largely H free and primarily associated with siloxane (Si-O-Si) bonding.[18]

A substantial number of the magnesite crystals formed were found to have irregular corners/edges, as seen in Figure 16, indicating particle abrasion accompanies rapidly stirred (1,500 rpm) carbonation. Abrasion can occur via particle-particle interactions and/or particle interactions with the reaction vessel/impeller. Intergrown magnesite/silica clusters typically exhibit preferential magnesite abrasion around the outer cluster edges, indicating the clusters formed during stirred carbonation and not after the reaction stops (Figure 16d). The intimate

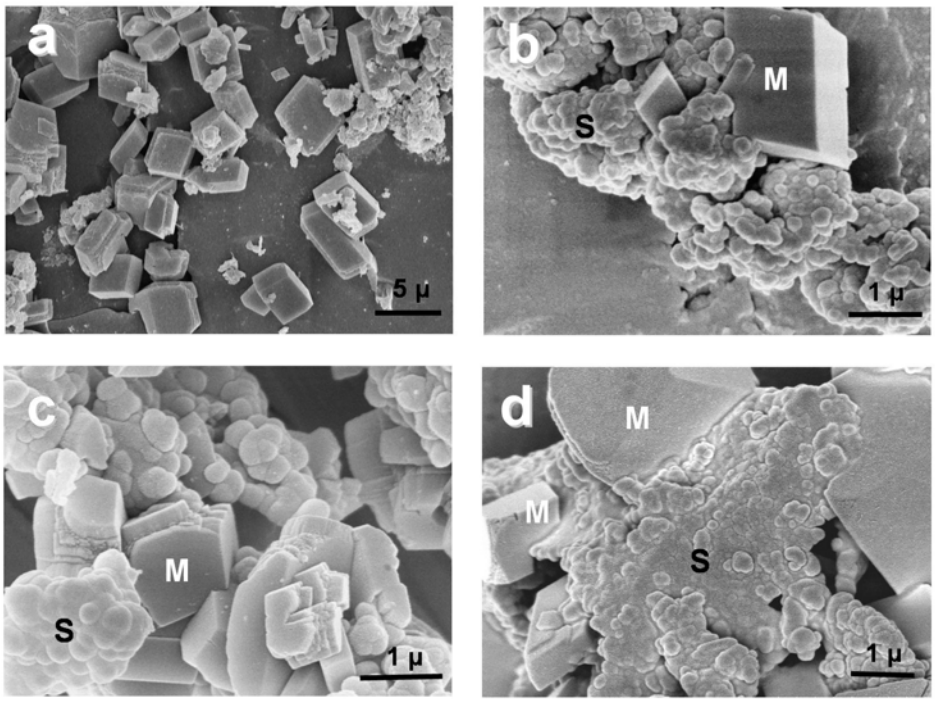

Figure 16. *FESEM images of olivine carbonation reaction products. Two types of particles are observed, crystals and irregularly shaped particles. The products are most often observed as separate particles and crystals, but are also observed to have aggregated into clusters during the mineral carbonation process. (a & b) magnesite crystals (M) and irregularly shaped silica-rich particles (S). (c) magnesite crystals with eroded edges and corners are often observed (e.g., the crystal marked "M"), suggesting substantial particle abrasion occurs during carbonation. (d) a close up of an intergrown silica/magnesite composite particle. Selective abrasion of the outer perimeter of the softer magnesite crystals, as observed for the two crystals in the upper left corner (indicated by "M"), indicates the intergrown particles form during carbonation and not as the result of precipitation (see also Figure 20).*

intergrowth of silica and magnesite during carbonation indicates that magnesite can nucleate and grow in association with silica formation, as well as directly from solution.

3. Investigation of the Olivine Reaction Surface/Interface.

Multiple reactions were stopped before completion to explore representative olivine reaction surfaces/interfaces that form during carbonation and the mechanisms that control reactivity. A few larger (> 200µ) olivine crystal fragments were added to explore the reaction surface/interface over larger areas. Silica-rich passivating layers and surface regions missing glass-like layer fragments were routinely observed to have formed on the olivine surface during carbonation, indicating passivating layer formation, cracking and exfoliation are integral to the carbonation process, as seen in Figure 17. Figure 17a shows a silica-rich passivating layer region where sections of the layer have fractured and exfoliated. Figure 17b shows a closer view of areas that have experienced passivating layer fracture and exfoliation. In addition to glass-like fracture and exfoliation of original layer fragments, new passivating layer regions have begun to regrow on the olivine surface areas exposed by exfoliation.

A small fraction of the surfaces observed (≤1%) were largely free of passivating layer formation.

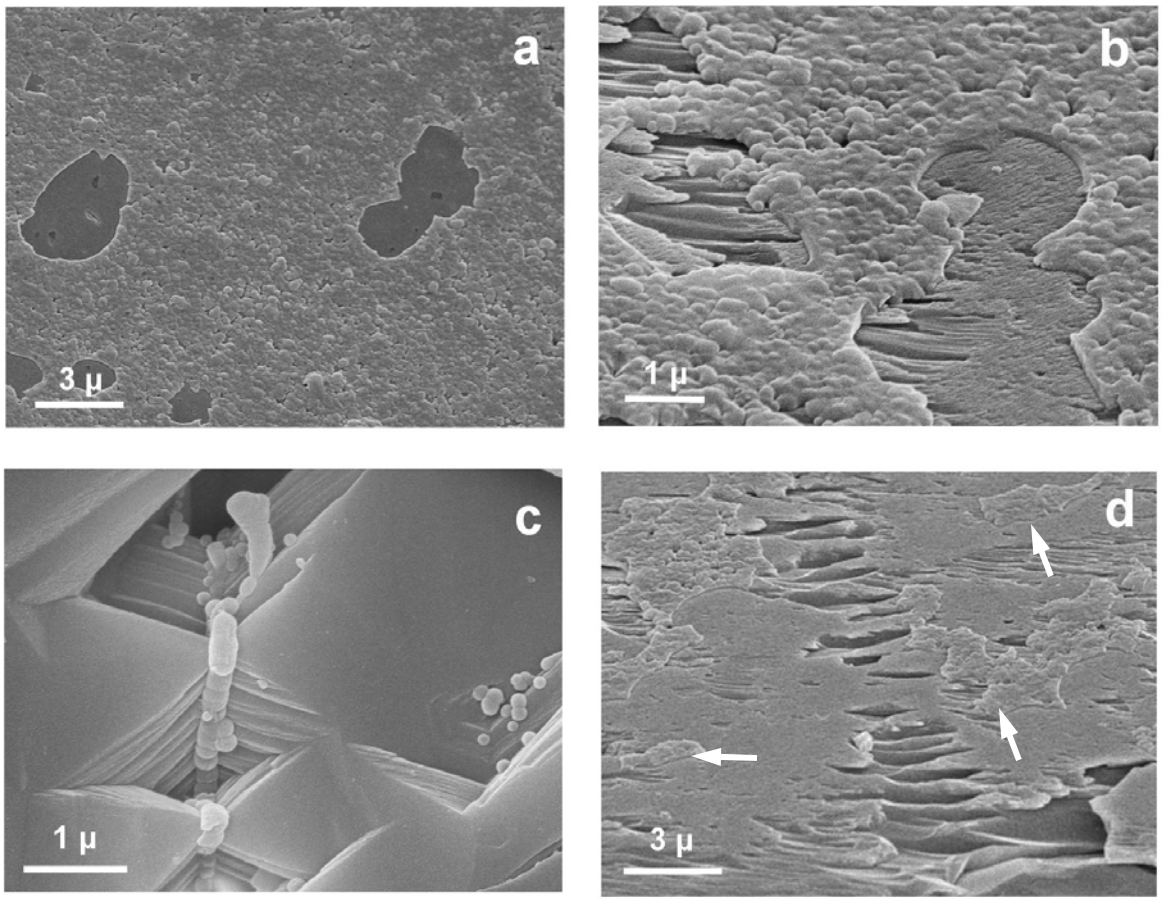

Figure 17. *FESEM images of the olivine reaction surface after partial carbonation in the standard aqueous reaction slurry with 1,500 rpm stirring at 185 ^{o}C under 150 atm CO_2. (a) a silica-rich passivating layer that has formed on the olivine reaction surface with areas that have fractured and exfoliated during reaction. (b) a closer view of areas that have experienced passivating layer fracture and exfoliation. Note the regrowth of new passivating layers where the old layer fragments previously exfoliated. (c) Etch pits that formed on the olivine surface during carbonation. Areas in and near the etch pits were often found to be devoid of passivating layer formation. Note the formation of the irregular silica-rich deposits in and on the etch pits, suggesting silica dissolution/precipitation. (d) An area showing regions that have experienced silica-rich passivating layer fracture, exfoliation and regrowth, and regions of fresh olivine surfaces that appear associated with olivine surface defects. Note the apparent olivine fragment that is partially broken away from the surface in the lower right corner. Passivating layer "island" remnants are often found on the reaction surface (indicated by the white arrows)*

Surface irregularities, especially etch pits, were generally found in these regions, as shown in Figure 17c. This suggests defects, such as dislocations, inclusions and low-angle grain boundaries, which are commonly found in San Carlos olivine,[19] can significantly impact local carbonation reactivity by raising the olivine surface energy via strain field formation. This, in turn, can lead to the locally enhanced congruent dissolution observed. Although passivating layers are not typically observed in these regions, irregular silica-rich deposits are occasionally found, suggesting they are largely associated with silica deposition, as seen in Figure 17c. The irregular surface morphology observed for the passivating layers is quite similar to that observed for individual silica particles, as well as for hydrothermally deposited silica,[17] suggesting silica deposition may also occur on passivating layer surfaces.

Figure 17d shows a region that has experienced silica-rich passivating layer fracture, exfoliation and regrowth, as well as exposed olivine surfaces. The olivine fragment that appears partially broken away from the surface suggests the exposed olivine surfaces may be associated with the cracking and breaking away of small olivine fragments during carbonation. Several independent passivating layer islands with glass-like fracture edges still remain after the particle has experienced substantial abrasion and layer exfoliation, indicating the layers that form are initially strongly bound to the olivine and associated with incongruent olivine dissolution. Single crystal samples were quenched early during unstirred carbonation to further explore initial passivating layer formation. Cross sectional observation reveals a well-bonded, silica-rich-passivating-layer/olivine inter-phase interface at the nanoscale, consistent with incongruent dissolution, as seen in Figure 18. Atomic-level high resolution transmission electron microscopy investigations

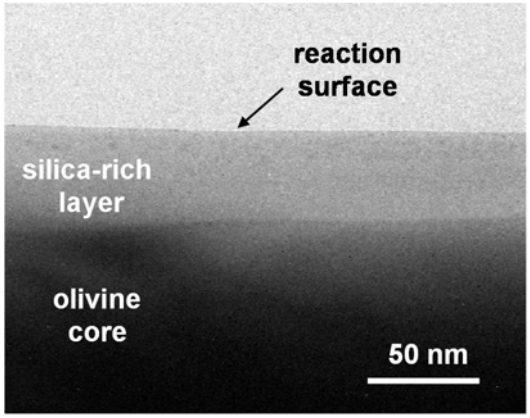

Figure 18. *Transmission electron microscope image of a cross section of the silica-rich passivating layer that forms on the olivine surface early in the carbonation process. The sample was prepared under the standard reaction conditions, but without stirring to protect the passivating layer that forms from abrasion. Note the well-bonded interface between the silica-rich passivating layer and the olivine surface.*

reveal the interface is well-bonded at the atomic level (see below). Hence, passivating layer formation can be associated with incongruent magnesium dissolution together with some silica deposition from solution on the reaction (e.g., passivating layer) surfaces that form. Interestingly, hydrothermal deposition has been observed to form similarly brittle silica.[17] The interfacial stress induced at the olivine/silica interface via incongruent olivine dissolution should induce shear forces associated with the reduction in silica volume as olivine is converted to silica at the reaction interface (discussed further below). These forces can further promote the observed fracture and exfoliation of brittle silica passivating layers during stirred carbonation.

Aqueous olivine dissolution is a complex process, with a range of dissolution rates and incongruent as well as congruent dissolution observed as a function of pH and the presence of anionic species that can impact dissolution at the reaction surface (*e.g.*, chelating agents, such as potassium acid phthalate, KHP).[20-23] We previously analyzed the aqueous solution equilibrium equations for a Na^+ buffered H_2O-CO_2 system to explore aqueous speciation and pH as a function of T & P under mineral carbonation reaction conditions. Similar activities of CO_2(aq) and HCO_3^- and a pH of 6-7 were found for the current reaction conditions.[24]

A currently accepted picture of olivine acid dissolution is based on the ion exchange reaction $Mg^{2+} \Leftrightarrow 2H^{+}$ coupled with the formation of >SiOH groups. These groups can either form siloxane bonds within the reaction layer via >Si-OH + HO-Si< $\rightarrow$ >Si-O-Si< + H_2O (e.g., during incongruent dissolution), or dissolve as $Si(OH)_4$ monomers that can later polymerize and precipitate via analogous siloxane bonding and H_2O evolution.[18,21-23] As the silica-containing samples observed herein are largely H-free, it is reasonable to assume that the >SiOH groups that form during carbonation are transitory, readily succumbing to siloxane bonding to yield the brittle passivating layers observed.

4. Simulation of Passivating Layer Formation: A classical force field approach was applied to investigate the stability, structure and permeability of siloxane passivating layer formation associated with incongruent dissolution. A 12,000 atom model that spans the region from within the olivine to the reaction region at the solution interface was used. The interaction between individual ions is represented by long-ranged coulomb interactions and short-ranged potentials consisting of an exponential repulsion and a van der Waals tail ("Born-Mayer" form).

Classical molecular dynamics simulations were carried out using the MOLDY computer program.[25] The force fields employed are based on those developed for $MgSiO_3$ by Matsui,[26] with slightly modified formal charges and Born-Mayer potential parameters for Mg and Si chosen to simultaneously reproduce the equations of state of α-quartz (SiO_2) and forsterite (Mg_2SiO_4). The pair-potential parameters employed are provided in Table 5 along with the effective ionic charges. The simulations of the basic crystalline phases were carried out in a supercell built from N×N×N replicas of the respective unit cells (N~3-6). In order to benchmark our procedure we calculated the equilibrium volume of both α-quartz (SiO_2) and forsterite (Mg_2SiO_4) at 300K over a pressure range of –20 to 80 GPa. All runs used an integration time

TABLE 5. Born-Mayer Potential Parameters for the Forsterite Simulations. Ionic Charges for O, Mg and Si ions are –1.365, 1.365 and 2.730 e respectively.

Pair	A_{ij} ($\times 10^{-3}$) (eV)	b_{ij} ($Å^{-1}$)	C_{ij} (eV $Å^6$)
O-O	1.622	3.333	30.22
O-Mg	8.038	4.951	0.0
O-Si	7.367	5.263	0.0
Mg-Mg	1310.1	9.615	0.0
Mg-Si	2329.2	10.870	0.0
Si-Si	5008.1	12.501	0.0

step of 0.5 fs, velocity rescaling every 10 time steps, and between 10,000-100,000 time steps per run. The energy volume data was fitted to a standard Birch-Murnaghan equation of state form[27] to extract the equilibrium volume (V_0) and bulk modulus (B_0) at ambient pressure. For forsterite we obtained V_0=69.3Å^3 and B_0=121 GPa (experimental values[28]: V_0=72.6Å^3, B_0=123 GPa) while for α-quartz we obtained V_0=39.1Å^3 and B_0 = 40 GPa (experimental values[28]: V_0=37.2Å^3, B_0=37 GPa). To further calibrate our procedure and test the ability of the pair-potentials to describe amorphous systems we undertook a brief study of silica glass. A structural model was obtained by melting an 648-atom cell of α-quartz and then quenching the structure from 3000K by simulated annealing in nine 300K cooling stages of 80,000, 0.5 fs time steps. The resulting

structure exhibits all of the hallmarks of thermal glass, including a fully connected corner-shared tetrahedral SiO_4 network, and a mean density of about 2.31 g/cc, which is slightly high compared with the experimental value of ~ 2.20 g/cc. To further quantify the bonding distribution of the simulated glass we computed the radial distribution function (RDF) and find that it closely reproduces the essential structure of the RDF observed by neutron scattering for annealed silica glass.[29]

As the dissolution rates associated with passivation-layer (PL) growth via incongruent dissolution are beyond the reach of our simulation times, we devised a synthetic procedure to simulate the low-temperature process. Beginning with a large forsterite slab, we randomly remove Mg and O atoms from the outermost region, 10 Å at a time and then carry out a brief relaxation run to re-equilibrate the defective structure without promoting significant Mg diffusion. We continue this process until Mg on one half of the full slab is removed. A final annealing run at 500K is then performed leading to the diffusion of Mg and the formation of a reaction interface approximately 20 Å in thickness and an ~50 Å PL with approximately SiO_2 stoichiometry, as seen in Figure 19a. Substantial contraction of the newly formed silica region relative to its extent in the olivine framework was observed in the simulated structure. The PL formed consists of a low-density glass-like SiO_2 network, with bonding very similar to thermal SiO_2 glass (O:Si ratio close to 2). The layer formed is quite stable thermally, remaining essentially unchanged during heating/cooling cycles from 300K to 600K.

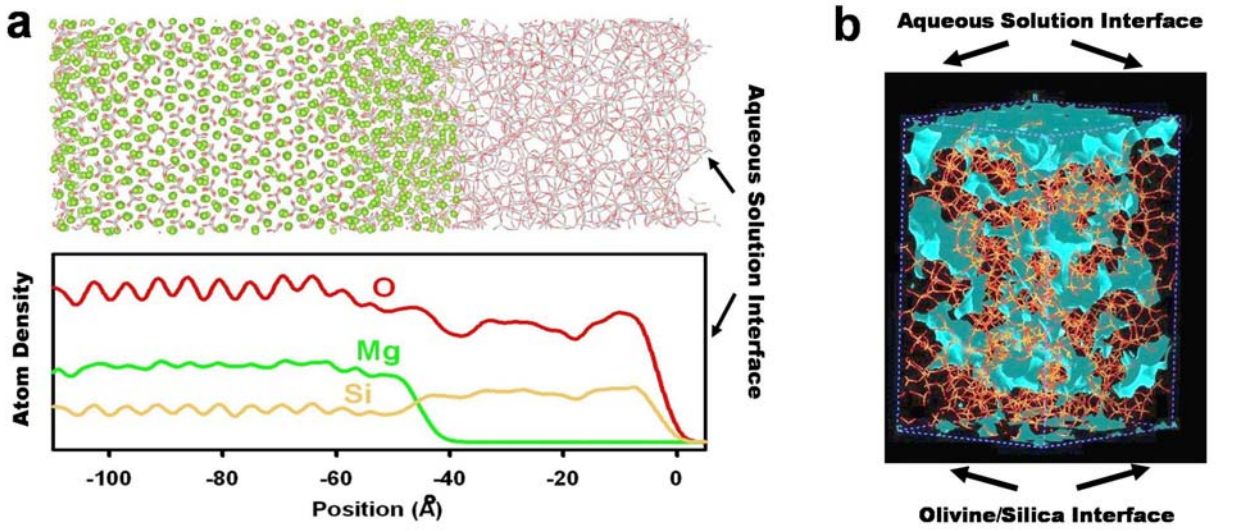

Figure 19. ***(a)*** *Simulated forsterite/passivation-layer reaction interface system containing ~12,000 atoms (above). The associated atom density as a function of distance from the aqueous solution interface is shown below. An ~ 20Å thick transition layer from Mg_2SiO_4 to "SiO_2" is observed. Mg, O and Si atoms are represented by green spheres, red sticks and gray sticks, respectively.* ***(b)*** *Map of regions that can accept a 4Å probe without making van der Waals contact in the silica layer (shown in blue). Note the presence of continuous permeable regions, which can facilitate the diffusion of reactant species in and through the layer.*

Layer permeability is critical for PL formation via incongruent dissolution, as it facilitates both the transport of Mg ions through the layer and the formation of water and its expulsion from the layer. Close examination of the simulated PL structure suggests that even without allowing for the structural disruption associated with >Si-OH formation, it may be permeable to key species

associated with mineral carbonation (*e.g.*, Mg^{2+}, H^+, and H_2O), consistent with incongruent dissolution. Such permeability does not exist in our quenched thermal SiO_2 glass model, but is found for the simulated PL structures. Interestingly, the RDFs calculated for the simulated SiO_2 glass and PL material were found to have significant similarities, suggesting their short-range structure is very similar.[30] To reveal the differences between the structures we appeal to a "free volume" analysis module available in the Cerius2 simulation software suite.[31] The occupiable volume is probed by overlaying grid points set at 0.5Å intervals throughout the structure. A probe particle is then placed at each grid point in sequence and the point is considered to be "occupiable" if there is no van der Waals contact with the PL structure in any of several hundred directions. Nine probe particles with diameters ranging from 2 Å to 6 Å were used. As expected on the basis of visual inspection and density, the strained PL structure, which retains residual strain as it was relaxed while bonded to the host olivine, exhibits the largest fractional occupiable volume. This is followed by the relaxed PL structure, which is first severed at the olivine interface and then relaxed as above, and thermal glass. About 7% of the occupiable volume of the strained PL material was found to be able to accommodate H_2O molecules (Dprobe ~ 2.8 Å),[32] while about 5% of the volume can accommodate H_2O in the relaxed PL material (even using the 2Å probe, the occupiable volume in thermal glass is negligible, as expected). Slightly greater occupiable volumes are expected for Mg^{2+} owing to its smaller diameter**.** In order to explore the potential impact of the strained and relaxed PL structures on the diffusion of the species associated with mineral carbonation, the regions of the PL that can accept different probe diameters were mapped out. Their interconnectivity, as illustrated in Figure 19b, is consistent with reactant species diffusion in/through the PL and incongruent dissolution.

The above simulations and experimental observations point to a passivating layer formation process that is associated with incongruent dissolution and some silica deposition. Both processes apparently involve the acid dissolution of Mg^{2+}/Fe^{2+} via the formation of >Si-OH groups, which can release $Si(OH)_4$ to solution or undergo condensation reactions prior to dissolution (>Si-OH + HO-Si< $\rightarrow$ Si-O-Si + H_2O) to form the siloxane bonds required for incongruent PL formation. Similar condensation reactions can facilitate $Si(OH)_4$ polymerization and deposition from solution, which can occur on PL surfaces and contribute to PL growth. The presence of strong siloxane bonding within the PLs is evidenced by their brittle fracture and exfoliation.

5. Intergrowth of Carbonate, Silica and Olivine During Aqueous Carbonation

Intergrowths of olivine, magnesite and silica were also observed on the surface of partially carbonated particles. The intergrowth on the surface in Figure 20 is generally representative of such particles. Selective erosion of the outside corners of the surface magnesite crystals was routinely observed, indicating (i) significant particle abrasion occurred during carbonation and (ii) the observed olivine/silica/magnesite intergrowth formed during carbonation and not via precipitation or particle settling after the reaction stopped.

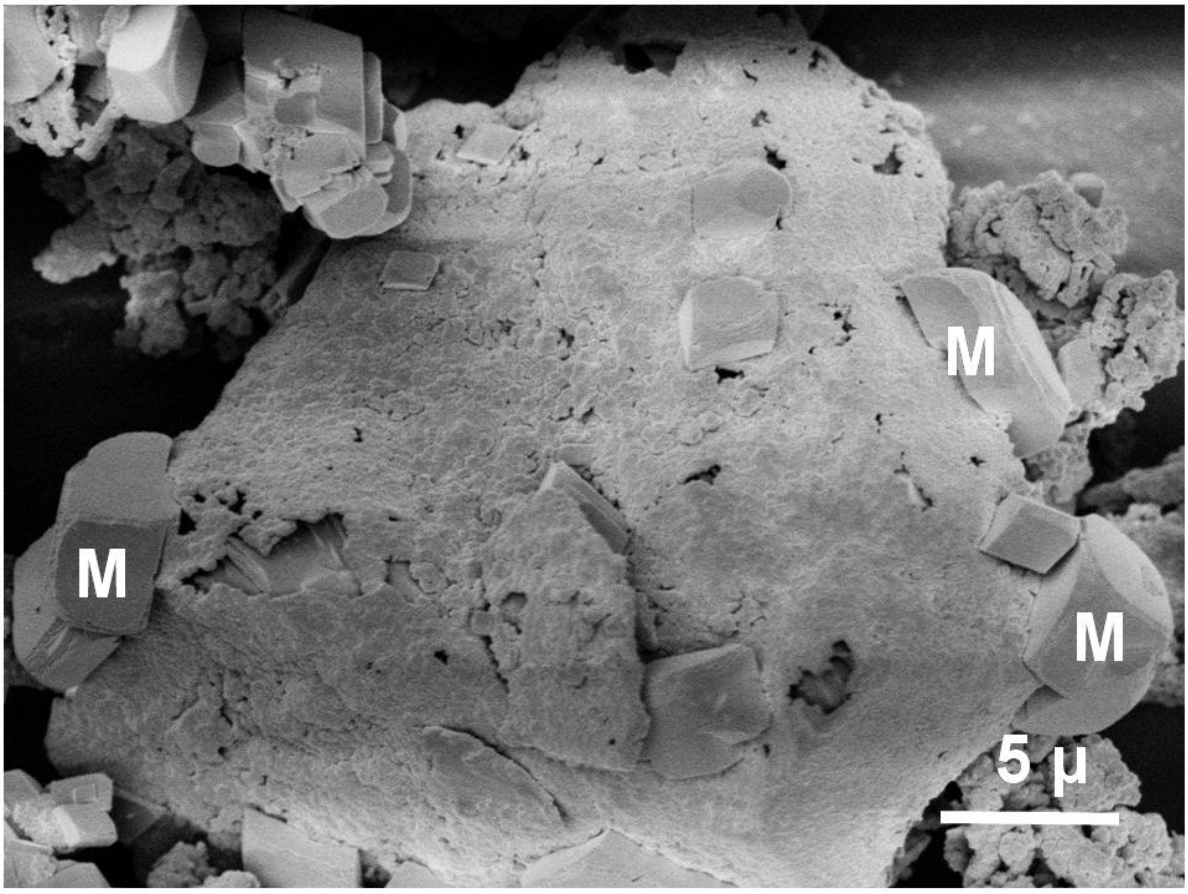

Figure 20. *FESEM image of the intergrowth between olivine, amorphous silica and magnesite crystals at the olivine reaction surface. Note the selective appearance of abrasive wear on the outside corners of the magnesite crystals (M) that have grown on the surface of the olivine/silica/magnesite reaction matrix, which indicate the composite particle formed during the 1,500 rpm stirred carbonation reaction and not as the result of precipitation after the reaction and stirring were stopped.*

Figure 21 shows FESEM/EDS analysis of the cross section of a similar partially reacted crystal, which illustrates the inward progression of the carbonation reaction from the olivine surface for the stirred mineral carbonation process. The olivine near the reaction layer interface appears structurally disrupted (e.g., cracked) *prior to* reaction penetration, which may be related to volume contraction of the silica-rich passivating layer that forms via incongruent dissolution at the olivine reaction interface. This observation underscores the key role structural disruption can play in enhancing carbonation reactivity, especially given how effective silica layer formation can be at local reaction passivation. In this case, some magnesite is observed in the silica reaction layer, as evidenced by the separate Si and Mg rich regions in the layer observed by EDS. The Mg and Fe maps demonstrate a strong correlation between Mg and Fe both in the olivine feedstock and product magnesite in the reaction layer, indicating both the Mg and Fe are transported into the product carbonate during carbonation. The silica regions observed are essentially Fe free.

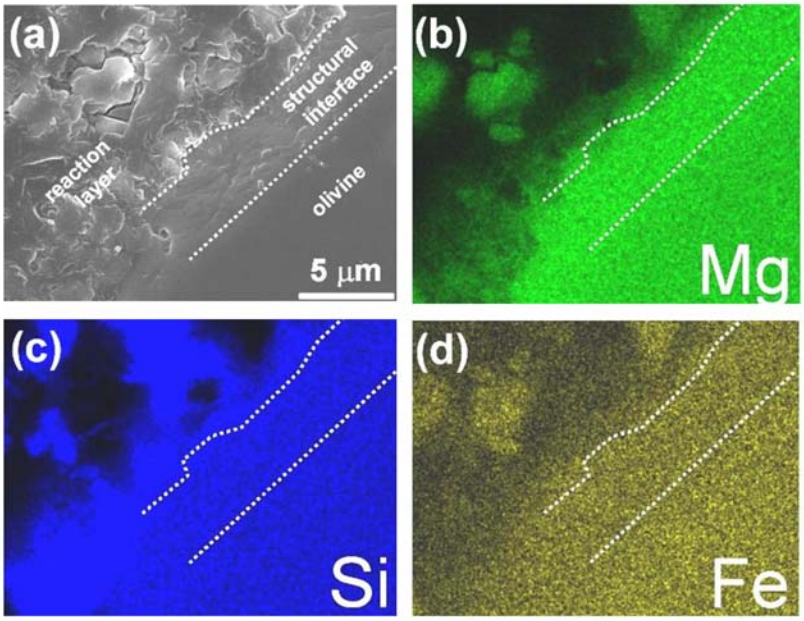

Figure 21. *a) FESEM secondary electron image of a cross-section of a partially carbonated olivine single crystal showing structural disruption of the olivine preceding the mineral carbonation process as the reaction front penetrates to the crystal interior. The crystal surface is in the upper left corner. b-d) Mg, Si, and Fe EDS maps of the reaction interface cross section.*

6. Controlled Particle Abrasion: Enhancing Passivating Layer Exfoliation and Carbonation.

Silica-rich passivating layer formation during mineral carbonation clearly has the potential to substantially inhibit carbonation reactivity. However, the layers that form are brittle, strained and susceptible to fracture and exfoliation that can expose fresh olivine surfaces that enhance reactivity. Hence, particle interactions may be expected to significantly enhance carbonation reactivity. To probe the potential that particle-particle interactions (abrasion) offer to erode passivating layers as they form and enhance carbonation reactivity, we investigated the extent of carbonation observed as a function of wt.% forsterite for stirred (1,500 rpm) carbonation, as seen in Figure 22. The systematic increase in the extent of carbonation with increasing wt.% forsterite (particle concentration) demonstrates the importance of particle-particle interactions (abrasion) in exposing fresh olivine reaction surfaces and enhancing carbonation reactivity. In recent simulations of colliding monodisperse spheres in forced isotopic turbulent flow, corresponding closely to the stirred tank conditions in our experiments, Derksen *et al.*[33] identified two distinct collision mechanisms: (i) primary collisions consisting of uncorrelated "kinetic gas"-like random contacts and (ii) highly correlated secondary collision processes, involving a repetitive "chattering" motion on a short time scale, due to short-range hydrodynamic effects (lubricating forces). Elementary geometric considerations deliver a length scale (L) dependence on weight % solids, W, proportional to $W^{-1/3}$. The removal rate of PL material, R_{PL}, is therefore proportional to $V_{avg}/L = AW^{1/3}$, where V_{avg} is the mean relative velocity between a pair of particles and A is a constant. If we assume that the diffusion of reactants through the PL is rate-limiting, and that

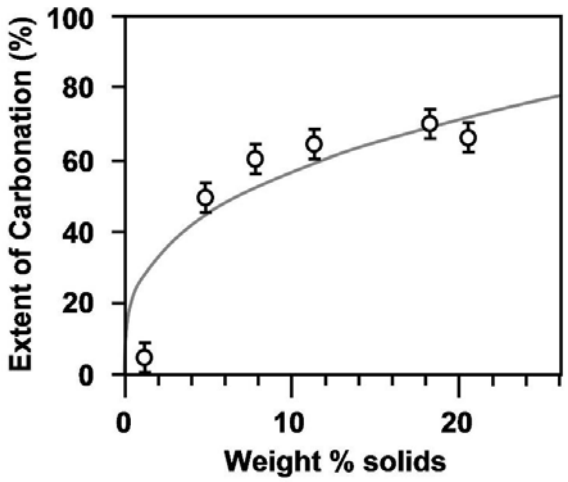

Figure 22. *Plot of the extent of carbonation observed as a function of weight % forsterite used in the aqueous carbonation solution (0.64M $NaHCO_3$ + 1.00M NaCl) at 1,500 rpm (185 ^oC; 150 bar CO_2; 1hr). The error bars shown represent the standard deviation typically observed for multiple runs under the same reaction conditions. The grey line is a fit to the form $AW^{1/3}$, where A~26.2. Note: The fit is not expected to continue for higher weight % solids where other contributing factors, such as particle-particle agglomeration, will eventually become substantial and reduce PL exfoliation and carbonation.*

complete passivation occurs in a time T_0 in an unstirred setting, then the extent of carbonation is proportional to $T_{RUN}\ R_{PL} \propto W^{1/3}$ where $T_{RUN} >> T_0$ is the duration of the stirred reaction experiment. This dependence on weight % solids is illustrated in Figure 22, where a best fit yields a proportionality constant of about 26.2, a value much larger than expected based on the presence of primary collisions alone. The large coefficient may be explained by a high frequency of secondary collision processes.

We have recently discovered that the inclusion of abrasive particles (e.g., quartz) can further enhance olivine carbonation, providing additional evidence for the importance of particle abrasion. Clearly, olivine carbonation reactivity can be substantially improved by enhancing abrasion. Controlling abrasion during *in situ* carbonation may also allow the effective use of larger olivine feedstock particle sizes, as discussed previously. This would substantially lower the cost of feedstock preparation, as the vast majority of the cost in grinding the olivine feedstock to < 37 microns is associated with particle-size reduction from <75 to <37 microns.[8]

7. Passivating Layer Formation during Unstirred Carbonation.

Single crystal samples with surface normal [010] were reacted using the standard aqueous mineral carbonation process developed by the Albany Research Center, but without stirring, to avoid the effects of particle-particle and particle-system abrasion. The resulting reaction surface and interface with the olivine substrate were investigated via scanning and transmission electron microscopy. The reacted olivine surface after 4 hrs is shown in Figure 23. Stereographic SEM imaging shows the as-reacted surface (after multiple H_2O rinses to remove soluble salts) to be covered with a buckled silica-rich passivating layer, with the buckling extending upward away from the substrate. Sonication in water after reaction removed the buckled regions, which were

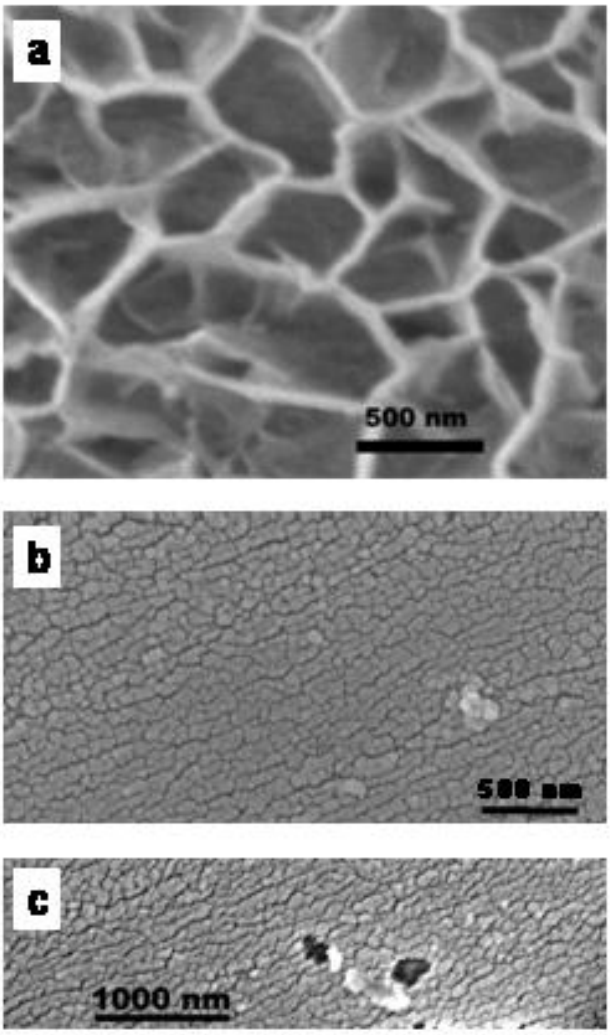

Figure 23. *SEM images of reacted olivine surfaces. surface normal = [010]. Reaction conditions: 150 bar CO_2, 185 ^oC and 4hrs. (a) cleaned surface after reaction exhibited debonded high SiO_x content reaction layers. (b) cleaned and sonicated reacted surface showing well bonded high SiO_x reaction layer islands separated by cracks. (c) Islands that debonded during sonication via interfacial cracking.*

not strongly bonded to the substrate, and revealed the underlying cracks in the passivating layer shown in Figure 23b. Energy dispersive x-ray nanospectroscopy showed that the RL "islands" that remained bonded to the substrate had high Si and O content relative to the bottom of the cracks, where the composition corresponded to olivine. The bottom of the cracks were thus high reactivity sites. The average size of the bonded islands was ~ 100 nm, and the crack width between islands was ~ 20 nm. Fig. 23c shows sonication can dislodge a small number of RL islands that became partially debonded during the reaction. The area under these was bare olivine or a very thin passivating layer.

Figure 24a shows a cross section HREM image of a passivating layer island at its interface with the olivine substrate, showing a typically well-bonded inter-phase interface boundary indicating incongruent magnesium dissolution substantially contributes to passivating layer formation.

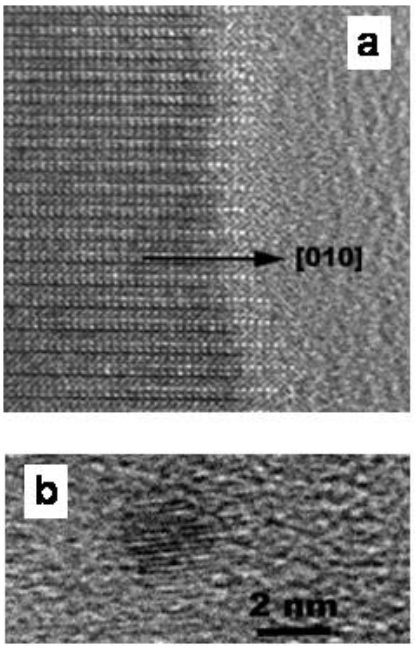

Figure 24. *TEM images of reacted olivine. 200 keV. (a) Cross section image of the olivine/PL interface. The passivating layer (PL) is amorphous. The transition across the olivine/PL boundary is not sharp, and should correspond to a steep [MgO] gradient, as predicted in Figure 19. (b) A typical $MgCO_3$ nanoparticle observed in the silica-rich passivating layer.*

The passivating layer region was amorphous on all specimens examined. Its interface with the olivine illustrates the transition from crystalline olivine to the amorphous silica-rich passivating layer is not structurally sharp. The passivating layers contain a distribution of randomly oriented crystalline nanoparticles (Figure 24b), which were identified as magnesite ($MgCO_3$) or periclase (MgO) via image analysis and FFT diffraction. As magnesite is well known to be extremely electron beam sensitive,[34] readily decomposing to periclase in the process, we conducted radiation effects experiments on both nanoparticle and bulk $MgCO_3$. These studies confirmed that magnesite, especially the magnesite nanocrystals present in the passivating layers, is very sensitive to both electron irradiation effects during HREM observation/analysis *and* ion beam damage during specimen preparation. Both processes readily cause decomposition to MgO, consistent with earlier electron irradiation observations made on bulk $MgCO_3$.[34] Thus, the nanoparticles that formed during carbonation were $MgCO_3$. The MgO particles observed are artifacts formed by $MgCO_3$ decomposition during specimen preparation or electron beam observation. This intriguing observation indicates that the passivating layers that form are not only permeable to Mg^{2+}, H^+, and H_2O associated with magnesium dissolution during the carbonation process, they are also permeable to the species responsible for carbonation (e.g., CO_2(aq), CO_3^{2-}, HCO_3^-). It is interesting to note that the interconnected occupiable volumes within the simulated passivating layer shown in Figure 19 can also support substantial CO_2, CO_3^{2-}, and/or HCO_3^- diffusion, consistent with the observed intralayer nanocrystal magnesite formation.

The average nanoparticle size was about 6 nm, and the particle volume fraction in the passivating layer was calculated to be ≈ 0.13, using TEM methods.[35-37] If the carbonation reaction proceeded simply by forming a mixture of magnesite and SiO_x on the olivine, the magnesite volume fraction in the passivating layer would have been much larger. The molar volumes of the reactants and products (V_M for olivine and magnesite are 43.6 and 28.0 cc/mol respectively,[38] and ≈ 26 cc/mol for SiO_x[39]) can be used to show that the magnesite volume fraction in the passivating layer would have been about 0.68. The much smaller magnesite fraction observed within the passivating layer indicates that most of it formed external to the layer (e.g., in the aqueous solution itself).

The interfacial bond between the olivine and the silica-rich passivating layer results in a strain gradient across the island thickness that induces bending moments in the film and peeling stresses at the interface.[40,41] These moments and stresses are largest at the PL island edges, and can contribute to crack propagation along the PL/olivine interface and peeling of the PL upward away from the substrate, ultimately resulting in the islands detaching from the olivine substrate. The surface observed in Figure 23a is consistent with debonded peeling PL, with the structures observed easily removed from the reacted specimen surface by sonication. Other examples of PL island debonding are visible in the middle of Figure 23c; these regions probably had partially cracked interfaces before sonication. The height of the structures observed in Figure 23a may well also be associated with local silica dissolution precipitation, with the structures growing away from the reaction interface into the solution.

8. Molecular Dynamics Simulations of Reactant Solutions

During the first year of the performance period we also initiated modeling studies of the standard aqueous reactant solution ($NaCl/NaHCO_3$ buffered H_2O + $scCO_2$), beginning with the thermodynamic simulation of the H_2O + $scCO_2$ system, as the reaction solution incorporated was found to have a dramatic impact on carbonation reactivity. Our equilibrium classical molecular dynamics simulations of the reactant solutions at various P and T are based on the COMPASS force field,[42] which has been exhaustively validated using a broad range of aqueous systems. However, because our work involves an excursion into the supercritical phase region of CO_2, where experimental data is scarce and validation has not been carried out, the results should be viewed as preliminary pending detailed benchmarking against results of *ab initio* simulation. As experimental information about the H_2O-CO_2-NaCl-$NaHCO_3$ system at T~185 ^oC and P_{CO2}~150 bar becomes available through our related work in other projects it will be used to tune the empirical parameters in our classical simulations and further validate our approach. Here we summarize our preliminary results.

The aqueous solutions were modeled using between 100 and 160 water molecules. CO_2 molecules were then added on the basis of CO_2 solubility data which has recently been accurately fitted to an analytic model by Duan and Sun.[43] The thermodynamic data indicates that CO_2 solubility generally decreases with increasing temperature, and increases with increasing CO_2 pressure. Typical values for our experimental conditions are between 0.1-1.2M CO_2, with the higher values corresponding to our reaction conditions (T ~ 185 ^oC, P_{CO2} ~ 150 bar). The initial structure of the water was generated by placing H_2O molecules on a grid corresponding to a volume of 30 $Å^3$ per molecule. The system was then relaxed using a simulated annealing

procedure to a static lattice energy minimum. Thermodynamic simulations were then undertaken using an NPT (constant number of particles: N, pressure: P, and temperature: T) ensemble in which P and T are specified to match either STP or our reaction conditions, with a 1 fs integration time step. Equilibration typically required about 40 ps (corresponding to 40,000 molecular dynamics steps). To calculate correlation functions and other properties we then carried out additional simulations in the NVE (constant number of particles: N, volume: V, and temperature: T) ensemble using 20,000 MD steps, using the final average densities and configurations from the NPT simulations. This approach produced low RMS fluctuations and accurate statistics for the ensemble averages.

To simulate the more complex NaCl-H_2O-CO_2 solutions we simply incorporated NaCl into the computational cells at the required concentrations. At STP a 1M NaCl solution consists of approximately 1 Na+Cl pair for every 55 water molecules. In order to keep our simulations consistent with our experiments we appealed to the Sun *et al* equation to determine the solubility of CO_2 in NaCl buffered H_2O. In general the addition of NaCl significantly suppresses the solubility of CO_2 (about a factor of 2 in going from pure water to a 2M NaCl aqueous solution).[43] Initial results of our simulation studies are presented in Table 6, which lists the simulated total energies and provides a comparison of simulated molar volumes with those

Table 6: Total energy (E) and molar volumes (Ω) of aqueous solutions obtained from a NPT ensemble simulation followed by a 10 ps NVE simulation. Experimental values from Ref. 44. Asterisks are values for pure water, used here as a proxy for comparison with the actual reactant solution.

System	*P(bar)*	*T (°C)*	*E(kcal/mol)*	Ω_{SIM}*(cc/mol)*	Ω_{EXP}^{H2O} *(cc/mol)*
Pure H2O	1	25	-575.5	18.3	18.1
1M CO_2 in H_2O	1	25	-571.5	18.4	18.1*
1M CO_2 in H_2O	150	185	-154.2	22.2	20.6*
1M CO_2 + 1M NaCl in H_2O	1	25	-731.0	19.0	18.1*
1M CO_2 + 1M NaCl in H_2O	150	185	-290.5	28.9	20.6*

obtained experimentally for pure water. For H_2O-CO_2 solutions predicted densities are in reasonable agreement with experiment, exhibiting a slight volume overestimate particularly at high pressures. Unfortunately, experimental molar volume data for the NaCl-H_2O-CO_2 solution has not been reported at the reaction conditions. For a 1M CO_2 + 1M NaCl in H_2O solution at T = 185 ^oC and P_{CO2}=150 bar, our simulations predict a ~ 50% increase in molar volume relative to STP. This is significantly greater than the corresponding molar increase in the H_2O-CO_2 system for the same conditions.

Understanding of hydrated ions as a function of temperature and pressure is fragmented and incomplete, and molecular dynamics simulations can provide direct information about atomic motion at the reaction conditions of interest. Therefore, to elucidate the origin of the concentration, temperature and P_{CO2} dependences in our carbonation experiments we calculated the diffusivity constants and solvation structures of all species in the reactant solution. This represents the first step in determining the importance and individual roles of various carbonaceous species (CO_2(aq), CO_3^{2-}, HCO_3^-, H_2CO_3*). Figure 25 shows a snapshot of the structure of the hydration shell surrounding the solutes Na^+, Cl^- and CO_2 at the simulated reaction conditions (T=185 ^oC, P_{CO2}=150 bar). Integration of the pair-correlation functions yields

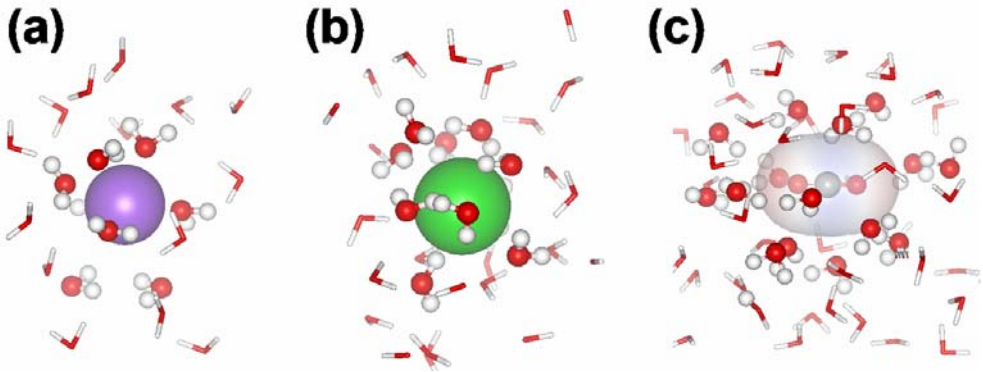

Figure 25: Snapshots of the hydration shell structure in 1M CO_2 + 1M NaCl + H_2O at T=185 ^oC and P_{CO2} = 150 bar: (a) sodium ion surrounded by H_2O molecules oriented with oxygen inward, (b) chloride hydration structure showing H_2O protons oriented inward, (c) hydration structure surrounding the CO_2 molecule (faded surface is a superposition of vdW radii). Inner hydration shell water molecules are shown as ball-stick for emphasis. From pair-correlation analysis the coordination numbers are 5.5, 6.5 and 9.1 for Na^+, Cl^- and CO_2, respectively.

coordination numbers 5.9, 7.2 and 9.1 for Na^+, Cl^- and CO_2, respectively. These values are very similar to those obtained at ambient conditions (5.6, 6.8 and 8.7) indicating that solute coordination is relatively weak function of pressure and temperature in these systems. One of the properties expected to play an important role in reactivity dependence on T and P is the translational self-diffusion. This is because the relative diffusivity of carbon bearing reactants in comparison to solvent and other reactant species, such as Mg^{2+}, is directly related to the reaction rate. Enhanced reaction is expected at P_{CO2} and T conditions which increase the diffusivity of all reactants in the solution. Our objective is to explore this dependence via simulation. The self-diffusion coefficient can be obtained from the long-time behavior of the mean-square displacements via

$$D = \underset{t\to\infty}{Lim} \frac{\left\langle [R(t) - R(0)]^2 \right\rangle}{6t} \qquad (1) \quad .$$

To calculate this property we equilibrated the systems using 50,000 time steps in the NPT ensemble and then collected trajectory data for an additional 50,000 steps in the NVE. Typically the slope of the function (1) was evaluated using the last 20,000 steps. Our results are presented in Table 7 which lists the diffusion coefficients for a range of systems at STP and at reaction conditions. At ambient conditions we find that the addition of CO_2 (1M CO_2 was chosen for simplicity) has a negligible effect on H_2O self-diffusivity and that the diffusion coefficient of CO_2 is slightly larger than that of water. Our simulations show that the addition of NaCl reduces the self diffusivities of H_2O by more than half, in agreement with the results of recent calculations for NaCl + H_2O solutions.[45] This suppression is alleviated by increasing P_{CO2} and temperature, as can be seen from the tabulated data, which indicates an order of magnitude increase in H_2O self-diffusion and a factor of ~ 2 increase in CO_2 self-diffusion at T = 185 ^oC and P_{CO2} = 150 bar. Another significant finding is that the self-diffusivity of Na^+ ions is systematically higher than that of their Cl^- anion counterparts under these conditions. In fact, at these conditions the self-diffusivity of Na^+ and CO_2 is found to be comparable and this may have

Table 7: Translational self-diffusion coefficients, in units of 10^{-5} cm^2/s, for H_2O, CO_2, Na^+ and Cl^- for a range of aqueous solutions. The experimental value for H_2O self-diffusion at STP is 2.5×10^{-5} cm^2/s.
[4]

System	*Diffusing Species*	*T=25 °C, P=1 bar*	*T=185 °C, P=150 bar*
H_2O	H_2O	**2.4**	**--**
1M CO_2 + H_2O	H_2O	**2.5**	**--**
	CO_2	**3.2**	**--**
1M NaCl + 1M CO_2 + H_2O	H_2O	**0.9**	**12.9**
	CO_2	**1.3**	**2.7**
	Na	**0.6**	**3.0**
	Cl	**0.9**	**1.5**

implications for olivine/passivating layer surface complexation and Mg dissolution kinetics. We plan to expand and refine these studies in the second year of our project, with special emphasis on establishing rigorous trends in solution kinetics with respect to solute concentration, pressure and temperature.

CONCLUSIONS

The species and their activities in the aqueous mineral carbonation solution can dramatically impact carbonation reactivity. Varying the alkali cation species present and their ratio resulted in the extent of carbonation varying by a factor of more than 20 from the least to the most effective alkali cation combination. The most promising solutions for enhancing carbonation discovered to date have nearly doubled the extent of carbonation observed using the previous optimum solution. High concentrations of $NaHCO_3$ (2.5M) and $KHCO_3$ (5.5M) were found to be particularly effective at enhancing carbonation. Although, the alkali chloride solutions studied to date exhibit poor carbonation reactivity, they can substantially enhance carbonation reactivity in combination with alkali bicarbonate under select conditions. CO_2(aq) and HCO_3^- exhibit quite poor carbonation reactivity separately; however, together they play key synergistic roles, substantially enhancing carbonation.

Multi-phase fluid modeling offers the potential to significantly enhance carbonation by controlling the slurry-flow parameters that impact exfoliation and carbonation (e.g., via particle-particle and particle-wall collisions). A newly developed microscopic wall roughness model indicates wall roughness may significantly enhance exfoliation and carbonation, by enhancing cross-stream particle transport and particle collisions. The Fluent code was validated for application to multiphase flows to assess the complex effects governing flow. Initial application has been made to components of the ARC Flow-Loop reactor. Initial results reveal the radial distribution of flow and the cross-stream olivine particle velocity vectors in a component pipe section can be a strong function of particle mass/size distribution and mixing history, parameters that may be able to be used to enhance carbonation. A new mixing design is being explored. Initial experimental results demonstrate that the flow dynamics and particle mass/size distribution present can substantially impact exfoliation/carbonation.

A controlled pressure (1 to 200 atm) and temperature (20 to 250 ^{o}C) 20 kHz 1500 watt sonication system was successfully developed for these studies. The system is fully operational over the complete range of carbonation reaction conditions of interest. Initial studies of the effects of sonication temperature, pressure and time at full power have not yet been effective at enhancing carbonation. These studies will be completed in Year 2, together with investigations of the effect of fluid composition, and reactant particle concentration and size. During Year 2 those parameters that have been found to be individually effective at cost-effectively enhancing carbonation reactivity (e.g., controlled fluid flow conditions and aqueous chemistry) will be combined to explore the potential to synergistically stimulate exfoliation and enhance carbonation.

Incongruent dissolution generally results in silica-rich passivating layer (PL) formation, with silica dissolution-precipitation likely further contributing to PL growth. Observations of magnesite nanocrystals within the passivating layers that form indicate the layers exhibit significant permeability to the key reactants present (e.g., Mg^{2+}, H^{+}, H_2O, CO_2, and HCO_3^{-}). The extent of carbonation is observed to increase dramatically with increasing weight % solids in stirred experiments, indicating particle-particle collisions are critical in enhancing exfoliation and carbonation. Addition of abrasive materials, such as quartz, can significantly enhance olivine carbonation, in further support of the importance of particle-particle collisions in exfoliation and carbonation processes. Multi-phase hydrodynamic calculations indicate secondary collisions can account for a large fraction of the abrasion/exfoliation observed. Large-scale atomic-level simulations of the reaction zone suggest that the PL possesses a “glassy” but highly defective SiO_2 structure that can permit the diffusion of key reactants. Studies in Year 2 will emphasize the impact that controlled aqueous speciation, activity and slurry-flow dynamics have on the mechanisms that control carbonation reactivity, as they appear to offer the greatest potential to substantially reduce olivine mineral sequestration process cost.

REFERENCES

1) *Carbon Sequestration Research and Development*, Offices of Science and Fossil Energy, U.S. Department of Energy (December 1999), and references therein.
2) Seifritz, W. *Nature* **345**, 486 (1990).
3) Lackner, K.; Wendt, C.; Butt, D.; Joyce Jr., E.; Sharp, D.; *Energy* **20**, 1153-70 (1995).
4) O'Connor, W., et al. *Proc. 25th Int. Tech. Conf. Coal Util. & Fuel Syst.* pp. 153-64 (2000).
5) O'Connor, W.K., et al. *Proc. 27th Int. Tech. Conf. Coal Util. & Fuel Syst.* pp. 819-30 (2002).
6) *Novel Approaches to Carbon Management* (National Academies Press, Wash. D.C., 2003)
7) O'Connor, W.K.; Walters, R.P.; Dahlin, D.C.; Rush, G.E.; Nilsen, D.N.; Turner, P.C.; *Proc. 26th International Technical Conference on Coal Utilization & Fuel Systems* **2001**, 765.
8) O'Connor, W.K.; Dahlin, D.C.; Rush, G.E.; Gerdemann, S.J.; Penner, L.R. *Proc. 29th International Technical Conference on Coal Utilization & Fuel Systems* **2004**, 71.
9) Yu, S.C.; Proc. Nat. Sci. Counc. A. ROC, **1997**, *21*, 173.
10) Ottonello, G.; Principalle, F.; Della Giusta, A.; *Phys. Chem. Miner.* **1990**, *17*, 301.
11) Sommerfeld, M., 2003, ``Analysis of collision effects for turbulent gas-particle flow in a horizontal channel: Part I. Particle transport", Int. Journal of Multiphase Flow, Vol. 29, pp. 675-699.
12) Sommerfeld, M., and Huber, N., 1999, ``Experimental analysis and modelling of particle-wall collisions", Int. Journal of Multiphase Flow, Vol. 25, pp. 1457-1489.
13) Patankar, S. V., "Numerical Heat Transfer and Fluid Flow", McGraw-Hill Book Company, 1980.
14) Lockhart R. W. and Martinelli R. C., "Proposed correlation of data for isothermal two-phase, two-component flow in pipes", Chemical Engineering Progress, 45(1), pp. 39-48, 1949.
15) Béarat, H.; McKelvy, M.; Chizmeshya, A.V.G.; Gormley, D.; Nunez, R.; Carpenter, R.W.; Squires, K. Environmental Science and technology (submitted).
16) Hurlbut, Cornelius, S.; Klein, Cornelis; *Manual of Mineralogy*, 19th Edition (John Wiley & Sons, New York, 1977).
17) Potapov, V.V.; *Glass Physics and Chemistry* **2004**, *30 (1)*, 82.
18) Weissbart, E.J.; Rimstidt, J.D.; *Geochim. Cosmochim. Acta* **2000**, *64 (23)*, 4007.
19) Johnson, C.L.; Hytch, M.J.; Buseck, P.R.; *Amer. Mineral.* **2004**, *89*, 1374; Wenk, H. Ed. *Electron Microscopy in Mineralogy* (Springer-Verlag, Berlin, 1976), Chapters 6.1 and 6.6.
20) Luce, R.W.; Bartlett, R.W.; Parks, G.A.; *Geochim. Cosmichim. Acta* **1972**, *36*, 35.
21) Wogelius, R.A.; Walther, J.V.; *Geochim. Cosmichim. Acta* **1991**, *55*, 943.
22) Jonckbloedt, R.C.L.; *J, Geochem. Explor.* **1998**, *62*, 337.
23) Chen, Y.; Brantley, S.L.; *Chem. Geol.* **2000**, *165*, 267.
24) Wolf, G.H.; Chizmeshya, A.V.G.; Diefenbacher, J.; McKelvy, M. J.; *Environ. Sci. Technol.* **2004**, *38*, 936.
25) Refson, K.; Moldy User's Manual, Rev. 2.25.2.6, release 2.16 (2001).
26) Matsui, M.; *Phys. Chem. Min*. **1988**, *16*, 234.
27) Birch, F.; *J. Geophys. Res.* **1978**, *83*, 1257.
28) Knittle, E.; *Mineral Physics and Crystallography: A Handbook of Physical Constants,* Ed. T.J. Ahrens, *American Geophysical Union*, **1995**, *2*, 98.
29) Johnson, P.A.V.; et al., *J. Non-Crys. Solids* **1983**, *58*, 109.

30) Chizmeshya, A.V.G.; McKelvy, M.J.; Gormley, D.; Nunez, R.; Kim, Y.; Carpenter, R. *Proc. 29th International Technical Conference on Coal Utilization & Fuel Systems* **2004**, *1*, 59.
31) Cerius2 Simulation Program, Accelrys Inc., San Diego, California (2003).
32) Franks, F; Water: *A matrix of life*, 2nd ed. (Royal Society of Chemistry, Cambridge, 2000).
33) Cate, A.T. ; Derksen J.J.; Portela, L.M.; van den Akker, H.E.A.; *J. Fluid Mech.* **2004**, *519*, 233.
34) Kim, M.G.; Dahman, U.; Searcy, A.W. *J. Amer. Ceram. Soc.***70**, 146 (1987).
35) J. E. Hilliard, *Trans. Met. Soc. AIME***224**, 906-917(1962).
36) J. M. Crompton, *Brit. J. Appl. Appl. Phys.***17**, 1301-1305(1966).
37) T. Malis, S. Chung, and R.F. Egerton, J. Elec. Micros. Tech.**8**, 193(1988).
38) J. R. Smyth and T. C. McCormick, Crystallographic Data for Minerals, in A Handbook of Physical Constants: Mineral Physics & Crystallography (Vol. 2), ed. T. J. Ahrens, American Geophysical Union(1995).
39) W. D. Kingery *et al*, *Introduction to Ceramics, 2nd Ed.,* John Wiley and Sons(1976)
40) G. C. Stoney, Proc. Roy. Soc. London **A82**, 172 (1909).
41) E. Suhir, J. Appl. Mech. **53**, 657-660(1986)
42) Sun, H. (1998). COMPASS: An ab Initio Force-Field Optimized for Condensed-Phase Applications-Overview with Details on Alkane and Benzene Compounds, *J. Phys. Chem. B*, **102**, 7338-64.
43) "An improved model calculating CO_2 solubility in pure water and aqueous NaCl solutions from 273 to 533 K and from 0 to 2000 bar", Z. Duan and R. Sun, *Chemical Geology* **193** (2003) 257– 271.
44) "Pressure-Volume-Temperature Properties of H_2O-CO_2 Fluids" T.S. Bowers, *Rock Physics and Phase Relations: Handbook of Physical Constants AGU Reference Shelf 3*, 1995.
45) "Concentration Effects in Aqueous NaCl Solutions. A Molecular Dynamics Simulation", A.P. Lyubartsev and A. Laaksonen, *J. Phys. Chem.* 1996, ***100,*** 16410-16418.

A NOVEL APPROACH TO MINERAL CARBONATION: ENHANCING CARBONATION WHILE AVOIDING MINERAL PRETREATMENT PROCESS COST

Type of Report:	Annual
Reporting Period Start Date:	June 22, 2005
Reporting Period End Date:	June 21, 2006
Principal Authors:	Michael J. McKelvy,* Andrew V.G. Chizmeshya, Kyle Squires, Ray W. Carpenter, and Hamdallah Béarat.
Date Report Issued:	November 2006
DOE Award Number:	DE-FG26-04NT42124
Submitting Organization:	Arizona State University Center for Solid State Science, Science and Engineering of Materials Graduate Program, and Department of Mechanical and Aerospace Engineering Tempe, AZ 85287-1704 * Phone: (480) 965-4535; FAX: (480) 965-9004; E-mail: mckelvy@asu.edu

DISCLAIMER

ABSTRACT

Known fossil fuel reserves, especially coal, can support global energy demands for centuries to come, ***if*** the environmental problems associated with CO_2 emissions can be overcome. Unlike other CO_2 sequestration candidate technologies that propose long-term storage, mineral sequestration provides permanent disposal by forming geologically stable mineral carbonates. Carbonation of the widely occurring mineral olivine (e.g., forsterite, Mg_2SiO_4) is a large-scale sequestration process candidate for regional implementation, which converts CO_2 into the environmentally benign mineral magnesite ($MgCO_3$). The primary goal is cost-competitive process development. As the process is exothermic, it inherently offers low-cost potential. Enhancing carbonation reactivity is key to economic viability. Recent studies at the U.S. DOE Albany Research Center have established that aqueous-solution carbonation using supercritical CO_2 is a promising process; even without olivine activation, 30-50% carbonation has been achieved in an hour. Mechanical activation (e.g., attrition) has accelerated the carbonation process to an industrial timescale (i.e., near completion in less than an hour), at reduced pressure and temperature. However, the activation cost is too high to be economical and lower cost pretreatment options are needed. Herein, we report our second year progress in exploring a novel approach that offers the potential to substantially enhance carbonation reactivity while bypassing pretreatment activation. As our second year progress is intimately related to our earlier work, the report is presented in that context to provide better overall understanding of the progress made.

We have discovered that robust silica-rich passivating layers form on the olivine surface during carbonation. As carbonation proceeds, these passivating layers thicken, fracture and eventually exfoliate, exposing fresh olivine surfaces during rapidly-stirred/circulating carbonation. We are exploring the mechanisms that govern carbonation reactivity and the impact that (i) modeling/controlling the slurry fluid-flow conditions, (ii) varying the aqueous ion species/size and concentration (e.g., Li^+, Na^+, K^+, Rb^+, Cl^-, HCO_3^-), and (iii) incorporating select sonication offer to enhance exfoliation and carbonation. We have succeeded in nearly doubling the extent of carbonation observed compared with the optimum procedure previously developed by the Albany Research Center. Aqueous carbonation reactivity was found to be a strong function of the ionic species present and their aqueous activities, as well as the slurry fluid flow conditions incorporated. High concentration sodium, potassium, and sodium/potassium bicarbonate aqueous solutions have been found to be the most effective solutions for enhancing aqueous olivine carbonation to date. Slurry-flow modeling using Fluent indicates that the slurry-flow dynamics are a strong function of particle size and mass, suggesting that controlling these parameters may offer substantial potential to enhance carbonation. Synergistic control of the slurry-flow and aqueous chemistry parameters offers further potential to improve carbonation reactivity, which is being investigated during the no-cost extension period.

During the first project year we developed a new sonication exfoliation system with a novel sealing system to carry out the sonication studies. We also initiated investigations into the potential that sonication offers to enhance carbonation reactivity. During the second project year, we extended our investigations of the effects of sonication on the extent of carbonation as a function of the following parameters: particle size distribution, the mass of solid reactant, volume fraction of aqueous solution present, sonication power, time, temperature, and CO_2 pressure. Thus far, none of the conditions investigated have significantly enhanced carbonation.

Mechanistic investigations of the stirred (~1,500 rpm) aqueous olivine carbonation process indicate the carbonation process involves both incongruent magnesium dissolution and silica precipitation, which results in robust silica-rich passivating layer formation. Secondary ion mass spectrometry observation of H within the passivating layer that forms during static carbonation suggests $2H^+/Mg^{2+}$ ion exchange is associated with incongruent dissolution. Apparently, H_2O forms at or near the olivine/passivating-layer

interface during the process and diffuses out through the passivating layers during the carbonation reaction. This is also consistent with the observation that magnesite nanocrystals form within the passivating layers, further indicating the layers offer significant permeability to the key solution reaction species present during carbonation (e.g., Mg^{2+}, H^{+}, H_2O, CO_2, and HCO_3^{-}). Cracking of the passivating layer surface during carbonation is routinely observed and can be related to the tensile stress associated with the dramatic volume decrease as olivine forms silica at the reaction surface. The addition of quartz particles as an abrasive slurry component significantly enhanced carbonation, further substantiating the importance of particle-particle abrasion in enhancing passivating layer exfoliation and carbonation. Studies during the no-cost extension period will emphasize the impact that controlled aqueous speciation and activity and slurry-flow dynamics have on the mechanisms that control carbonation reactivity and the potential they offer to substantially reduce olivine mineral sequestration process cost.

TABLE OF CONTENTS

EXECUTIVE SUMMARY

CO_2 mineral sequestration provides permanent carbon dioxide disposal by forming geologically stable and environmentally benign mineral carbonates. Carbonation of olivine (e.g., forsterite, Mg_2SiO_4) is a large-scale sequestration process candidate for regional implementation. Cost-effectively enhancing carbonation reactivity is central to economically viable process development. Aqueous-solution carbonation shows particular promise. However, the associated mineral activation cost currently needed to suitably enhance carbonation is too high. Lower cost pretreatment options are needed. During the second year of this project, we have continued to explore the potential to substantially enhance carbonation reactivity via a novel approach that bypasses pretreatment activation altogether. As our second year progress is intimately related to our earlier work, the report is presented in that context to provide better overall understanding of the progress made.

We have discovered that silica-rich passivating layers form on the olivine surface during carbonation. The process appears to be associated with both incongruent olivine dissolution (i.e., preferential magnesium dissolution) and silica precipitation, which together lead to the formation of the robust silica-rich passivating layers that form. During carbonation, the layers thicken, fracture and exfoliate during rapidly-stirred/circulating carbonation. This project is exploring the potential to cost-effectively enhance carbonation, while avoiding the cost of olivine pretreatment activation. Three approaches are being targeted: (i) controlling the aqueous chemistry (e.g., Li^+, Na^+, K^+, Rb^+, Cl^-, and HCO_3^- activities), (ii) integration of slurry flow modeling with experiment, and (iii) incorporating select sonication. The focus of these studies is on (1) mitigating passivating layer effectiveness, (2) enhancing exfoliation and (3) enhancing carbonation. We have succeeded in nearly doubling the extent of carbonation compared with that observed for the optimum procedure previously developed by the Albany Research Center (ARC).

During the first year, we discovered carbonation reactivity is a complicated function of the aqueous solution species/activities. Varying the aqueous alkali cation species in the optimum solution developed by the ARC (0.64M $NaHCO_3$ + 1.00M NaCl) found that the alkali cation species present and their ratio dramatically impact carbonation reactivity, with up to a factor of 20 difference in the extent of carbonation observed. High concentrations of $NaHCO_3$ and $KHCO_3$ were discovered to be particularly effective at enhancing carbonation. During the second year, we extended our investigations to explore the extent of carbonation vs. Na and K bicarbonate concentration, the Na/K ratio associated with the bicarbonate, temperature, and CO_2 pressure. Carbonation was found to increase with increasing Na and K bicarbonate concentration until very high concentrations, where it begins to decrease. The optimum concentrations for $NaHCO_3$ and $KHCO_3$ were found to be ~2.5M and ~5.5M, respectively, with higher concentrations resulting in lower extents of carbonation. This is consistent with initial solubility simulations that suggest that decreasing carbonation at very high bicarbonate concentrations may be associated with decreasing CO_2 solubility with increasing bicarbonate concentrations. Carbonation was observed to continuously increase with increasing CO_2 pressure, while an optimum temperature of 185 ^oC was observed below and above which the carbonation decreased. Alkali chloride solutions were further investigated in combination with high concentration Na, K, and Na/K bicarbonate solutions, partially motivated by the initial success of the ARC standard solution (0.64M $NaHCO_3$ + 1.00M NaCl). However, none of these aqueous solutions were as effective as the high concentration bicarbonate solutions. CO_2(aq), Na^+ and/or K^+, and HCO_3^- play key synergistic roles in enhancing carbonation, as carbonation drops off dramatically in the presence of Na^+/K^+ + HCO_3^-(aq) or CO_2(aq) alone.

During the first project year, multi-phase fluid modeling and experimental investigations were initiated to elucidate important slurry-flow parameters that enhance exfoliation and carbonation (e.g., via particle-particle and particle-wall collisions). A new, well validated, microscopic wall roughness model was developed. Simulations indicated wall roughness can strongly enhance cross-stream transport, particle

collisions and carbonation. The Fluent code was validated for application to multiphase flows to assess the complex effects governing flow and initially applied to components of the ARC flow-loop reactor. Results indicate the radial flow distribution in a component pipe can be a strong function of particle mass/size distribution and mixing history. Particle mass and carbonation flow characteristics were found to be important factors in carbonation reactivity, with the ASU batch reactor showing markedly enhanced carbonation in comparison with the ARC flow-loop reactor for <150 μ Twin Sisters olivine. As a result, during the second year of this project we have focused our simulation efforts on the simpler ASU batch reactor, which provides the critical advantage of being able to simulate the multiphase fluid flow for the whole system. This allows direct connection with experimental observations as we seek to utilize our simulations to control the multiphase fluid flow dynamics to enhance particle-particle and particle-reactor passivating-layer abrasion and carbonation. Initial whole system simulations as a function of particle size indicate it can dramatically impact both the particle concentration profile and velocity vectors, key factors that can substantially impact particle-particle abrasion, exfoliation, and carbonation. These studies, and complimentary experimental studies, are continuing during the no-cost extension.

A controlled pressure and temperature 20 kHz sonication system was successfully developed for these studies during the first year. During the second year the system was refined to utilize an improved sonic probe design that substantially extends the lifetime of the probe. During the second year, the system has been utilized to explore the effects of sonication on the extent of carbonation as a function of the weight % olivine present, particle size distribution, volume fraction of aqueous solution present, and sonication power, time, temperature, and CO_2 pressure. None of the conditions investigated significantly enhanced carbonation. As sonication is energy intensive, we have refocused our efforts to deepen our studies of the effects that aqueous solution chemistry and multiphase fluid flow can have on carbonation reactivity, as they offer the greatest promise for cost-effectively enhancing aqueous olivine carbonation.

Mechanistic investigations have extended the fundamental understanding of the passivating layer formation process during the second project year, with many of these results discussed in our recently published article "Carbon Sequestration via Aqueous Olivine Mineral Carbonation: Role of Passivating Layer Formation," in *Environmental Science and Technology (2006).* These investigations indicate both incongruent magnesium dissolution and silica precipitation contribute to silica-rich passivating layer formation. Secondary ion mass spectrometry observations of the hydrogen concentration within the passivating layer suggests $2H^+/Mg^{2+}$ ion exchange occurs in association with incongruent dissolution. In the process, H_2O forms in the olivine/passivating-layer interface region and diffuses out through the layers. Internal passivating-layer diffusion of key reaction species is also consistent with our observation of magnesite nanocrystals having formed within the passivating layers. Thus, during carbonation the layers have significant permeability to key reaction species such as Mg^{2+}, H^+, H_2O, CO_2, and HCO_3^-.

Cracking of the passivating layer surface during carbonation is routinely observed during both static and stirred investigations. This is related to the tensile stress at the interface between the silica-rich passivating layer and the underlying olivine host, due to the large volume reduction as the silica forms from its olivine host. The impact of abrasion on passivating layer exfoliation and carbonation was investigated via the addition of significant weight fractions of similarly sized quartz particles as an abrasive slurry. This process significantly enhanced carbonation under otherwise identical conditions, further substantiating the importance of particle-particle abrasion as a pathway for enhancing both passivating layer exfoliation and carbonation. Studies during the no-cost extension period will emphasize the impact that controlled aqueous speciation and activity and slurry-flow dynamics have on the mechanisms that control carbonation reactivity, as they offer the greatest potential to substantially reduce olivine mineral sequestration process cost.

INTRODUCTION

Fossil fuels are well positioned to supply the world's energy needs for centuries to come if carbon sequestration technology can be developed that is (i) permanent, (ii) environmentally benign, and (iii) economically viable.[1] CO_2 mineral sequestration provides permanent disposal, by forming geologically stable mineral carbonates.[2-5] The materials produced are also environmentally benign and found in vast quantities in nature. The primary challenge is economically viable process development. As permanent disposal inherently avoids the ongoing monitoring, remediation and liability costs associated with long-term storage, the key is reducing mineral sequestration process cost. Cost effectively enhancing carbonation reactivity is critical. Enhancing mineral carbonation during geological (below-ground) sequestration is highly desirable as well, as it can similarly ensure long-term sequestration stability via the formation of thermodynamically stable mineral carbonates.[6] Investigating and evaluating candidate technologies that incorporate mineral sequestration (above and below ground) is the primary focus of the CO_2 Mineral Sequestration Working Group, which is managed by DOE (Fossil Energy), and consists of members from the Albany Research Center, Argonne National Laboratory, Arizona State University, Los Alamos National Laboratory, and the National Energy Technology Laboratory.

Above ground carbonation of Mg-rich olivine minerals (e.g., forsterite, Mg_2SiO_4) is a leading mineral sequestration process candidate.[7,8] These minerals are available worldwide in quantities sufficient to support the regional implementation of above-ground mineral sequestration.[8] Their low-cost (~$4-5/ton for mined and milled feedstock)[7,8] and exothermic carbonation (reaction 1), provide the potential for economically viable process development.

(1) $\frac{1}{2}Mg_2SiO_4 + CO_2 \rightarrow MgCO_3 + \frac{1}{2}SiO_2 + 88$ kJ/mol

Recent studies at the Albany Research Center indicate aqueous solution carbonation is a promising approach.[7,8] Even without special activation, 30-50% carbonation has been achieved in an hour for <37 micron olivine reacted at 185 ^oC and 150 bar CO_2. Mechanical pretreatment via intense attrition accelerates carbonation to near completion in less than an hour and at reduced pressures and temperatures. However, the activation cost is too high for cost-effective sequestration.[8]

Economically viable process development will require novel approaches that enhance mineral carbonation reactivity, while bypassing costly mineral pretreatment. The potential to develop low-cost chemical pretreatment processes has been explored for years, but success remains elusive.[6] Enhancing carbonation, while avoiding the expense of olivine pretreatment, would substantially reduce process cost and provide a significant advance. We recently discovered that aqueous olivine mineral carbonation is associated with robust passivating layer formation, which substantially inhibits mineral carbonation. Herein, we are exploring novel low-cost approaches with the potential to mitigate passivating layer effectiveness, enhance carbonation and develop an atomic level understanding of the associated mechanisms. The goal is to develop the understanding needed to engineer new low-cost carbonation processes that avoid the cost of pretreatment activation. The primary focus is on mitigating passivating layer effectiveness, e.g.,

by enhancing exfoliation processes that expose fresh olivine surfaces, an approach with the potential to substantially enhance carbonation while avoiding the need for and cost of olivine pretreatment activation.

EXPERIMENTAL

Single crystal olivine fragments from San Carlos, Arizona, were used to explore the effects of aqueous solution chemistry, particle size and sonication on olivine carbonation reactivity, as well as the mechanisms that govern passivating layer formation and exfoliation processes. The elemental composition was determined to be $(Mg_{0.915}Fe_{0.085})_2SiO_4$ by electron microprobe and particle induced X-ray emission analysis. X-ray diffraction (XRD) of powdered samples showed the lattice constants are in good agreement with those observed for olivine containing ~8% Fe (a = 4.763Å, b = 10.223Å, c = 5.993Å).[9,10] Trace impurities observed were well below 1%, with Ca being the principle trace impurity. Single crystals and single crystal fragments were used to facilitate microscopic observation of passivating layer formation/exfoliation and the reaction surfaces and interfaces that form during carbonation. Synthetic forsterite (Mg_2SiO_4) (99% Mg_2SiO_4; Alfa Aesar) was used for select carbonation investigations. Twin Sisters olivine was used for the flow-loop reactor studies carried out in collaboration with the Albany Research Center.[7] The flow-loop reactor has been previously described.[8] All of the olivine size fractions investigated herein (<37 micron, 37-75 micron, < 75 micron, 75-150 micron and <150 micron) were wet screened. The extent of carbonation observed is compared with the optimum process to date for enhancing carbonation developed by the Albany Research Center (ARC),[7,8] which is summarized below for forsterite carbonation.

$$Mg_2SiO_4 + 2CO_2 \xrightarrow[0.64\ M\ NaHCO_3,\ 1M\ NaCl]{\sim 185\ ^\circ C,\ \sim 150\ atm\ CO_2} 2MgCO_3 + SiO_2$$

Reactions were carried out using a variety of aqueous species (e.g., Li^+, Na^+, K^+, Rb^+, Cl^-, HCO_3^-) and species activities, particle size ranges and reaction times to probe their effect on carbonation and passivating layer formation/exfoliation. 1,500 rpm stirring was used to replicate the ARC process in the studies at Arizona State University. These mineral carbonation reactions were performed using a 100ml Autoclave Engineers EZE-Seal Hastelloy C-276 reactor, which is a smaller scale version of the 2,000 ml EZE-Seal Hastelloy C-276 reactor used at the Albany Research Center. Unstirred (static) experiments were undertaken to explore passivating layer formation in the absence of particle abrasion. San Carlos olivine single crystals (~1x1x0.1cm) with well-defined initial surface orientations were incorporated to follow the reaction interface that forms down to the atomic level.

The extent of carbonation and hydrogen content of the product materials were assessed using a Perkin Elmer Series II CHNS Elemental Analyzer. Comparative standards gave total carbon and hydrogen accuracies of ± 0.3 wt%. Extent of carbonation observations were compared with XRD intensity analysis of the product materials and found to be in good agreement. Select reaction products were analyzed structurally, morphologically, and analytically versus their extent of reaction to probe the mechanisms that govern carbonation.

XRD patterns were obtained using a Rigaku D/MAX-IIB X-ray diffractometer with Cu$K\alpha$ radiation. Scans were taken over different 2θ ranges between 10º to 70º, with 0.01º/s steps.

Reaction products were imaged using a Hitachi S-4700 field-emission scanning electron microscope (FESEM) or a FEI XL-30 Environmental FESEM. Elemental analysis of individual product particles was accomplished via energy dispersive X-ray spectroscopy (EDS). Cross-sectioned samples of reaction interfaces were analyzed via FESEM and EDS mapping and high-resolution transmission electron microscopy (HRTEM) using a JEOL 2010 with EDS and electron energy loss spectroscopy (EELS) capabilities. Secondary ion mass spectrometry (SIMS) analyses were performed using a spectrometer (Model3f, CamecaIMS, Courbevoie, France).

Controlled pressure and temperature studies of the impact of sonication on olivine exfoliation/carbonation were carried out using our batch mineral carbonation reaction system described above and our specially developed controlled pressure and temperature sonication system described below. Sonication/carbonation studies have been carried out in stages. Hour-long carbonation studies are separated into three stages: (1) a half hour long run in the batch reactor, followed by (2) controlled sonication in the sonication system (e.g., one minute) and (3) a second half hour in the batch reactor. The above sonication runs are compared to both the standard one-hour carbonation runs using the batch reactor and runs that incorporate the sonication reaction stages (1/2 hour plus 1/2 hour batch reaction format), but without sonication.

RESULTS AND DISCUSSION

Technical Accomplishments: Enhancing the Sonic Exfoliation System

During the first project year we developed a controlled pressure and temperature 20 kHz sonication system for these studies. The system is based on a Sonics 1500 watt power supply and a special probe to adapt to our custom controlled pressure (1 to 200 atm) and temperature (20 to 250 ^{o}C) sonication vessel. The pressure and temperature control system used is the same system used to conduct our aqueous carbonation reactions. The impeller driven stirring system is replaced by the sonic probe. Other than the interchangeable sonication and impeller components, the remainder of the system remains essentially the same. During the second year, the sonic probe failed prematurely, and it became apparent that the design of the probe needed to be modified. The design was refined and improved in collaboration with Sonics Inc. based on the failure mode for the first generation of probes. The new design has substantially extended the life of the probe and has been utilized for the second year sonication studies described below.

Scientific Progress: Effects of Aqueous Chemical Speciation and Activity on Olivine Carbonation Reactivity.

We are investigating the effect of aqueous solution species/activity on extent of carbonation using our 100 ml batch carbonation reaction system. The extent of carbonation observed for these investigations is compared with that observed using the optimum conditions to enhance carbonation developed by the ARC, which incorporates an aqueous solution of 0.64M $NaHCO_3$ + 1.00 M NaCl, and 1 hour reaction time at 185 ^{o}C, under 2200 psi of CO_2, with ~ 1500rpm stirring. <38μ San Carlos olivine (essentially single crystal fragments) was used for the comparative studies. The objective of these investigations is to further evaluate (i) the effect of

aqueous chemical speciation and concentration on olivine passivating layer formation and carbonation reactivity and (ii) the potential controlling them offers to enhance carbonation. During the second project year the primary focus has been on the effect of the activities of the alkali cation, chloride and bicarbonate species present. As substantial increases in the extent of carbonation were observed using higher concentration Na/K bicarbonate solutions, our studies have emphasized a thorough exploration of the potential these solutions offer to enhance carbonation as a function of their activity, Na/K ratio, and the associated reaction temperature and pressure (P_{CO2}). All results are compared to the extent of carbonation observed using the standard 0.64M $NaHCO_3$ + 1.0 M NaCl aqueous solution developed at the Albany Research Center (ARC).[7] Other than varying the above parameters, the impact of which are the primary focus of these studies, the other conditions associated with the optimum procedure developed by the ARC were used throughout. The carbonation extents reported are calculated based on elemental carbon analysis of the product materials, which are semi-quantitatively verified via X-ray powder diffraction analysis. All of the product carbonate formed herein is identified as magnesite.

1. Exploring the Potential that Potassium/Sodium Bicarbonate Solutions Offer to Enhance Aqueous Olivine Carbonation Reactivity

High aqueous bicarbonate concentrations were observed to substantially enhance olivine carbonation reactivity in comparison with the standard ARC 0.64M $NaHCO_3$ + 1.00 M NaCl aqueous solution. In order to more fully explore the potential high aqueous bicarbonate concentrations offer to enhance carbonation reactivity, we investigated the carbonation reactivity associated with $NaHCO_3$ and $KHCO_3$ solutions as a function of their aqueous concentration and Na/K ratio. Plots of extent of carbonation versus [$NaHCO_3$] and [$KHCO_3$] are shown in Figures 1 & 2 below. A strong increase in carbonation extent is observed with increasing bicarbonate concentrations for both sodium and potassium bicarbonate, which peaks at relatively high bicarbonate concentrations and begins to decrease at still higher bicarbonate concentrations. The peak extent of carbonation is ~2.5M for $NaHCO_3$ and ~5.5M for $KHCO_3$. Aqueous solutions containing CO_2(aq) and Na^+ or K^+, and HCO_3^- have provided the best synergistic combination of solution ions for enhancing mineral carbonation to date, nearly doubling the extent of carbonation observed using the standard ARC solution. It is interesting to note the strong positive effect that Na^+ has on carbonation in comparison with similar concentrations of K^+, highlighting the important role that cation species can play in carbonation. It is also important to note that further increasing the bicarbonate concentration eventually leads to lower carbonation extents.

If the above effect were simply associated with reaching the solubility limit of $NaHCO_3$ and $KHCO_3$ at 185 ^oC and 150 atm CO_2, the extent of carbonation might be expected to reach a plateau at the highest bicarbonate concentrations, with any further bicarbonate that is added simply remaining in solid form. Instead, the extent of carbonation decreases significantly for increasingly high Na/K bicarbonate concentrations, which may be associated with decreasing CO_2 solubility with increasing ionic Na/K bicarbonate concentrations. This hypothesis is

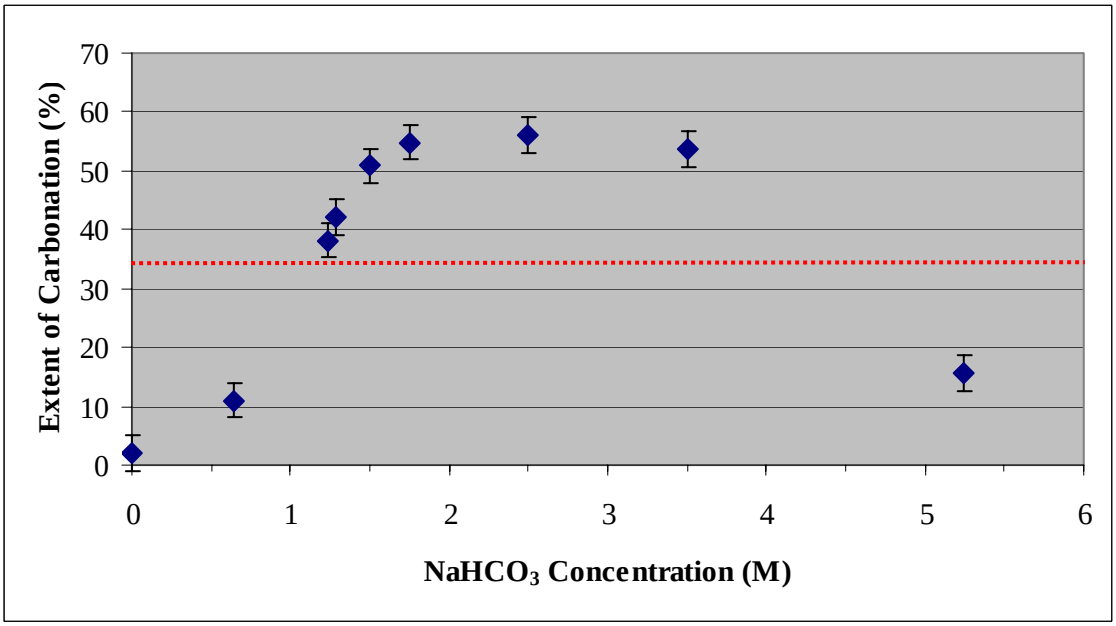

Figure 1: *Extent of carbonation of < 38 µ San Carlos Olivine as a function of $NaHCO_3$ concentration after 1h of carbonation at 185°C, under 2200psi of CO_2, and with ~1500rpm stirring. The dashed horizontal red line represents the extent of carbonation observed using the standard 0.64M $NaHCO_3$ + 1.00 M NaCl aqueous solution under the same reaction conditions.*

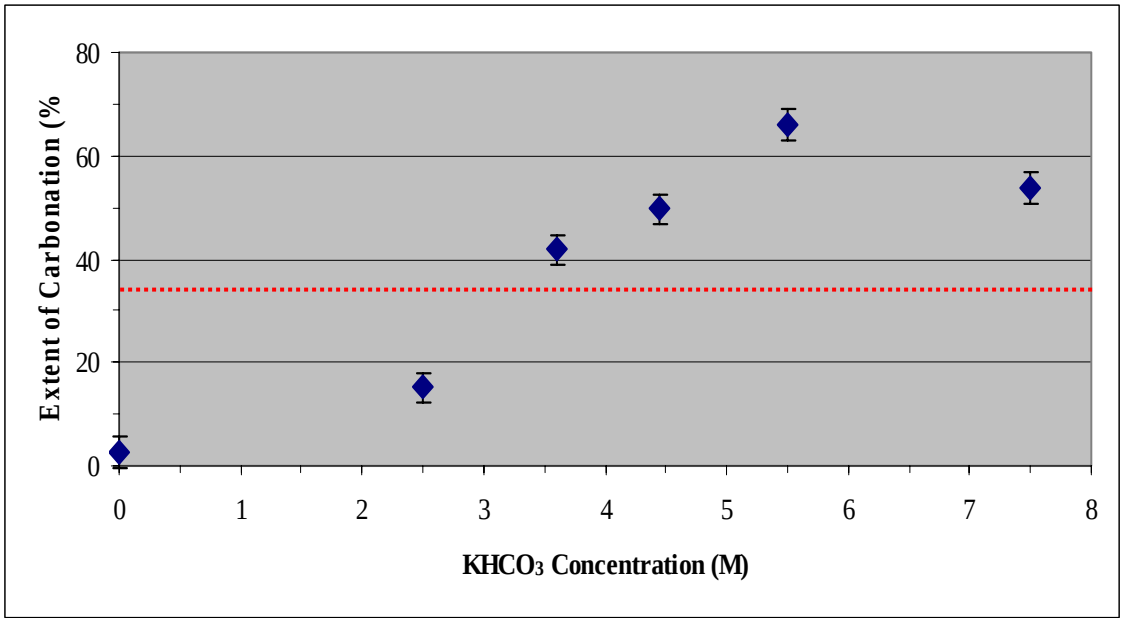

Figure 2: *Extent of carbonation of < 38 µ San Carlos Olivine as a function of $KHCO_3$ concentration after 1h of carbonation at 185°C, under 2200psi of CO_2, and with ~1500rpm stirring. The dashed horizontal red line represents the extent of carbonation observed using the standard 0.64M $NaHCO_3$ + 1.00 M NaCl aqueous solution under the same reaction conditions.*

consistent with previous simulations that indicate that increasing ionic NaCl concentrations may significantly reduce aqueous CO_2 solubility (see below). Future NMR probe and simulation investigations are planned to explore the effect of increasing Na/K bicarbonate concentrations on CO_2 solubility to assess the extent to which the above decrease in carbonation extent may be related to decreasing aqueous CO_2 solubility at very high bicarbonate concentrations.[11,12]

We have previously observed that using mixtures of $NaHCO_3$ and $KHCO_3$ and varying the Na^+/K^+ ratio can significantly improve the extent of olivine carbonation when starting with the standard solution of 0.64M $NaHCO_3$ + 1.00 M NaCl, as seen in Figure 3. This led us to explore the potential for further enhancing carbonation reactivity by varying the Na^+/K^+ ratio for high bicarbonate concentrations [i.e., 2.5 M $(Na/K)HCO_3$]. As seen in Figure 4, the Na^+/K^+ ratio has a dramatic impact on carbonation reactivity. The extent of carbonation dramatically increases with increasing Na^+/K^+ ratio, but does not exceed the value observed for 2.5 M $NaHCO_3$. Although a few more data points are needed at lower Na/K ratios, varying the ratio does not appear to hold much promise for enhancing carbonation.

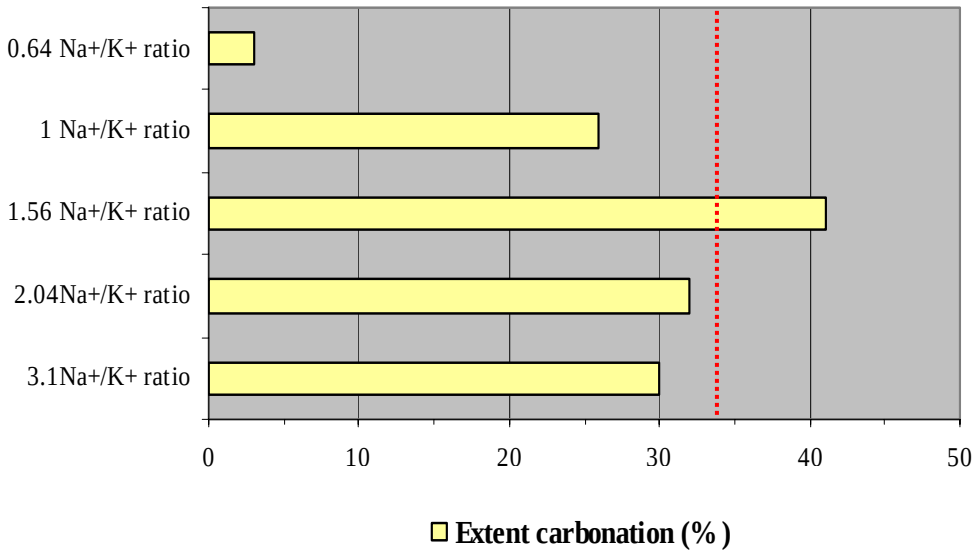

***Figure 3**: Extent of carbonation of San Carlos olivine as a function of Na^+/K^+ molar ratio, at 0.64M HCO_3^-, 1.0M Cl^-, and 1.64M M^+ (M = Na + K). The dotted red line indicates the average extent of carbonation observed using the standard 0.64M $NaHCO_3$ + 1.0M NaCl aqueous solution.*

We also explored the effect of reaction temperature and pressure on the extent of carbonation observed for high bicarbonate concentrations using 2.5 M $NaHCO_3$. $NaHCO_3$ offered the highest extent of carbonation for relatively low, e.g. 2.5M, bicarbonate concentrations (56% vs. 34% for the standard solution 0.64M $NaHCO_3$ + 1.00 M NaCl) and was used as the aqueous solution for these studies. In Figure 5 below, the extent of carbonation of <38µ San Carlos olivine as a function of reaction temperature is shown. The extent of carbonation is clearly very sensitive to reaction temperature, with carbonation decreasing dramatically with decreasing reaction temperature below 185 ^oC. In contrast, a modest increase in the reaction temperature above 185 ^oC did not improve carbonation.

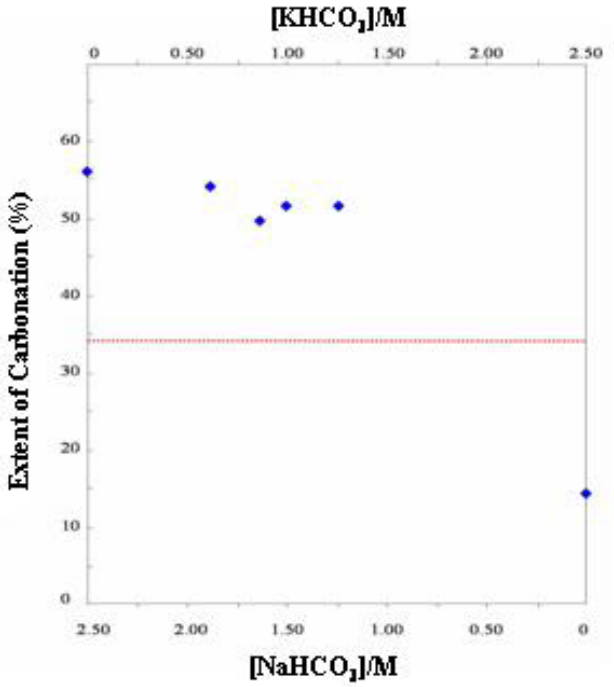

Figure 4: *Extent of carbonation versus the $NaHCO_3/KHCO_3$ ratio. Reaction conditions are: 1h, 185°C, 2200psi CO_2, and stirring at 1500rpm. The $[HCO_3^-]$ was maintained at 2.5M. The dashed horizontal red line represents the extent of carbonation observed using the standard 0.64M $NaHCO_3$ + 1.0M NaCl aqueous solution.*

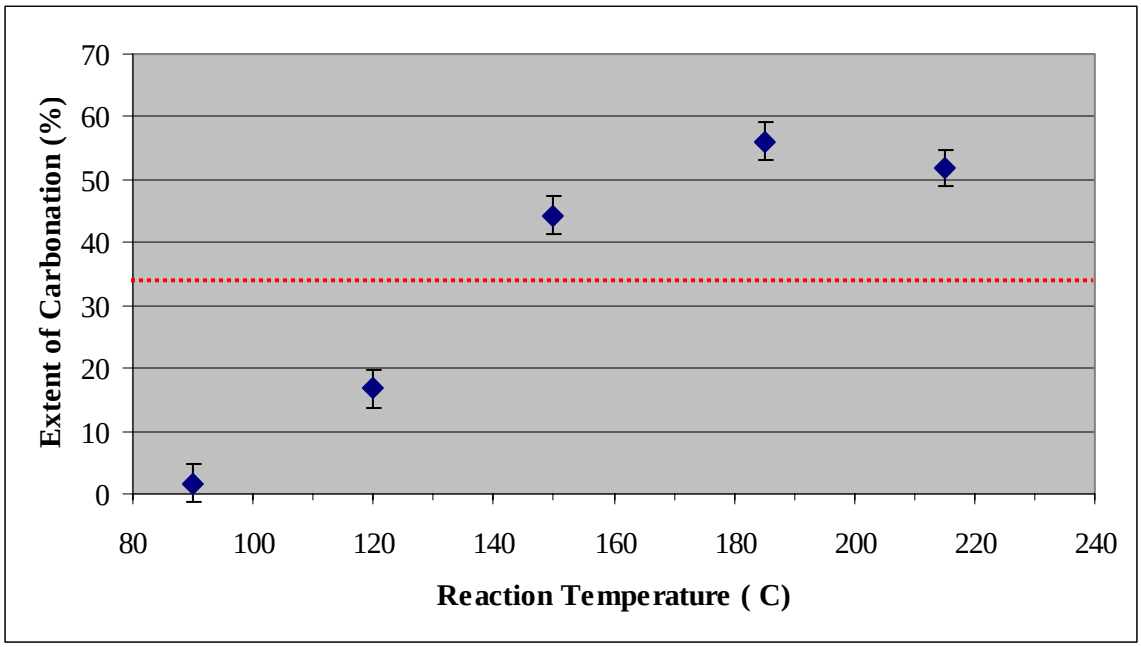

Figure 5 *The effect of reaction temperature on the extent of carbonation of San Carlos olivine (<38µ). Reaction conditions: 1h, 2,200 psi CO_2, 1500rpm stirring, and 2.5M $NaHCO_3$. The dashed red line represents the average extent of carbonation observed using the standard aqueous solution (0.64M $NaHCO_3$ + 1.00 M NaCl) at 185 ^oC.*

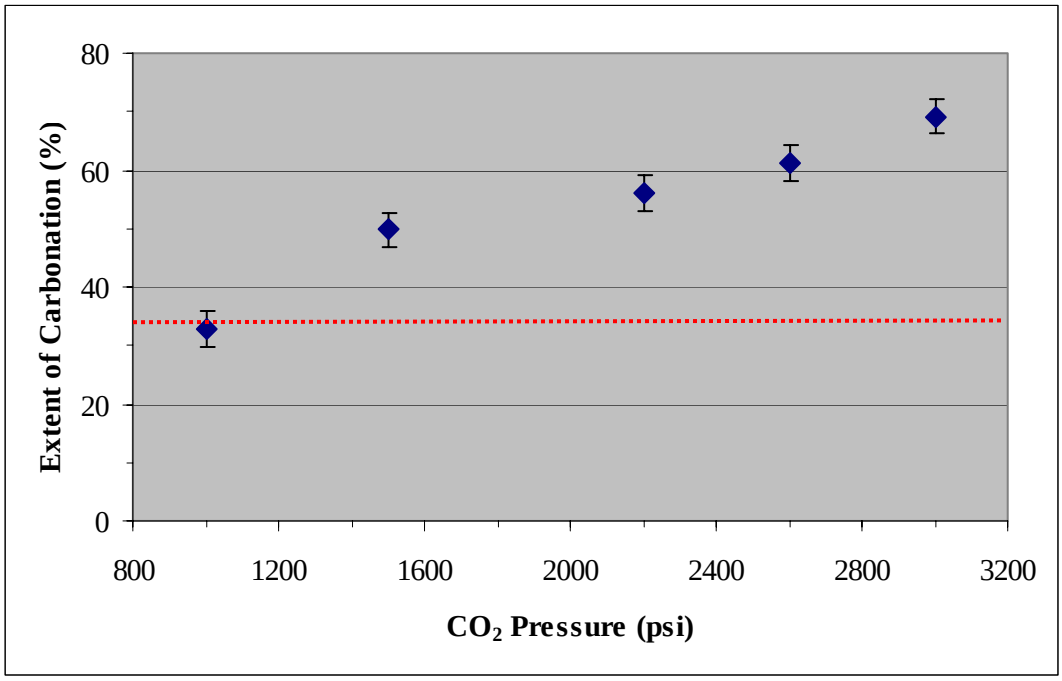

Figure 6: *The effect of reaction pressure on the extent of carbonation of San Carlos olivine (<38μ). Reaction conditions: 1h, 185 °C, 1500rpm stirring, and 2.5M $NaHCO_3$. The dashed red line represents the average extent of carbonation observed using the standard aqueous solution (0.64M $NaHCO_3$ + 1.00 M NaCl) at 2,200 psi.*

Figure 6 shows the effect of reaction pressure on the extent of carbonation observed using 2.5M $NaHCO_3$. 185°C was selected as the optimal carbonation temperature for 2.5M $NaHCO_3$. The same feedstock material (<38μ San Carlos olivine) was tested with the other reaction conditions identical to those used for the reaction temperature studies. The extent of carbonation is a strong function of CO_2 reaction pressure, exhibiting a strong increase in carbonation with increasing pressure (e.g., from 32% at 1,000 psi to 70% at 3,000 psi), consistent with increasing CO_2(aq) activity increasing the extent of carbonation. It is informative to compare these results with our observations for increasing bicarbonate concentrations in Figures 1 and 2. Increasing extents of carbonation with increasing CO_2(aq) activities is further consistent with the hypothesis that increasing bicarbonate concentrations may suppress CO_2(aq) solubility and carbonation for high bicarbonate concentrations. Again, NMR probe and simulation investigations are planned to further explore this possibility by investigating the effect of increasing Na/K bicarbonate concentrations on CO_2(aq) solubility.[11,12]

Scientific Progress: Multi-phase Fluid Modeling and Experimental Investigations to Elucidate Key Slurry-Flow Parameters that Enhance Exfoliation and Carbonation

1. **Exploring the Effect of Feedstock Particle-Size Distribution on Aqueous Olivine Carbonation Reactivity**

Our recent slurry-flow modeling investigations (below) indicate that the spatial olivine particle distribution and the associated velocity vectors during aqueous mineral carbonation (using the

100ml ASU batch reactor) are highly dependent on the feedstock particle size distribution, as discussed below. These studies suggest that controlling the particle size distribution during mineral carbonation may provide a cost-effective avenue to enhance particle abrasion and olivine carbonation. To begin to explore the associated potential to enhance carbonation, the extent of carbonation was explored as a function of the particle-size distribution associated with 10 gram San Carlos olivine mineral carbonation feedstock samples. The extent of carbonation for particle size fractions of freshly ground and wet-sieved San Carlos olivine were investigated in both the standard 0.64M $NaHCO_3$ + 1M NaCl and 2.5M $NaHCO_3$ aqueous solutions. Duplicate runs using the standard solution gave reproducible extent of carbonation results for these feedstock batches as follows: <38μ feedstock: 37%; 38-75μ feedstock: 5%; 75-150μ feedstock: 4%.

The <38μ and 38-75μ batches were mixed to generate <75μ fractions with different weights of the <38μ and 38-75μ particle size fractions. The extent of carbonation observed using the standard aqueous solution (0.64M $NaHCO_3$ + 1M NaCl) for the various particle size distributions is shown in Figure 7. The average extent of carbonation observed above for the <38μ and 38-75μ particle-size fractions were used to calculate the "predicted" extent of carbonation if carbonation is independent of the feedstock particle size distribution. The predicted extents of carbonation are compared with the experimental results for a series of mixtures of the <38μ and 38-75μ particle size fractions in Figure 7. In this case, varying the particle size distribution by blending different amounts of the 38-75μ fraction with the <38μ fraction did not significantly impact the extent of carbonation observed, indicating in this case varying the particle size distribution did not significantly impact particle abrasion and exfoliation. In other words, the <38μ and 38 to 75μ feedstock materials appear to experience the same extent of carbonation independent of the wt% ratio used.

The extent of carbonation was also explored for select <38μ, <75μ, and <150μ feedstock materials using an aqueous 2.5M $NaHCO_3$ solution to probe whether the highly reactive aqueous solution chemistry associated with high bicarbonate concentrations impacts the relative reactivity of different particle size distributions. In this case, we explored the relative carbonation reactivity of the above particle size ranges for the standard 0.64M $NaHCO_3$ + 1M NaCl and 2.5M $NaHCO_3$ aqueous solutions. Figure 8 compares the average extent of carbonation observed for the above particle-size fractions for both solutions. A 35% improvement in carbonation is observed for the <38μ fraction using 2.5M $NaHCO_3$. By comparison, a 146% and 158% improvement is observed for the <75μ, and <150μ fractions, respectively, suggesting high concentration bicarbonate solutions can substantially further enhance the relative carbonation reactivity of larger olivine particle-size fractions. Being able to effectively carbonate olivine feedstocks with such larger particle-size fractions offers the potential to substantially reduce feedstock grinding cost and substantially lower mineral sequestration process cost.

2. Exploring the Effect of Abrasive Slurry Additives on Passivating-Layer Exfoliation and Olivine Carbonation

To further explore the role of particle abrasion on the extent of carbonation, quartz particles were

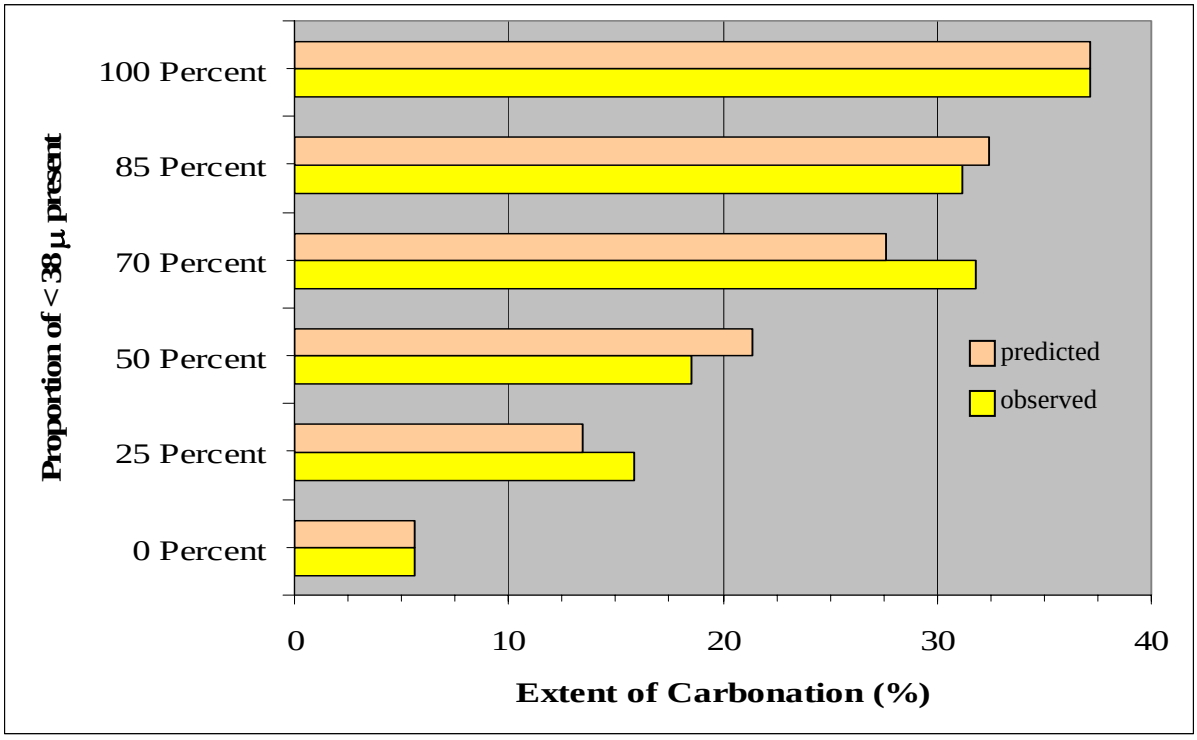

Figure 7: *Effect of mixing <38µ and 38-75µ fractions on the extent of carbonation of San Carlos olivine using the standard aqueous 0.64M $NaHCO_3$ + 1M NaCl solution, with a reaction time of 1h at 185 ^oC, under 2200psi CO_2, and with ~1500rpm stirring. The proportion of <38 µ olivine used is given in weight percent.*

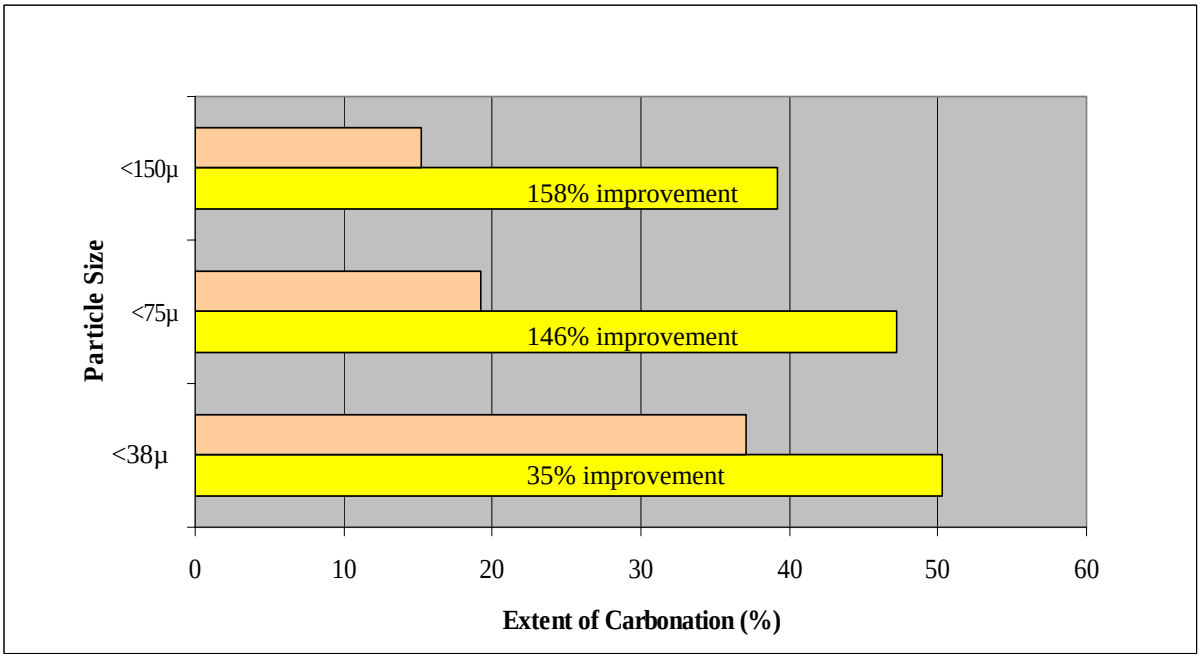

Figure 8: *Effect of particle size distribution on the extent of carbonation observed for San Carlos olivine using the standard (0.64M $NaHCO_3$ + 1M NaCl) aqueous solution (orange bars) and 2.5M $NaHCO_3$ aqueous solution (yellow bars). Note the dramatic improvement in the extent of carbonation observed for the larger particle-size feedstock material when 2.5M $NaHCO_3$ is used.*

incorporated during olivine mineral carbonation as a potential abrasive agent for promoting passivating-layer exfoliation and carbonation. In this case, synthetic olivine (forsterite: Mg_2SiO_4) was used as the feedstock. The weight % quartz was varied from 0 to 80% of the 10g feedstock charge used. The carbonation studies were performed using the standard aqueous solution (0.64M $NaHCO_3$ + 1M NaCl), with the reactions carried out for 1h at 185°C under 2200 psi CO_2, with ~1500rpm stirring. The results are shown in Figure 9. Without the addition of the quartz abrasive, a 68% extent of carbonation was observed. The extent of olivine carbonation observed increased with increasing wt. % quartz up to 84% carbonation for 60 weight % quartz, consistent with enhanced passivating-layer abrasion. However, carbonation decreased at higher quartz concentrations (i.e., 80 wt. %), which may be associated with increasing quartz-quartz particle abrasion reducing its effectiveness at passivating-layer abrasion. To explore this hypothesis, 10g of quartz was run for an hour under the same mineral carbonation conditions, including 1,500 rpm stirring to simulate the enhanced quartz-quartz abrasion that may occur when high quartz concentrations are used as an abrasive to enhance olivine carbonation. The product was filtered, rinsed, and dried. 6g of the "abraded quartz" was run with 4g of forsterite to explore its abrasive potential. As seen in Figure 9, the extent of carbonation is substantially lower than that observed with fresh quartz, consistent with self abrasion reducing the effectiveness of quartz as a passivating-layer abrasive agent at higher quartz concentrations. This reduced effectiveness may be associated with both particle-size reduction and smoothing of the quartz particle edges at higher quartz concentrations.

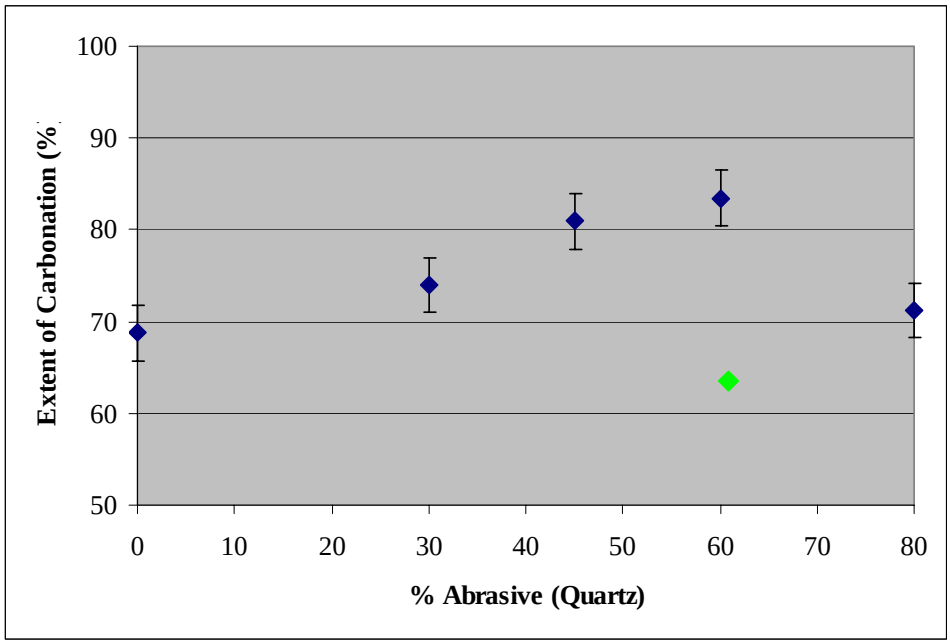

Figure 9: *Extent of carbonation observed for synthetic olivine as a function of the wt. % quartz abrasive added (blue diamonds). Reaction conditions are 0.64M $NaHCO_3$ + 1M NaCl, 1h, 185°C, 2200 psi CO_2, and 1500rpm stirring. The green diamond shows the extent of carbonation observed using self-abraded quartz particles.*

3. Effect of Quartz Abrasives on Carbonation as a Function of Temperature

As reaction temperature may affect the properties of the passivating layers that form during

olivine carbonation, we explored the impact of temperature on the effectiveness of quartz passivating-layer abrasion. Two preliminary runs were conducted with 10 and 20 wt% quartz. 10 wt% did not significantly enhance carbonation, whereas 20% was effective. Figure 10 shows the extent of olivine carbonation with and without the addition of 20 wt% quartz abrasive. Significant enhancement in the extent of carbonation is observed over the range of temperatures where carbonation is reasonably effective, indicating that abrasive quartz additives are effective at enhancing passivating-layer exfoliation and carbonation at least from 155 to 215 ^{o}C. It is particularly interesting to note the extent of carbonation observed with and without the quartz abrasive at 185 ^{o}C. In this case, the enhanced extent of carbonation observed is greater per 10g of feedstock (61% vs. 56% per 10g feedstock), even though 20% of the feedstock, quartz, cannot carbonate. This key observation indicates that controlled use of low cost abrasives may offer the potential to reduce mineral sequestration process cost. Any effort to optimize carbonation with such controlled abrasive additions should, of course, be integrated together with control of the slurry fluid-flow conditions to maximize particle abrasion and passivating-layer exfoliation.

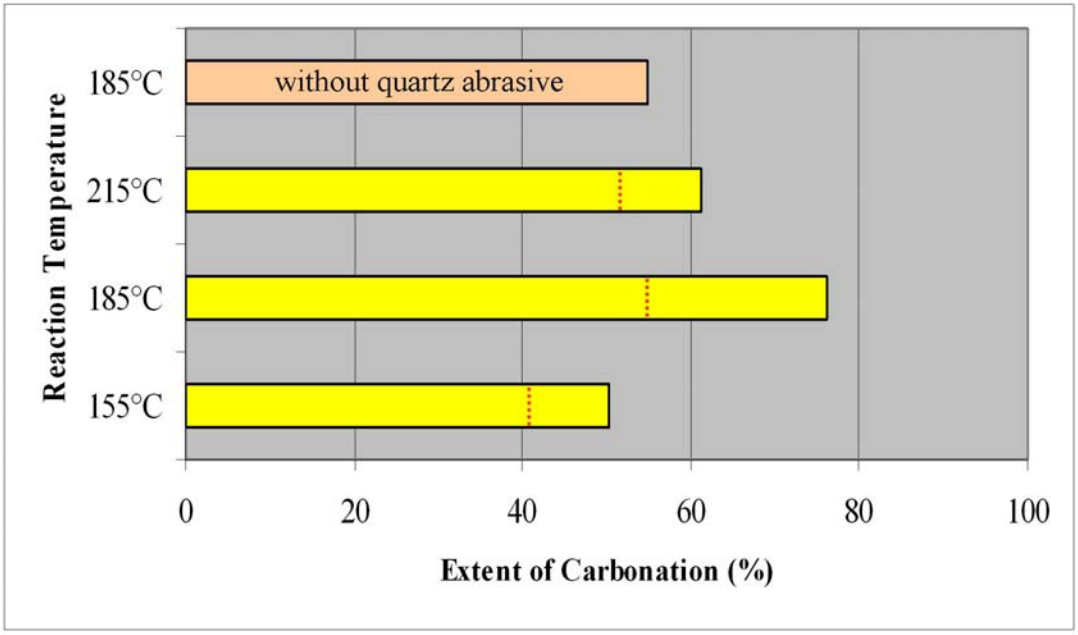

Figure 10: *Extent of carbonation of <38μ San Carlos olivine, mixed with 20 wt% quartz abrasive as a function of reaction temperature. The carbonation conditions are 1h reaction time, 2200psi of CO_2, and 1500rpm stirring using a 2.5M aqueous $NaHCO_3$ solution. The full yellow bars indicate the extent of carbonation with the quartz abrasive. The dashed vertical red lines indicate the extent of olivine carbonation observed in the absence of the quartz abrasive for the same olivine feedstock batch.*

4. Effect of Quartz Abrasives on Carbonation as a Function of Reaction Pressure

Since the reaction pressure may affect the properties of the passivating layers that form during olivine carbonation, we also explored the impact of pressure on the effectiveness of quartz passivating-layer abrasion. The optimal reaction temperature in Figure 10 (185 ^{o}C) was selected for these investigations, with 20 wt% quartz again used as the passivating-layer abrasive. The

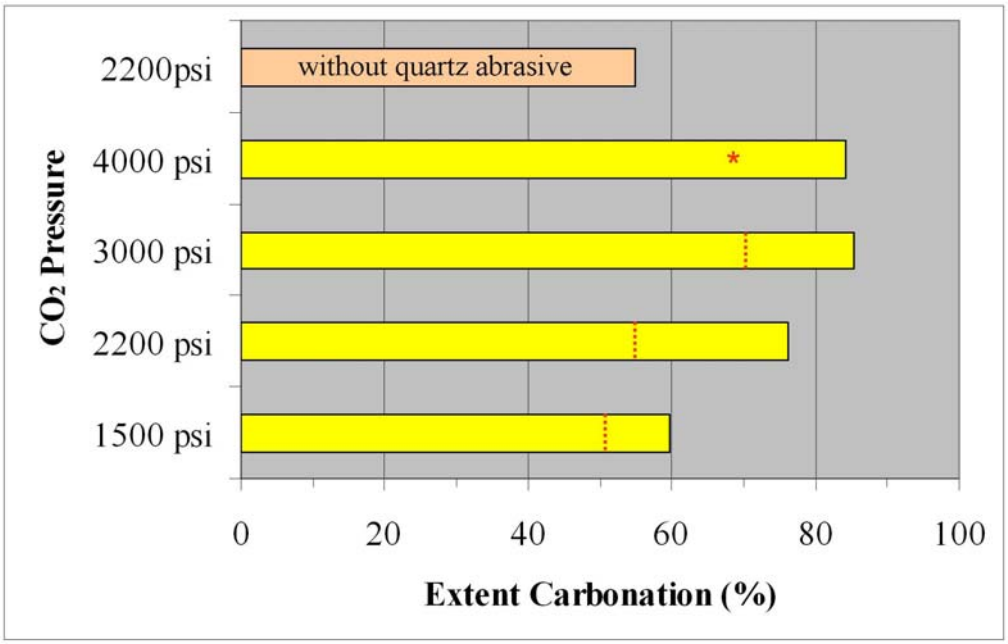

Figure 11: *Extent of carbonation of <38μ San Carlos olivine, mixed with 20 wt% quartz abrasive as a function of reaction pressure. The carbonation conditions are 1h reaction time, 185 ^{o}C, and 1500rpm stirring using a 2.5M aqueous $NaHCO_3$ solution. The full yellow bars indicate the extent of carbonation with the quartz abrasive. The dashed vertical red lines indicate the extent of olivine carbonation observed in the absence of the quartz abrasive. The extent of carbonation at 4,000 psi in the absence of the quartz abrasive* has not yet been explored.*

quartz abrasive was observed to effectively enhance olivine carbonation over the range of pressures studied to date (1,500 to 3,000 psi), as shown in Figure 11, indicating that quartz is effective as a passivating layer abrasive over a range of pressures as well as a range of temperatures. The above studies as a function of pressure and temperature indicate the silica-rich passivating layers that form retain their brittleness and ability to exfoliate over a range of reaction temperatures and pressures relevant to aqueous olivine mineral carbonation.

The above observations underscore the importance of passivating-layer exfoliation/abrasion in enhancing olivine carbonation reactivity. In these studies, quartz was selected as a model low-cost abrasive that should not significantly impact the aqueous solution chemistry, hence providing insight into the potential abrasives offer to enhance carbonation. The addition of such abrasives is not limited to quartz or the slurry-flow conditions described herein. Indeed, these results suggest that a reaction process that offers the potential to better enhance feedstock abrasion, such as a fluidized-bed approach, may lead to significant further improvements in carbonation reactivity. In either case the associated slurry/fluidized bed flow dynamics can greatly impact the effectiveness of passivating layer abrasion/exfoliation and olivine mineral carbonation reactivity.

5. Exploring the Slurry-Flow Dynamics during Olivine Carbonation via Multiphase Fluid Modeling

During the first project year, work in this area of the project focused on two hierarchies of multiphase fluid-flow modeling. Both microscopic and macroscopic approaches were applied. The over-arching aim of the investigations in this portion of the project is to attempt to isolate and to understand effects that may be crucial to optimizing the fluid dynamics of sequestration processes to enhance passivating layer exfoliation and carbonation. The simulations used to assess "microscopic" fluid flow modeling illustrated that particle transport and mixing can be enhanced by interactions with roughened surfaces. While the current simulations used to assess the roughness model are idealized, in order to enable the application of simulation techniques that resolve turbulent fluctuations, the computations illustrated the importance of the basic effect of roughness, which is to transfer the mean streamwise momentum of the particles to the fluctuating velocities that are normal to the surface. This is an important mechanism for enhancing transport across the entire channel and facilitating particle-particle and particle-wall collisions, exfoliation and carbonation.

Macroscopic approaches, which emphasized simulating the slurry-flow behavior of a section of the Albany Research Center's (ARC's) flow-loop reactor,[8] indicated that the reactant particle size distribution may be a key factor that affects particle collision frequency, momentum transfer, exfoliation and carbonation. Due to the complexity of the flow-loop reactor, we have emphasized full system simulations of the 100ml batch ASU minireactor during the second year of this project. Such simulations have the decided advantage that they can provide insight into whole system slurry-flow dynamics, which can be directly compared with experiment. Once the impact of the slurry flow dynamics are better understood in the ASU batch reactor, the developed understanding can then be transferred to develop a better understanding of the effects that the slurry-flow dynamics have on olivine mineral carbonation in the ARC flow-loop reactor shown in Figure 12.

Figure 12: *The Albany Research Center's Flow-Loop Reactor.*

The primary focus of the slurry-flow modeling investigations during the second project year has been on developing a better understanding of the impact that the slurry-flow dynamics can have on olivine carbonation and passivating layer exfoliation at the macroscopic level for reactions carried out using the 100 ml ASU minireactor. The multiphase slurry in the minireactor is being modeled using Computational Fluid Dynamics (CFD) via Fluent. An example of the motivation for the simulations of the slurry dynamics in the minireactor comes from the wide variation in extent of carbonation observed for the same feedstock materials, such as the 23% vs. 2% extent of carbonation observed for <150μ Twin Sisters olivine run in the ASU minireactor and ARC flow-loop reactor, respectively. Experimental measurements of the extent of carbonation as a function of solids size fraction -- expressed in terms of the surface area available for reaction -- are summarized in Figure 13. As seen in the plot, the decrease in the surface area available for carbonation results in a decrease of the extent of carbonation, however, the decrease is not reflected to the same degree for both reactors, with the flow-loop reactor exhibiting anomalously low carbonation for the <150μ Twin Sisters olivine. This poor correlation becomes particularly interesting as different methods are employed to agitate the slurry in each of the reactors, underscoring that the slurry-flow dynamics incorporated during carbonation can dramatically impact the extent of carbonation observed. As discussed above, our second year slurry-flow modeling investigations have focused on whole system simulations of the ASU minireactor.

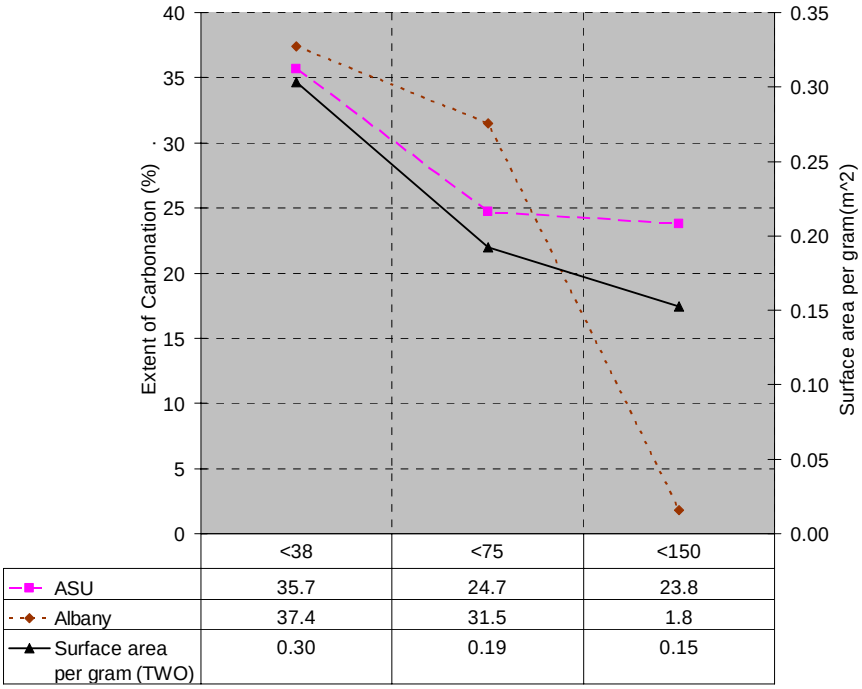

Figure 13: *Surface area available vs. extent of carbonation measured for the <150μ Twin Sisters Olivine (TWO) samples using the 100ml ASU batch minireactor and the ARC flow-loop reactor.*

Herein, we summarize the overall methodology of the simulations, consisting of generation of a three-dimensional grid representing the reactor geometry, computing the flow properties via solution of the model equations developed to describe the system, and analysis of the results. The computations are performed using the commercial software Fluent, which includes the

module Gambit used to generate the grids. Post-processing and analysis are also accomplished using Fluent.

Simulation Overview

Grid generation is the process of subdividing a region of interest into a set of small control volumes, which are then used to resolve the equations used to model the slurry. Associated with each control volume are one or more values of the dependent flow variables, which in this work are the phase velocities, pressure, volume fraction, turbulent kinetic energy, and dissipation rate. The model equations corresponding to the equations for conservation of mass, and momentum are solved numerically using the finite-volume method available in Fluent.

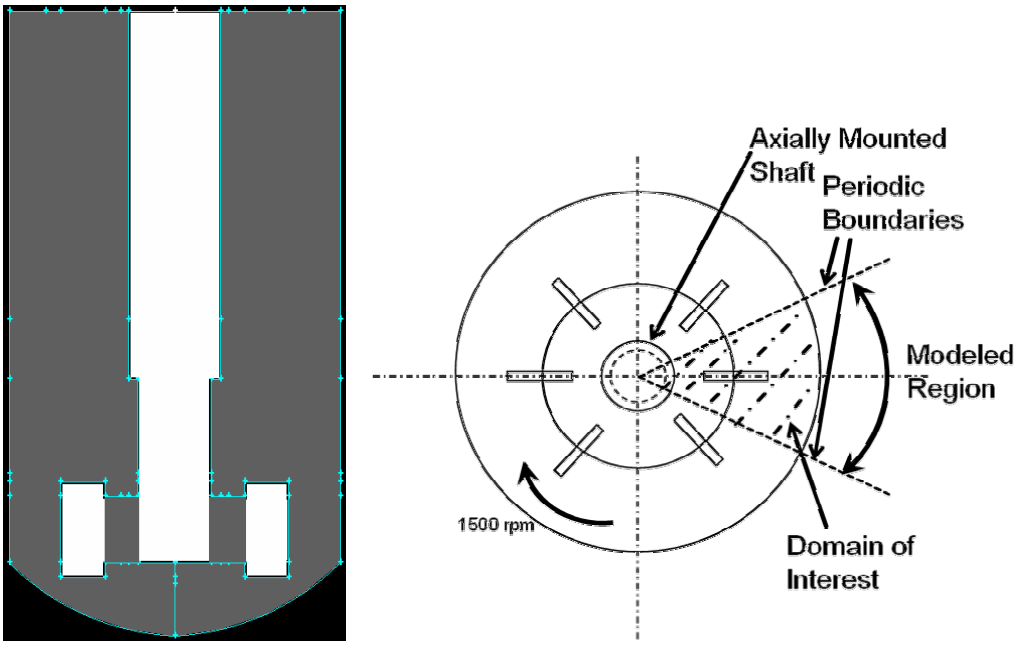

Figure 14: *(a) Wireframe view of the ASU mini-reactor, gray portion indicating the flow region and white portion indicating the rotating shaft and paddles; (b) Top view of the reactor highlighting the paddles, the central shaft, and the periodic boundaries applied to the computational domain (Figure not to scale).*

The ASU minireactor geometry is modeled using Gambit in which a computational mesh is created within a computer-aided drawing of the reactor vessel. Figure 14(a) shows a wireframe view of the minireactor. The minireactor used at ASU consists of a hollow cylindrical container with a nearly hemi-spherical bottom. A shaft attached to a motor runs centrally along the axis of the cylinder. A set of six blades arranged at 60 degree increments are attached to the shaft, which rotates at 1500 rpm. This top view is depicted in Figure 14(b). A spiral cooling tube is entwined around the central shaft, through which cold water is circulated during the post-reaction cooling process. A metal lid closes the top of the reactor during the carbonation process which is carried out for one hour in the experiments. To simplify mesh generation and reduce the simulation time, the spiral tube that transports cooling water during the post-reaction step

was not included in the computational representation of the minireactor. To reduce the computational expense, symmetry conditions were utilized to advantage with a grid generated for 1/6th of the reactor. Periodic conditions as shown in Figure 14(b) were applied to the solution variables at the bounding planes. Periodic boundary conditions ensure that the volume of fluid and particles crossing either of the bounding planes migrate back into the domain at the other plane.

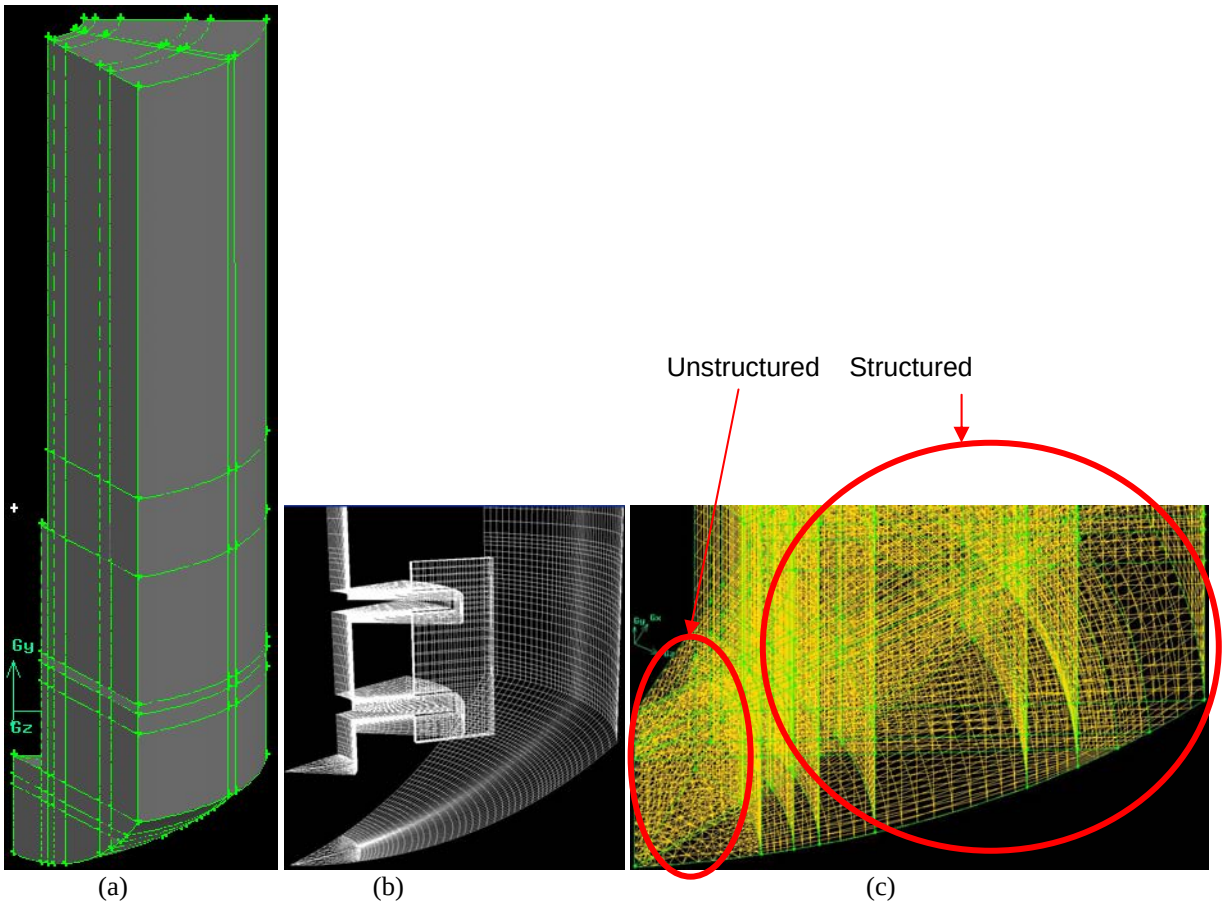

Figure 15: *Isometric views of (a) the solid section modeled (b) open view of the paddle wheel with the periodic faces removed (c) zoomed view of the lower region with the unstructured mesh.*

The steps comprising the mesh generation process are creation of nodes/vertices that define the geometry, joining the nodes to form edges, joining the edges to form surfaces and in the present simulations, due to the cylindrical shape of the reactor, by revolving the surfaces to form volumes. Following this process, meshing of the volume was accomplished by first generating a grid along the edges, followed with the faces and finally by extending the meshing process to accommodate the volumes. To simplify the grid generation process, the entire reactor was divided into smaller zones, which were then meshed individually. The mesh generated for the minireactor consisted of both structured and unstructured mesh elements. The bottom region of the cylinder could be meshed using either structured or unstructured grid elements. However, meshing the lowermost part of the container using a structured grid resulted in distortion of the geometry and an inaccurate representation of the hemi-spherical bottom. To avoid a drastic

change in the geometry of the model, an unstructured grid was used, which helped retain the near hemi-spherical shape of the bottom of the cylinder. Figure 15(a) shows the solid view of the modeled section. Figure 15(b) shows the open view of the paddle wheel with the mesh on the faces of the blades and the wall, while Figure 15(c) zooms in on the unstructured part of the geometry. The initial mesh that was generated consisted of approximately 2.25 million cells. The grid generation task was repeated in order to develop a coarser grid consisting of approximately 140,000 cells that enables relatively efficient simulations to be performed.

Mathematical Model

The mathematical model is based on an Eulerian-Eulerian approach in which the secondary phase (olivine) is treated as a continuum. The commercial flow solver Fluent was used to solve the mass conservation equation (Equation 1) and momentum equation (Equation 2) for each phase.

$$\frac{\partial}{\partial t}\left(\alpha_l \rho_l\right) + \nabla \cdot \left(\alpha_l \rho_l \vec{v}_l\right) = 0 \tag{1}$$

$$\frac{\partial}{\partial t}\left(\alpha_l \rho_l \vec{v}_l\right) + \nabla \cdot \left(\alpha_l \rho_l \vec{v}_l \vec{v}_l\right) = -\alpha_l \nabla p + \nabla \cdot \bar{\bar{\tau}}_l + \alpha_l \rho_l \vec{g} + \sum_{l=1}^{n}\left(K_{ls}\left(\vec{v}_l - \vec{v}_s\right)\right) \tag{2}$$

Here α_l represents the volume fraction of phase *l* (liquid phase), while the density is represented by ρ. $\vec{v}_l$ and $\vec{v}_s$ represent the velocity of liquid phase *l* and solids phase *s*, and the pressure which is uniform across all the phases is represented by *p*. $\bar{\bar{\tau}}_q$ represents the solids stress tensor, *g* represents the acceleration of gravity and K_{ls} accounts for the momentum transfer between the solids and liquids phase. The momentum equation governing the solid phase is analogous to the momentum equation for the liquid phase, wherein each term representing the liquid phase (*l*) is replaced with a corresponding solid phase term (*s*).

To obtain a solution of the momentum equations, the *k-ε* model was used.[13] Since the volume fraction of olivine used in the reactor is high, a discrete phase solution approach is employed in which separate equations are defined for each phase. In the present effort, the primary phase consists of an aqueous solution-CO_2 mixture and with olivine particles comprising the secondary phase. External forces such as virtual mass (which occurs when the particulate phase accelerates relative to the fluid phase) and lift forces (acting on particulate phase mainly due to velocity gradients in primary phase flow field) are neglected in the computations that have been performed to date. Solving equations 1 and 2 require several constitutive relationships. For example, a model proposed by Gidaspow[14-16] to model the interphase momentum transfer term is employed and takes the form,

$$K_{sl} = \frac{3}{4} C_D \frac{\alpha_s \alpha_l \left|\vec{v}_s - \vec{v}_l\right|}{d_s} \alpha_l^{-2.65},$$

where C_D represents the coefficient of drag and is related to the Reynolds number (Re_s) as:

$$C_D = \frac{24}{\alpha_l \,\mathrm{Re}_s}\left[1 + 0.15\left(\alpha_l \,\mathrm{Re}_s\right)^{0.687}\right].$$

An important term governing the motion of the particulates is the fluid-particle interaction force, which is expressed as a function of the relative velocity between the solids and the aqueous phase $\left|\vec{v}_s - \vec{v}_l\right|$.

Solution Procedure and Results

Following the grid generation step, the grid was imported into Fluent where flow properties were defined that model the aqueous solution-carbon dioxide mixture and olivine ore in the closed cylinder. To solve the partial differential equations summarized above, approximate initial and boundary conditions are needed for realistic simulations. The boundary values along the walls were set to represent a no-slip boundary condition and the boundary value for the impeller blades were set to represent an angular velocity corresponding to a shaft speed of 1500 rpm. Initially, the simulations were carried out for cases corresponding to steady state in the reactor (a representation corresponding to a long-time average of the state of the minireactor). Solution of the steady-state flow enables a computationally efficient view of the system. To obtain a steady-state solution, the simulation process for obtaining the flow solution was divided into two stages, the first stage was the solution of the flow for the aqueous phase/CO_2 fluid mixture (only), the converged solution of which forms the initial condition for the second stage in which the solids phase was incorporated. Ten grams of olivine, as used in the ASU experiments, was added to the bottom of the cylinder. The height to which the olivine settles when filled in the reactor was measured experimentally and this height was patched as the initial distribution of olivine in the model. In the simulations, the solids phase was initially prescribed at the bottom of the reactor vessel at the maximum permissible packing limit of 63%.

The NIST Chemistry web-book (http://webbook.nist.gov/chemistry/fluid/) was used as a reference to obtain values for density and viscosity of water and CO_2 for use in the simulations. Density values for the water-CO_2 mixture were obtained by taking an average of the densities of water and CO_2. Since the viscosity calculations do not follow the average rule, and since there are no known experimental values of viscosity of the aqueous mixture (of water and CO_2) under the specified temperature and pressure, the current simulations were performed using the viscosity of water at the elevated conditions (150 atm and 185^{o}C) as the viscosity of the aqueous phase/CO_2 fluid mixture. The simulations do not account for temperature variations in the mixture, i.e., an isothermal system is computed with the elevated temperature being reflected in the density and viscosity values of the mixture. Coupling between the fluid and solid phases is achieved using inter-phase momentum transfer terms that account for the momentum transfer between the granular olivine phase and the mixed-fluid phase formed by mixing water and CO_2. The paddle blades along with the central shaft rotate at 1500 rpm. This is accounted for in the simulations by sliding parts of the mesh around the blades through the remainder of the grid.

Initial simulations were performed using a time step of 1 second. Considering the rotational speed of the impeller in the reactor at 1500 rpm, a time step of 1 second corresponds to 25 revolutions or 9000 degrees. These initial studies were performed using this relatively large time

step in order to provide a preliminary assessment of the influence of particle size on the subsequent flow field solutions. The results obtained indicate that substantial differences exist in the phase distribution and velocity distribution patterns for different particle size fractions.

Following these initial computations, the simulations for the unsteady phase were performed using much smaller time steps in order to improve the temporal accuracy of the CFD model. The time-step used in the unsteady simulations correspond to a paddle wheel rotation of approximately 5 degrees per step. Numerical tests show that convergence of the system of equations occurs after approximately 25 iterations within each time step. Preliminary simulations performed with smaller time-steps (2 degrees per time step) did not yield significant changes in the results, justifying the time step corresponding to 5 degrees of revolution.

The simulations have been performed for two size fractions: a solids phase consisting of 37μ diameter particles and a second simulation using 150μm diameter particles. Simulations for a size fraction of 75μ diameter particles are being performed during the current no-cost extension period (the number of concurrent calculations is limited by a fixed number of licenses, we have invested in 4 additional licenses during the no-cost extension to enhance system evaluation.)

Steady state as well as time accurate solutions representing the flow field in the minireactor were obtained using first-order accurate discretization of the model equations. Using current resources, the time required to compute 1000 iterations of the multiphase solution is approximately 24 hours on a single processor AMD Athlon 64 bit 2.0GHz workstation equipped with 2 GB memory. Each iteration computes the values of flow variables in every cell of the domain. This process is continued until the difference in the values of the flow variables (residuals) between consecutive iterations is O(1e-6).

Figures 16(a) and 16(b) show the aqueous-phase velocity vectors in the steady-state solution for the single phase (aqueous mixture of water and CO_2 only) case. While Figure 16(a) shows the velocity vectors colored by the absolute velocity, Figure 16(b) shows the velocity vectors colored by the radial velocity. The figures show that the fluid velocities are largest in the vicinity of the paddle, as expected, given the entrainment and mixing produced by the paddle. In addition, a closer inspection of the figures shows that the vectors in different axial planes away from the paddle possess different orientations, indicative of mixing effects even at relatively larger distances from the paddle.

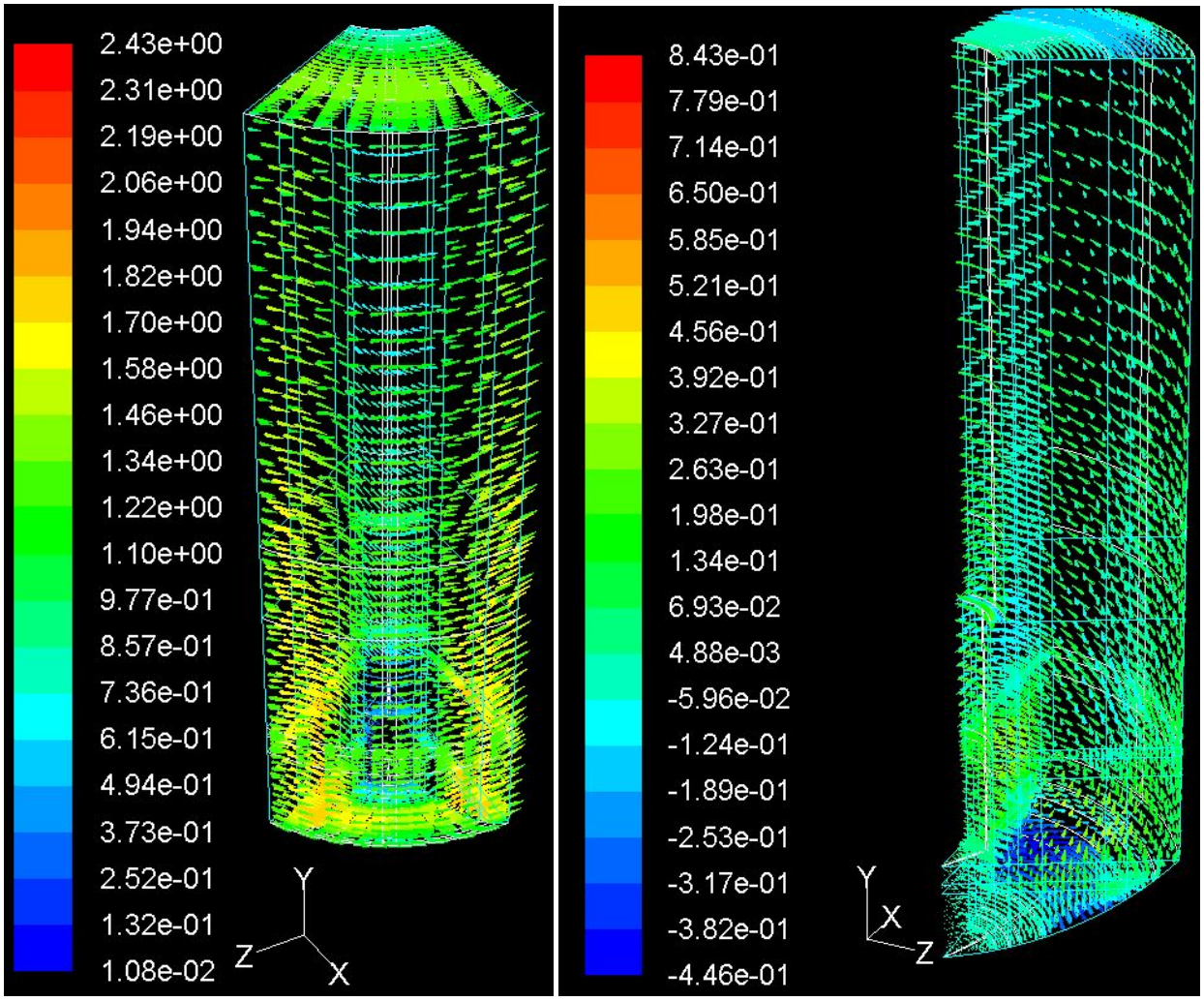

(a) (b)

Figure 16: *Aqueous-phase velocity vectors for the single phase flow, (a) shows the vectors colored by absolute velocity, (b) shows the vectors colored by radial velocity. The vectors indicated in (a) and (b) point counter-clockwise indicating the rotation existing in the cylinder due to the presence of the moving paddlewheel (units in m/s).*

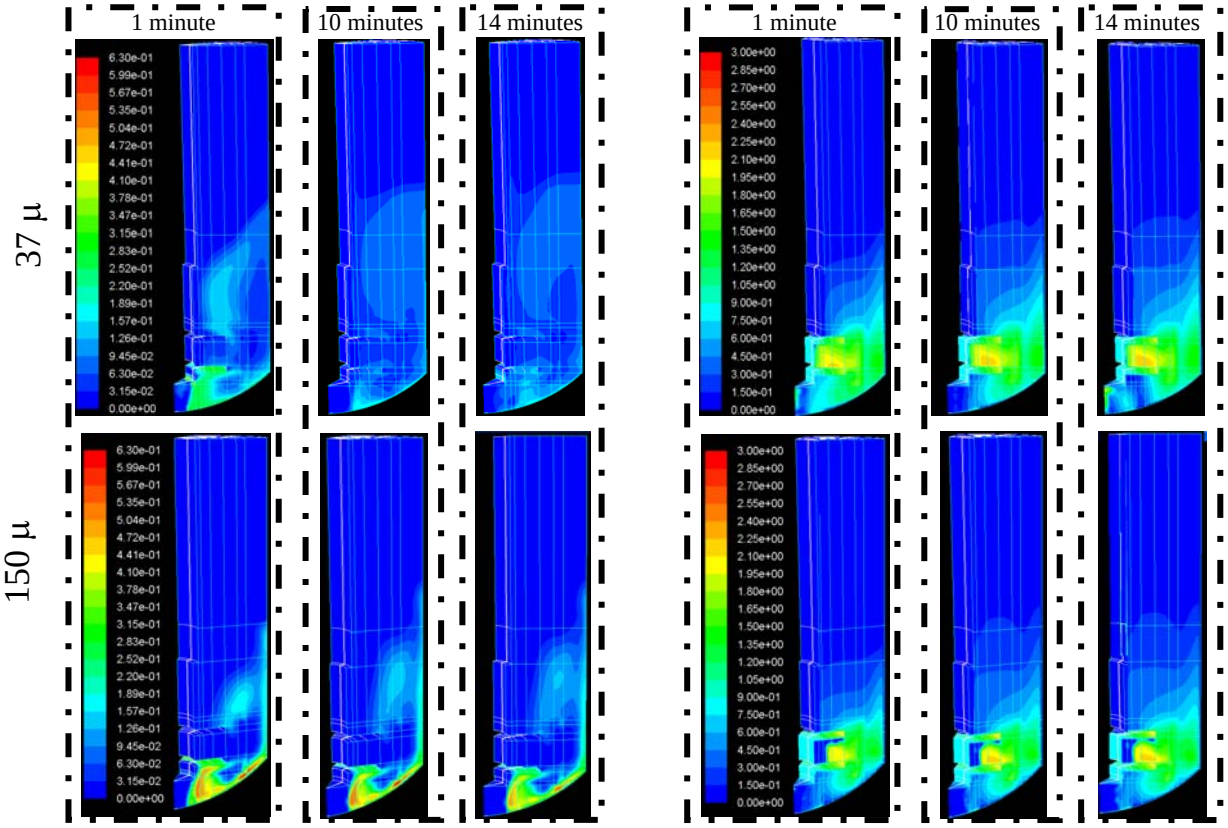

Figure 17: *Contours of (a) volume fraction of olivine, values in fraction, shown to the left (b) velocity distribution of olivine, using larger time step value (dt = 1 second), values in m/s, shown to the right.*

Figure 17 shows contours of the olivine volume fraction distribution for the 37μ case and the 150μ case for time intervals corresponding to t=1, 10 and 14 minutes from the start of the paddle-wheel rotation. A clear demarcation can be observed in the contours, red indicating higher values and blue indicating lowering values of volume fraction. The figure shows that the olivine volume fraction for the 150μ runs exhibits a substantially higher concentration at the bottom of the cylinder and that the contours for the 37μ run correspond to smaller gradients indicative of a substantially greater mixing of the particles with the fluid mixture. This is expected because lighter particles with lower inertia are more susceptible to follow the fluid flow patterns. Larger particles on the other hand behave in a manner that is consistent with their higher inertia. Figure 17(b) shows contours of the particle velocity distribution for the corresponding cases for the same time intervals. Higher velocity is observed near the vicinity of the paddle wheel due to the rotation. The contour profiles indicate the swirling movement of the olivine particles, which are shown to gradually rise toward the top of the reactor, from their initial location at the reactor bottom.

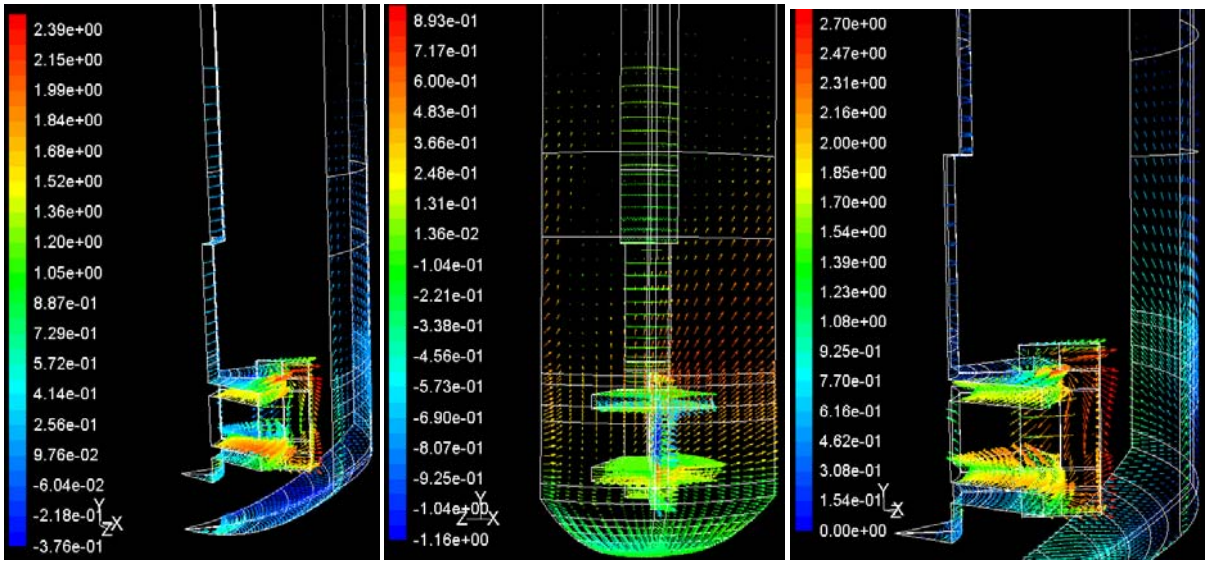

(a) (b) (c)

Figure 18: *Contours of velocity of olivine after t=2 seconds in the reactor colored by (a) x-velocity component, (b) y-velocity component, (c) relative velocity magnitude, values in m/s. (37μm case and time step of 5.56e-4 seconds)*

Phase distribution patterns for the large time step case indicate that substantial differences do exist for the particle behavior of each size fraction. To obtain more accurate results, the time step for each calculation was reduced from 1 second (corresponding to 9000 degrees of revolution) to dt=5.56e-4 seconds (corresponding to 5 degrees of revolution). Figure 18 displays the velocity vectors of olivine within the reactor for simulations corresponding to a time step of 5.56e-4 seconds. The magnitude of the individual velocity components are observed to be as high as 2.39 m/s within the reactor, as seen in Figure 18a. Rough estimates indicate that two olivine particles approximately 15μm in diameter colliding each other at 1 m/s can cause a fracture. Velocity vectors indicate that the paddle wheel causes the olivine particles to accelerate to speeds of up to approximately 2.4 m/s. Olivine particles impinging on each other and with the reactor walls or paddle blades with those high velocities are highly susceptible to fracture. This can be contribute as one of the possible mechanisms that cause a reduction in particle size during carbonation within the reactor. Also, velocity vectors in Figure 18(a) indicate a negative velocity at the hemi-spherical bottom of the reactor, while positive velocities are found in regions at the center of the paddle wheel. This velocity pattern indicates entrainment of the particles towards the center in region below the paddle wheel, while the particles are thrown towards the wall in the region near the paddle wheel center. Similarly, velocity vectors indicate that particles are entrained towards the central shaft in the region above the paddle wheel. This indicates two swirling motions, one counter-clockwise and one clockwise in regions above and below the paddle wheel respectively. Figure 18b shows the y-velocity component of the olivine particles. At the wall of the reactor vessel, the velocity vectors are directed upwards, which indicates olivine particles being pushed to the top section of the reactor. Furthermore, in the zone near the axially located shaft, the y-velocity vectors are negative, which indicate the swirling motion of the particles from bottom to the top at the wall and from the top to the bottom at the axially mounted shaft. However, the results shown above indicate the distribution at t=2

seconds and these simulations need to progress further in time to determine the time dependence on the distribution of olivine particles. Figure 18c shows the relative velocity of olivine within the reactor. The relative velocity is observed to be as high as 2.7 m/s and, as mentioned before, this velocity is sufficiently high enough to cause particle fracture on impact.

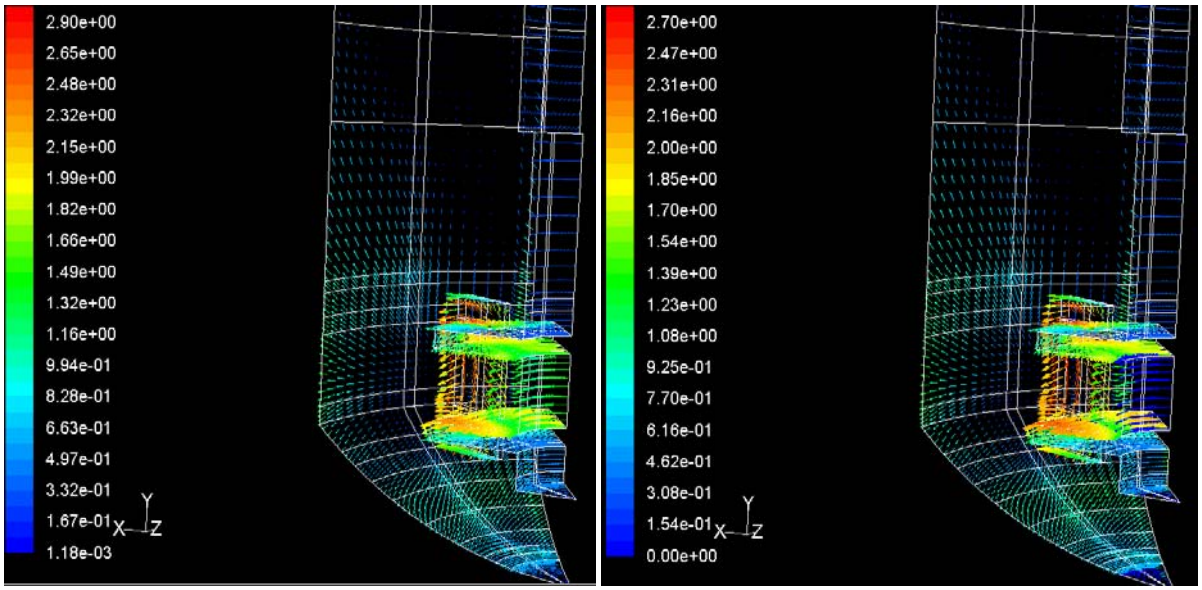

(a) (b)

Figure 19: *Absolute velocity vectors of (a) water and (b) olivine at t=2 seconds for 37μm case, values in m/s (dt=5.56e-4 seconds)*

Figures 19(a) and 19(b) indicate the vectors of absolute velocity of water-CO_2 aqueous mixture and olivine respectively within the reactor at t=2 seconds for the 37μ case. An interesting observation here is the difference in velocity magnitude of the olivine particles and the water-CO_2 mixture. The velocity profile of olivine follows the velocity profile of water closely; however, the velocity magnitude of olivine particles are observed to lag the corresponding values for the water-CO_2 mixture. It however remains to be seen if this effect is reflected in the 150μ case where the particle inertia is higher than the 37μ particles. Simulations are currently in progress for the 150μ case. During the first project year they have not yet progressed sufficiently in time to make a similar comparison.

37mu_phase_distro.wmv

Movie 1: *Movie depicting movement of the olivine phase in the ASU minireactor for the 37μ case (Double click to start). Contour values (in fraction) dynamically change as time progresses.*

Volume fraction distribution of the 37μ particles for 0.84 seconds of paddle wheel rotation (corresponding to 21 revolutions) is presented as a movie file (Movie 1). The movie file highlights the motion of the olivine phase when subjected to the agitation imposed by the impeller. This movie was generated by taking snapshots of volume fractions as the simulations progress at different time intervals. These snapshots were then combined to generate a movie

file. Generally throughout the simulation, the rotation of the paddle causes movement of the olivine particles within the reactor. These olivine particles are then forced upwards due to the high speed of the paddle blades, which causes a swirling motion within the reactor. As the olivine is dispersed throughout the reactor, the initial volume packing fraction of 63% reduces dramatically. This reduction is relatively gradual in its initial stages and the effect is seen on the level which is displayed as a color bar on the left. A swirling motion is observed and this is consistent with the velocity vector plots shown in Figures 18a-c.

Generally throughout the simulation, the rotation of the paddle causes gradual movement of the olivine particles along the direction of the paddle rotation. These olivine particles are then carried upwards entrained in the fluid flow associated with the high speed of the paddle blades, which also induces a swirling motion within the reactor, as observed in Movie 1. Analysis of the structural features of the flow in the minireactor as well as the statistics associated with the olivine volume fraction and velocity distributions for the different size fractions are of key interest for enhancing particle abrasion, passivating layer exfoliation and mineral carbonation. The objective is to engineer cost-effective reaction flow dynamics that enhance particle abrasion via particle-particle and particle-vessel interactions, which in turn enhance passivating layer exfoliation and carbonation.

During the no-cost extension, we are continuing to carry out simulations using much smaller time steps than in the initial runs, time steps that correspond to a paddle wheel rotation of approximately 5 degrees per step. To shorten the associated computational time required to complete the analysis, we have purchased three additional licenses for the Fluent code to be utilized during the no-cost extension period. To verify the accuracy of these simulations, we are currently constructing a transparent plexiglass reaction vessel for the minireactor to perform experiments using water-olivine slurries at ambient temperature and pressure and 1500 rpm stirring. Visualizations of the slurries will be compared to the flow dynamics predicted by the CFD model to further assess the model's validity.

Scientific Progress: Investigation of the Potential that Sonication Offers to Enhance Exfoliation and Carbonation

As during the first year investigations, the second year sonication experiments were carried out by stopping the standard mineral carbonation reaction after a half hour, introducing a brief sonication period, and following with a second half-hour exposure to the standard aqueous mineral carbonation process. The overall carbonation reaction conditions remained the same as the standard carbonation conditions throughout the two half-hour mineral carbonation steps. Extent of carbonation runs that mimic the sonication runs, but without the intermediate sonication exposure, were again used for baseline comparison. In each case 10 or 20 g of <38μ or <75μ San Carlos olivine was mixed with 50ml or 75ml of the standard aqueous solution (1M NaCl + 0.64 M $NaHCO_3$) and added to the batch reaction system. After 30 min of stirred reaction under the standard conditions, the reaction was stopped and rapidly cooled by using the internal cooling coil and placing the reaction vessel in ice water. This results in the temperature dropping to ~40°C within 10 minutes. After cooling is complete, the system is depressurized and the batch reaction stirring system is replaced with the sonication system (Figure 20). The system

is purged with CO_2 and subsequently brought to the starting sonication temperature and pressure. Once at temperature and pressure, sonication is then run for controlled periods of time. Once sonication is done, the vessel rapidly cooled in ice water and then depressurized. The vessel containing the reaction mixture is next reattached to the batch reaction system and the second half-hour carbonation step is performed.

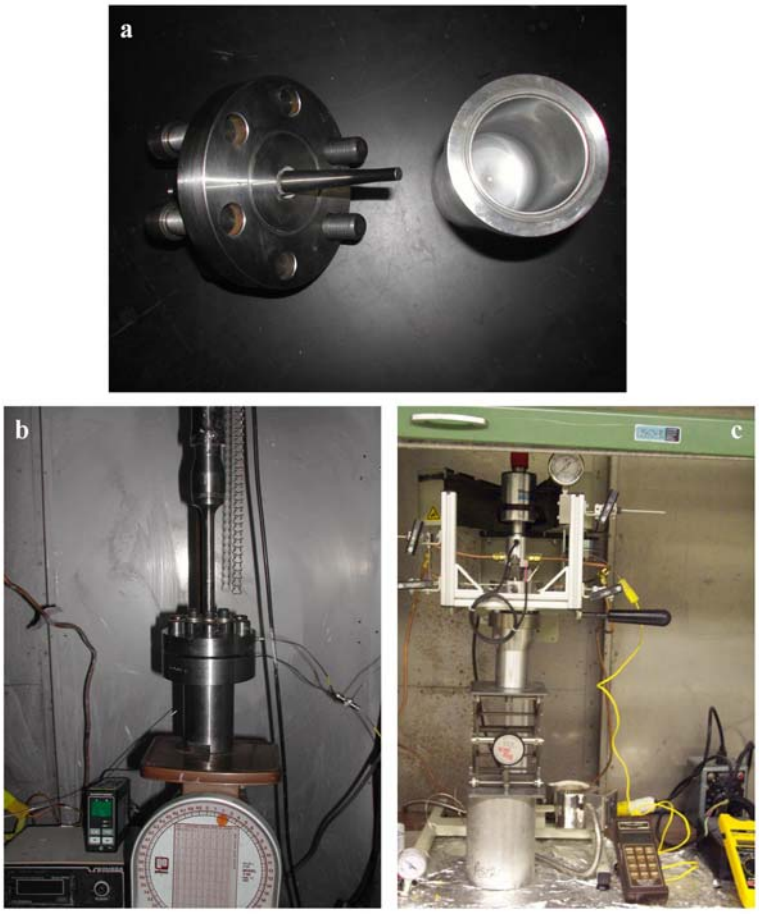

Figure 20: *The sonication and batch reaction systems at Arizona State University: (a) The sonication probe and reaction vessel; (b) the reaction vessel sealed to its sonication assembly; (c) the same reaction vessel shown in a and b sealed to the batch reactor stirring assembly.*

During the first project year, the effects of full-power sonication on the extent of carbonation were explored as a function of sonication time, temperature and pressure (1 to 10 minutes; 20 to 185 ^{o}C; 15 to 2,200 psi CO_2) . Under none of the conditions investigated did the sonication process enhance carbonation. Given that the extent of carbonation varies by as much as ±5% for the same reaction conditions in these studies, the results suggest that sonication may even inhibit carbonation. This suggests that full-power (1500 watt) sonication may significantly reduce carbonation.

During the second project year, the effects of sonication on the extent of carbonation were explored at reduced power, as the full-power investigations carried out during the first year did not show any indication that full-power sonication could enhance carbonation, let alone enhance

it cost effectively. Studies were carried out as a function of the weight % olivine present, the olivine particle-size distribution, the volume fraction of the aqueous solution present, and sonication power, time, temperature, and CO_2 pressure. Representative results are shown in Table 1 below. None of the conditions investigated to date have significantly enhanced carbonation. Indeed, many of the conditions employed appear to inhibit carbonation. As sonication is relatively costly (energy intensive) compared with the other two approaches being investigated (aqueous chemistry and slurry-flow control) and has not shown promise for low-cost enhancement of carbonation, the other two approaches will be primarily explored during the no-cost extension period.

Table 1: Effect of Sonication on the Extent of San Carlos Olivine Carbonation

Exp #	Particle Size	Mass (g) Olivine	Sonication Conditions	*Extent of carbonation**
303	<38μ	10	1min, 185 °C, 2200psi CO_2, 40% power	**8.16**
304	<38μ	10	no sonication	**31.14**
305	<38μ	10	1min, 100 °C, 2200psi CO_2, 40% power	**9.20**
306	<38μ	10	1min, 100 °C, 900psi CO_2, 40% power	**10.39**
307	<38μ	10	1min, 100 °C, 900psi CO_2, 30% power	**13.55**
308	<75μ	10	1min, 100 °C, 900psi CO_2, 40% power	**4.40**
309	<38μ	20	1min, 100 °C, 900psi CO_2, 40% power	**29.08**
310	<38μ	10	5min, 100 °C, 900psi CO_2, 40% power	**22.19**
311	<38μ	10	1min, 100 °C, 900psi CO_2, 40% power	**18.48**
312	<38μ	10	1min, 20 °C, 900psi CO_2, 40% power	**32.91**

* The carbonation reaction conditions are: standard solution of 0.64M $NaHCO_3$ + 1.00M NaCl for ½ hour at 185 °C, 2200psi CO_2 and stirring at ~1500rpm using 50ml of aqueous solution. The only difference is for #311, which used 75ml, instead of 50ml of aqueous solution for both the carbonation and sonication steps. In each case, carbonation is carried out for 30 minutes before and after the above sonication exposures. The run that did not incorporate sonication (#304) replicated the two 30-minute carbonation runs for each of the sonication runs, including the cooling and depressurization cycles between the two 30-minute carbonation runs.

Figure 21 shows typical field emission scanning electron microscopy (FESEM) secondary electron images of partially reacted olivine particles after the three primary stages of the sonication process: after ½ carbonation, after ½ hour of carbonation followed by sonication, and after ½ hour of carbonation, sonication and a second ½ hour of carbonation. Interestingly, all the particle surfaces show similar surface bound silica-rich passivating layers and magnesite crystals for the particles observed, indicating that sonication is not effective at enhancing passivating-layer exfoliation or breaking the olivine feedstock into smaller olivine particles. Why sonication appears to inhibit carbonation in many cases is not well understood and is being investigated during the no-cost extension.

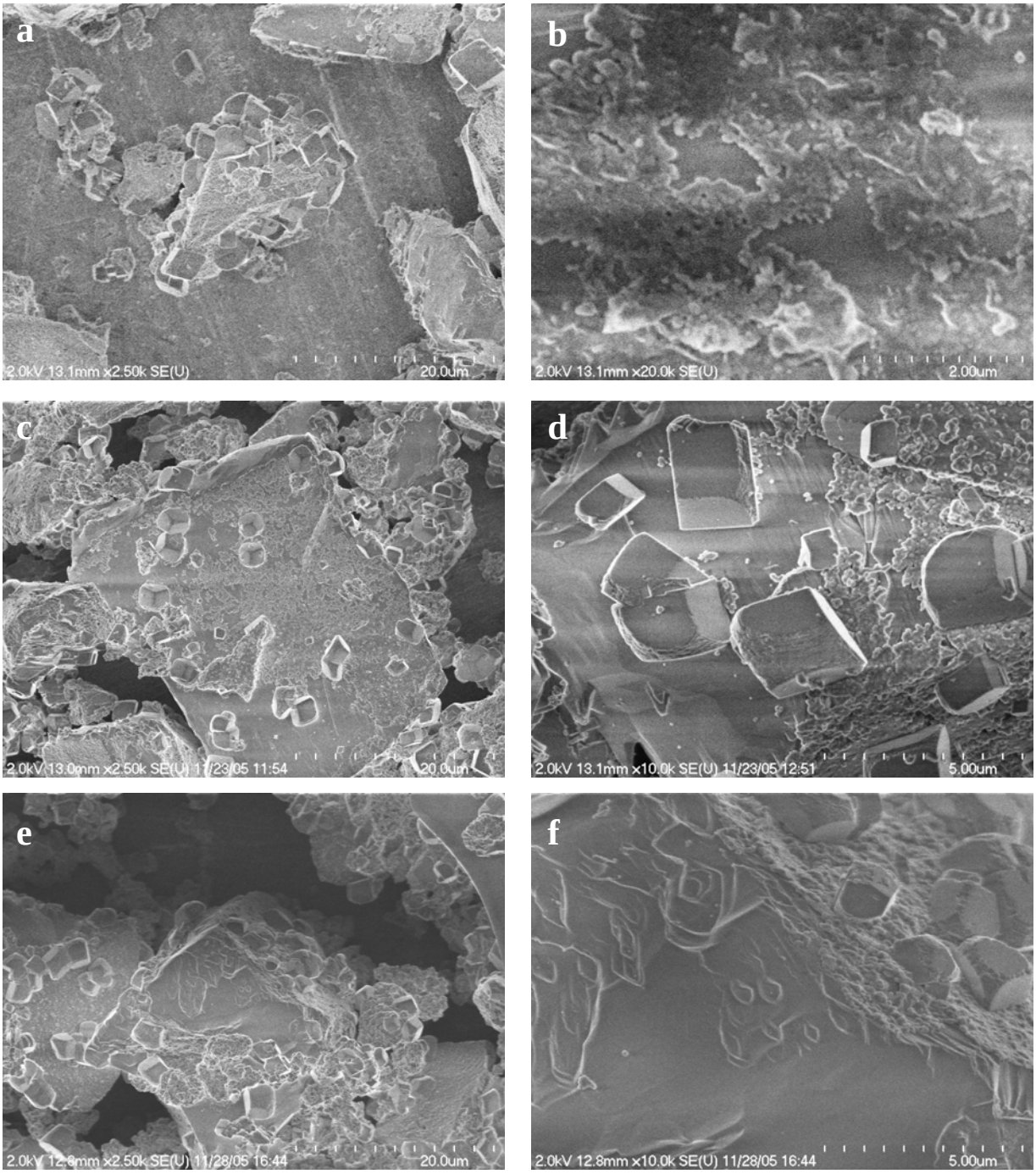

Figure 21: *Field emission scanning electron microscopy secondary electron images showing the surface morphology of the partially reacted/carbonated olivine grains: (a) & (b) after ½ h carbonation, but before sonication; (c) & (d) after ½ h carbonation and one minute of sonication at ambient temperature under 15 psi CO_2 ; (e) & (f) after ½ h reaction/carbonation, one minute of sonication at ambient temperature under 15 psi CO_2,, and a second ½ hour of reaction/carbonation under the standard conditions.*

Scientific Progress: Understanding the Mechanisms that Control Passivating Layer Formation and the Impact the Above Approaches Have on Exfoliation and Carbonation Mechanisms

During the second project year, we have evaluated the effectiveness of a variety of reaction flow dynamics, alkali cation solution chemistry, and sonication approaches to enhance carbonation. These studies have involved carbon elemental analysis and X-ray powder diffraction of many scores of product samples. The primary objective is to identify those approaches that are most effective in enhancing carbonation. Our mechanistic investigations have substantially focused on enhancing our understanding of passivation layer structure, composition and behavior. The objective is to enhance our fundamental understanding of the passivating-layer formation, growth and exfoliation process, while we are exploring in parallel the impact that reaction flow dynamics, alkali cation solution chemistry, and sonication have on exfoliation/carbonation. During the no-cost extension, we will explore the impact that the approaches that are identified as being most effective in enhancing carbonation have on the mechanisms that govern passivation layer formation, properties, exfoliation, and carbonation reactivity. Substantial progress has been made in enhancing our understanding of passivating layer formation processes during the second project year. A substantial amount of our progress during the first and second project years is summarized in our recent publication of a comprehensive paper describing the silica-rich passivating-layer formation, growth, and exfoliation processes that accompany olivine mineral carbonation. This article emphasizes our mechanistic observations associated with stirred carbonation. As a copy of this article is included in Appendix A,[17] the associated progress will not be repeated here. Additional studies carried out during the second project year are described below.

Overview of the feedstock incorporated: Olivine forms a solid solution series between its end members forsterite (Mg_2SiO_4) and fayalite (Fe_2SiO_4), with naturally occurring olivine generally richer in magnesium.[18] It adopts an orthorhombic structure, with Mg and Fe interchangeably occupying the same lattice sites. The cell parameters generally increase with increasing Fe content, exhibiting Vegard-like behavior between the forsterite and fayalite end members (e.g., Mg_2SiO_4: a = 4.76Å, b = 10.20Å, and c = 5.98Å; Fe_2SiO_4: a = 4.82Å, b = 10.48Å, c = 6.11Å).[18] The single crystal San Carlos olivine fragments used in the following investigation of the mechanisms that control carbonation at the aqueous solution/olivine reaction interface contain ~8.5% Fe - $(Mg_{0.915}Fe_{0.085})_2SiO_4$.

Mechanistic Observations Associated with the Static Aqueous Carbonation Process. Investigation of passivating-layer formation and growth processes under static, rather than stirred, conditions offer the opportunity to explore the formation and growth behavior in the absence of particle abrasion and passivating-layer exfoliation. Our mechanistic observations associated with the stirred aqueous mineral carbonation process indicated that a silica-rich passivating layer forms on the olivine surface during carbonation. FESEM imaging, energy-dispersive X-ray analysis, X-ray diffraction analysis, elemental analysis and auxiliary techniques identified the olivine carbonation reaction products as amorphous silica and magnesium carbonate, along with residual unreacted olivine and established the extent of the reaction. However, the character of the reaction interface and the passivating-layer formation process were clouded by particle abrasion that is inherent in the rapidly stirred carbonation process. In order to gain greater insight into the passivating-layer formation and growth process, we

undertook experiments using oriented single crystal San Carlos olivine specimens in the standard carbonation environment applied by the Albany Research Center (aqueous solution containing 1.00M NaCl and 0.64M $NaHCO_3$ at 185 ^oC under 2,200 psi CO_2 pressure), but without stirring in order to preserve the passivating layer and the associated reaction interfaces that form. We then examined the passivating layers and the reaction interfaces using various high resolution electron microscopy (HREM) methods, secondary ion mass spectroscopy (SIMS), and auxiliary methods.

High-resolution transmission electron microscopy (HRTEM) results, some of which were reported earlier, showed that a silica-rich amorphous reaction layer, referred to herein as a passivation layer, had formed on the olivine surface during the carbonation reaction under the conditions noted above. A HRTEM image of the passivating-layer/olivine particle core interface region is shown in Figure 22. The passivating layers observed routinely contain a dispersion of magnesium carbonate nanocrystals, which have been identified as $MgCO_3$ (magnesite) by image analysis and Fourier nanodiffraction, as discussed in our first year progress report. The subsequent application of Fresnel and STEM annular dark field imaging methods during the second year of the project did not identify additional chemical or structural heterogeneitities in the passivating layer, and in particular, in the passivating-layer/olivine interface region. Interestingly, the intervening equilibrium phase between SiO_2 and forsterite is enstatite, but this phase was not observed providing further support that magnesium dissolution and carbonation results in direct silica formation. Apparently, the CO_2 that results in the high CO_2 activity in the aqueous solution also penetrates the silica-rich passivating layers that form, leading to the formation of magnesite within, as well as external to the passivating layers.

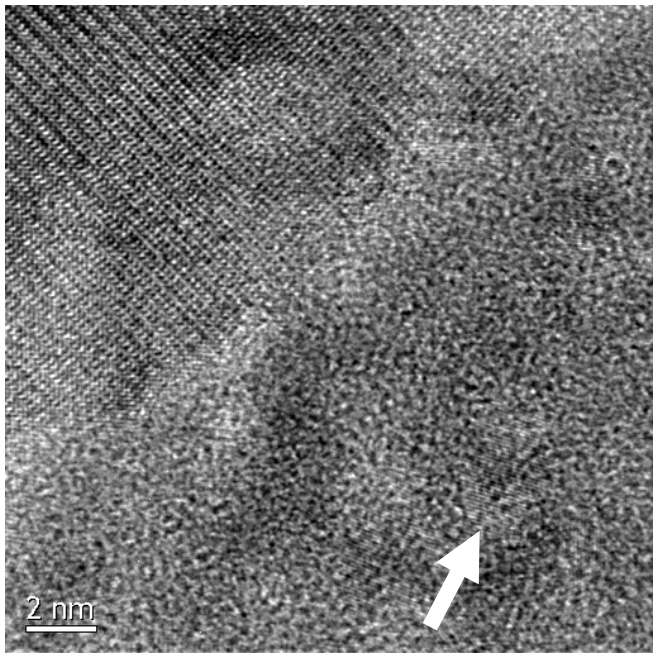

Figure 22: *HRTEM cross section image of the well-bonded interface between olivine and the passivating layer, (4h carbonation at 185 ^oC under 2,200 psi CO_2). The host olivine is at the upper left. The passivating layer is ~40 nm thick. The arrow on the image points to a typical $MgCO_3$ nanocrystal in the amorphous passivating layer matrix.*

HRTEM methods were used to determine how broadly applicable our first year observation that the $MgCO_3$ volume fraction in the passivating layer was about 13% is. An average of 14% was observed for various specimens/regions during the second year. Electron energy loss spectroscopy was then incorporated to determine the low loss peak energy of the passivating layer, which was 23±1 eV in good agreement with the value for SiO_2;[19] core edge analysis indicated that the O/Si ratio was slightly less than 2, confirming the carbonation reaction of interest both at the reaction interface and overall can be best described as:

$$Mg_2SiO_4 + 2CO_2 = SiO_2 \bullet 2MgO + 2CO_2 = SiO_2 + 2MgCO_3 \qquad (2)$$

Using reaction 2 and the known molar volumes of the products and reactants, which are 43.6, 28.0, and 26 cc/mol for olivine, $MgCO_3$, and amorphous SiO_2, respectively,[20] the calculated expected volume fraction $MgCO_3$ in the reaction product layer is ~ 67%, which is far greater than the amount observed. The balance of the magnesite was found to reside in the trace reaction residue that was found at the bottom of the reactor. Post-reaction X-ray diffraction and elemental (PIXE) analysis of the residue collected from the bottom of the reaction pressure vessel showed the presence of magnesite, smaller amounts of amorphous SiO_2, and still less olivine, confirming the conclusion that most of the $MgCO_3$ formed external to the passivating layer itself. $MgCO_3$ nanocrystals were never observed in the olivine itself, indicating that CO_2 penetrates the passivating layer up to, but not beyond, the passivating-layer/olivine reaction interface during carbonation. This is consistent with a relatively high concentration of $Mg^{2+}$and O^{2-} forming near the interface, which is available to react with the in-diffusing CO_2 to form the $MgCO_3$ nanocrystals observed. The relatively low concentration of $MgCO_3$ nanoparticles in the passivating layer indicates that they nucleate inhomogeneously; however, the character of the preferred nucleation sites is not clear at present.

As discovered in the first project year, the olivine surface reacted under static conditions exhibits a silica-rich sponge-like morphology, as shown in the left of Figure 23. Sonication of the as-reacted surface in aqueous media exposes the underlying cracked silica-rich surface morphology shown in the right of Figure 23. Energy dispersive x-ray spectroscopy showed that the passivating-layer regions for both unsonicated and sonicated specimens were silica rich, while the areas at the bottom of the fractures in the sonicated passivating layers corresponded to olivine. Although the former result is not quantitative, as the incident electron beam penetrated through the passivating layer and the x-ray emission volume included regions of passivating layer and the underlying olivine, qualitative observations from multiple samples have clearly established that the passivating layers seen in Figure 23 are silica-rich, in agreement with the above analytical HRTEM observations.

The complex morphology of the curled-up silica-rich surface structure of the passivating layer shown in the left of Figure 23 is not entirely due to the stress system developed in the near-surface region of the specimen, which is discussed below. Part of this morphology is also due to the solubility of SiO_2 in neutral to slightly acidic water with a pH very similar to the aqueous solution incorporated herein (pH ~ 6.85; See Appendix A).[17] Several investigators have shown that small amounts of amorphous SiO_2 will dissolve in neutral to slightly acidic water,[21,22] and the presence of aqueous NaCl can enhance the dissolution kinetics.[23]

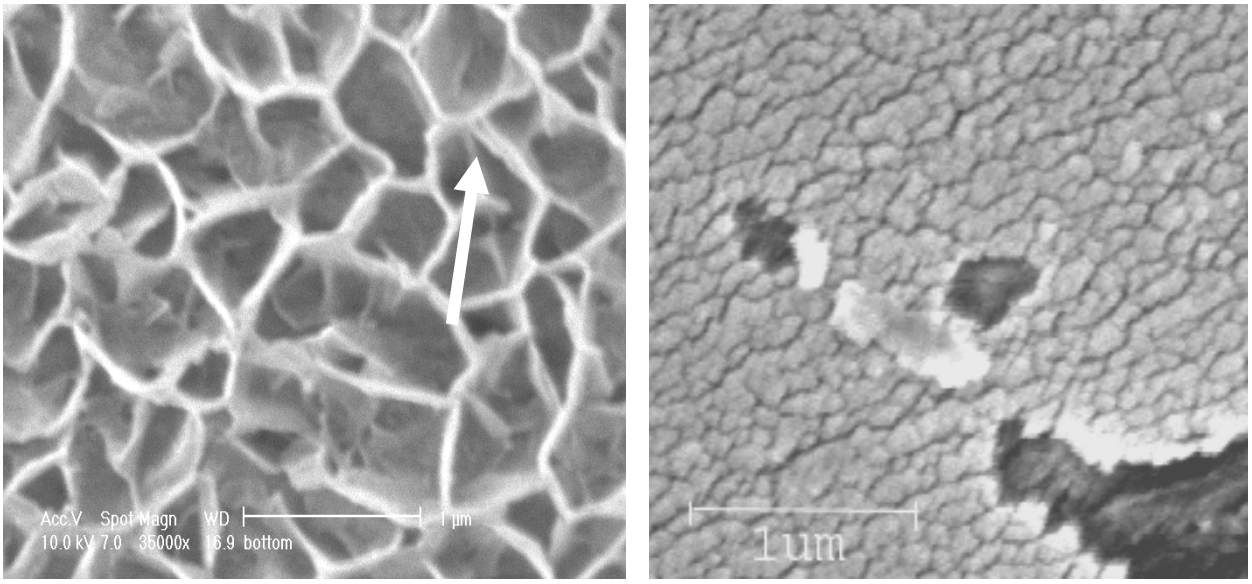

Figure 23: *FESEM images (secondary electron) of the olivine surface after reaction for 4 hours at 185 ^{o}C under 2,200 psi CO_2. The left image, recorded before sonication, shows the sponge-like character of the silica-rich passivating layer that has curled up/grown away from the olivine reaction interface. One region where two curled up pieces are separated by a narrow crack is highlighted by the arrow. The right image, after sonication, shows that the curled passivating-layer structure is removed by sonication to reveal the underlying fractured, silica-rich island-like structure shown. Some of the silica-rich islands have broken away from the surface to reveal the underlying olivine- rich crystal core.*

Hence, the amorphous silica that forms during carbonation can exhibit significant mobility via the aqueous phase and be transported via dissolution-precipitation.

The possible role of hydrogen/water within the passivating layers during carbonation is of substantial interest, as proton/Mg^{2+} exchange may occur with water formation near the olivine/passivating-layer interface during olivine dissolution/carbonation. Several investigators have shown that small amounts of water molecules can dissolve and diffuse in SiO_2, forming SiOH groups in the process. The possible sites for such silanol formation are associated with dangling silicon or oxygen bonds in the network or on glass surfaces. For example, SiOH has been shown to form easily at dangling bonds on amorphous silica fracture surfaces.[24] There are several possible locations for high concentrations of dangling bonds in the passivating-layer/interface regions during carbonation, including free surfaces, vertical cracks that penetrate the passivating layer, and within the passivating layer itself, through which the aqueous carbonation species can diffuse.

In order to better understand the potential roles that $2H^{+}/Mg^{2+}$ exchange and water diffusion play during passivating-layer formation and carbonation, we explored the passivating-layer/olivine surface reaction region using O^{+} SIMS profiling. An example of the results for a sonicated passivating-layer reaction surface are shown in Figure 24. A layer of Si was deposited by e-beam

evaporation under UHV prior to SIMS analysis of the surface, to establish a steady state SIMS profiling rate before beginning to analyze the passivating-layer region. The initial rise of the Si curve is due to the Si cap layer. Analysis of the surface of the passivating layer begins at the left side of the slat Si maximum. Note that the H curve exhibits a maximum at the beginning of the passivating layer, and then a secondary maximum near the passivating-layer/olivine interface. The position of the interface is defined by the steep rise of the Mg curve and the drop in the Si curve from its value in the passivating layer to its lower value in the olivine matrix. The moderate slopes of these curves result from oxygen ion beam induced mixing during the experiment, which is a common feature of any sputter depth profiling procedure. The two most important conclusions to be drawn from our SIMS results are that hydrogen did diffuse through the passivating layer during carbonation, and the resulting hydrogen distribution, likely associated with SiOH formation, is enhanced near the passivating-layer surface and the passivating-layer/olivine interface. Hydrogen diffusion through the passivating layer during carbonation is consistent with proton/Mg^{2+} exchange occurring near the olivine/passivating-layer interface during olivine dissolution/carbonation. It is also probable that SiOH groups form on the vertical crack surfaces associated with the passivating-layer, as shown in the right side of Figure 23. Future studies are planned using a sputter-deposited gold capping layer to more quantitatively resolve the composition of the near-surface region of the passivating layer.

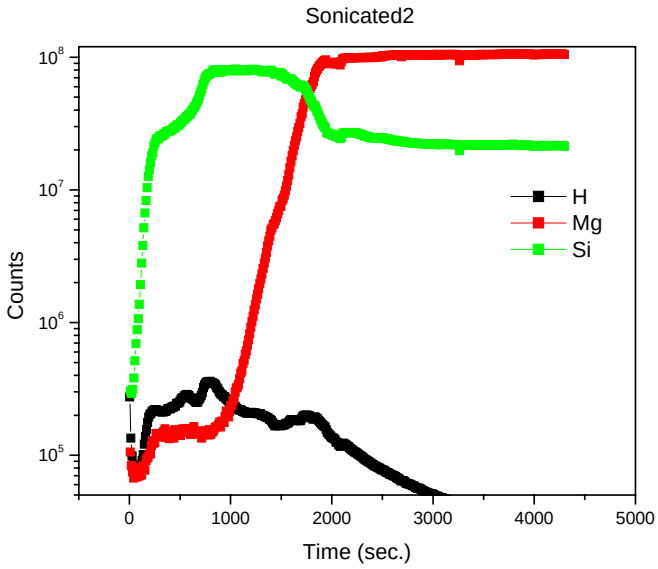

Figure 24: *SIMS depth profiles for H, Mg and Si for the surface of a sonicated passivating-layer region of a sample after a 4 h static reaction. The free surface is at left, and the olivine substrate is at right.*

The strains responsible for the cracking and exfoliation of the passivating layers are due to transformation strains that occur when the olivine rejects Mg and O during its transformation to amorphous SiO_2. From the molar volumes summarized as a function of magnesite content within the passivating layers in Table 2, it is clear that the passivating layers that form are in a state of biaxial tension. The calculated stress is quite large because the molar volume difference between

Table 2: Molar Volume of the Passivating Layer Region (Products) Compared to Host Olivine (Reactants) as a Function of the Volume of Magnesite Nanocrystals within the Passivating Layer.

%$MgCO_3$ In layer	V(products) / V(reactants)	Strain State of layer	$MgCO_3$ % Volume in layer
100%	1.91	*compression*	67%
90%	1.78	*compression*	65%
80%	1.65	*compression*	62%
70%	1.52	*compression*	59%
60%	1.39	*compression*	55%
50%	1.26	*compression*	51%
40%	1.13	*compression*	45%
30%	1.01	*compression*	38%
20%	0.88	*tension*	29%
10%	0.75	*tension*	17%*
0%	0.62	*tension*	0%

* HRTEM

olivine and SiO_2 is large; the presence of the small $MgCO_3$ particles observed via HRTEM only partially offsets the induced stress as their volume fraction is relatively small. Most of the passivating layer "islands" observed between the vertical cracks, easily visible in the right of Figure 23, are strongly bonded to the olivine substrate, as shown by the images of their interfaces (e.g., Figure 22). The bond at these interfaces creates a strain gradient in the passivating layer, from the olivine interface up to the free surface. The strain gradient induces shear stresses and normal, peeling, stresses at the interface between the olivine and the passivating layer. These are similar to misfit stresses between a thin film and its substrate induced by differential thermal contraction, when a film/substrate combination is cooled from its deposition temperature.[25,26] However, in the present case the stresses are associated with the transformation strain induced by the differences in molar volume, not differential thermal contraction, which, in turn drive the passivating-layer cracking/exfoliation process.

A model that is consistent with the passivating-layer cracking process is shown in Figure 25. Initially the passivating layer forms as a thin film on the olivine single crystal surface. As it thickens, biaxial tensile stress causes cracks through the layer. Then bending moments and interface shears can lead to exfoliation and detachment. As these events occur, new secondary passivating-layer formation can begin associated with the newly exposed olivine surfaces. The presence of water-induced silanol formation may impact the fracture/exfoliation process, as silanol groups are thought to reduce the surface energy of Griffith cracks in glass by forming at crack tips as they propagate.[27,28] This should enhance the fracture/exfoliation process under our experimental conditions. It is important to note the large relief of the unsonicated silica-rich passivating layer structure in the left of Figure 23. Such high features are not possible via passivating layer bending away from the olivine interface alone. Indeed, it appears that silica

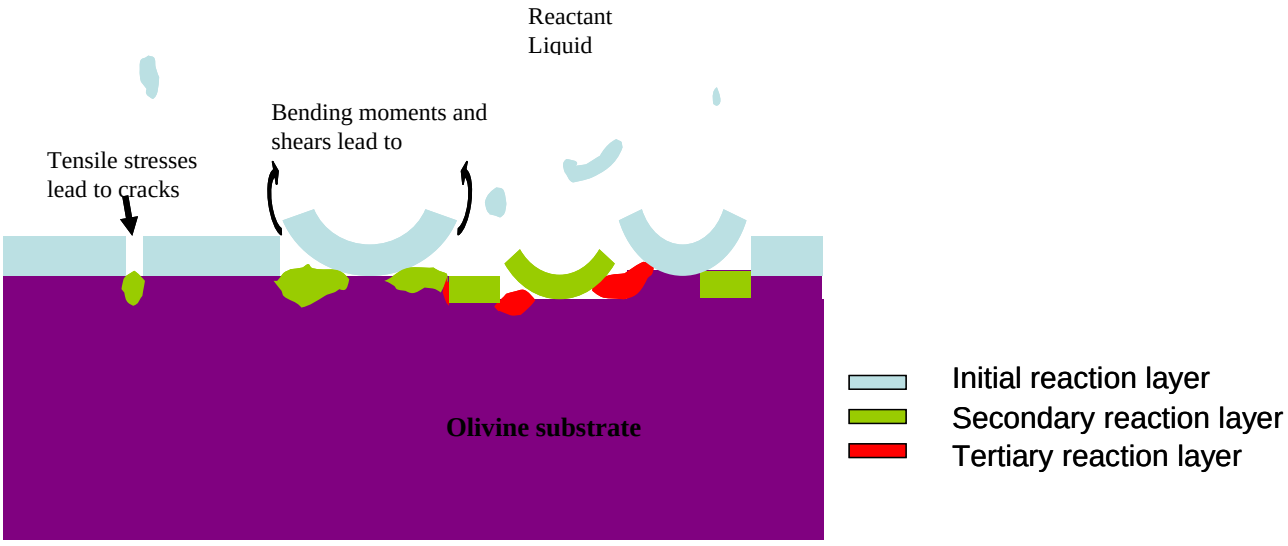

Figure 25: *A possible model of the passivating layer formation and fracture process, which is combination with silica dissolution/precipitation, may lead to the silica-rich passivating-layer surface features observed in the left of Figure 23.*

dissolution/precipitation plays a significant role in the passivating layer formation and growth process observed under static reaction conditions. Close examination of the surface structures in the left of Figure 23 are consistent with (1) silica dissolution being able to occur at the base of and along passivating-layer cracks that extend to the olivine interface and (2) silica precipitating along the vertical silica-rich passivating layer structure as it diffuses away from the passivating-layer/olivine interface. Such a process allows for the growth of silica-rich structures away from the interface, as observed in the left of Figure 23.

Scientific Progress: Simulations of Reactant Solutions

As discussed above, we found that reactions carried out in high concentration bicarbonate solutions (e.g., $KHCO_3$ and $NaHCO_3$) significantly enhance carbonation. However, at the highest bicarbonate concentrations we routinely observe a slight but systematic decrease in carbonation, which may be related to the solubility behavior of CO_2(aq) at high pressures and temperatures. Unfortunately, the experimental phase diagram for this system at the conditions of interest is currently not available. Therefore, to gain some preliminary insight we have calculated the solubility of CO_2 over the range P_{CO2} = 20–160 bar and T = 10–200 ^oC in the presence/absence of NaCl using a highly quantitative model recently introduced by Duan at al.[29] Currently this model is limited to the incorporation of Na^+, K^+, Mg^{2+}, Ca^{2+}, Cl^- and SO_4^{2-} species in an H_2O-CO_2 solution. Some representative results for H_2O-CO_2 and H_2O-CO_2-NaCl are provided in Figure 26 below, which shows the temperature dependence of the CO_2 solubility for a range of isobars.

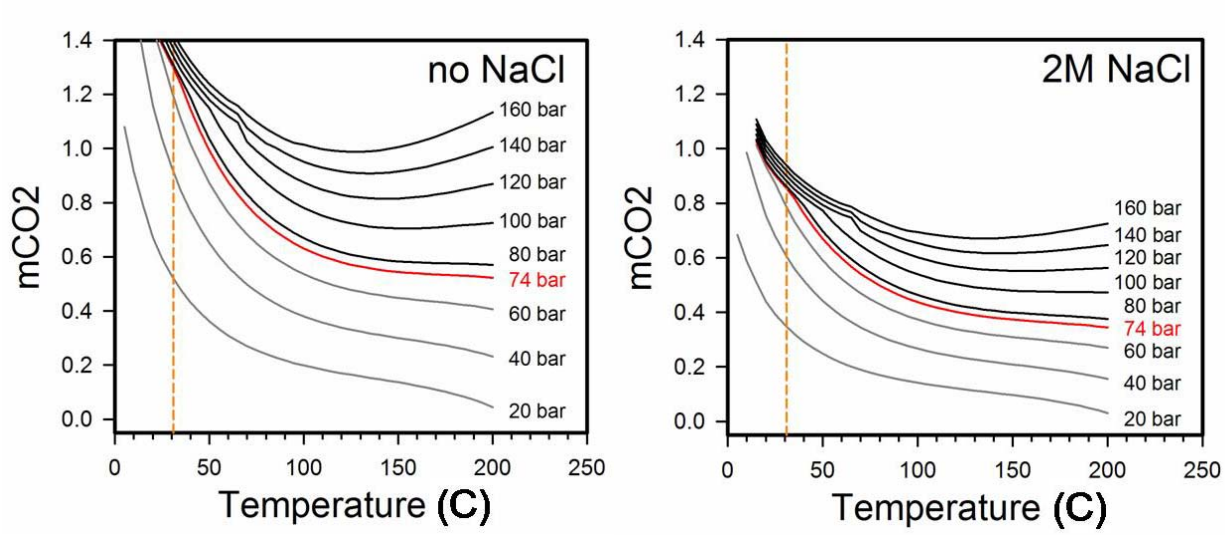

Figure 26: *Calculation of CO_2 solubility in H_2O without and with the presence of 2M NaCl.*

The calculations indicate the addition of NaCl substantially reduces CO_2 solubility in general, as expected. However, while the solubility decreases with increasing temperature for pressures below 74 bar, a minimum is observed near 130 ^oC at high pressure. Thus, for example, in a 2M NaCl solution the solubility of CO_2 at 160 bar is expected to be the same (~ 0.73M) at 83 ^oC and 200 ^oC. Importantly, the above results indicate that the addition of NaCl to saturated aqueous solutions of CO_2 can substantially decrease the activity of CO_2(aq) present. During the no-cost extension, we plan to explore to what extent these findings extend to the presence of $NaHCO_3$ vs. NaCl in the aqueous solution.

CONCLUSIONS

Robust silica-rich passivating layers have been discovered to form on the olivine surface during mineral carbonation. These passivating layers thicken, fracture and exfoliate during rapidly-stirred carbonation, exposing fresh olivine surfaces that enhance carbonation reactivity. Aqueous carbonation reactivity is a strong function of (1) the ionic species present, (2) their aqueous activities, and (3) the slurry flow conditions present during carbonation. The most effective carbonation solutions to date are high concentration sodium, potassium, and sodium/potassium bicarbonate aqueous solutions. The most effective of these solutions (5.5M $KHCO_3$) has been found to nearly double the extent of carbonation observed using the standard aqueous solution developed by the Albany Research Center. High concentration aqueous bicarbonate solutions have also been found to preferentially enhance the relative carbonation reactivity of olivine containing larger particle-size fractions (e.g., <75µ and <150µ vs. <38µ). Being able to effectively carbonate olivine feedstocks containing such larger particle-size fractions offers the potential to substantially reduce feedstock grinding cost and lower mineral sequestration process cost.

Slurry-flow dynamics have been found to be a strong function of particle size and mass via macroscopic simulations using Fluent, suggesting that controlling these parameters may offer

substantial potential to enhance passivating-layer abrasion/exfoliation and carbonation. Synergistic control of the slurry-flow and aqueous chemistry parameters incorporated during carbonation appears to offer the best potential to further improve carbonation reactivity for unactivated olivine feedstock materials.

During the second project year we improved the design of the sonication exfoliation system developed during the first year and extended our investigations of the effects sonication can have on the extent of carbonation as a function of particle size distribution, the mass of solid reactant, volume fraction of aqueous solution present, sonication power, time, temperature, and CO_2 pressure. None of the conditions investigated have significantly enhanced carbonation.

Aqueous olivine carbonation involves both incongruent magnesium dissolution and silica precipitation, which result in robust silica-rich passivating layer formation. Secondary ion mass spectrometry investigations of the H content and profile within the passivating layers suggests $2H^+/Mg^{2+}$ ion exchange is associated with incongruent dissolution. These observations are consistent with H_2O forming at or near the olivine/passivating-layer interface within the passivating layer during the carbonation process. After forming, the water diffuses out through the passivating layers during the carbonation reaction. Together with the observation that magnesite nanocrystals form within the passivating layers during carbonation, this indicates that the passivating layers offer substantial permeability to the key solution reaction species present during carbonation (e.g., Mg^{2+}, H^+, H_2O, CO_2, and HCO_3^-).

Substantial tensile stress builds in the passivating layers and at the passivating-layer/olivine interface associated with the dramatic volume decrease as olivine forms silica at the reaction surface. This stress facilitates passivating layer cracking and exfoliation. The importance of particle abrasion in enhancing carbonation reactivity was confirmed via the addition of quartz particles as an abrasive slurry, which significantly enhanced carbonation. Studies during the no-cost extension period will take full advantage of progress to date, further exploring the potential that the aqueous chemistry and slurry-flow dynamics associated with carbonation offer to enhance carbonation reactivity and reduce olivine mineral sequestration process cost.

REFERENCES

1) *Carbon Sequestration Research and Development*, Offices of Science and Fossil Energy, U.S. Department of Energy (December **1999**), and references therein.
2) Seifritz, W. *Nature* 345, 486, **1990**.
3) Lackner, K.; Wendt, C.; Butt, D.; Joyce Jr., E.; Sharp, D.; *Energy* **1995,** 20, 1153-70.
4) O'Connor, W., et al. *Proc. 25th International Technical Conference on Coal Utilization & Fuel Systems* **2000,** pp. 153-64,.
5) O'Connor, W.K., et al. *Proc. 27th International Technical Conference on Coal Utilization & Fuel Systems* **2002** pp. 819-30.
6) *Novel Approaches to Carbon Management* (National Academies Press, Wash. D.C., **2003**)
7) O'Connor, W.K.; Walters, R.P.; Dahlin, D.C.; Rush, G.E.; Nilsen, D.N.; Turner, P.C.; *Proc. 26th International Technical Conference on Coal Utilization & Fuel Systems* **2001,** 765.

8) O'Connor, W.K.; Dahlin, D.C.; Rush, G.E.; Gerdemann, S.J.; Penner, L.R. *Proc. 29th International Technical Conference on Coal Utilization & Fuel Systems* **2004,** 71.
9) Yu, S.C.; Proc. Nat. Sci. Counc. A. ROC, **1997,** 21, 173.
10) Ottonello, G.; Princivalle, F.; Della Giusta, A.; *Phys. Chem. Miner.* **1990**, 17, 301.
11) McKelvy, M.J.; Chizmeshya, A.V.G.; Soignard, E.; Marzke, R.; Wolf, G.; Béarat, H.; Doss, B. *Proc. 31st International Technical Conference on Coal Utilization & Fuel Systems* **2006** 1-17.
12) McKelvy, M.J.; Diefenbacher, J.; Chizmeshya, A.V.G.; Wolf, G.; G.; Marzke, R.; Béarat, H.. *Proc. 30th International Technical Conference on Coal Utilization & Fuel Systems* **2005,** 26, 265-79.
13) Launder, B.E.; Spalding, D.B. *Lectures in Mathematical Models of Turbulence*, Academic Press, London, England, **1972**.
14) Ding J.; Gidaspow, D. *AIChE J*., **1990**, 36(4):523-538.
15) Gidaspow, D.; Bezburuah, R.; Ding, J. *In Fluidization VII, Proceedings of the 7th Engineering Foundation Conference on Fluidization*, **1992**, pages 75-82.
16) Gidaspow, D. *Multiphase Flow and Fluidization* (Academic Press, Boston, **1994**).
17) Béarat, H.; McKelvy, M.J.; Chizmeshya, A.V.G.; Gormley, D.; Nunez, R.; Carpenter, R.W.; Squires, K. *Environmental Science & Technology* **2006,** 40, 4802-8.
18) Hurlbut, Cornelius, S.; Klein, Cornelis; *Manual of Mineralogy*, 19th Edition (John Wiley & Sons, New York, **1977**).
19) Skiff, W.M.; Carpenter, R.W.; Lin, S.H. *J. Appl. Phys* **1988,** 64(11), 6328-6335.
20) Kingery, W. D. et. al., **Introduction to Ceramics**, 2nd edition, John Wiley and Sons (**1976**).
21) Rimstidt, J.D.; Barnes, H.L. *Geochimcia et Comochimica Acta* **1980,** 44**,** 1683-99.
22) Alexander, G.B.; Heston, W.M.; IIer, R.K. *J. Phys. Chem.* **1954,** 58(6), 453.
23) Dove, P.M.; Crerar, D.A. *Geochimica et Cosmochimica Acta* **1990,** 54, 955-69.
24) D'Souza, A.D.; Pantano, C.G. *J. Amer. Ceram. Soc.* **1999,** 82(5), 1289-93.
25) Stoney, G.C. *Proc. Roy. Soc. London* **1909,** A82, 172.
26) Suhir, E. *J. Appl. Mech.* **1986**, 53, 657-60.
27) Chiang, Y-M., Birnie, D.; Kingery, W.D. *Physical Ceramics*, John Wiley & Sons (**1997**).
28) Doremus, R. H. *Glass Science*, 2nd edition, John Wiley & Sons (**1994)**.
29) Duan, Z.; Sun, R.; Zhu C.; Chou, I-M. *Marine Chemisty* **2006,** 98, 131-39.

APPENDIX

Environmental Science & Technology **2006,** 40, 4802-8.

Environ. Sci. Technol. **2006**, *40,* 4802−4808

Carbon Sequestration via Aqueous Olivine Mineral Carbonation: Role of Passivating Layer Formation

HAMDALLAH BÉARAT,[†] MICHAEL J. MCKELVY,*[,†,‡] ANDREW V. G. CHIZMESHYA,[†,‡] DEIRDRE GORMLEY,[‡] RYAN NUNEZ,[‡] R. W. CARPENTER,[†,‡] KYLE SQUIRES,[§] AND GEORGE H. WOLF[||]

Center for Solid State Science, Science and Engineering of Materials Graduate Program, Departments of Mechanical and Aerospace Engineering and Chemistry and Biochemistry, Arizona State University, Tempe, Arizona 85287

CO_2 sequestration via carbonation of widely available low-cost minerals, such as olivine, can permanently dispose of CO_2 in an environmentally benign and a geologically stable form. We report the results of studies of the mechanisms that limit aqueous olivine carbonation reactivity under the optimum sequestration reaction conditions observed to date: 1 M NaCl + 0.64 M $NaHCO_3$ at $T \approx 185$ °C and $P_{CO2} \approx 135$ bar. A reaction limiting silica-rich passivating layer (PL) forms on the feedstock grains, slowing carbonate formation and raising process cost. The morphology and composition of the passivating layers are investigated using scanning and transmission electron microscopy and atomic level modeling. Postreaction analysis of feedstock particles, recovered from stirred autoclave experiments at 1500 rpm, provides unequivocal evidence of local mechanical removal (chipping) of PL material, suggesting particle abrasion. This is corroborated by our observation that carbonation increases dramatically with solid particle concentration in stirred experiments. Multiphase hydrodynamic calculations are combined with experiment to better understand the associated slurry-flow effects. Large-scale atomic-level simulations of the reaction zone suggest that the PL possesses a "glassy" but highly defective SiO_2 structure that can permit diffusion of key reactants. Mitigating passivating layer effectiveness is critical to enhancing carbonation and lowering sequestration process cost.

Introduction

World energy consumption is growing exponentially, driven by the increasing global standard of living (*1*, *2*). Although a diverse portfolio of energy generation technologies is available, the world depends on fossil fuels for over 80% of its energy needs. Coal satisfies a large fraction of this demand because of its wide availability, high energy density, and low cost. Known reserves can satisfy global energy demands well into the next century if the environmental concerns associated with atmospheric carbon dioxide emissions can be overcome (*1*−*5*). As alternative energy technologies are unlikely to satisfy this demand in the foreseeable future (*1*−*3*), carbon sequestration provides an important option for mitigating emissions (*1*−*3*, *5*). Relatively inexpensive options to reduce emissions are available in the near term, including fuel switching (e.g., coal to gas), enhanced fossil fuel generation efficiency, renewable energy generation, and terrestrial sequestration. Although these options cannot address the expected magnitude of long-term emissions, they can buy time to develop large-scale technologies that can.

Candidate large-scale technologies (e.g., ocean, geological, and above-ground mineral sequestration) are the subject of intense research (*1*, *2*). Of these, above-ground mineral sequestration offers the advantage of CO_2 disposal in geologically stable and environmentally benign form (*2*, *4*−*9*). However, process cost reductions are needed. Cost-effectively enhancing carbonation reactivity is key to economically viable process development. Enhancing mineral carbonation is also desirable during geological (below-ground) sequestration as it can ensure long-term sequestration stability via formation of thermodynamically stable mineral carbonates. Carbonation also induces volume expansion of the mineral feedstock, suggesting controlled carbonation may be used to promote reservoir seal integrity—a current topic of great practical interest. Investigating and evaluating candidate technologies that incorporate mineral sequestration (above and below ground) are the primary focus of the CO_2 Mineral Sequestration Working Group, which is managed by DOE (Fossil Energy), and consists of members from the Albany Research Center (ARC), Argonne National Laboratory, Arizona State University, Los Alamos National Laboratory, and the National Energy Technology Laboratory.

Carbonation of olivine minerals (e.g., forsterite, Mg_2SiO_4) is a leading mineral sequestration process candidate (*6*, *9*). Deposits are sufficient to support regional implementation of above-ground sequestration (*9*). Their low cost (~$4−5/ton for mined and milled feedstock) and exothermic carbonation (reaction 1) provide potential for economically viable process development (*5*, *6*, *9*).

$$^1/_2Mg_2SiO_4 + CO_2 \rightarrow MgCO_3 + {}^1/_2SiO_2$$

Recent ARC studies indicate aqueous solution carbonation is promising (*6*, *9*). Even without special activation, 30−50% carbonation has been achieved in an hour for <37 μm olivine at 185 °C and 135 bar CO_2. Pretreatment via intense attrition accelerates carbonation to near completion at reduced pressures and temperatures. However, the activation cost is high (*9*). Economically viable process development requires novel approaches that enhance carbonation while bypassing costly mineral pretreatment. Better understanding the mechanisms that control carbonation reactivity is central to engineering lower cost processes. The aqueous olivine carbonation process has been explored down to the nanoscale with particular emphasis on the changes that occur at the olivine reaction surface/interface. Silica-rich passivating layer formation, fracture, and exfoliation govern carbonation reactivity. Novel approaches that enhance fracture and exfoliation will likely substantially lower process cost.

Experimental Section

Olivine, $(Mg_xFe_{1-x})_2SiO_4$, forms a solid solution series between its end members forsterite (Mg_2SiO_4) and fayalite (Fe_2SiO_4) with naturally occurring olivine generally richer in

* Corresponding author phone: (480)965-4535; fax: (480)965-9004; e-mail: mckelvy@asu.edu.
[†] Center for Solid State Science.
[‡] Science and Engineering of Materials Graduate Program.
[§] Department of Mechanical and Aerospace Engineering.
[||] Department of Chemistry and Biochemistry.

10.1021/es0523340 CCC: $33.50
Published on Web 06/15/2006

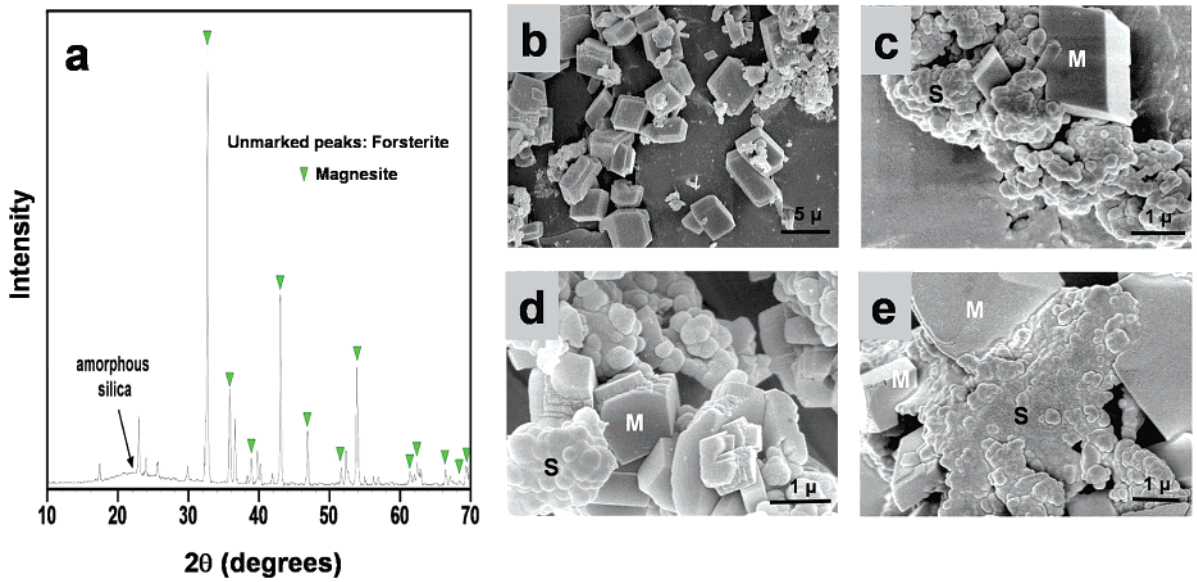

FIGURE 1. (a) XRD pattern of the olivine carbonation products. (b−e) FESEM of the magnesite crystals (M) and silica particles (S) that form during carbonation. Separate particles and crystals are frequently observed (b), but intergrowths are often observed as well (c−e). (d) Eroded magnesite crystal edges/corners are common (e.g., the crystal marked "M"), suggesting particle abrasion occurs during carbonation. (e) Intergrown silica/magnesite composite particle. Note the erosion of the outer edges of the softer magnesite crystals indicated by "M" indicating the composite particle formed during stirred carbonation (see also Figure 5).

magnesium (*10*). It adopts an orthorhombic structure with Mg and Fe occupying the same lattice sites. The cell parameters generally increase with increasing Fe content (e.g., Mg_2SiO_4: a = 4.76 Å, b = 10.20 Å, and c = 5.98 Å. Fe_2SiO_4: a = 4.82 Å, b = 10.48 Å, c = 6.11 Å) (*11*). Olivine from San Carlos, AZ, was used to explore the reaction surface/interface. Its composition $(Mg_{0.915}Fe_{0.085})_2SiO_4$ was determined using electron microprobe and particle-induced X-ray emission analysis. X-ray diffraction (XRD) showed the lattice constants are in good agreement with those for olivine containing ~8% Fe (a = 4.763 Å, b = 10.223 Å, c = 5.993 Å) (*12*). Trace impurities were well below 1%. Single crystals and their fragments were used to observe the olivine reaction surface/interface that forms during carbonation. Synthetic forsterite (Mg_2SiO_4) (99% Mg_2SiO_4; Alfa Aesar) was used for select investigations.

The optimum process to date for enhancing carbonation was developed by the Albany Research Center (ARC) based on extensive derivative investigations related to natural mineral weathering (*6*, *9*) and employed herein (185 °C, 135 bar CO_2, and aqueous 0.64 M $NaHCO_3$ + 1.00 M NaCl). Various particle sizes and reaction times were incorporated to probe the reaction/product materials vs reaction progression. 1500 rpm stirring further replicated the ARC process. The feedstock for the reaction surface/interface investigations contained equal weights of <37 and 37−200 μm single-crystal olivine fragments and occasionally a few larger (>200 μm) fragments. Mineral carbonation reactions were performed using an Autoclave Engineers EZE-Seal Hastelloy C-276 reactor.

The reaction products were analyzed structurally, morphologically, and analytically. XRD was obtained using a Rigaku D/MAX-IIB X-ray diffractometer with Cu Kα radiation. Scans were taken for 2θ ranges from 10° to 70° with 0.01°/s steps. A Hitachi S-4700 field-emission scanning electron microscope (FESEM) with energy-dispersive X-ray spectroscopy (EDS, Phoenix-EDAX) was used for imaging and analysis. Extent of carbonation and hydrogen content were assessed using a Perkin-Elmer Series II CHNS Elemental Analyzer. Comparative standards gave total carbon and hydrogen accuracies of ±0.3 wt %. Extent of carbonation observations were in good agreement with XRD product analysis.

Results and Discussion

Investigation of the Carbonation Reaction Products. XRD indicates aqueous carbonation produces magnesite, amorphous silica, and unreacted olivine (Figure 1a). The amorphous product is identified as a silica-like material by its characteristic broad scattering intensity around 22° 2θ (*13*). FESEM of the product materials reveal two characteristic particle shapes: (i) crystals and (ii) irregularly shaped product particles (Figure 1b−e). The crystals and particles are usually observed separately but are also found intergrown in clusters. The morphology of the irregular particles and the broad XRD intensity around 22° are consistent with hydrothermally formed amorphous silica (*13*). Detailed analysis of the scattering structure is needed to establish the associated short-range silica order and will be the subject of a future investigation. EDS confirms the irregular particles exhibit strong Si and O signals expected for silica and the polyhedral crystals exhibit the expected strong Mg and O signals for magnesite. Elemental analysis of the reaction products shows they do not contain H within experimental error (±0.3 wt %), indicating the silica-rich material is largely H free and primarily associated with Si−O−Si bonding (*14*).

Many magnesite crystals had irregular corners/edges (Figure 1d,e), indicating particle abrasion accompanies rapidly stirred (1500 rpm) carbonation. Abrasion can occur via particle−particle and/or particle−wall/impeller interactions. Intergrown magnesite/silica clusters were observed and typically exhibited preferential magnesite abrasion around the outer cluster edges, indicating they formed during stirred carbonation (Figure 1d,e). Intimate intergrowth of silica and magnesite indicates magnesite can nucleate/grow in association with silica formation as well as directly from solution.

Investigation of the Olivine Reaction Surface/Interface. Multiple reactions were stopped before completion to explore the olivine reaction surfaces/interfaces that form and the mechanisms that control reactivity. Silica-rich reaction layers and surface regions missing glasslike layer fragments were routinely observed (Figure 2), indicating reaction-layer formation, cracking, and exfoliation are integral to the carbonation process. As these layers are found to inhibit the

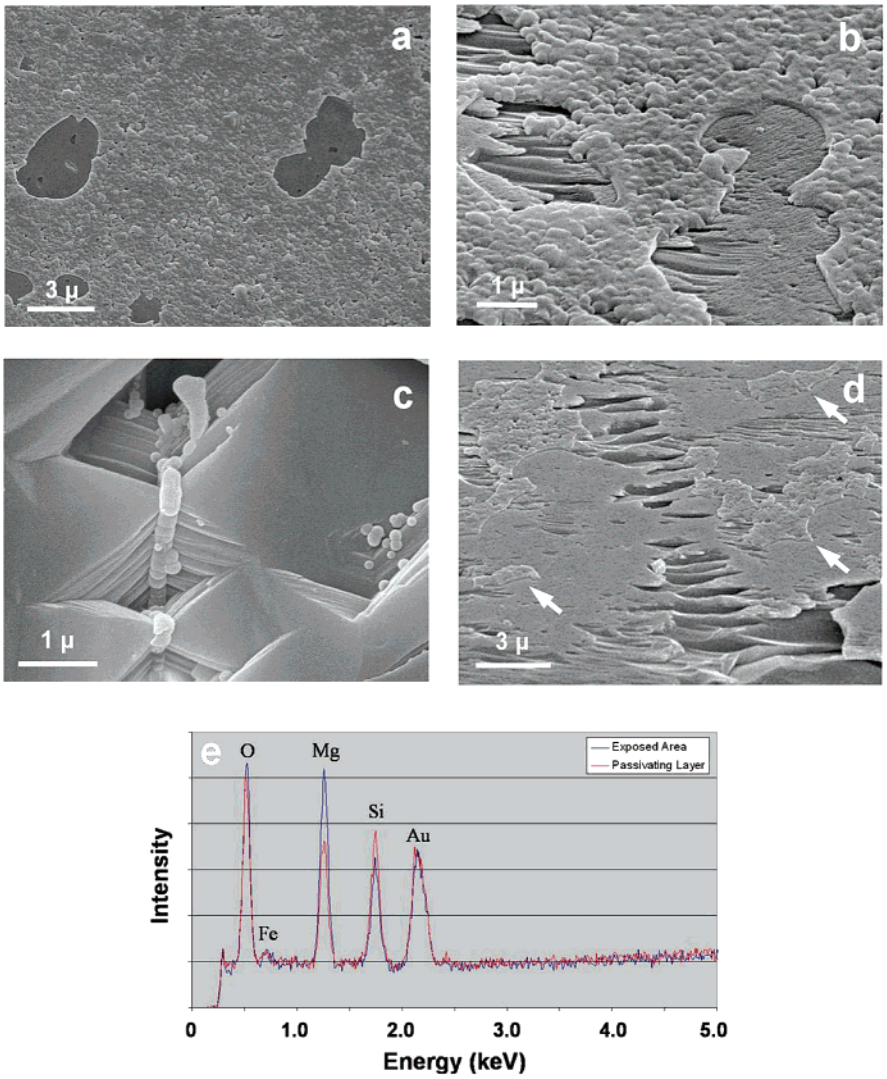

FIGURE 2. FESEM images of reaction surfaces formed during 1500 rpm stirred carbonation. (a) Silica-rich passivating layer showing regions that experienced fracture and exfoliation. (b) Regrowth of new layers in exfoliated regions. (c) Regions near etch pits were often devoid of passivating layers but occasionally show evidence of silica dissolution/precipitation. (d) Region that experienced passivating layer fracture, exfoliation, and regrowth. The exposed olivine surfaces appear associated with olivine defects. Note the olivine fragment that appears partially broken away (lower right). Passivating layer "island" remnants are indicated by white arrows. (e) EDS of the reaction surface shown in b. Analysis of the passivating layer and exposed olivine surfaces are shown by the red and blue curves, respectively. The sample is gold coated to minimize charging.

carbonation process, as discussed later, they are hereafter referred to as passivating layers. Figure 2b shows an area that has experienced glasslike fracture and exfoliation where new passivating layer regions have begun to regrow on the exposed olivine surfaces, highlighting that passivating layer growth, cracking, exfoliation, and regrowth occur repeatedly during carbonation. The silica-rich nature of the layers that form is evident in Figure 2e, which shows EDS spectra for passivating-layer and recently exfoliated (olivine exposed) regions. The thin silica-rich passivating layers that form reduce and increase the Mg and Si peak intensities, respectively, for the passivating-layer region observed as the EDS sampling depth includes both the passivating layer and some underlying olivine.

A small fraction of the surfaces observed (≤1%) were largely free of passivating layer formation. Surface irregularities, especially etch pits, were generally found in these regions (Figure 2c). This suggests defects such as dislocations, inclusions, and low-angle grain boundaries commonly found in San Carlos olivine (*10*) can significantly impact local carbonation reactivity by raising the olivine surface energy via strain field formation and lead to the locally enhanced congruent dissolution observed. Although passivating layers are not typically observed in these regions, irregular silica-rich deposits are occasionally found, suggesting they are largely associated with silica deposition (Figure 2c). The irregular surface morphology of the passivating layers is quite similar to that observed for individual silica particles as well as hydrothermally deposited silica (*13*), suggesting silica deposition may also occur on passivating layer surfaces. Figure 2d shows a region that has experienced passivating layer fracture, exfoliation, and growth/regrowth and exhibits exposed olivine surfaces. The fragment that appears partially broken away from the surface suggests the exposed surfaces may be associated with the breaking away of small olivine fragments during carbonation. Several independent passivating layer islands with glasslike fracture edges still remain after the particle has experienced substantial abrasion and exfoliation, indicating the layers are initially strongly bound to the olivine and consistent with incongruent olivine dissolution.

We are conducting a parallel investigation of the passivating layer/olivine interface using large, olivine single crystals reacted *without* stirring to avoid particle collisions

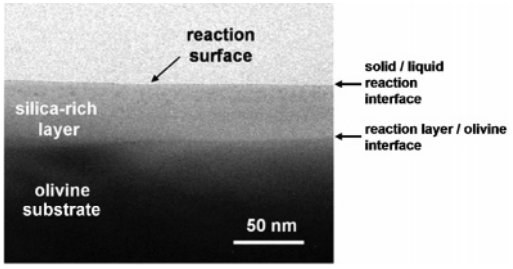

FIGURE 3. TEM cross-section image of the thin amorphous reaction layer that formed on the olivine single-crystal substrate early during unstirred carbonation.

eroding the layer that forms. Cross-section specimens are examined by high-resolution transmission analytical electron microscopy. Imaging and diffraction showed the passivating layer to be thin and amorphous; nanospectroscopy (electron energy loss and characteristic X-ray) showed the layer composition to be SiO_x with $x \leq 2$ (*15*). An example of the structure is shown in Figure 3. A small volume fraction of crystalline magnesite nanoparticles was also present in the layer with the layer best described as a dilute nanoparticle distribution in an amorphous ($\sim SiO_2$) matrix (*15*). The layer formed is highly stressed due to the large difference in molar volume between SiO_2 and olivine. Such stress can facilitate the passivating layer fracture and exfoliation observed during stirred carbonation.

Passivating layer formation appears to be a complex process that can be associated with incongruent dissolution and silica deposition on the reaction (e.g., passivating layer) surfaces that form. Hydrothermal deposition is known to be able to form brittle silica (*13*). Combined with the interfacial passivating layer/olivine stress associated with incongruent dissolution, the resulting passivating layers are expected to be highly susceptible to fracture and exfoliation, as observed.

Aqueous olivine dissolution is a complex process with a range of dissolution rates and incongruent as well as congruent dissolution observed as a function of pH and the presence of anionic species that can impact dissolution at the reaction surface (e.g., chelating agents, such as potassium acid phthalate, KHP) (*16*−*20*). To better ascertain the activities and pH during carbonation, solution equilibrium thermodynamics was analyzed using FactSage (v54) thermochemical modeling software (*21*). The Helgeson aqueous solution database was used with extended Debye−Huckel Davies activity coefficients. For the equilibrium solution calculations, the gas-phase CO_2 fugacity was fixed to the value obtained from the Duan et al. CO_2/H_2O equation of state for the same P_{CO2} and T conditions (*22*). Equilibrium aqueous speciation distribution and activities were obtained over a range of temperatures and P_{CO2} values for aqueous 1 M NaCl + 0.64 M $NaHCO_3$ and are similar to those previously reported (*7*). The pH was found to be 6.85 for $P_{total} = 150$ bar, where P_{CO2} is ~135 bar ($f_{CO2} \approx 115$ bar).

A currently accepted picture of olivine dissolution for pH < 9 under ambient conditions is based on the ion-exchange reaction $Mg^{2+} \Leftrightarrow 2H^+$ and formation of >SiOH groups (*16*, *17*). These groups can either condense to form oxide bonds within the reaction layer via

$$>Si{-}OH + HO{-}Si< \rightarrow >Si{-}O{-}Si< + H_2O$$

during incongruent dissolution or dissolve as $Si(OH)_4$ monomers that can later condense/polymerize and precipitate via >Si−O−Si< bonding and H_2O evolution (*14*, *16*−*20*). As the silica-containing samples observed in this study are largely H free (see above), it is reasonable to assume that >SiOH groups that form during carbonation are transitory, readily succumbing to >Si−O−Si< bonding to yield the brittle passivating layers observed. Indeed, the brittle fracture observed suggests substantial >Si−O−Si< bonding is present in the in-situ passivating layers that form. The formation of silica-rich layers (<20 Å thick) has been previously observed during ambient olivine dissolution for pH < 9 (*16*, *17*), suggesting the layers contain some permeability to the species associated with dissolution (e.g., Mg^{2+}, H^+, and H_2O).

Simulation of Passivating Layer Formation. Although the level of >Si−O−Si< bonding present in the passivating layers is not clear, our ex-situ observations show they are largely H free. Consequently, we simulated the anhydrous amorphous silica-rich layer to provide a plausible representation of the ex-situ anhydrous mineral surface investigated. A classical force field approach was applied to investigate the stability, structure, and permeability of siloxane passivating layer formation associated with incongruent dissolution. A 12 000 atom model that spans the region from within the olivine to the reaction region and the solution interface was used. The interaction between individual ions is represented by long-range coulomb interactions and short-range potentials consisting of an exponential repulsion and a van der Waals tail ("Born−Mayer" form).

Classical molecular dynamics simulations were carried out using the MOLDY computer program (*23*). The force fields employed are based on those developed for $MgSiO_3$ by Matsui (*24*) with slightly modified formal charges and Born−Mayer potential parameters for Mg and Si chosen to simultaneously reproduce the equations of state of α-quartz (SiO_2) and forsterite (Mg_2SiO_4). The pair potential parameters, given as pairs (A, b) for the repulsive part of the Born−Mayer form $V = Ae^{-br} - C/r^6$ are as follows: O−O (1.622, 3.333), Mg−O (8.038, 4.951), Si−O (7.367, 5.263), Mg−Mg (1301.1, 9.615), Mg−Si (2329.2, 10.87), and Si−Si (5008.1, 12.501), where the units are 10^{-3} eV and $Å^{-1}$, respectively. Only the O−O pair has a nonvanishing van der Waals C parameter, which is 30.22 eV $Å^6$. Ionic charges for O, Mg, and Si ions are −1.365, 1.365, and 2.730 e, respectively.

To benchmark our procedure we calculated the equilibrium volume of both α-quartz (SiO_2) and forsterite (Mg_2SiO_4) at 300 K over a pressure range of −20 to 80 GPa. The simulations of the basic crystalline phases were carried out in a supercell built from $N \times N \times N$ replicas of the respective unit cells ($N \approx 3$−6). All runs used an integration time step of 0.5 fs, velocity rescaling every 10 time steps, and between 10 000−100 000 time steps per run. The energy volume data was fitted to a standard Birch−Murnaghan equation of state form (*25*) to extract the equilibrium volume (V_0) and bulk modulus (B_0) at ambient pressure. For forsterite we obtained $V_0 = 69.3$ $Å^3$ and $B_0 = 121$ GPa (experimental values (*26*) $V_0 = 72.6$ $Å^3$, $B_0 = 123$ GPa), while for α-quartz we obtained $V_0 = 39.1$ $Å^3$ and $B_0 = 40$ GPa (experimental values (*26*) $V_0 = 37.2$ $Å^3$, $B_0 = 37$ GPa). To further calibrate our procedure and test the ability of the pair potentials to describe amorphous systems we undertook a brief study of silica glass. A structural model was obtained by melting a 648-atom cell of α-quartz and quenching from 3000 K by simulated annealing in nine 300 K cooling stages of 80 000, 0.5 fs time steps. The resulting structure exhibits all of the hallmarks of thermal glass, including a fully connected corner-shared tetrahedral SiO_4 network, and a mean density of about 2.31 g/cc, which is slightly high compared with the experimental value of ~2.20 g/cc. To further quantify the bonding distribution of the simulated glass we computed the radial distribution function and found it closely reproduces the essential structure observed by neutron scattering for annealed silica glass (Figure 4a,b) (*27*).

As the dissolution rates associated with passivating layer (PL) growth via incongruent dissolution are beyond the reach of our simulation times, we devised a synthetic procedure to simulate the low-temperature process. Beginning with a

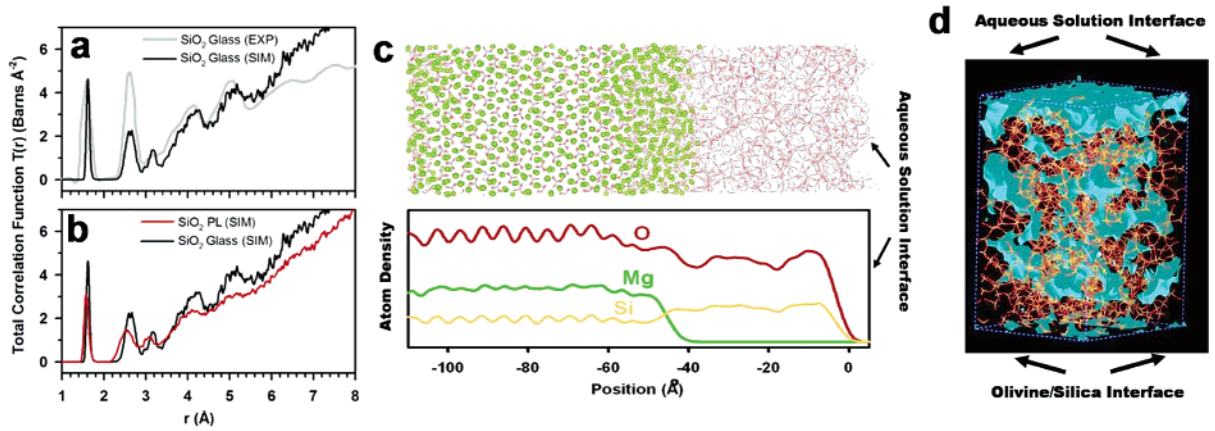

FIGURE 4. (a) Total correlation function of SiO_2 glass obtained from neutron scattering experiments (*27*) (gray trace) and molecular dynamics simulation (black trace). (b) Comparison of the total correlation function of simulated SiO_2 glass (black trace) and PL silica (red trace). (c) Simulated forsterite/passivating layer reaction interface and its atom density vs distance from the aqueous solution interface. Mg, O, and Si atoms correspond to green spheres, red sticks, and gray sticks, respectively. The variation of Mg, O, and Si atoms throughout the structure is plotted in the frame below the model. Note that the apparent densification of Mg atoms near −50 Å is due to the projection employed, which emphasizes the departure from periodic crystalline order in the transition region (ca. −65 to −40 Å). (d) PL regions that can accept a 4 Å probe without making van der Waals contact (shown in blue). The presence of continuous permeable regions can facilitate reactant species diffusion in and through the PL.

large forsterite slab, we randomly remove Mg and O atoms from the outermost region, 10 Å at a time, and then carry out a brief relaxation run to re-equilibrate the defective structure without promoting significant Mg diffusion. We continue this process until Mg on one-half of the full slab is removed. A final annealing run at 500 K is performed, leading to diffusion of Mg and formation of a reaction interface approximately 20 Å in thickness and an ∼50 Å PL with approximately SiO_2 stoichiometry (Figure 4c). Substantial contraction of the newly formed silica region relative to its extent in the olivine framework was observed. The PL formed consists of a low-density glasslike SiO_2 network with bonding very similar to thermal SiO_2 glass (O:Si ratio close to 2). The layer formed is thermally stable, remaining essentially unchanged during heating/cooling cycles from 300 to 600 K. The RDF of the PL material is compared with that of the simulated bulk silica glass in Figure 4b. The results indicate a marked change in medium-range order, consistent with a slight reduction in first shell coordination and the presence of ring structures.

Layer permeability is critical for PL formation via incongruent dissolution as it facilitates both the transport of Mg ions through the layer and formation of water and its expulsion from the layer. Close examination of the simulated PL structure suggests it may be permeable to key species associated with mineral carbonation (e.g., Mg^{2+}, H^+, and H_2O), consistent with incongruent dissolution. Such permeability does not exist in our quenched thermal SiO_2 glass model but does for the simulated PL structures. Interestingly, the RDFs calculated for the simulated SiO_2 glass and PL material have significant similarities, suggesting very similar short-range structures (Figure 4b). To reveal the differences between the structures we appeal to a "free volume" analysis module available in the Cerius2 simulation software suite (*28*). The occupiable volume is probed by overlaying grid points set at 0.5 Å intervals throughout the structure. A probe particle is sequentially placed at each grid point with the point considered "occupiable" if there is no van der Waals contact with the PL structure in any of several hundred directions. Nine probe particles with diameters ranging from 2 to 6 Å were used. As expected on the basis of visual inspection and density, the strained PL structure, which was relaxed while bonded to the host olivine, exhibits the largest fractional occupiable volume. This is followed by the relaxed PL structure, which is first severed at the olivine interface and then relaxed as above, and thermal glass. About 7% of the occupiable volume of the strained PL material was found to be able to accommodate H_2O molecules ($\mathbf{D}_{probe} \approx 2.8$ Å) (*29*), while about 5% of the volume can accommodate H_2O in the relaxed PL material (even using the 2 Å probe, the occupiable volume in thermal glass is negligible). Slightly greater occupiable volumes are expected for Mg^{2+} owing to its smaller diameter. To explore the potential impact of the strained and relaxed PL structures on the diffusion of the species associated with mineral carbonation, the regions of the PL that can accept different probe diameters were mapped out. Their interconnection, as illustrated in Figure 4d, suggests plausible diffusion pathways for reactant species within the PL produced during incongruent dissolution.

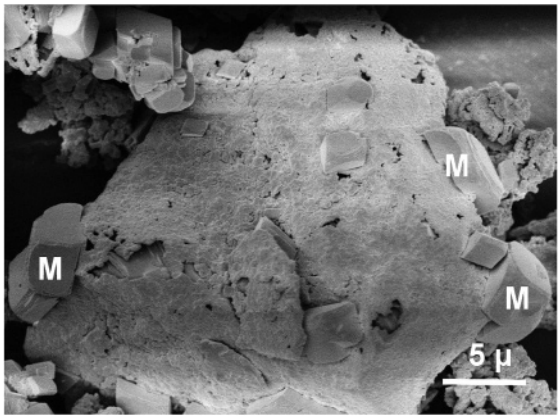

FIGURE 5. FESEM image of the intergrowth between olivine, silica, and magnesite at the olivine reaction surface. Selective abrasion of the outer magnesite (M) crystal surfaces indicate the composite particle formed during stirred carbonation.

Intergrowth of Carbonate, Silica, and Olivine During Aqueous Carbonation. Intergrowths of olivine, magnesite, and silica were also observed on the surface of partially carbonated particles, as seen in Figure 5. Selective erosion of the outside corners of surface magnesite crystals was routinely observed, confirming (i) significant particle abrasion occurs during carbonation and (ii) the observed olivine/silica/magnesite intergrowth formed during carbonation and not via precipitation or particle settling after reaction completion. Figure 6 shows cross-section analysis of a similar partially reacted crystal, which illustrates the inward progression of

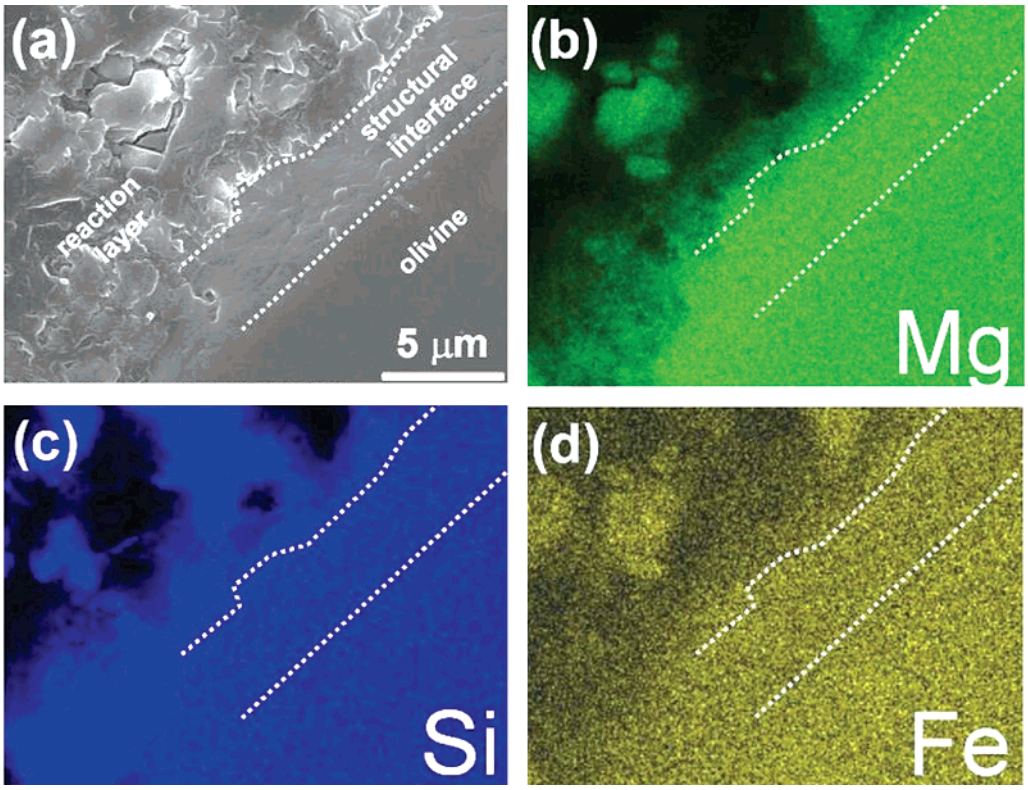

FIGURE 6. (a) FESEM secondary electron image of a cross-section of a partially carbonated olivine single crystal showing structural disruption of the olivine preceding carbonation as the reaction penetrates to the crystal interior. The crystal surface is in the upper left corner. (b–d) Mg, Si, and Fe EDS maps of the region in a.

the reaction from the olivine surface during stirred carbonation. The olivine near the reaction layer interface appears structurally disrupted (e.g., cracked) *prior to* reaction penetration, which may be related in part to volume contraction associated with silica-rich passivating layer formation via incongruent dissolution at the olivine reaction interface. This observation underscores the key role structural disruption can play in enhancing carbonation reactivity, especially given how effective silica layer formation can be at local reaction passivation. In this case, some magnesite is observed in the silica reaction layer, as evidenced by the separate Si- and Mg-rich regions in the layer observed by EDS. The strong correlation between Mg and Fe in the olivine feedstock and the magnesite in the reaction layer (Figure 6) indicates Fe is also incorporated into the carbonate during carbonation. The silica regions observed are essentially Fe free.

Controlled Particle Abrasion: Enhancing Passivating Layer Exfoliation and Carbonation. Silica-rich passivating layer formation during mineral carbonation clearly has the potential to substantially inhibit carbonation reactivity. However, the layers that form are brittle, strained, and susceptible to fracture and exfoliation that can expose fresh olivine surfaces that enhance reactivity. Hence, particle interactions may significantly enhance carbonation reactivity. To probe the potential particle–particle interactions (abrasion) offer to erode passivating layers as they form and enhance reactivity, we investigated the extent of carbonation vs wt % forsterite for stirred (1500 rpm) carbonation, as seen in Figure 7. The systematic increase in the extent of carbonation with increasing wt % forsterite (particle concentration) demonstrates (1) the importance of particle–particle interactions (abrasion) in exposing fresh olivine reaction surfaces and enhancing carbonation and (2) that the observed silica-rich surface layers substantially inhibit (passivate) carbonation. In recent simulations of colliding monodisperse spheres in forced isotropic turbulent flow, corresponding closely to the stirred tank conditions in our

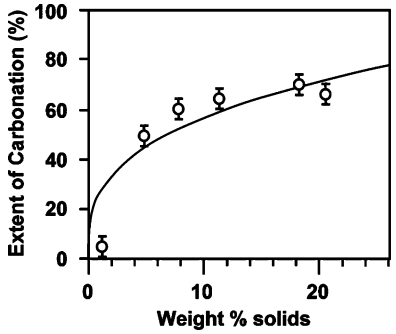

FIGURE 7. Extent of carbonation vs wt % forsterite. The error bars show the standard deviation typically observed for multiple runs under the same reaction conditions. The gray line is a fit to the form $AW^{1/3}$, where $A \approx 26.2$. (We note that the assumed functional form is only expected to be valid in the absence of particle agglomeration, which is expected to be significant in higher wt % solid regimes).

experiments, Derksen et al. (*30*) identified two distinct collision mechanisms: (i) primary collisions consisting of uncorrelated "kinetic gas"-like random contacts and (ii) highly correlated secondary collision processes involving repetitive "chattering" motion on a short time scale due to short-range hydrodynamic effects (lubricating forces). Elementary geometric considerations deliver a length scale (L) dependence on wt % solids, W, proportional to $W^{1/3}$. The removal rate of PL material, R_{PL}, is therefore proportional to $V_{avg}/L = AW^{1/3}$, where V_{avg} is the mean relative velocity between a pair of particles and A is a constant. If we assume that the diffusion of reactants through the PL is rate limiting and that complete passivation occurs in a time T_0 in an unstirred setting, then the extent of carbonation is proportional to $T_{RUN}\,R_{PL} \propto W^{1/3}$ where $T_{RUN} \gg T_0$ is the duration of the stirred reaction experiment. This dependence on wt % solids is illustrated in Figure 7, where a best fit yields a

proportionality constant of about 26.2, a value much larger than expected based on primary collisions alone. The large coefficient may be explained by a high frequency of secondary collision processes.

We recently discovered the inclusion of abrasive particles (e.g., quartz) leads to a marked increase in carbonation. This indicates controlling particle abrasion by optimizing slurry flow parameters may provide an effective mechanism for disrupting passivating layers as they form. The effective use of larger feedstock particles may promote this effect and substantially lower sequestration process cost as the vast majority of the cost in grinding the olivine feedstock to the current process size (<37 μm) is associated with particle-size reduction from <75 to <37 μm (*9*).

Acknowledgments

This work was prepared with the support of the U.S. Department of Energy, under Award No. DE-FG26-04NT42124. However, any opinions, findings, conclusions, or recommendations expressed herein are those of the author(s) and do not necessarily reflect the views of the DOE. We also gratefully acknowledge the National Energy Technology Laboratory of the U.S. Department of Energy for prior support through Awards DE-FG26-01NT41282 and DE-FG26-01NT41295 and thank the Center for Solid State Science for use of the Goldwater Materials Science Laboratories, including the Materials and Ion Beam Facilities and the Goldwater Materials Visualization Facility. We acknowledge the Department of Chemistry and Biochemistry for use of the X-ray Diffraction and Microprobe Facilities and the Center for Solid State Electronics Research for use of the FESEM.

Literature Cited

(1) *Novel Approaches to Carbon Management*; National Academies Press: Washington, DC, 2003.
(2) Lackner, K. S. Carbonate chemistry for sequestering fossil carbon. *Annu. Rev. Energy Environ.* **2002**, *27*, 193.
(3) Halmann, M.; Steinberg, M. *Greenhouse Gas Carbon Dioxide Mitigation, Science and Technology*; Lewis Publishers: London, 1999.
(4) Seifritz, W. CO_2 Disposal by means of silicates. *Nature* **1990**, *345*, 486.
(5) Lackner, K.; Wendt, C.; Butt, D.; Joyce, E., Jr.; Sharp, D. Carbon dioxide disposal in carbonate minerals. *Energy* **1995**, *20*, 1153.
(6) O'Connor, W. K.; Walters, R. P.; Dahlin, D. C.; Rush, G. E.; Nilsen, D. N.; Turner, P. C. Carbon dioxide sequestration by direct aqueous mineral carbonation. *Proc. 26th International Technical Conference on Coal Utilization & Fuel Systems* **2001**, 765.
(7) Wolf, G. H.; Chizmeshya, A. V. G.; Diefenbacher, J.; McKelvy, M. J. In situ observation of CO_2 sequestration reactions using a novel microreaction system. *Environ. Sci. Technol.* **2004**, *38*, 932.
(8) McKelvy, M. J.; Chizmeshya, A. V. G.; Diefenbacher, J.; Béarat, H.; Wolf, G. H. Exploration of the role of heat activation in enhancing serpentine carbon sequestration reactions. *Environ. Sci. Technol.* **2004**, *38*, 6897.
(9) O'Connor, W. K.; Dahlin, D. C.; Rush, G. E.; Gerdemann, S. J.; Penner, L. R. Energy and economic considerations for ex situ aqueous mineral carbonation *Proc. 29th International Technical Conference on Coal Utilization & Fuel Systems* **2004**, 71.
(10) Johnson, C. L.; Hytch, M. J.; Buseck, P. R. Displacement and strain fields around a [100] dislocation in olivine measured to sub-angstrom accuracy. *Am. Mineral.* **2004**, *89*, 1374. *Electron Microscopy in Mineralogy*; Wenk, H., Ed.; Springer-Verlag: Berlin, 1976; Chapters 6.1 and 6.6.
(11) Hurlbut, C. S.; Klein, C. *Manual of Mineralogy*, 19th ed.; John Wiley & Sons: New York, 1977.
(12) Ottonello, G.; Princivalle, F.; Della Giusta, A. Temperature, composition, and fO2 effects on intersite distribution of magnesium and iron(2+) in olivines. Experimental evidence and theoretical interpretation. *Phys. Chem. Miner.* **1990**, *17*, 301.
(13) Potapov, V. V. Formation of Solid Deposits of Amorphous Silica in a Flow of Hydrothermal Solution. *Glass Phys. Chem.* **2004**, *30*, 82.
(14) Weissbart, E. J.; Rimstidt, J. D. Wollastonite: Incongruent dissolution and leached layer formation. *Geochim. Cosmochim. Acta* **2000**, *64*, 4007.
(15) Kim, Y.; Nunez, R.; Carpenter, R. W.; Chizmeshya, A. V. G.; McKelvy, M. J. The nanoscale mechanism for San Carlos olivine carbonation *Microsc. Microanal.* **2005**, *11* (Suppl 2), 1530.
(16) Pokrovsky, O. S.; Schott, J. Forsterite surface composition in aqueous solutions: A combined potentiometric, electrokinetic, and spectroscopic approach. *Geochim. Cosmichim. Acta* **2000**, *64*, 3299.
(17) Pokrovsky, O. S.; Schott; J. Kinetics and mechanism of forsterite dissolution at 25 °C and pH from 1 to 12. *Geochim. Cosmichim. Acta* **2000**, *64*, 3313.
(18) Wogelius, R. A.; Walther, J. V. Olivine dissolution at 25 °C: effects of pH, CO_2, and organic acids. *Geochim. Cosmichim. Acta* **1991**, *55*, 943.
(19) Jonckbloedt, R. C. L. Olivine dissolution in sulphuric acid at elevated temperatures−implications for the olivine process, an alternative waste acid neutralizing process. *J. Geochem. Explor.* **1998**, *62*, 337.
(20) Chen, Y.; Brantley, S. L.; Dissolution of forsteritic olivine at 65 °C and 2<pH<5 *Chem. Geol.* **2000**, *165*, 267.
(21) Bale, C. W.; Chartrand, P.; Decterov, S. A.; Eriksson, G.; Hack, K.; Mahfoud, R. B.; Melançon, J.; Pelton, A. D.; Petersen, S. FactSage Thermochemical Software and Databases. *Calphad J.* **2002**, *62*, 189.
(22) Duan, Z.; Moller, N.; Weare, J. H. An equation of state for the CH_4–CO_2–H_2O system: II. Mixtures from 50 to 1000C and 0 to 1000bar *Geochim. Cosmochim. Acta* **1992**, *56*, 2619.
(23) Refson, K. *Moldy User's Manual*, Rev. 2.25.2.6, release 2.16; Department of Earth Sciences: Oxford, United Kingdom, 2001.
(24) Matsui, M. Molecular dynamics study of $MgSiO_3$ perovskite. *Phys. Chem. Miner.* **1988**, *16*, 234.
(25) Birch, F. Finite Strain isotherm and velocities for single-crystal and polycrystalline NaCl at high pressures and 300 K. *J. Geophys. Res.* **1978**, *83*, 1257.
(26) Knittle, E. *Mineral Physics and Crystallography: A Handbook of Physical Constants*; Ahrens, T. J., Ed.; American Geophysical Union: Washington, DC, 1995; Vol. 2, p 98.
(27) Johnson, P. A. V.; Wright, A. C.; Sinclair, R. N. Neutron scattering from vitreous silica II. Twin-axis diffraction experiments. *J. Non-Cryst. Solids* **1983**, *58*, 109.
(28) *Cerius2 Simulation Program*; Accelrys Inc.: San Diego, CA, 2003.
(29) Franks, F. *Water: A matrix of life*, 2nd ed.; Royal Society of Chemistry: Cambridge, 2000.
(30) Cate, A. T.; Derksen, J. J.; Portela, L. M.; van den Akker, H. E. A. Fully resolved simulations of colliding monodisperse spheres in forced isotropic turbulence. *J. Fluid Mech.* **2004**, *519*, 233.

Received for review November 18, 2005. Revised manuscript received March 23, 2006. Accepted May 5, 2006.

ES0523340

A NOVEL APPROACH TO MINERAL CARBONATION: ENHANCING CARBONATION WHILE AVOIDING MINERAL PRETREATMENT PROCESS COST

Type of Report:	Annual
Reporting Period Start Date:	June 22, 2006
Reporting Period End Date:	June 21, 2007
Principal Authors:	Andrew V.G. Chizmeshya,* Michael J. McKelvy, Kyle Squires, Ray W. Carpenter, Hamdallah Béarat, and Karalee Jarvis.
Date Report Issued:	December 2007
DOE Award Number:	DE-FG26-04NT42124
Submitting Organization:	Arizona State University Department of Chemistry and Biochemistry, Center for Solid State Science, Science and Engineering of Materials Graduate Program, and Department of Mechanical and Aerospace Engineering Tempe, AZ 85287-1604

*Department of Chemistry and Biochemistry,
Phone: (480) 965-6072; FAX: (480) 965-2747;
E-mail: chizmesh@asu.edu

DISCLAIMER

ABSTRACT

Known fossil fuel reserves, especially coal, can support global energy demands for centuries to come, ***if*** the environmental problems associated with CO_2 emissions can be overcome. Unlike other CO_2 sequestration candidate technologies that propose long-term storage, mineral sequestration provides permanent disposal by forming geologically stable mineral carbonates. Carbonation of the widely occurring mineral olivine (e.g., forsterite, Mg_2SiO_4) is a large-scale sequestration process candidate for regional implementation, which converts CO_2 into the environmentally benign mineral magnesite ($MgCO_3$). The primary goal is cost-competitive process development. As the process is exothermic, it inherently offers low-cost potential. Enhancing carbonation reactivity is key to economic viability. Recent studies at the U.S. DOE Albany Research Center have established that aqueous-solution carbonation using supercritical CO_2 is a promising process; even without olivine activation, 30-50% carbonation has been achieved in an hour. Mechanical activation (e.g., attrition) has accelerated the carbonation process to an industrial timescale (i.e., near completion in less than an hour), at reduced pressure and temperature. However, the activation cost is too high to be economical and lower cost pretreatment options are needed.

We have discovered that robust silica-rich passivating layers form on the olivine surface during carbonation. As carbonation proceeds, these passivating layers thicken, fracture and eventually exfoliate, exposing fresh olivine surfaces during rapidly-stirred/circulating carbonation. We are exploring the mechanisms that govern carbonation reactivity and the impact that (i) modeling/controlling the slurry fluid-flow conditions, (ii) varying the aqueous ion species/size and concentration (e.g., Li^+, Na^+, K^+, Rb^+, Cl^-, HCO_3^-), and (iii) incorporating select sonication offer to enhance exfoliation and carbonation. *Thus far, we have succeeded in nearly doubling the extent of carbonation observed compared with the optimum procedure previously developed by the Albany Research Center.* Aqueous carbonation reactivity was found to be a strong function of the ionic species present and their aqueous activities, as well as the slurry fluid flow conditions incorporated. High concentration sodium, potassium, and sodium/potassium bicarbonate aqueous solutions have been found to be the most effective solutions for enhancing aqueous olivine carbonation to date. Slurry-flow modeling using Fluent indicates that the slurry-flow dynamics are a strong function of particle size and mass, suggesting that controlling these parameters may offer substantial potential to enhance carbonation.

During the first project year we developed a new sonication exfoliation apparatus with a novel sealing system to carry out the sonication studies. We also initiated investigations to explore the potential that sonication may offer to enhance carbonation reactivity. During the second project year, we extended our investigations of the effects of sonication on the extent of carbonation as a function of the following parameters: particle size distribution, the mass of solid reactant, volume fraction of aqueous solution present, sonication power, time, temperature, and CO_2 pressure. Thus far, none of the conditions investigated have significantly enhanced carbonation. Mechanistic investigations of the stirred (~1,500 rpm) aqueous olivine carbonation process indicate the carbonation process involves both incongruent magnesium dissolution and silica precipitation, which results in robust silica-rich passivating layer formation. Secondary ion mass spectrometry observation of H within the passivating layer that forms during static carbonation suggests $2H^+/Mg^{2+}$ ion exchange is associated with incongruent dissolution. Apparently, H_2O

forms at or near the olivine/passivating-layer interface during the process and diffuses out through the passivating layers during the carbonation reaction. This is also consistent with the observation that magnesite nano-crystals form within the passivating layers, further indicating the layers offer significant permeability to the key solution reaction species present during carbonation (e.g., Mg^{2+}, H^{+}, H_2O, CO_2, and HCO_3^{-}). Cracking of the passivating layer surface during carbonation is routinely observed and can be related to the tensile stress associated with the dramatic volume decrease as olivine forms silica at the reaction surface. In our YEAR 2 studies we also demonstrated that the addition of quartz particles as an abrasive slurry component significantly enhanced carbonation, further substantiating the importance of particle-particle abrasion in enhancing passivating layer exfoliation and carbonation.

Work during the no-cost extension period focused on the completion of various subtasks initiated in YEAR 2 aimed at elucidating the carbonations mechanisms including: (a) Extension of the CFD slurry-flow simulation studies to the intermediate 75 μm case, (b) studies of the effect of intrinsic nickel impurities in olivine, and the role of parasitic impurities on the olivine carbonation process in high concentration salt H_2O-CO_2 solutions and (c) investigation of the nano-morphology of olivine reacted in 2.5M $KHCO_3$ under and 5.5M $KHCO_3$ solutions.

TABLE OF CONTENTS

EXECUTIVE SUMMARY

CO_2 mineral sequestration provides permanent disposal by forming geologically stable and environmentally benign mineral carbonates. Carbonation of olivine (e.g., forsterite, Mg_2SiO_4) is a large-scale sequestration process candidate for regional implementation. Cost-effectively enhancing carbonation reactivity is central to economically viable process development. Aqueous-solution carbonation shows particular promise. However, the associated mineral activation cost currently needed to suitably enhance carbonation is too high. Lower cost pretreatment options are needed.

Collectively our work to date indicates that carbonation reactivity is a very complicated function of the aqueous solution species and their activities. Studies varying the aqueous alkali cation species present in the optimum solution developed by the ARC (0.64M $NaHCO_3$ + 1.00M NaCl) were undertaken to selectively compare cation effectiveness in enhancing carbonation/exfoliation. The alkali cation species present and their ratio were found to dramatically impact carbonation reactivity, with extent of carbonation varying by a factor of 20 from the least to the most effective alkali cation combination. The most promising solutions for enhancing carbonation to date have provided substantial increases in extent of carbonation, nearly doubling it. High concentrations of $NaHCO_3$ (2.5M) and $KHCO_3$ (5.5M) were found to be particularly effective at enhancing carbonation, with the extent of carbonation again exhibiting a strong dependence on the alkali cation species present. In contrast, the alkali chloride solutions studied to date have exhibited poor carbonation reactivity by themselves, but can substantially enhance carbonation reactivity in combination with alkali bicarbonate under select conditions. CO_2(aq) and HCO_3^- play key synergistic roles in enhancing carbonation, as carbonation drops off dramatically in the presence of HCO_3^-(aq) or CO_2 (aq) alone.

During the 2 year performance period of this project multi-phase fluid modeling and experimental investigations were also carried out to elucidate important slurry-flow parameters that enhance exfoliation and carbonation (e.g., via particle-particle and particle-wall collisions). A new microscopic wall roughness model was developed and extensively validated. Subsequent computational investigations were found to indicate wall roughness can strongly enhance cross-stream transport, particle-particle collisions and carbonation. The Fluent code was validated for application to multiphase flows to assess the complex effects governing flow. Calculation of whole systems, such as the flow loop reactor at the ARC, remains a substantial challenge. However, initial results for system components have revealed the radial distribution of flow in a component pipe can be a strong function of particle mass/size distribution and mixing history. As particle mass was found to be an important factor in cross-stream particle transport, we initiated a series of studies to explore the effect of particle mass/size distribution on exfoliation and carbonation in collaboration with the ARC using the ARC flow loop reactor and the ASU batch reactor. Initial results demonstrate that the flow dynamics and particle mass/size distribution present can substantially impact exfoliation/carbonation.

Finally, a controlled pressure and temperature 20 kHz sonication system was successfully developed for these studies during the first year. During the second year the system was refined to utilize an improved sonic probe design that substantially extends the lifetime of the probe. During the second year, the system has been utilized to explore the effects of sonication on the

extent of carbonation as a function of the weight % olivine present, particle size distribution, volume fraction of aqueous solution present, and sonication power, time, temperature, and CO_2 pressure. None of the conditions investigated significantly enhanced carbonation. As sonication is energy intensive, we have refocused our efforts to deepen our studies of the effects that aqueous solution chemistry and multiphase fluid flow can have on carbonation reactivity, as they offer the greatest promise for cost-effectively enhancing aqueous olivine carbonation.

Mechanistic investigations have extended the fundamental understanding of the passivating layer formation process during the second project year, with many of these results discussed in our recently published article "Carbon Sequestration via Aqueous Olivine Mineral Carbonation: Role of Passivating Layer Formation," in *Environmental Science and Technology (2006).*[1] These investigations indicate both incongruent magnesium dissolution and silica precipitation contribute to silica-rich passivating layer formation. Secondary ion mass spectrometry observations of the hydrogen concentration within the passivating layer suggests $2H^+/Mg^{2+}$ ion exchange occurs in association with incongruent dissolution. In the process, H_2O forms in the olivine/passivating-layer interface region and diffuses out through the layers. Internal passivating-layer diffusion of key reaction species is also consistent with our observation of magnesite nanocrystals having formed within the passivating layers. Thus, during carbonation the layers have significant permeability to key reaction species such as Mg^{2+}, H^+, H_2O, CO_2, and HCO_3^-. Cracking of the passivating layer surface during carbonation is routinely observed during both static and stirred investigations. This is related to the tensile stress at the interface between the silica-rich passivating layer and the underlying olivine host, due to the large volume reduction as the silica forms from its olivine host. The impact of abrasion on passivating layer exfoliation and carbonation was investigated via the addition of significant weight fractions of similarly sized quartz particles as an abrasive slurry. This process significantly enhanced carbonation under otherwise identical conditions, further substantiating the importance of particle-particle abrasion as a pathway for enhancing both passivating layer exfoliation and carbonation.

Studies during the no-cost extension period emphasized the impact that controlled aqueous speciation and activity and slurry-flow dynamics have on the mechanisms that control carbonation reactivity, as they offer the greatest potential to substantially reduce olivine mineral sequestration process cost. Specifically, work during the no-cost extension period focused on the completion of various subtasks initiated in YEAR 2 aimed at elucidating the carbonations mechanisms including: (a) Extension of the CFD slurry-flow simulation studies to the intermediate 75 μm case, (b) studies of the effect of intrinsic nickel impurities in olivine, and the role of parasitic impurities on the olivine carbonation process in high concentration salt H_2O-CO_2 solutions and (c) investigation of the nano-morphology of olivine reacted in 2.5M $KHCO_3$ under and 5.5M $KHCO_3$ solutions.

The focus during the no-cost extension period was to bring the experimental and simulation aspects of the project to a point of closure. **It should be noted that a significant portion of the NCE year work was inadvertently included in the YEAR 2 report submitted around December of 2006. Accordingly, the current report covers work performed from January to about May of 2007.** An over-arching summary of the project outcomes, including a cumulative assessment of project goal achievements, will be provided in the project final report.

INTRODUCTION

Coal, in particular, and fossil fuels, in general, are well positioned to supply the world's energy needs for centuries to come if carbon sequestration technology can be developed that is (i) permanent, (ii) environmentally benign, and (iii) economically viable.[2] CO_2 mineral sequestration provides permanent disposal, by forming geologically stable mineral carbonates.[3-6] The materials produced are also environmentally benign and found in vast quantities in nature. The primary challenge is economically viable process development. As permanent disposal inherently avoids the ongoing monitoring, remediation and liability costs associated with long-term storage, the key is reducing mineral sequestration process cost. Cost effectively enhancing carbonation reactivity is critical. Enhancing mineral carbonation during geological (below-ground) sequestration is highly desirable as well, as it can similarly ensure long-term sequestration stability via the formation of thermodynamically stable mineral carbonates.[7]

Carbonation of Mg-rich olivine minerals (e.g., forsterite, Mg_2SiO_4) is a leading mineral sequestration process candidate.[8,9] These minerals are available worldwide in quantities sufficient to support the regional implementation of above-ground mineral sequestration.[9] Their low-cost (~$4-5/ton for mined and milled feedstock)[8,9] and exothermic carbonation (Eq. 1) (8), provide the potential for economically viable process development.

$$\tfrac{1}{2}Mg_2SiO_4 + CO_2 \rightarrow MgCO_3 + \tfrac{1}{2}SiO_2 + 88\ kJ/mol \qquad (1)$$

Recent studies at the Albany Research Center indicate aqueous solution carbonation is a promising approach.[8,9] Even without special activation, 30-50% carbonation has been achieved in an hour for <37 micron olivine reacted at 185 ^oC and 150 bar CO_2. Mechanical pretreatment via intense attrition accelerates carbonation to near completion in less than an hour and at reduced pressures and temperatures. However, the activation cost is too high for cost-effective sequestration.[9]

Economically viable process development will require novel approaches that enhance mineral carbonation reactivity, while bypassing costly mineral pretreatment. The potential to develop low-cost chemical pretreatment processes has been explored for years, but success remains elusive.[7] Enhancing carbonation, while avoiding the expense of olivine pretreatment, would substantially reduce process cost and provide a significant advance. We recently discovered that aqueous olivine mineral carbonation is associated with robust passivating layer formation, which substantially inhibits mineral carbonation. Herein, we are exploring novel low-cost approaches with the potential to facilitate passivating layer exfoliation to enhance carbonation and develop an atomic level understanding of the associated mechanisms. The goal is to develop the understanding needed to engineer new low-cost carbonation processes that avoid the cost of pretreatment activation. The primary focus is on enhancing passivating layer exfoliation, which has the potential to substantially enhance carbonation without the need for pretreatment activation.

EXPERIMENTAL

Single crystal olivine fragments from San Carlos, Arizona, were used to explore the effects of aqueous solution chemistry, particle size and sonication on olivine carbonation reactivity, as well as the mechanisms that govern passivating layer formation and exfoliation processes. The

elemental composition was determined to be $(Mg_{0.915}Fe_{0.085})_2SiO_4$ by electron microprobe and particle induced X-ray emission analysis. X-ray diffraction (XRD) of powdered samples showed the lattice constants are in good agreement with those observed for olivine containing ~8% Fe (a = 4.763Å, b = 10.223Å, c = 5.993Å).[10,11] Trace impurities observed were well below 1%, with Ca being the principle trace impurity. Single crystals and single crystal fragments were used to facilitate microscopic observation of passivating layer formation/exfoliation and the reaction surfaces and interfaces that form during carbonation. Synthetic forsterite (Mg_2SiO_4) (99% Mg_2SiO_4; Alfa Aesar) was used for select carbonation investigations. Twin Sisters olivine was used for the flow-loop reactor studies carried out in collaboration with the Albany Research Center.[8] The flow-loop reactor has been previously described.[9] All of the olivine size fractions investigated herein (<37 micron, 37-75 micron, < 75 micron, 75-150 micron and <150 micron) were wet screened. The extent of carbonation observed is compared with the optimum process to date for enhancing carbonation developed by the Albany Research Center (ARC),[8,9] which is summarized below for forsterite carbonation.

$$Mg_2SiO_4 + 2\,CO_2 \xrightarrow[0.64\ M\ NaHCO_3,\ 1\ M\ NaCl]{\sim 185\ ^\circ C,\ \sim 150\ atm\ CO_2} 2\,MgCO_3 + SiO_2$$

Reactions were carried out using a variety of aqueous species (e.g., Li^+, Na^+, K^+, Rb^+, Cl^-, HCO_3^-) and species activities, particle size ranges and reaction times to probe their effect on carbonation and passivating layer formation/exfoliation. 1,500 rpm stirring was used to replicate the ARC process in the studies at Arizona State University. These mineral carbonation reactions were performed using a 100ml Autoclave Engineers EZE-Seal Hastelloy C-276 reactor, which is a smaller scale version of the 2,000 ml EZE-Seal Hastelloy C-276 reactor used at the Albany Research Center. Unstirred (static) experiments were undertaken to explore passivating layer formation in the absence of particle abrasion. San Carlos olivine single crystals (~1 x 1 x 0.1cm) with well-defined initial surface morphologies were incorporated to follow the reaction interface that forms down to the atomic level.

The extent of carbonation and hydrogen content of the product materials were assessed using a Perkin Elmer Series II CHNS Elemental Analyzer. Comparative standards gave total carbon and hydrogen accuracies of ± 0.3 wt%. Extent of carbonation observations were compared with XRD intensity analysis of the product materials and found to be in good agreement. Select reaction products were analyzed structurally, morphologically, and analytically versus their extent of reaction to probe the mechanisms that govern carbonation.

XRD patterns were obtained using a Rigaku D/MAX-IIB X-ray diffractometer with Cu$K\alpha$ radiation. Scans were taken over different 2θ ranges between 10º to 70º, with 0.01º/s steps. Reaction products were imaged using a Hitachi S-4700 field-emission scanning electron microscope (FESEM) or a FEI XL-30 Environmental FESEM. Elemental analysis of individual product particles was accomplished via energy dispersive X-ray spectroscopy (EDS). Cross-sectioned samples of reaction interfaces were analyzed via FESEM and EDS mapping and high-resolution transmission electron microscopy (HRTEM) using a JEOL 2010 with energy dispersive x-ray spectroscopy (EDXS) and electron energy loss spectroscopy (EELS) capabilities.

As no additional work on sonication was carried out during the no-cost extension period of the award, we forego a description of the sonication apparatus (a complete description is contained within the Experimental Section of the YEAR 2 report).

RESULTS AND DISCUSSION : NO-COST EXTENSION YEAR

1(a) Scientific Progress: *Multi-phase Fluid Modeling and Experimental Investigations to Elucidate Key Slurry-Flow Parameters that Enhance Exfoliation and Carbonation*

We have continued analysis of the slurry-flow simulations performed using monodisperse size fractions of 37μ, 75μ and 150μ particles. The goal at the current stage is to understand the influence of particle size on the distributions of the solids phase velocity and volume fraction within the ASU mini-reactor. Simulations reported during YEAR 2 were performed for two size fractions: a solids phase consisting of 37 μm diameter particles and a second simulation using 150 μm diameter particles. Simulations for a size fraction of 75 μm diameter particles were performed during the current no-cost extension period. During the YEAR 2 investigations the number of concurrent calculations was limited by a fixed number of licenses. We therefore invested in 4 additional licenses during the no-cost extension to enhance system evaluation.

A detailed analysis of the structural features of the flow in the minireactor, as well as the statistics associated with the olivine volume fraction and velocity distributions for the different size fractions are of key interest for enhancing particle abrasion, passivating layer exfoliation and mineral carbonation. Our ultimate objective is to engineer cost-effective reaction flow dynamics that enhance particle abrasion via particle-particle and particle-vessel interactions, which in turn enhance passivating layer exfoliation and carbonation. Although the no-cost extension period simulations emphasized the size fraction of 75μm we also carried out a limited number of addiitonal simulations for particle sizes of 37μm and 150μm to illustrate the differences between the simulation results. We reported in detail our collective results for the 37μm and 150μm size-fraction simulations at the 6th International Conference on Multiphase Flow, ICMF 2007, in Leipzig, Germany in July 2007. These results were summarized in a full-length archival format conference paper (attached as Appendix A).

As with the 37μm and the 150μm cases, the simulations for the 75μm case were carried out using the coarse grid, and an adaptive mesh refinement was then subsequently performed on the mesh. This was done using gradients of the volume fraction of the solids phase as the refining parameter, which resulted in a finer grid with extra grid cells only in the regions where required. Steady state, as well as accurate time-dependent solutions representing the flow field in the mini-reactor were obtained using reliable first-order discretization of the model equations (see YEAR 2 report, and attached paper in Appendix A). At temporal iteration in the multiphase simulation the values of flow variables in every cell of the domain are computed. As in our prior work, this process is continued until the difference in the values of the flow variables (residuals) between consecutive iterations is on the order of 10^{-6}. The simulation is then allowed to evolve in time and the results are extracted at t = 5 seconds. Figure 1 shows the contours of volume fraction of olivine for the 75μm case. We note that the maximum volume fraction concentration of olivine is found to be 0.556, which lies in-between the values observed for the 37μm and the 150μm

cases. Also, the cloud height was observed to be lower than the 37μm case, but significantly higher than the 150μm case. The maximum concentration was observed to be in the vicinity of the paddle wheel along the direction of rotation, which indicates the sweeping nature of the flow.

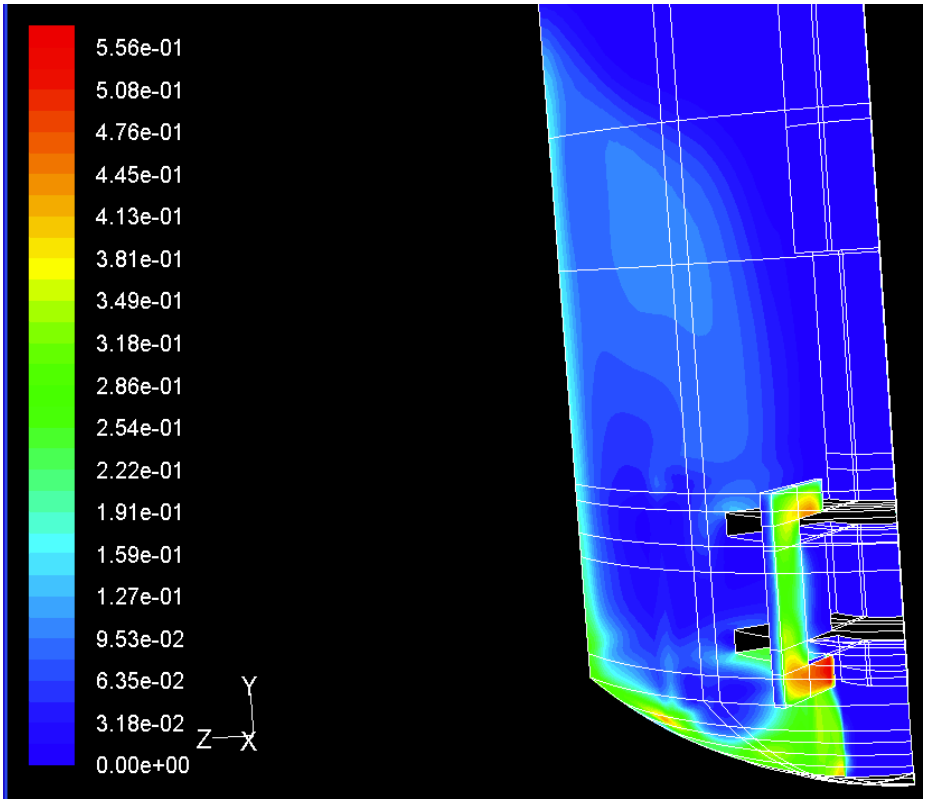

Figure 1: *Contours of volume fraction of olivine (fractional scale is shown on the left).*

Figures 2 shows the contours of the velocity magnitude of olivine and water, respectively. An interesting observation is that the velocity profile of olivine closely follows that of the water, in quantitative similarity to the 37 μm results reported in our YEAR 2 simulations. As in the latter case, a section-wise comparison of the contour plots indicates that the velocity magnitude of the 75μm olivine particles to lag the corresponding values for the water-CO_2 mixture. However, there are a few grid cells where the olivine velocity is observed to be higher than the water velocity.

Figures 3 show the contours of axial velocity and radial velocities of olivine for the 75μm case. Axial velocities of olivine indicate the movement of olivine along the central axis, where positive velocities point to flow directed upwards, while negative velocities indicate downward flow. Similarly, radial velocities signify the movement along the radial direction, from the center to the outer periphery of the cylinder. Along similar lines, positive velocity indicates motion of particles towards the outer cylinder walls, while negative velocities indicate a motion towards the central shaft. Note that the left panel of Figure 3 shows the presence of both positive and negative velocities, which gives an indication of swirl taking place along the vertical direction, while the right panel highlights the motion of particles being thrown towards the outer

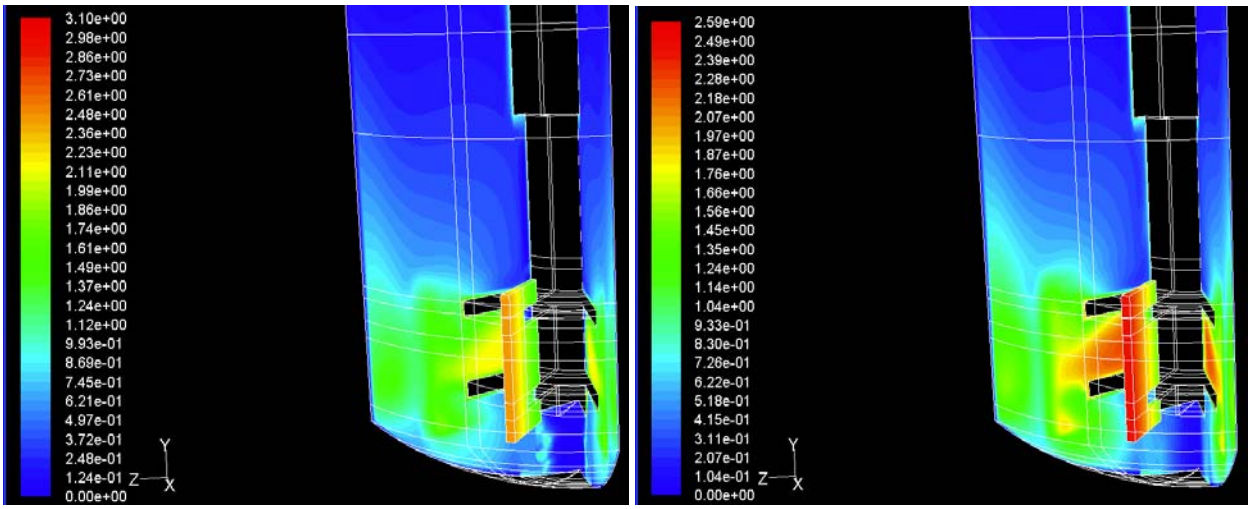

Figure 2: *Contours of velocity magnitude (in m/s) of olivine (left pane), and the water-CO_2 mixture (right panel) at t=5 seconds.*

cylinder walls and then being entrained towards the inner region near the centrally located shaft. As in our earlier reported results for the 37 μm case, these figures show that the fluid velocities are largest in the vicinity of the paddle, as expected, given the entrainment and mixing produced by the paddle. Furthermore, the vectors in different axial planes away from the paddle possess different orientations, indicating again in the 75 μm case that mixing effects are operative even at relatively larger distances from the paddle. A further detailed analysis of the velocity patterns corresponding to the contour patterns indicates entrainment of the particles towards the center in a region below the paddle wheel, while the particles are thrown towards the wall in the region near the paddle wheel center. In analogy with our results for the 37 μm case, the present simulations indicate that particles are entrained towards the central shaft in the region above the paddle wheel. This again implies that two swirling motions are present; one counter-clockwise and one clockwise in regions above and below the paddle wheel respectively.

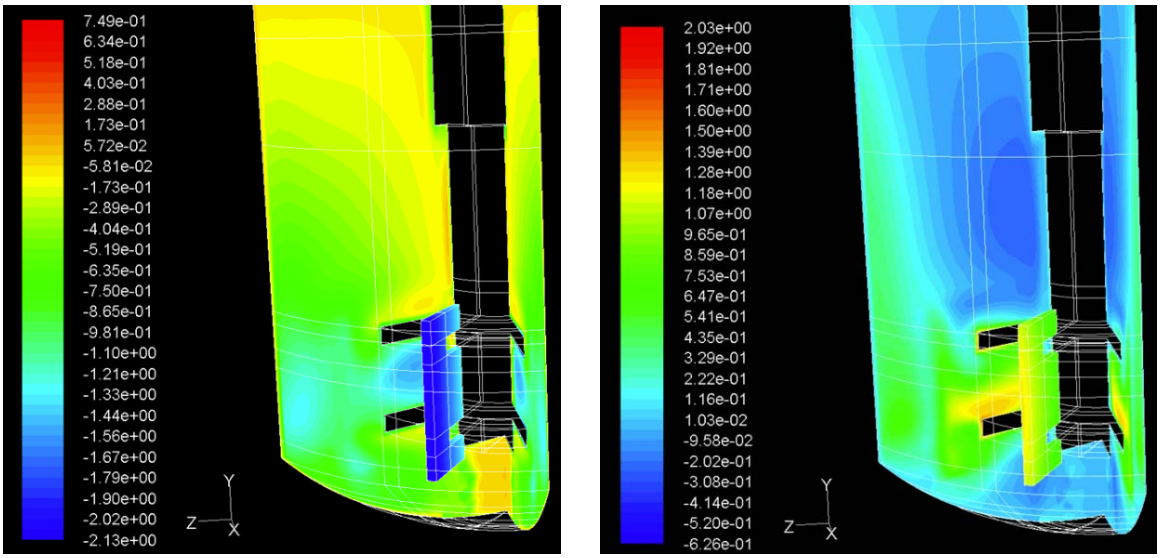

Figure 3: *Contours of axial velocity (left panel) and radial velocity (right panel) fields of olivine.*

1(b) Scientific Progress: *Comparison of ambient temperature and pressure slurry-flow CFD simulations with experiments using a transparent Plexiglas vessel.*

To verify the accuracy of the slurry-flow simulations, we constructed a transparent plexiglass reaction vessel for the mini-reactor to perform experiments using water-olivine slurries at ambient temperature and pressure and 1500 rpm stirring. Visualizations of the slurries obtained in these experiments can be compared to the flow dynamics predicted by the CFD model to further assess the model's validity. Experiments were conducted using a mini-reactor based on an autoclave mechanism at ASU. An EZE-Seal Hastelloy C- 276 autoclave reactor manufactured by Autoclave engineers was deployed for the reactions. The mini reactor is constructed using a cylindrical vessel with a volumetric capacity of 120 ml. A pump operating at 1500 rpm rotates a Rushton turbine impeller mounted on a shaft placed axially within the cylinder, which mixes the slurry. The experimental setup is shown in Figure 4. The pump driving the Rushton turbine is located at top of the figure, while the mini-reactor chamber containing the slurry is in the lower region. An open view of the reactor shows the Rushton turbine. Reaction steps involve filling the reactor with a measured amount of slurry (50 ml), elevating the temperature to 185◦C and then charging the system to a pressure of 165 atmospheres by injecting carbon dioxide. The valves are closed to seal the system and the reaction is allowed to progress for an hour under continuous stirring. The reactor is finally cooled to room temperature by circulating cooling water through the cylinder body, following which the contents of the reactor are emptied, filtered, dried and sampled for analysis.

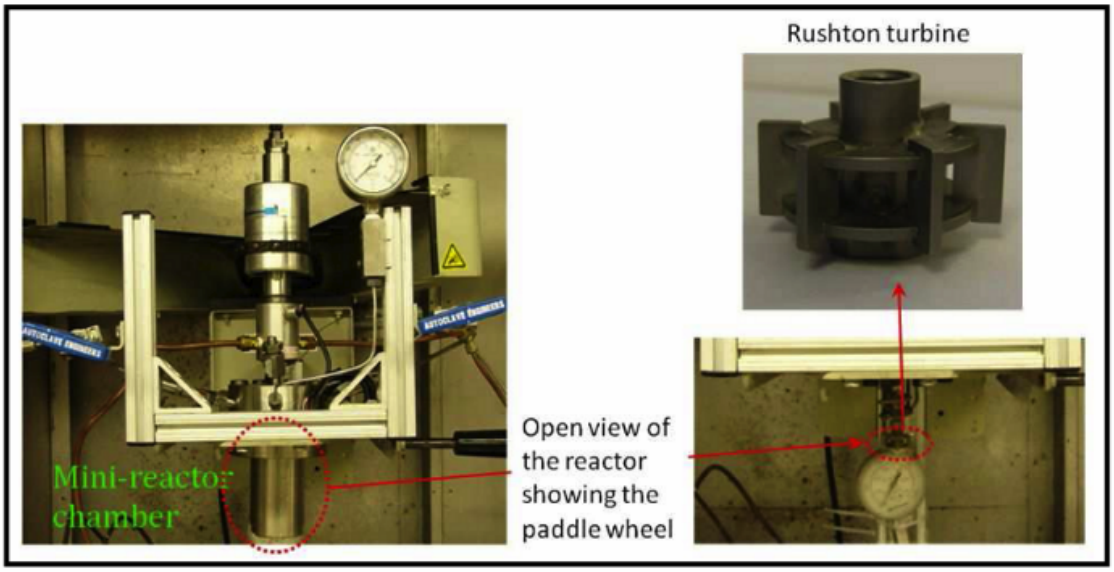

Figure 4: *Mini-reactor configuration used in experiments conducted at Arizona State University.*

To ensure a meaningful comparison of the flow patterns occurring in the mini-reactor and to circumvent visibility issues, the dimensions of the transparent Plexiglas reactor were chosen to exactly match those of the Hastelloy reactor. The outer body of the reactor was machined with plexiglas, while the Rushton turbine blades from the previous setup were used. Since Plexiglas cannot maintain its structural integrity under high temperature and pressure, the operating conditions for experiments conducted using the Plexiglas reactor were maintained at room temperature and pressure.

Experiments conducted in the Plexiglas reactor were solely for the purpose of studying the flow patterns and the samples used in these experiments were not used for reactivity analysis. Experiments were performed using 120 ml of distilled water solution with 10 grams of olivine at room temperature and pressure. The impeller speed was varied to study the lift of the particles for different size fractions and different speeds. Impeller rotation was varied from 1500 rpm to 5000 rpm and three size fractions of <37μm, 37-75μm and 75μm- 150μm were visualized. Experiments using the Plexiglas reactor, where the rotational speed of the impeller was varied from 1500 rpm to 4000 rpm showed that the solids were observed to reach greater cloud heights at higher speeds. However, turbidity of the slurry solution prevented actual measurement of cloud heights for the experiments performed. Additional details are provided in the published account (see Appendix A).

2. Scientific Progress: *Static mineral carbonation investigations into the mechanisms that control aqueous olivine mineral carbonation.*

During the no-cost extension period we continued our static mineral carbonation investigations into the mechanisms that control aqueous olivine mineral carbonation. In these latter studies we found that aqueous mineral carbonation reactions involving *very small single crystal olivine* samples (e.g., milligrams) and *high aqueous bicarbonate concentrations* leach significant amounts of nickel from the Hastelloy C-276 minireactor, which becomes incorporated in the magnesite that forms. We have successfully circumvented this contamination issue by incorporating ~10 grams of fine particle olivine with the single crystal olivine samples, which effectively absorbs the nickel, diluting any nickel contamination associated with our single crystal studies to below detection (SEM/EDXS).

Our prior work on single crystal carbonation based on the standard (ARC) aqueous solution protocol has shown two main surface constituents on reacted particles: (i) crystalline grains containing mostly magnesium, oxygen and carbon and a web like structure high in silicon and oxygen. In addition, transmission electron microscopy (TEM) images reveal an amorphous silica layer at the reaction surface. Our recent work during the no-cost extension period has shown that some reaction particles contain high levels of nickel (in some cases even higher than the magnesium) and small amount of calcium. Interestingly, the web like (presumably silica) structure is no longer observed on these reactant particles. Instead, TEM images show an amorphous reaction layer of yet undetermined chemical composition. Figure 5 shows scanning electron microscopy (SEM) images and corresponding energy-dispersive X-ray spectroscopy (EDXS) spectrum for reaction particle on olivine single crystal coupons oriented along the <010> axis reacted in the standard solution. The EDXS spectrum of product particles in the absence and presence of nickel contamination are compared in Fig 5(a) and 5(b), respectively. The calcium evident in Fig 5(b) likely originates from the salts used to make the solution (e.g. even at analytical grade, sodium chloride still contains trace amounts of calcium). In the reactions in which nickel is found to be present its signature EDXS peaks in the carbonate particles in the standard reaction solution (*1.0M NaCl/0.64M* $NaHCO_3$) have been found to match or exceed the corresponding magnesium peak in magnitude. A further remarkable observation is that the reacted olivine surface in the nickel-free experiments is very rough and shows an exfoliating silicon rich passivating layer, while the surface in the presence of the nickel contaminant is much smoother and shows no silicon rich layer.

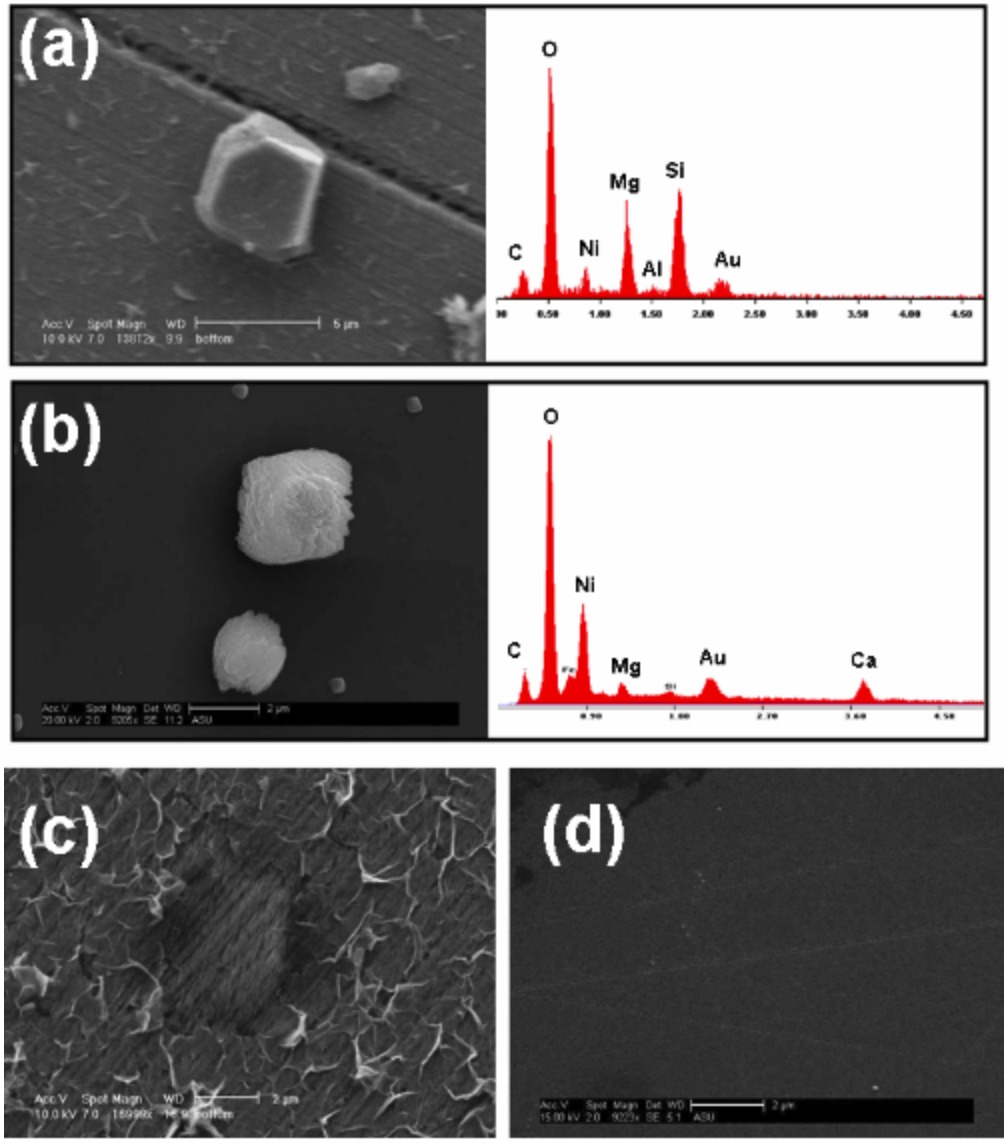

Figure 5: *Single crystal olivine reacted in 1.0M NaCl/0.64M $NaHCO_3$. a) Carbonate particle from reaction 1 and corresponding EDXS b)carbonate particle from reaction 2 and corresponding spectrum c) surface of reaction 1 and d) surface of reaction 2.*

Similar results are found carbonation experiments using a 5.5M $KHCO_3$ solution. Some representative micrographs and EDSX spectra from this study are presented in Figure 6, which elucidates the morphology of the particles and their corresponding surface structures. As noted earlier the systematic incorporation of powdered olivine (reaction 3) discourages the reaction of nickel with the single crystal olivine (explained further below). This parasitic effect of the powdered reactant is confirmed by the absence of nickel in the resulting carbonate product, as confirmed by its EDXS spectrum shown in Figure 6(a). By contrast the height of the nickel peak obtained without the addition of olivine powder (reaction 4) is almost equal in height to that of magnesium. Moreover, the surfaces are very different. Reaction 3 produces precipitates on the surface, including silicon-rich spheres and significant degree of peeling of the silicon layer. Reaction 4, on the other hand, is characterized by the precipitation of fewer particles, the absence

of silica layer peeling, and a very rough surface morphology. In addition to confirming that nickel alters reaction mechanism, these results suggest that adding extra olivine surface area to the reaction reduces the level of nickel contamination/substitution in the carbonate.

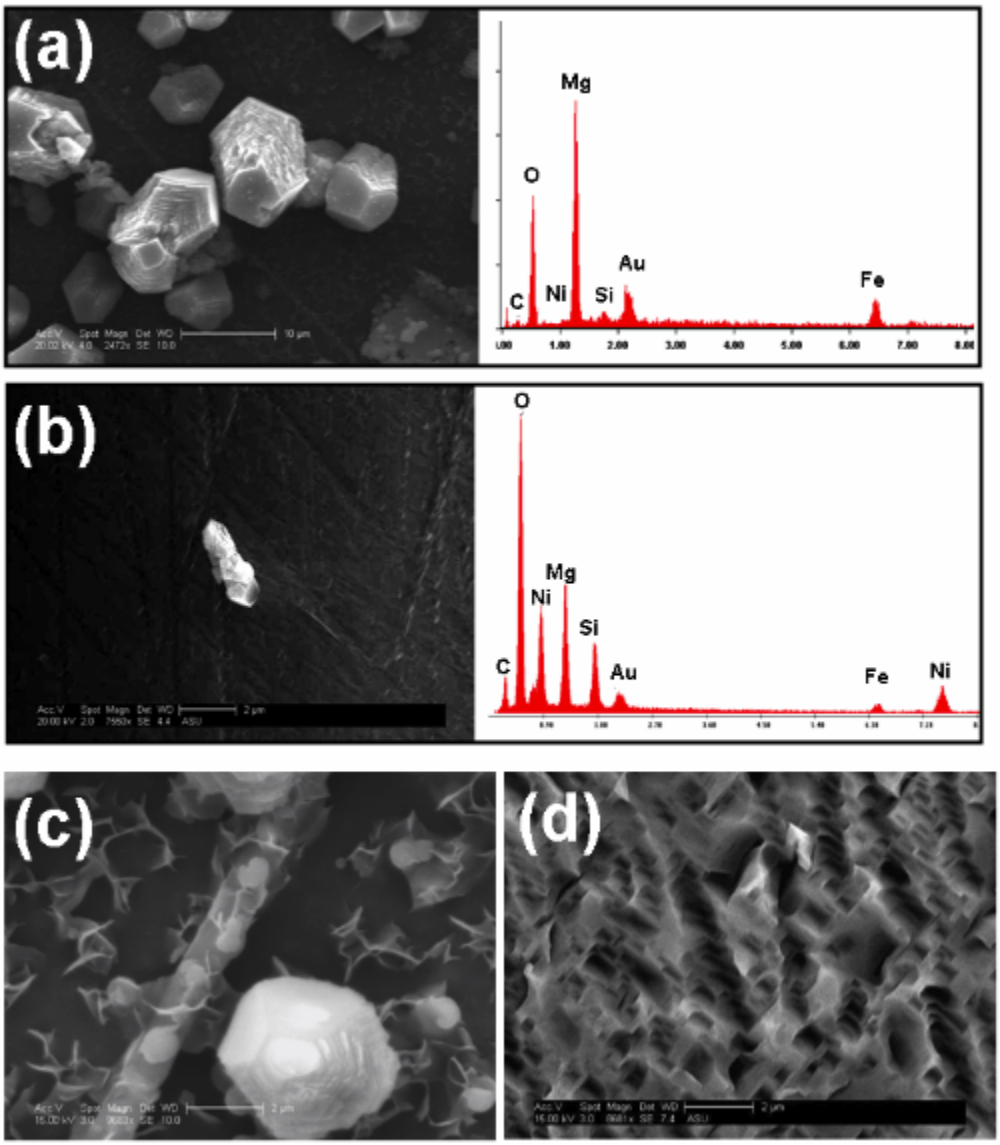

Figure 6: *Single crystal olivine reacted in 5.5M $KHCO_3$. a) Carbonate particle from reaction 3 containing olivine powder b) carbonate particle from reaction 4 without powder c) surface of reaction 3 and d)surface of reaction 4.*

In general when the surface area of olivine is increased, the amount of magnesium in solution increases. Therefore, reactions including olivine powder will increase the magnesium/nickel ratio to a sufficiently high degree to prevent the nickel ions from playing a major roll in surface reaction mechanisms. The ratio depends on the surface area of olivine, and therefore on the particle size of the olivine. Reactions containing <38 micron size particles of olivine reduce nickel; however, reactions containing 75-150 micron size particles do not reduce nickel. The minimal ratio of magnesium to nickel needed to alter the reaction is not known, and work is

underway to determine a limiting value. However, this can be estimated from the difference in solubility products of $MgCO_3$ and $NiCO_3$. The former is about at least 50 times more soluble than the latter. So, $[Mg^{+2}]$ should be largely in excess compared to $[Ni^{+2}]$ to have magnesite precipitating as main carbonate product. This should be consistent with the observation that incorporating 10g of olivine powder minimizes the Ni contamination of the carbonate product, as more Mg^{+2} is leached from the olivine than Ni^{+2} from the alloy. Meanwhile, when only a single crystal olivine sample is tested, less magnesium is being leached compared to the nickel and therefore Ni-contamination of the carbonate product is prominent.

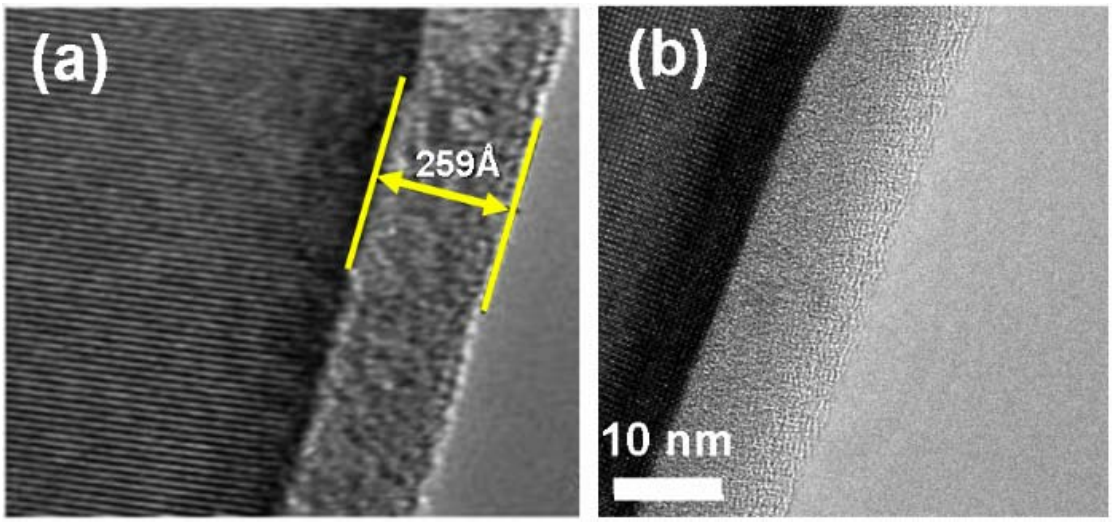

Figure 7: *TEM images of cross section of single crystal olivine reacted in 1.0M NaCl/0.64M $NaHCO_3$, a) with no nickel and b) with nickel.*

While no silicon layer was observed in the runs containing contamination, TEM cross sectional analysis shows an amorphous reaction layer. TEM cross sections for single crystal run with and without nickel contamination are compared in Figure 7. The amorphous layer in the image (Fig 7(b)) appears to be about 11 nm, however its composition has not yet been identified. In the reaction with no contamination, the amorphous layer (~ 25nm thick) has been identified as SiO_x. Further investigation is needed to determine if any difference exists between these amorphous layers. Our results described here indicate that nickel can significantly alter the reaction mechanism in olivine sequestration. In addition to reducing the magnesium precipitation as a carbonate an intriguing finding is that the thickness and morphology of the surface reaction layers is significantly modified. In view of the above findings, additional studies to quantify the role of nickel on carbonation reaction *rates* are warranted.

Nickel Source: The first step in controlling nickel contamination requires the systematic identification of all possible sources of nickel. In our specific mini-reactor setting potential sources include: the reaction vessel and temperature probe (and reactor internal parts: propeller, shaft, cooling coil, and thermocouple well), the olivine, the reaction solution, the vessel cleaning method (Scotch Brite pad), metal washers, bolts and o-ring. The Scotch Brite pad was eliminated as a potential source because although it contained nickel, the reaction vessel and temperature probe were sonicated for a half hour in distilled water after being scrubbed to remove any particle left by the pad. San Carlos olivine naturally contains up to 0.44% NiO (0.3457%Ni)[13] The coupons used are about $0.05cm^3$ and on average have a density of about

3.32g/cm^3. Assuming 1% of the Ni in the single crystal leaches into solution, 5.74μg of Ni ions would be present in the salt solution. In a 50ml solution, there would be 109 ppb of nickel in solution. Based on averaging the carbonate particles on a single crystal reacted before significant nickel was seen, the carbonate particles take up about 7.25% of the area of the total surface. Starting with a 1cm × 0.5cm single crystal and assuming the particle is 2μm high, the total

Ni[a]	Co	Cr	Mo	W	Fe	Si	Mn	C	Others
57	2.5**	16	16	4	5	0.08**	1**	0.01**	V-0.35**

*The undiluted deposited chemical composition of alloy C-276 covered electrodes has 0.02 percent maximum carbon, 0.20 percent maximum silicon, 0.03 percent maximum phosphorus, and 0.015 percent maximum sulfur.
**Maximum
[a]= As Balance

Table 1: *Chemical Composition of Hastelloy C- 276*

carbonate volume is 7.25×10^6 μm^3. Using the density of magnesium carbonate is 3×10^{-6} μg/μm^3, 2.14×10^1 μg of $MgCO_3$ precipitate on the surface of the single crystal.[14] From semi-quantitative EDXS analysis of the carbonate from, about 1% by weight of the precipitate is Ni. Consequently, 2.14×10^{-1} μg (4.28ppb) of Ni must be present in solution to account for the precipitation on the single crystal. Therefore, the nickel impurities in olivine could easily supply enough nickel (109ppb) to account for 1% of nickel present in magnesite particles from reactions in the standard solution (See EDSX spectrum in Figure 5(a). Using a similar calculation for a reaction with 5.5M $KHCO_3$, about 45% of the surface is carbonate. The density for gaspeite (a nickel magnesium iron carbonate) is 3.71g/cc[15] and about 40% of the particle is nickel (see Figure 6(b)). Assuming a particle height of 2 μm, 1340 ppb of nickel would have to be present in solution to account for the nickel in the carbonate product. Consequently, it would appear that there is not enough nickel in olivine to account for the levels of nickel present on the reacted single crystal suggesting that another source must be supplying nickel.

We next focused on the reaction solution. Ion chromatography analysis of the standard solution (prior to reaction) showed no nickel, leaving the reaction vessel and other metal contacts as remaining potential sources. To eliminate the latter (washer, bolts and o-ring) as contamination sources we coated them with gold prior to each run, but the nickel contamination persisted. We therefore indentified the reaction vessel as the dominant source of nickel contamination. The latter is composed of Hastelloy C-276 which contains 57 weight % nickel,[16] (see Table 1). However, this material is also widely accepted as one of the most corrosion resistant reaction-vessel alloys. In order for Hastelloy C-276 corrosion to occur, there must first be a breakdown of the passivating layer (chromium oxide) formed on the alloy surface. Petterssone et al.[17] studied KCl reactions with steels under O_2 and H_2O. They found that the potassium (rather than the chlorine) attacks the protective chromium oxide layer, thus exposing the alloy to a corrosive environment. They also demonstrated that when chromium is rapidly extracted from the alloy bulk chromium diffuses to the surface to replace the chromium lost in the oxide layer. It follows that if the alloy is low in chromium the oxide layer cannot be replenished with chromium fast enough to reform, leading to exposure of the surface to an oxidizing environment.[17] This study suggests that when the (low chromium) Hastelloy reacts with sufficiently high levels of Na^+, K^+ or Rb^+, the protective passivation layer on the alloy can be compromised. Thus, once the Hastelloy surface has corroded it is likely that subsequent runs, even at low salt concentrations, may cause nickel dissolution from the vessel. In this connection we occasionally detected small

pieces of the vessel wall flaking off under standard reaction conditions following a corrosive solution run. A compositional analysis of the sample revealed Ni, Cr, Mo, and Fe (see Figure 8) -- the main component in Hastelloy C-276. Interestingly, the latter particle also contained Mg, Si and O, not found in Hastelloy, suggesting the possible precipitation of olivine reactant constituents within the same particle (deposition of reactant olivine particles on the Hastelloy grain surface). Further evidence of vessel corrosion is indicated by the present of a thin green film composed primarily of olivine and silica, following most reactions. Combined with all the other evidence, the vessel it believed to be the largest contributor to the source of nickel in the carbonate particles.

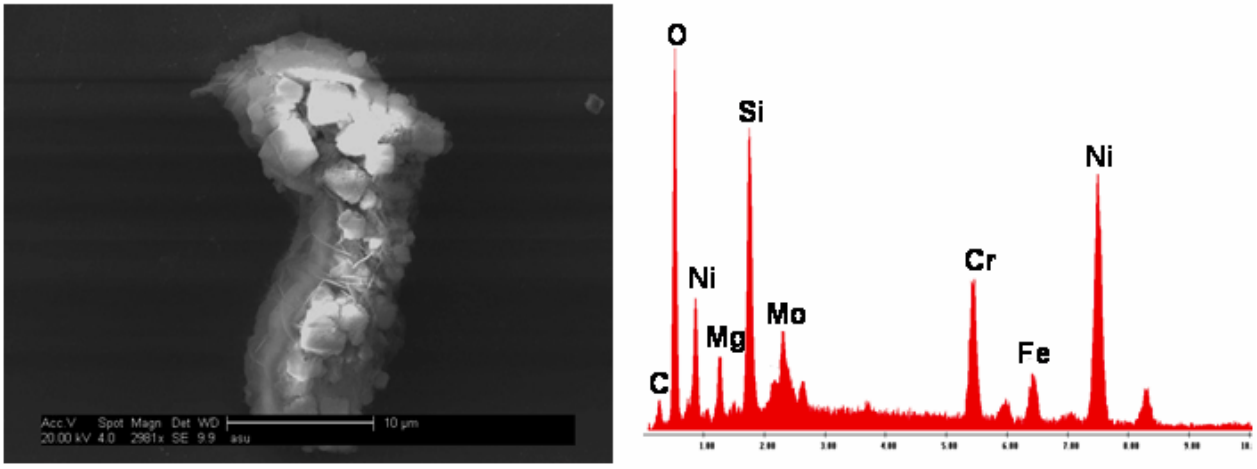

Figure 8: *Particle on surface of olivine single crystal reacted in 1.0M NaCl/0.64M $NaHCO_3$ with 75-100µm olivine powder and corresponding spectrum.*

To negate the potential corrosive effects of the high concentration salt solutions we fitted the reaction vessel with a Teflon cup. A Teflon sleeve was also fabricated to cover the temperature probe (also made of Hastelloy C-276). Although the Teflon cup was large enough to completely contain the solution, it did not cover the entire inner reaction vessel alloy surface and consequently a small amount of contamination was still detected. As a next step, the vessel and probe were re-machined, polished and then coated with 0.001 inches of platinum. Unfortunately, reaction studies using this coating approach still yielded reaction particles containing minor amounts of nickel. Post-reaction analysis revealed the presence of small black spots and particles in the vessel (not on the probe) suggesting that the platinum layer was not continuous. Accordingly, the entire vessel and probe were machined and polished to a depth sufficient to expose new metal that had not been corroded. Finally, a heat treatment step then produced an oxide passivation layer on the alloy, preventing any nickel contamination. Our studies indicate that prolonged reaction runs involving high salt concentration buffer solutions likely lead to permanent alloy damage, and nickel leaching and that the Hastelloy C-276 reaction vessel can not be used to systematically study these systems under high temperature and pressure conditions using these buffers.

3. Scientific Progress: *Mineral carbonation investigations into the mechanisms that control aqueous olivine mineral carbonation*

In our YEAR 2 studies we found that both 2.5M $NaHCO_3$ and 5.5M $KHCO_3$ solutions had shown high carbonation. A plot comparing the extent of carbonation versus concentration for both $NaHCO_3$ and $KHCO_3$ is shown in Figures 9 below. Both salts show similar effect on carbonation, increasing as a function of the bicarbonate salt concentration up to a certain limit before dropping thereafter. This limit is ~2.5M for [$NaHCO_3$] and ~5.5M for [$KHCO_3$].

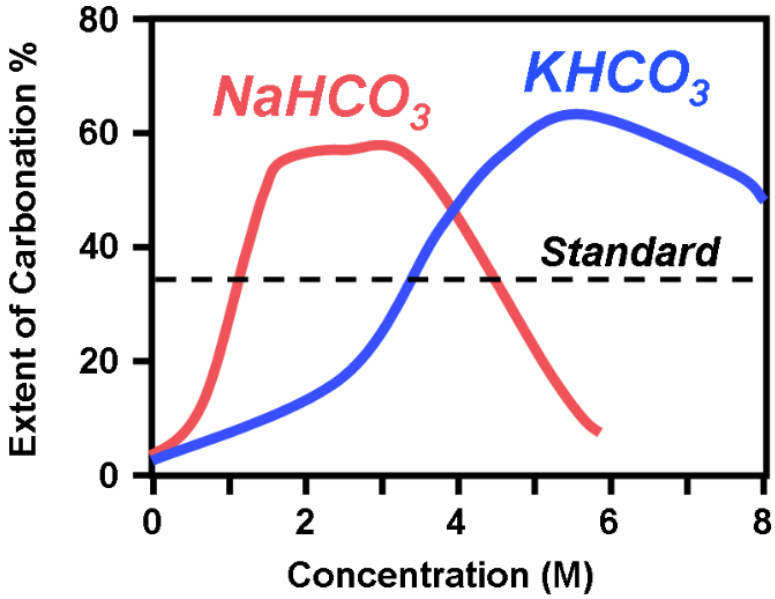

Figure 9: *Extent of carbonation of San Carlos Olivine as a function of $NaHCO_3$ and $KHCO_3$ concentration after 1h at 185°C, 2200psi of CO_2, and stirring at ~1500rpm. Dashed horizontal line represents the extent of carbonation (~34%) of a run using the standard solution 1.0M NaCl + 0.64M $NaHCO_3$.*

Given that these salts have different solubilities, there is good reason to suspect that these maximum carbonation limits may correspond to the respective saturation limits of these salts.

To further elucidate the origin of the enhanced reactivity under high concentrations of alkali bicarbonates we undertook a brief study of the nano-morphology of the reacted samples during our no-cost extension period. Figure 10 shows secondary electron images taken of olivine grains tested in different solutions but under similar conditions as compared with unreacted olivine grains. Reaction in water and CO_2 shows very little carbonation (~3%). The grains show little change, with only some isolated islands of silica–rich layers and very few crystals of $MgCO_3$ (Figure 10(b)). Reacting the olivine in a solution of 2.5M $KHCO_3$ shows larger amount of $MgCO_3$ crystals and a thick and continuous layer of amorphous silica around the reacting grains (Figure 10(c)). At the same conditions, reaction of olivine in a solution of 2.5M $NaHCO_3$ produces a substantial amount of $MgCO_3$, in form of rhombohedral crystals forming and clustering in the solution and intergrown with the silica-rich amorphous phase around the olivine grains (Figure 10(d)). The latter is found to fracture and exfoliate, exposing fresh surface of olivine for further reaction. When comparing the reaction product of this experiment presenting

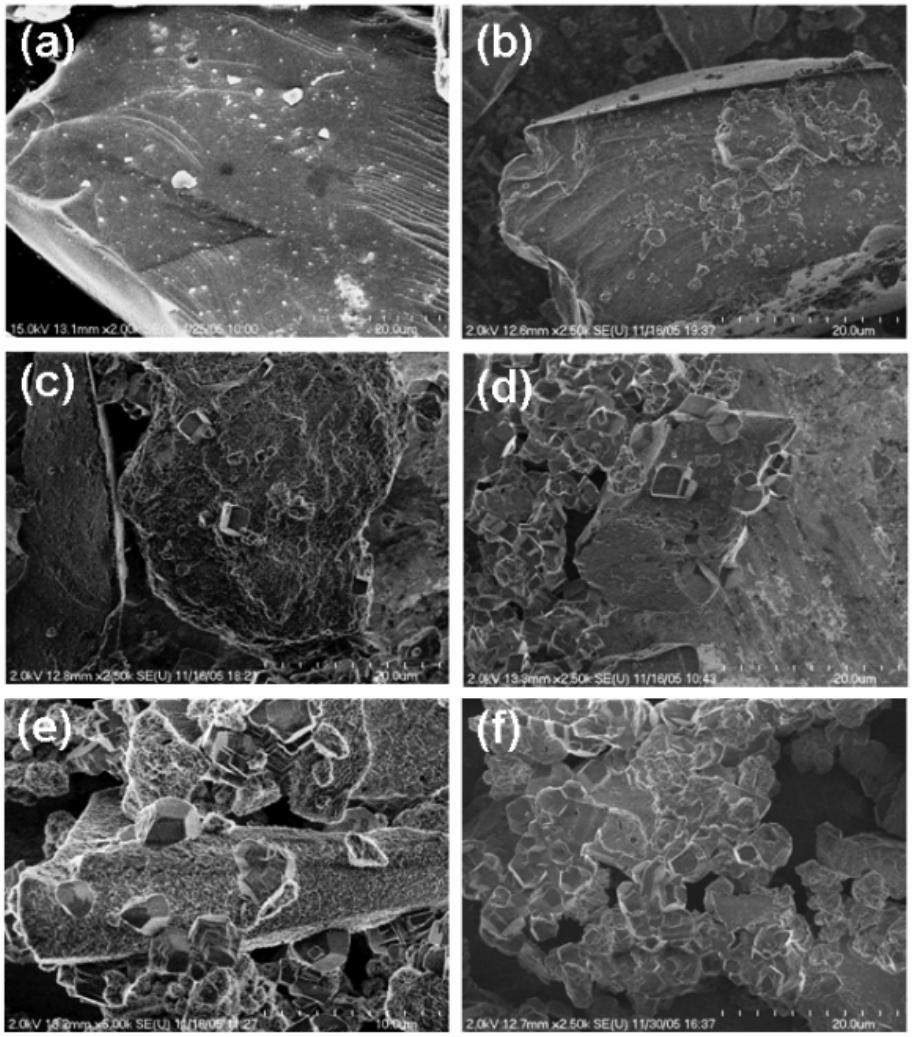

Figure 10: *FESEM secondary electron images of olivine: (a) unreacted; (b) reacted in H_2O under 2200psi of CO_2; (c) reacted in 2.5M $KHCO_3$ under 2200psi CO_2; (d) reacted in 2.5M $NaHCO_3$ under 2200psi CO_2; (e) reacted in 5.5M $KHCO_3$ under 2200psi He; (f) reacted in 5.5M $KHCO_3$ under 2200psi CO_2. All experiments were performed at 185°C and stirred at 1500rpm.*

the showing maximum carbonation result for sodium salts with that obtained with for maximum carbonation result for potassium salts (5.5M $KHCO_3$) one notices the similarity in form of the silica layer (porous, fractured, and with a cauliflower morphology). However, these experiments give carbonate products different in aspect: almost complete rhombohedra for the former and incomplete pyritohedra for the latter (Figure 10 (d) and (f)). These incomplete pyritohedra are also observed in the reaction product of the olivine in 5.5M $KHCO_3$ under helium as shown in Figure 10(e). It is worth noting that in the latter experiment the silica-rich layer has a significantly different morphology than in the other experiments. In particular, its open "spongy" structure suggests that its mechanical properties may be solution chemistry and pH dependent.

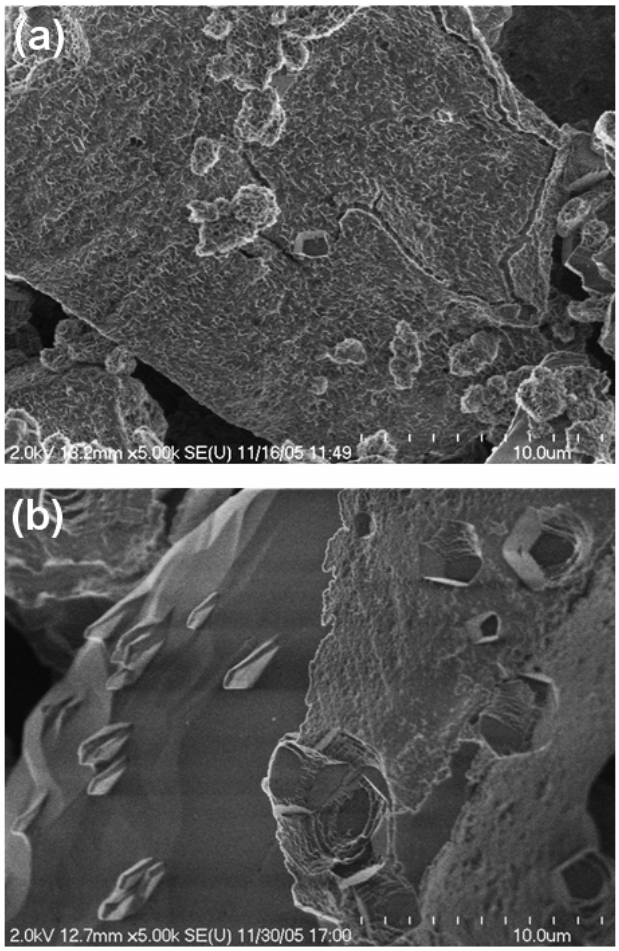

Figure 11: *Secondary electron images of reacted San Carlos olivine grains in 5.5M $KHCO_3$ solution for 1h at 185C and stirring at 1500rpm: (a) under 22psi of He; and (b) 2200psi of CO_2. Note the continuous Si-rich layers in the former run and the cracked and exfoliating layers in the latter.*

As the HCO_3^- is depleted through precipitation of $MgCO_3$, and is not regenerated through dissolution of CO_2, as in the run under CO_2 pressure, the solution chemistry changes and certainly the pH, too. Under 2200psi He, the reacting olivine grains appear to be wholly covered with the Si-rich spongy layers as shown in Fig 11(a), while under 2200psi CO_2 the Si-rich layers appear to be cracked, exfoliating, and thus exposing fresh olivine surface for further reaction (see Fig 11(b)). The morphology of the Si-rich layers observed in these cases strongly suggests that they may have different mechanical properties, such as hardness/elasticity, leading to different passivating effects.

CONCLUSIONS

During the no-cost extension period we extended our mini-reactor slurry-flow dynamics simulations to the case of mono-disperse 75 μm olivine particles. As in the case of the 38 μm and 150 μm flow visualizations indicate a swirling flow pattern that is formed in the cylinder. The flow is characterized by radially outwards motion along the cylindrical walls, followed by "crawling" along the sidewalls, and finally recirculating along the central axial shaft. Velocity profiles of the solids phase and aqueous phase indicate differences in the volume fraction

distribution for each phase, which varies with the size fraction under consideration. The 75 μm particle distributions are intermediate to those for the 38 μm and 150 μm particles. However, the volume fraction distribution for the larger particles was concentrated around the reactor walls, unlike the smaller particle size simulations, where the volume fraction distribution was more uniform across the reactor.

We also used the no-cost extension period to study in detail the influence of nickel contamination associated with reaction runs involving high concentration $NaHCO_3$ and $KHCO_3$ solutions. Prolonged use of the mini-reactor under these harsh conditions requires re-machining, polishing and annealing of the Hastelloy reactor wall material in order to avoid subsequent nickel contamination. The dominant source of nickel was identified as the reactor vessel Hastelloy C-276 alloy. A detailed understanding of the interaction of corrosive solutions with the reactor walls is critical to the practical implementation of any above-ground sequestration process involving the new class of high concentration bicarbonate solutions.

Finally, at the end of the performance period we undertook a brief study of the morphology of the carbonate products obtained in the high carbonation 2.5M $NaHCO_3$ and 5.5M $KHCO_3$ solution studies, identified as new high efficiency mineral sequestration process candidates. Further studies should be aimed at elucidating the origin of the decrease in the extent of carbonation beyond these saturation limits. We anticipate that measurement of CO_2, HCO_3^- and CO_3^- activities at these conditions (using our recently developed high-pressure, high-temperature NMR) may shed some light on the behavior of the CO_2 solubility in this high-concentration regime.

REFERENCES

1) Bearat, H.; McKelvy, M.J.; Chizmeshya, A.V.G.; Gormley, D.; Nunez, R.; Carpenter, R. W.; Squires, K.; Wolf, G.H. *Environmental Science & Technology* **40**(15), 4802-4808 (2006).
2) *Carbon Sequestration Research and Development*, Offices of Science and Fossil Energy, U.S. Department of Energy (December 1999), and references therein.
3) Seifritz, W. *Nature* **345**, 486 (1990).
4) Lackner, K.; Wendt, C.; Butt, D.; Joyce Jr., E.; Sharp, D.; *Energy* **20**, 1153-70 (1995).
5) O'Connor, W., et al. *Proc. 25th Int. Tech. Conf. Coal Util. & Fuel Syst.* pp. 153-64 (2000).
6) O'Connor, W.K., et al. *Proc. 27th Int. Tech. Conf. Coal Util. & Fuel Syst.* pp. 819-30 (2002).
7) *Novel Approaches to Carbon Management* (National Academies Press, Wash. D.C., 2003)
8) O'Connor, W.K.; Walters, R.P.; Dahlin, D.C.; Rush, G.E.; Nilsen, D.N.; Turner, P.C.; *Proc. 26th International Technical Conference on Coal Utilization & Fuel Systems*, 765 (2001).
9) O'Connor, W.K.; Dahlin, D.C.; Rush, G.E.; Gerdemann, S.J.; Penner, L.R. *Proc. 29th International Technical Conference on Coal Utilization & Fuel Systems*, 71 (2004).
10) Yu, S.C.; Proc. Nat. Sci. Counc. A. ROC, **21**, 173 (1997).
11) Ottonello, G.; Princivalle, F.; Della Giusta, A.; *Phys. Chem. Miner.* **17**, 301 (1990).
13) Galoisy, L., Calas, G., Brown Jr., G.E. Amer. Mineralogist. **80** 1089 (1995).
14) "Magnesite: Mineral Data," <http://webmineral.com/data/Magnesite.shtml > (accessed Feb. 2007).
15) "Gaspeite: Mineral Data," <http://webmineral.com/data/Gaspeite.shtml> (accessed Feb. 2007).
16) Haynes International. "Hastelloy C-276." Product Brochure.
17) Pettersson, C., Pettersson, J., Asteman, H., Svensson, J.E., Johansson, L.G. Corrosion *Science*. **48,** 1368 (2006).

APPENDIX A

"*Simulation and modeling of a slurry mixture for applications to carbon-dioxide sequestration*"
Kringan K. Saha, Kyle D. Squires and Michael J. McKelvy,
in *Proceedings of the 6th International Conference on Multiphase Flow*, ICMF 2007, in Leipzig, Germany in July 2007

6th International Conference on Multiphase Flow,
ICMF 2007, Leipzig, Germany, July 9 – 13, 2007

Simulation and modeling of a slurry mixture for applications to carbon-dioxide sequestration

Kringan K. Saha†, Kyle D. Squires† and Michael J. McKelvy‡

†Mechanical and Aerospace Engineering Department, ‡LeRoy Eyring Center for Solid State Science,

Arizona State University

Tempe, AZ, 85287-6106, USA

squires@asu.edu

Keywords: multiphase flows, stirred reactors, Euler-Euler models, sequestration

Abstract

The principal objective of this work is the application and assessment of numerical simulations to predict the influence of solids size distribution on the flow fields in a stirred batch reactor. Mixing is achieved in the reactor configuration using six Rushton turbine blades mounted on a shaft inside a cylindrical vessel. The slurry is comprised of an aqueous phase comprised of water and supercritical carbon-dioxide and a granular solid phase with material characteristics matching those of olivine (raw mineral form of magnesium silicate). The multiphase flow has been modeled using an Eulerian-Eulerian method. Simulations were carried out for different mono-dispersed size fractions comprised of spherical particles with diameters of 37μm and 150μm and with an olivine mass loading of 0.15, (solids volume fraction of 10%). Momentum transfer between the phases, the solid-fluid drag, and the granular viscosity for the solids phase is modeled following the approach outlined by Gidaspow (1992). An algebraic formulation obtained by neglecting the convection and diffusion terms in the corresponding transport equation was used to model the granular temperature. The simulations show considerable variations in the solids distributions in the reactor for each size fraction. Flow visualizations indicate that a swirling flow develops within the reactor chamber, with the solids pushed to the bottom of the cylinder and gradually crawling along the sidewalls, and finally recirculating downwards along the central axis. Velocity profiles of the granular phase and the aqueous phase indicate differences in velocity profiles and volume fraction distribution for each size fraction computed, which also varies with the size fraction under consideration. The volume fraction distribution of the largest size fraction was concentrated around the reactor walls, unlike the smaller solid size fraction case, where the volume fraction distribution was more uniform. In addition, partial suspension, wherein solids remain at the bottom of the vessel, was observed for the 150μm diameter particles.

Introduction

Sequestration of carbon dioxide – capture, separation and storage or reuse – is of significant current interest as a means to stabilize and reduce concentrations of greenhouse gases. Of the various sequestration methods currently available, e.g., geological, ocean, biological, and terrestrial, mineral sequestration is a relatively new approach. Mineral sequestration may possess several advantages over other approaches. The process produces environmentally benign and geologically stable products for disposal, and provides the overarching motivation to the current study.

The chemistry behind mineral sequestration involves converting carbon dioxide in the presence of finely ground olivine ore (primarily consisting of magnesium silicate), which results in the formation of magnesite and silica. This reaction process is exothermic and a low-cost solution as external energy is not required for the reaction to progress. Because the natural reaction rate is too slow to be viable in applications, the reaction environment and the carrier solution are modified to accelerate the sequestration process (O'Connor *et al.* 2001, 2002, 2004), with experiments typically conducted at around 150 atmospheres and 185°C.

One of the most significant issues associated with mineral sequestration is process optimization of aspects controlled by the fluid dynamics of the multiphase mixture. McKelvy *et al.* (2006) studied the effects of volume fraction variation on the extent of carbonation where the extent of carbonation was measured as the amount of carbon dioxide converted to magnesium carbonate ($\mathrm{MgCO_3}$). Finely ground forsterite ore having chemical composition similar to olivine ore was used in experiments. The solids loading was varied from 1% to 20% (by weight). A systematic increase in extent of carbonation was measured with increasing weight percent of forsterite. The extent of carbonation peaked at approximately 18 weight percent solids, then decreased with increasing solids loading, as illustrated in Figure 1. Part of the increase in extent of carbonation with increasing solids loading depicted in the figure arises from the increase in available surface area as the solids fraction is increased. More

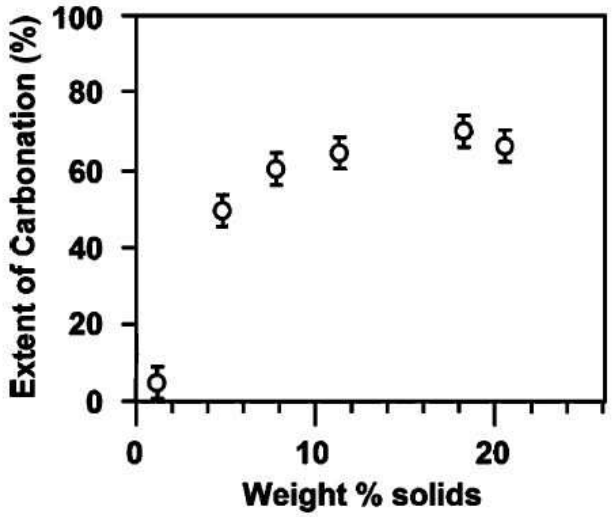

Figure 1: Extent of carbonation as a function of solids loading from McKelvy *et al.* (2006).

importantly, the figure shows a non-linear increase in extent of carbonation with increase in solids loading for lower loadings followed by a reduction in reactivity beyond 18%. This behavior provides evidence of additional mechanisms important to the reaction process, beyond those arising from a simple increase in surface area with solids loading.

Experiments conducted at Arizona State University (ASU) and the National Energy Technology Laboratory (NETL) as part of the current study indicate that extent of carbonation is correlated to the size distribution of the solids phase. To investigate size fraction effects, experiments were conducted using a solids phase (olivine ore) sieved into specific size ranges: a bulk sample consisting of particles less than 150μm in diameter, and more narrow distributions with particle diameters less than 37μm, within the range of 37μm-75μm, and less than 75μm. In the experiments summarized briefly in this manuscript, the solids mass loading is 10% for all cases. As will be highlighted in greater detail below, the extent of carbonation varies from as high as 36% to as low as 23%, depending on the particle size distribution.

The variation in reactivity highlights the complex dynamics governing sequestration processes and provides the main motivation for the present contribution focusing on the numerical simulation of the slurry flow in a stirred vessel. A simulation tool provides access to details of the flow that cannot be measured, enabling a broader understanding of certain aspects of the process and also laying the foundation for refined analysis and optimization of systems employed in mineral sequestration.

One of the challenges in assessing numerical simulations of such complex, three-dimensional and time-dependent flows are measurements that can guide assessment of simulation results. While there are not detailed measurements of the velocities and volume fraction distributions for the current configuration, a qualitative comparison is possible using the results reported by Whitelaw *et al.* (1992). In their experiments, laser Doppler velocimetry was used to study the motion of particles in solid-liquid turbulent flows in stirred vessels driven by Rushton turbine blades at rotation rates lower than those in the present work (150, 300 and 313 rpm). Whitelaw *et al.* (1992) investigated the effect of particle size, density, and volumetric concentration on velocity distribution. The maximum concentration was restricted to 2.5% due to limitations in the measuring technique employed.

Whitelaw *et al.* (1992) showed that the mean radial particle velocity in the impeller stream lagged behind the fluid and the lag was more pronounced near the plane of the impeller disc. Axial and radial particle mean velocities decreased with increasing particle concentration everywhere in the vessel. These investigators found that the radial and axial components of particle velocity also lagged the corresponding velocity components of the fluid in the regions near the impeller and the wall.

The main objective of the present effort is application and assessment of numerical simulation to the slurry flow in a stirred vessel. Summarized in the next section is the mathematical model followed by an overview of the experimental configuration and measurements that provide the basis for the current simulations. The numerical simulation procedures are then presented followed by a characterization of the flow using visualizations and statistics of the fluid and solids phases. Finally, a summary and perspectives on the work conclude the manuscript.

Approach

A multiphase, non-Newtonian, three dimensional computational model was used to predict the properties of the continuous aqueous and dispersed solids phases. The principal difference of the multi-phase model compared with a single-phase model is the appearance of the volume fraction for each phase, as well as terms that model the exchange of momentum and mass transfer between the phases (e.g., see Gidaspow 1994). The secondary solids phase consists of a few million micron sized particles and the computational expense associated with accounting for the motion of each particle restricts the use of particle-tracking approaches. Thus, an Eulerian-Eulerian multiphase model is applied in which the secondary granular phase is treated as a continua. In the current computations, the aqueous solution defines the primary carrier phase, while the secondary granular phase is defined by the finely ground olivine ore.

The mass balance for each phase is given by

$$\frac{\partial}{\partial t}(\alpha_q \rho_q) + \nabla \cdot (\alpha_q \rho_q \vec{v}_q) = 0 \qquad (1)$$

where ρ_q is density, α_q is volume fraction, and $\vec{v}_q$ represents the velocity of phase q. Further, the volume fraction occupied by each phase cannot be occupied by the other phase and the sum of the volume fractions must equal unity. Momentum transport for each phase q is given as,

$$\frac{\partial}{\partial t}(\alpha_q \rho_q \vec{v}_q) + \alpha_q \rho_q \vec{v}_q \cdot \nabla \vec{v}_q = -\alpha_q \nabla p + \alpha_q \rho_q \vec{g} + \nabla \cdot \overline{\overline{\tau}}_q + \sum_{q=1}^{n} K_{qp}(\vec{v}_q - \vec{v}_p) + \vec{F}_q \qquad (2)$$

where p is the pressure, $\overline{\overline{\tau}}_q$ is the stress tensor of the q^{th} phase, g is the gravity force and $\vec{F}_q$ is the external force. The term K_{qp} represents the interaction between the liquid and solid phases (q and p).

Aqueous phase stress tensor
The stress tensor of the aqueous phase is,

$$\overline{\overline{\tau_q}} = \alpha_q \mu (\nabla \vec{v}_q + \nabla \vec{v}_q^{\mathrm{T}}) + \alpha_q (\lambda_q - \frac{2}{3}\mu_q) \nabla \cdot \vec{v}_q \overline{\overline{I}} \quad (3)$$

Here α_q is the volume fraction of the liquid phase, $\overline{\overline{I}}$ is the unit tensor, and λ_q and μ_q are the bulk and the shear viscosities for the aqueous phase respectively.

Solids phase stress tensor
The stress tensor for the granular phase, resulting from the forces experienced by the particles as a result of contact with other particles is,

$$\overline{\overline{\tau_s}} = -p_s \delta + \alpha \mu_s (\nabla \vec{v}_s + \nabla \vec{v}_s^T) + \alpha_s (\lambda_s - \frac{2}{3}\mu_s) \nabla \cdot \vec{v}_s \overline{\overline{I}} \quad (4)$$

where δ is the Kronecker delta and the other terms are the corresponding values of the solids phase (e.g., the viscosities). The solids stress tensor contains shear (μ_s) and bulk viscosities (λ_s) arising from particle momentum exchange due to translation and collision. The solids shear viscosity is formed by adding the collisional and kinetic components. The solids bulk viscosity (λ_s) accounts for the resistance of the solids to compression and expansion and are modeled based on formulations proposed by Gidaspow (1994). The solids pressure p_s represents the inter-particle pressure which is due to the collision of the particles amongst themselves or with the surrounding walls. The solids pressure is calculated independently and used for the pressure gradient term, ∇p_s, in the granular-phase momentum equation. The solids pressure consists of a kinetic term and a second term due to particle collisions:

$$p_s = \alpha_s \rho_s \Theta_s + 2\rho_s (1 + e_{ss}) \alpha_s^2 g_{0,ss} \Theta_s \quad (5)$$

The term e_{ss} represents the coefficient of restitution, and it accounts for inelastic or elastic collisions. Since experimentally measured values of the coefficient of restitution are not available for the companion experiments, a value of 0.85 is assumed. The term $g_{0,ss}$ represents the radial distribution function, which is a correction factor that modifies the probability of collisions between grains when the solid granular phase becomes dense. The granular temperature, Θ_s, is proportional to the kinetic energy of the fluctuating particle motion and is derived from the kinetic theory of gases.

External forces
Solid particles suspended in the aqueous phase are subjected to drag by the surrounding fluid. The interphase momentum exchange coefficient (fluid-solid exchange coefficient K_{sl}) as proposed by Gidaspow (1994) is given by:

$$K_{sl} = \frac{3}{4} C_D \frac{\alpha_s \alpha_l \rho_l |\vec{v}_s - \vec{v}_l|}{d_s} \alpha_l^{-2.65} \quad (6)$$

where the drag coefficient C_d on a single sphere is related to the particle Reynolds number by:

$$C_D = \frac{24}{\alpha_l Re_s} \left[1 + 0.15(\alpha_l Re_s)^{0.687}\right] \quad (7)$$

Particles obtained by grinding olivine ore for use in the experiments exist in a variety of shapes and are represented as spheres in the simulations. Further, particle size reduction and mass transfer due to reaction with the surrounding aqueous medium is not considered in the present simulations.

The simulations are performed using FLUENT ($ver.$ 6.2.16), which employs a finite-volume method to solve the governing equations. The solutions are obtained using staggered grids. A phase coupled SIMPLE (PC-SIMPLE) algorithm (Vasquez 2000) is used for obtaining a solution to the flow field. The k-ϵ Reynolds-averaged Navier Stokes (RANS) model was used to represent the effects of fine-scale turbulence. Standard values of the model constants were retained in the k-ϵ model. To ensure proper treatment for each phase, a per phase k-ϵ turbulence model was used. Coupling between the phases was achieved using inter-phase momentum transfer terms that account for the momentum transfer between the solid olivine phase and the aqueous phase formed by mixing water and $\mathrm{CO_2}$.

Experimental Configuration

Experiments were conducted using a mini-reactor based on an autoclave mechanism at ASU. An EZE-Seal Hastelloy C-276 autoclave reactor manufactured by Autoclave engineers was deployed for the reactions. The mini-reactor is constructed using a cylindrical vessel with a volumetric capacity of 120 ml. A pump operating at 1500 rpm rotates a Rushton turbine impeller mounted on a shaft placed axially within the cylinder, which mixes the slurry. The experimental setup is shown in Figure 2. The pump driving the Rushton turbine is located at top of the figure, while the mini-reactor chamber containing the slurry is in the lower region. An open view of the reactor shows the Rushton turbine. Reaction steps involve filling the reactor with a measured amount of slurry (50 ml), elevating the temperature to 185°C and then charging the system to a pressure of 165 atmospheres by injecting carbon dioxide. The valves are closed to seal the system and the reaction is allowed to progress for an hour under continuous stirring. The reactor is finally cooled to room temperature by circulating cooling water through the cylinder body, following which the contents of the reactor are emptied, filtered, dried and sampled for analysis.

To enhance understanding of the flow patterns occurring in the mini-reactor and to circumvent visibility issues, a reactor with dimensions identical to the Hastelloy reactor was fabricated from transparent plexiglas. The outer body of the reactor was machined with plexiglas, while the Rushton turbine blades from the previous setup were used. Since plexiglas cannot maintain its structural integrity under high temperature and pressure, the operating conditions for experiments conducted using the plexiglas reactor were maintained at room temperature and pressure.

Experiments conducted in the plexiglas reactor were solely for the purpose of studying the flow patterns and the samples

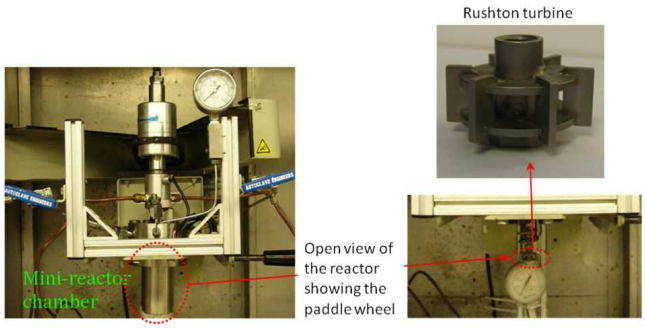

Figure 2: Mini-reactor configuration used in experiments conducted at Arizona State University.

used in these experiments were not used for reactivity analysis. Experiments were performed using 120 ml of distilled water solution with 10 grams of olivine at room temperature and pressure. The impeller speed was varied to study the lift of the particles for different size fractions and different speeds. Impeller rotation was varied from 1500 rpm to 5000 rpm and three size fractions of $<37\mu$m, 37-75μm and 75μm-150μm were visualized.

Simulation Approach

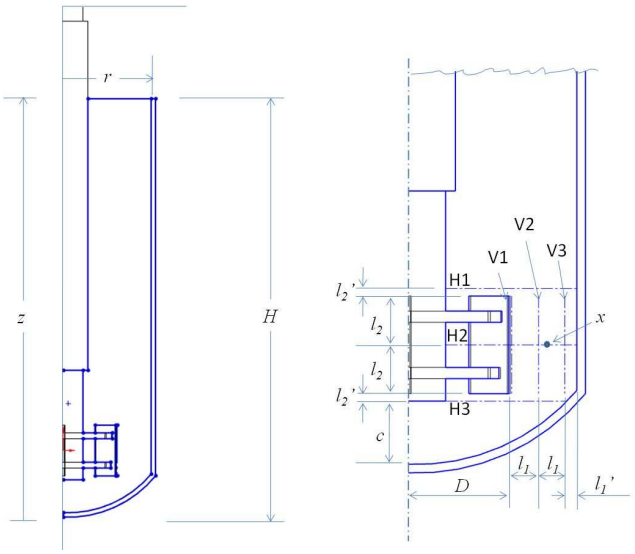

Figure 3: CAD geometry of ASU Mini-reactor.

Figure 3 shows a wire frame view of the mini-reactor, the feature dimensions of which are detailed in Table 1.

The mesh generated consists of both structured and unstructured grids and is shown in Figure 4. To reduce the computational expense, the symmetry of the reactor is utilized and grid generated for only one-sixth of the geometry. Periodic boundary conditions are applied to the solution variables at the bounding planes. Periodic boundary conditions imply that the volume of fluid and particles crossing either of the bounding planes then re-enters the domain at the other plane. Periodic faces along the sides have been opened in Figure 4 to show the arrangement of the blade that is attached to two discs located at the bottom of the axially running shaft.

Variable	Value in mm
H	85
D	15.5
c	7.5
r	22.5
l_1	2.3
l_1'	1.1
l_2	15
l_2'	5

Table 1: Mini reactor dimensions

Meshing the hemispherical bottom of the reactor part using a structured grid resulted in distortion of the geometry and the spherical shape of the bottom could not be maintained. To avoid a drastic change in the geometry of the model, an unstructured grid was used, which helped retain the near hemispherical shape at the bottom of the cylinder. The initial mesh consisted of approximately 2.25×10^6 cells. This mesh when imported to Fluent could not be used to obtain a flow solution using available computer resources. The grid generation task was then repeated in order to develop a coarser grid consisting of approximately 1.3×10^5 cells, which was subsequently used in the initial computations.

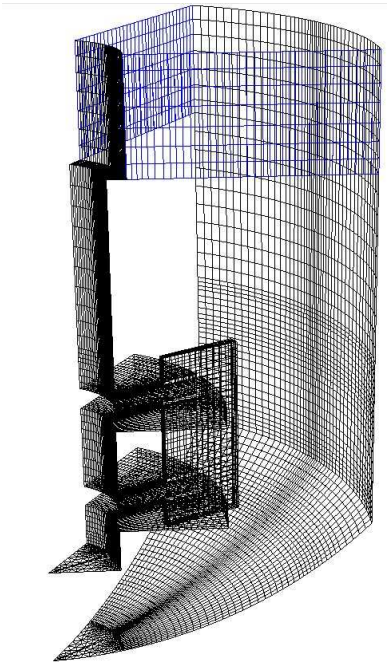

Figure 4: Initial coarse mesh of the mini-reactor.

In the simulations, the solids phase was initially seeded at the bottom of the vessel at the maximum permissible packing limit of 63%. Values of density and viscosity as obtained from the NIST thermo-chemistry database were used to specify material properties. The density of the liquids phase is obtained by assuming a homogeneous mixture of water and carbon-dioxide at the elevated temperature and pressure. Based on this assumption, a value of 550 kg/m^3 was obtained for the aqueous phase. Measured viscosity values of the mixture consisting of water and carbon-dioxide at

elevated temperature and pressure are unavailable. Hence, water viscosity at the elevated thermodynamic conditions (1.4928e-4 cP) was used. The simulations were performed under isothermal conditions and the elevated temperature characterizing the experiments was accounted for the density and viscosity values of the mixture.

The configuration consists of multiple moving parts (central shaft, blades) and has stationary surfaces (outer cylinder) in the same geometry. The model is then divided into multiple zones - stationary and rotating with interface boundaries separating the zones. A Multiple Reference Frame (MRF) model detailed by Luo *et al.* (1994), which provides a solution for problems involving rotating geometries is used to model the problem. The mesh used in the model is divided into rotating and stationary zones. At the interfaces between these zones, a local reference frame transformation is performed to enable flow variables in one zone to be used to calculate fluxes at the boundary of the adjacent zone. The relative motion of a moving zone with respect to adjacent zones, which may be moving or stationary, is not accounted for as the grid remains fixed for the computation in the MRF model.

Simulation results which are detailed in the following sections were obtained using a time step of 5.56e-4 seconds, which corresponds to a shaft rotation of 5 degrees. This, in turn, corresponds to an impeller rotational speed of 1500 rpm. Numerical tests show that convergence of the system of equations occurs after approximately 25 sub-iterations within each time step (1800 time steps are required for 1 second and each time step requires approximately 25 iterations to converge). Preliminary simulations performed with smaller time steps (2 degrees per time step) did not yield significant changes in the results.

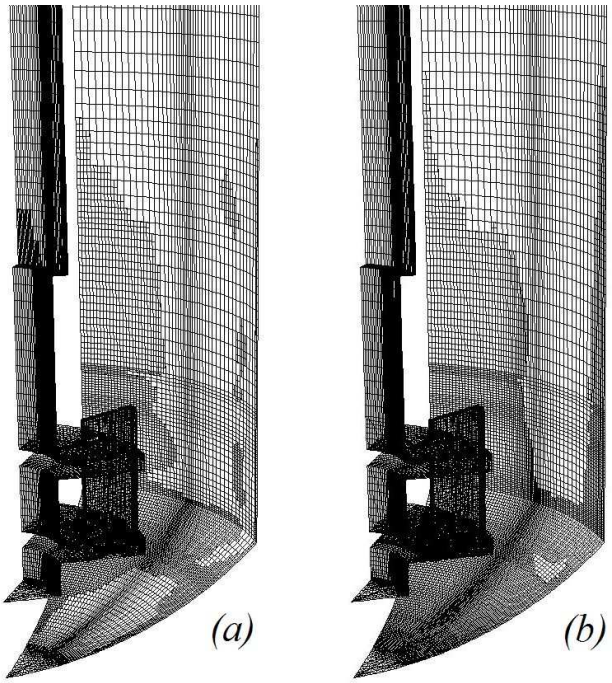

Figure 5: Adapted mesh for (a) 37μm case; (b) 150μm case

Two mono-disperse size fractions – 37μm and 150μm – are considered in the computations with the initial converged solution obtained using the coarse mesh. The initial solution was assessed at time equal to 5 seconds of rotation and was characterized by regions of relatively sharp gradients in velocity and volume fraction. An adaptive meshing scheme was subsequently used to refine the mesh only in the regions where the gradients were large across cell zones. The solution-adaptive mesh refinement allowed the grid to be refined based on geometric and numerical solution data. Using this method, the cells are added only to regions where additional resolution is needed. The initial coarse-mesh solution was used to determine regions where additional cells were required.

Following the initial simulations, a gradient adaptation function based on volume fraction gradients of the solids phase was used to refine the grid. This adaptation process was carried out for each size fraction. The mesh structure for the 37μm and 150μm size fraction simulations following the adaptation process is shown in Figures 5. The figure shows that the regions in which the grid is refined are different for each size fraction, consistent with the different volume fraction distributions (gradients) obtained. The visualizations and statistical properties summarized next are obtained using the adapted grid.

Results

Reactivity Measurements

Particle size Feedstock (μm)	Extent of Carbonation (%)	Size fraction below $<$37μm (%)
$<$37	35.7	96.1
37-75	5.35	16.6
$<$75	31.4	72.1
$<$150	23.75	53.8

Table 2: Measured carbonation levels in the ASU mini-reactor using San Carlos olivine.

Extent of carbonation achieved after an hour of reaction in the ASU mini-reactor, using a range of size fractions of feedstock material is detailed in Table 2. The table reflects the extent of reaction averaged over a few runs. The $<$37μm feedstock sample after an hour of reaction, exhibited an average extent of carbonation of 35.7%, while the feedstock sample in the $<$75μm size range displayed a corresponding average extent of carbonation of 31.4%. The extent of carbonation decreased with increasing feedstock size fraction, which becomes more evident for the $<$150μm size fraction, where the measured extent of carbonation was 23.75%. Another interesting observation is the drastic drop in the extent of carbonation for an intermediate size range of particles (37μm-75μm), with the extent of carbonation decreasing to 5.35%.

To understand surface area effects on extent of carbonation for different size fractions, a sedigraph particle size analyzer was used to perform surface area and size analysis of feedstock and product samples. The third column of Table 2 indicates the exposed surface area of the feedstock sample below 37μm. If a linear relationship is assumed between the

reactivity and surface area, then the reactivity contribution in the <75μm by the <37μm for the feedstock sample will be approximately 25%. Similarly, for the <150μm sample, the corresponding value is 19.2%. The additional increase in the extent of carbonation caused by addition of particles larger than 37μm does not follow a linear relationship. This indicates that there are factors other than the exposed surface area available for carbonation playing an important role.

Simulation Results

To analyze the motion of particles within the reactor, flow visualization of velocity vectors and line plots of velocity at different regions of the reactor are presented. Velocities were plotted at horizontal test locations identified as H1, H2 and H3 in Figure 3 and also at vertical locations V1, V2, and V3. Data locations H1 and H3 are located 0.5 centimeter above the turbine blade, while the data location H2 bisects the blade horizontally. Similarly, along the vertical direction, locations V1, V2, and V3 are marked equidistant in the region between the blade and cylinder walls. Data location V1 is adjacent to the blade.

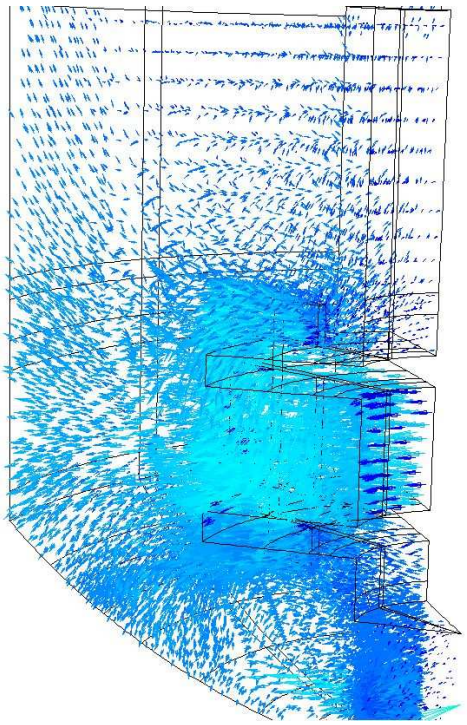

Figure 6: Aqueous phase velocity vectors.

Aqueous phase velocity vectors in the lower region of the reactor are shown in Figure 6. The figure highlights the movement of the slurry within the vessel, the vectors being aligned along two main directions: a diagonally upward direction and a downward direction along the hemi-spherical bottom walls. These vectors indicate existence of two distinct loops that are formed in the reactor - one above and one below the impeller. Mixing of the aqueous phase with the solids phase occurs because of these flow loops. Studies have shown that flow patterns formed depend on a variety of factors, including geometry of the blade, reactor shape, size, distance of impeller blade from reactor walls, speed of impeller, density and viscosity of solids, and aqueous phases (Paul *et al.* , 2004).

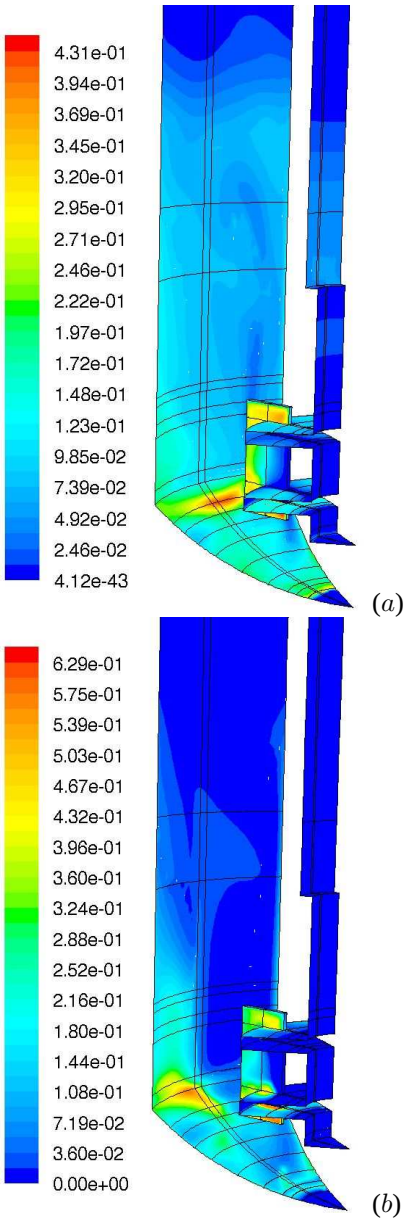

Figure 7: Volume fraction contours of olivine on the adapted mesh. (a) 37μm case; (b) 150μm case.

Contours of the olivine volume fraction for the 37μm and 150μm size fractions in the lower region of the reactor are shown in Figure 7. Comparison of the contours for different size fractions indicate a sharp contrast in the volume fraction distribution for each diameter. The solids are more evenly dispersed into the upper regions of the reactor for the smaller size fraction (37μm) as opposed to the larger size fraction (150μm). The impellers generate a flow pattern indicated by the vector plot shown in Figure 6 which sweep the particles from the cylinder bottom and suspends them into the reactor. The cloud height, defined by the distance from the bottom

of the cylinder to the height at which most of the solids are lifted again depends on many different factors, one of which is impeller rotational speed. Experiments using the plexiglas reactor, where the rotational speed of the impeller was varied from 1500 rpm to 4000 rpm showed that the solids were observed to reach greater cloud heights at higher speeds. However, turbidity of the slurry solution prevented actual measurement of cloud heights for the experiments performed. In the contours shown in Figure 7, a band of elevated volume fraction is observed at the hemispherical bottom region of the reactor for both particle sizes. This is the region where the slurry flow distributes into the upper loop and the lower loop and forms a region of high olivine concentration.

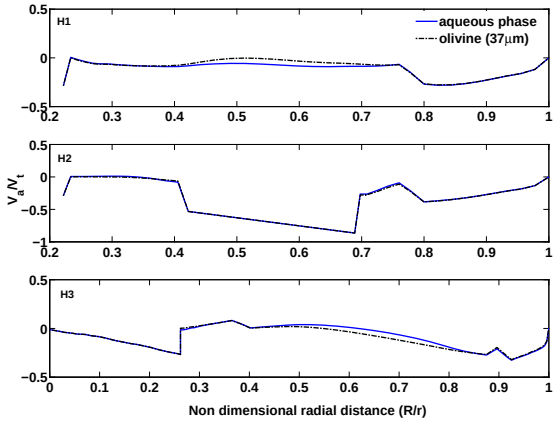

Figure 8: Axial velocities of the aqueous phase and olivine (37μm case) at horizontal locations.

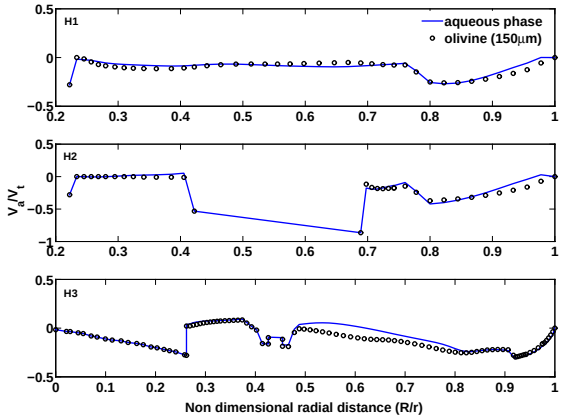

Figure 9: Axial velocities of the aqueous phase and olivine (150μm case) at horizontal locations.

Axial velocities at horizontal test locations H1, H2 and H3 for the 37μm and 150μm cases are shown in Figures 8, 9 and 10, with analogous plots of the radial velocities at vertical test locations V1, V2 and V3 shown in Figures 11, 12 and 13. The velocities shown in Figures 8- 13 have been non-dimensionalized by the absolute velocity at the outer tip of the impeller blade (V_t). Further, the radial locations within the reactor have been non-dimensionalized with the radius of the vessel at the corresponding horizontal location.

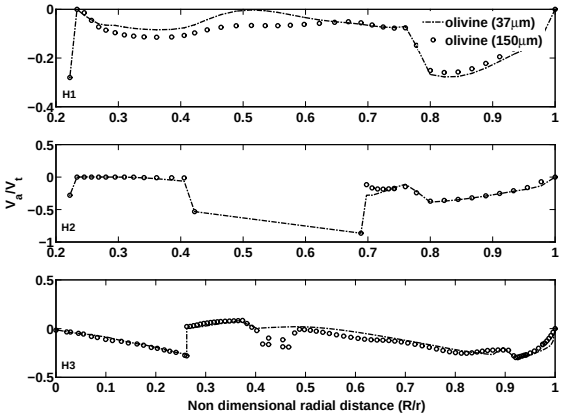

Figure 10: Axial velocities of the solids phase.

Figures 8 and 9 show axial velocities of the aqueous and solids phases for simulations conducted using the 37μm and 150μm size fractions, respectively. In both the cases, the axial velocity of the solids lags the corresponding aqueous phase velocity in the region below the impeller (H3). In region above the impeller (indicated by H1), the smaller size fraction 37μm case leads the aqueous medium in certain zones. On the other hand, for the 150μm case, the axial velocity of the particles are observed to be higher than corresponding aqueous phase values for the region above the impeller and lower in regions closer to the shaft and cylinder wall. However, in the central zone (H2), the particles closely follow the fluid for both size fractions. The axial velocities indicate the speed at which the particles are being displaced along the vertical direction and are critical because a difference in axial velocities in the same vertical plane could be an indication of higher probability of collisions amongst the particles.

Axial velocity magnitudes in the region close to the impeller for test locations H2 and H3 indicate that the particles at H2 are being directed downwards with a velocity magnitude that is twice the corresponding values in region H3. For data locations H1, H2 and H3, the magnitudes of axial velocity were observed to decrease in regions closer to the cylinder walls. This variation in the velocity could be indicative of an abrasion mechanism occurring amongst the particles moving in the vertical direction. Another interpretation of the axial velocity magnitude variation is a circular flow pattern occurring within the reactor in regions below the blade. Visual observation of experiments performed with a plexiglas reactor confirm this interpretation.

Two distinct swirling flow patterns were observed in the vertical planes of the reactor - a counter clockwise flow pattern directed upwards and a clockwise flow pattern directed to the bottom of the reactor. Figure 10 provides an indication of the difference in velocities for different size fractions along the axial directions. A very minor difference in the velocities of different size fractions is observed at the central location H2, whereas in the regions above and below the blade (H1 and H3) respectively, the axial velocity of the 150μm particle is slightly higher than for the smaller particles.

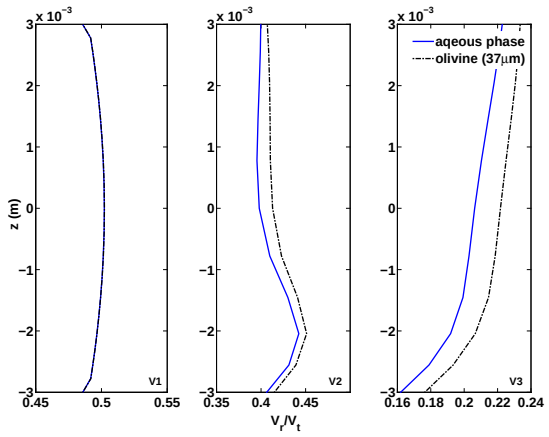

Figure 11: Radial velocities of the aqueous phase and olivine (37μm case) at vertical locations.

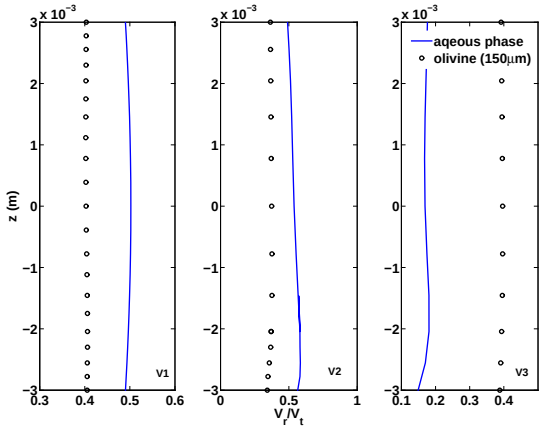

Figure 12: Radial velocities of the aqueous phase and olivine (150μm case) at vertical locations.

Radial velocities are shown at vertical locations V1, V2 and V3 for both size fraction with differences observed in the radial velocity patterns shown in Figures 11 and 12. These figures highlight distinct velocity patterns for the smaller and larger particle sizes. For the smaller size fraction, radial velocities of the aqueous phase closely match the solids phase near the blade, while the particles tend to lead the fluid in regions near the cylinder walls. There is a substantial reduction of both aqueous phase and particle phase velocities away from the blade and near the cylinder walls. The aqueous phase displays a similar pattern of axial velocity reduction along the radially outward direction for the larger particle size. However, the radial component of particle velocities for the larger size fraction remains steady along the radial direction. Further, for the 150μm case, the particle radial velocity component lags the corresponding aqueous phase velocity component in the vicinity of the blade and leads in the regions in the vicinity of the wall.

Differences in the velocities of the 37μm and the 150μm size fractions can be observed in Figure 13. Regions in the reactor closer to the wall are the regions where the larger particles move at higher velocities than the smaller particles, while in the regions closer to the blade, the smaller particles move at higher velocities than the large particles. In the experiments performed by Whitelaw *et al.* (1992), it was observed that the solids phase lagged or led the bulk carrier fluid when the flow direction was upwards or downwards, respectively, in qualitative agreement with the present results.

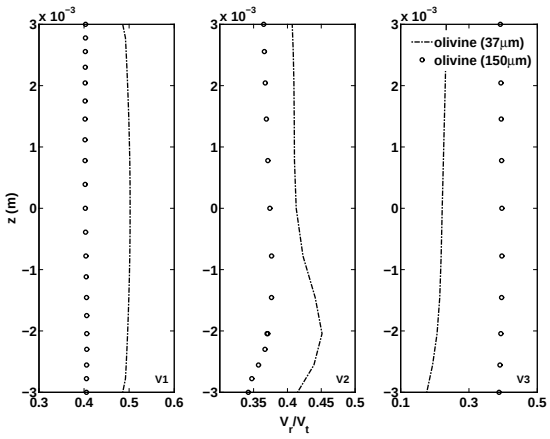

Figure 13: Radial velocities of the solids phase.

Conclusion

Hostile operating conditions prevent direct experimental measurements of velocity fields and volume fraction distribution of solids and the aqueous phase within stirred reactors used in sequestration applications. Numerical models therefore have an important role to play, allowing access to details of the flow that cannot be measured. In the present work, flow visualizations indicate development of swirling flow within the reactor chamber, which is consistent with the experimental observations performed using a plexiglas model. The swirling flow pattern that is formed in the cylinder results in the slurry being thrown radially outwards along the cylindrical walls, which then crawls along the sidewalls, and finally recirculates along the central axial shaft. Velocity profiles of the solids phase and aqueous phase indicate differences in velocity profiles and volume fraction distribution for each phase, which further varies with the size fraction under consideration. Volume fraction distribution of the larger particles was concentrated around the reactor walls, unlike the smaller size experiments, where the volume fraction distribution was more uniform across the reactor.

Acknowledgements

Financial support from the Department of Energy, USA under Award Number DE-FG26-04NT42124 is gratefully acknowledged. However, any opinions, findings, conclusions, or recommendations expressed herein are those of the author(s) and do not necessarily reflect the views of the DOE. The authors also thank the LeRoy Eyring Center for Solid State Science for use of the Goldwater Materials Science Laboratories and NETL for providing resources to conduct sequestration experiments.

References

Béarat, H., McKelvy, M.J., Chizmeshya, A.V.G., Sharma, R., Carpenter, R.W. Magnesium Hydroxide Dehydroxylation/Carbonation Reaction Processes: Implications for Carbon Dioxide Mineral Sequestration. J. Am. Ceram. Soc., 85(4), 742-748 (2002).

Béarat, H., McKelvy, M.J., Chizmeshya, A.V.G., Nunez, R., Carpenter, R.W. Investigations of the Mechanisms that Govern Carbon Dioxide Sequestration via Aqueous Olivine Mineral Carbonation. Proceedings of the 28th International Technical Conference on Coal Utilization & Fuel Systems, 1, 307-318 (2003).

Béarat, H., McKelvy, M.J., Chizmeshya, A.V.G., Gormley, D., Nunez, R., Carpenter, R.W., Squires, K., Wolf, G.H. Carbon Sequestration via Aqueous Olivine Mineral Carbonation: Role of Passivating Layer Formation. Environ. Sci. Technol., 40(15), 4802-4808 (2006).

Diefenbacher, J., McKelvy, M.J., Chizmeshya, A.V.G., Wolf, G.H. Externally Controlled Pressure and Temperature Microreactor for In Situ X-ray Diffraction, Visual and Spectroscopic Reaction Investigations Under Supercritical and Subcritical Conditions. Rev. Sci. Instrum., 76, 05103 (2005).

Gale, J. Geological Storage of CO_2: What do we know, where are the gaps and what more needs to be done?. Energy, 29, 1329-1338 (2004).

Gidaspow, D., Bezburuah, R., and Ding, J. Hydrodynamics of Circulating Fluidized Beds, Kinetic Theory Approach. Fluidization VII, Proceedings of the 7th Engineering Foundation Conference on Fluidization, 75-82 (1992).

Gidaspow, D. Multiphase Flow and Fluidization: Continuum and Kinetic Theory Descriptions. New York: Academic Press (1994).

Luo, J.Y., Issa, R.I., Gosman A.D. Prediction of Impeller-Induced Flows in Mixing Vessels Using Multiple Frames of Reference. IChemE Symposium Series, 136, 549-556 (1994).

Nouri, J.M., Whitelaw J.H. Particle velocity characteristics of dilute to moderately dense suspension flows in stirred reactors. Int. J. Multiphase Flow, 18(1), 21-33 (1992).

O'Connor, W.K., Dahlin, D.C., Nilsen, D.N., Walters, R.P., Turner, P.C. Carbon Dioxide Sequestration by Direct Mineral Carbonation with Carbonic Acid. Proceedings of the 25th International Technical Conference on Coal Utilization & Fuel Systems, 153-164 (2000).

O'Connor, W.K., Dahlin, D.C., Nielsen, D.N., Gerdemann, S.J., Rush, G.E., Penner, L.R., Walters, R.P., Turner, P.C. Continuing studies on direct aqueous mineral carbonation for CO_2 sequestration. Proceedings of the 27th International Technical Conference on Coal Utilization & Fuel Systems, 819-830 (2002).

O'Connor, W. K., Dahlin, D.C., Rush, G.E, Gerdemann, S. J., Penner, L.R. Energy and economic considerations for ex-situ and aqueous mineral carbonation. Proceedings of the 29th International Technical Conference on Coal Utilization and Fuel Systems, 71-82 (2004).

Paul E. L., Atiemo-Obeng, V.A., Kresta, S.M. Handbook of Industrial mixing. New Jersey: Wiley-Interscience (2004).

Seifritz, W. CO_2 disposal by means of silicates. Nature, 345, 486 (1990).

Thermophysical properties database at:
`http://webbook.nist.gov/chemistry/fluid/`

Vasquez, S. A., Ivanov, V. A. A Phase Coupled Method for Solving Multiphase Problems on Unstructured Meshes. Proceedings of ASME FEDSM'00: ASME 2000 Fluids Engineering Division Summer Meeting, Boston (2000).